COMPUTATIONAL FRACTURE PREDICTION IN STEEL MOMENT FRAME STRUCTURES WITH THE APPLICATION OF ARTIFICIAL NEURAL NETWORKS

A Dissertation

by

XIAO LONG

Submitted to the Office of Graduate Studies of
Texas A&M University
in partial fulfillment of the requirements for the degree of

DOCTOR OF PHILOSOPHY

August 2012

Major Subject: Civil Engineering

Computational Fracture Prediction in Steel Moment Frame Structures with the Application of Artificial Neural Networks

COMPUTATIONAL FRACTURE PREDICTION IN STEEL MOMENT FRAME STRUCTURES WITH THE APPLICATION OF ARTIFICIAL NEURAL NETWORKS

A Dissertation

by

XIAO LONG

Submitted to the Office of Graduate Studies of
Texas A&M University
in partial fulfillment of the requirements for the degree of

DOCTOR OF PHILOSOPHY

Approved by:

Chair of Committee,	Gary T. Fry
Committee Members,	Harry L. Jones
	Stefan Hurlebaus
	Anastasia Muliana
Head of Department,	John M. Niedzwecki

August 2012

Major Subject: Civil Engineering

ABSTRACT

Computational Fracture Prediction in Steel Moment Frame Structures with the Application of Artificial Neural Networks. (August 2012)

Xiao Long, B.S., Tsinghua University, China;

M.S., Tokyo Institute of Technology, Japan

Chair of Advisory Committee: Dr. Gary T. Fry

Damage to steel moment frames in the 1994 Northridge and 1995 Hyogken-Nanbu earthquakes subsequently motivated intensive research and testing efforts in the US, Japan, and elsewhere on moment frames. Despite extensive past research efforts, one important problem remains unresolved: the degree of panel zone participation that should be permitted in the inelastic seismic response of a steel moment frame. To date, a fundamental computational model has yet to be developed to assess the cyclic rupture performance of moment frames. Without such a model, the aforementioned problem can never be resolved. This dissertation develops an innovative way of predicting cyclic rupture in steel moment frames by employing artificial neural networks.

First, finite element analyses of 30 notched round bar models are conducted, and the analytical results in the vicinity of the notch root are extracted to form the inputs for either a single neural network or a competitive neural array. After training the neural networks, the element with the highest potential to initiate a fatigue crack is identified,

and the time elapsed up to the crack initiation is predicted and compared with its true synthetic answer.

Following similar procedures, a competitive neural array comprising dynamic neural networks is established. Two types of steel-like materials are created so that material identification information can be added to the input vectors for neural networks. The time elapsed by the end of every stage in the fracture progression is evaluated based on the synthetic allocation of the total initiation life assigned to each model.

Then, experimental results of eight beam-to-column moment joint specimens tested by four different programs are collected. The history of local field variables in the vicinity of the beam flange – column flange weld is extracted from hierarchical finite element models. Using the dynamic competitive neural array that has been established and trained, the time elapsed to initiate a low cycle fatigue crack is predicted and compared with lab observations.

Finally, finite element analyses of newly designed specimens are performed, the strength of their panel zone is identified, and the fatigue performance of the specimens with a weak panel zone is predicted.

ACKNOWLEDGEMENTS

A special debt of gratitude is owed to Dr. Gary T. Fry for providing guidance and support throughout the course of this research.

Thanks also go to my committee members, Dr. Harry L. Jones, Dr. Stefan Hurlebaus, and Dr. Anastasia Muliana.

Other people who have been supportive of this program and deserve special mention: Dr. Brett A. Story, Dr. Potchara Tangtragulwong, Dr. Olivier W. Bertacchini, Mr. Luis Eduardo Peternell Altamira, and Mr. Thanh Ngo.

For invaluable assistance in the preparation of this dissertation, Mrs. Amy White is gratefully acknowledged.

This work was coordinated under the auspices of and supported financially by the National Science Foundation (NSF) and units within the Texas A&M University System (the Texas Engineering Experiment Station, the Department of Civil Engineering, and the Texas A&M Supercomputing Facility).

Finally, thanks to my daughter Sophia, my wife Ming Lu, and my in-laws for their encouragement, patience, and love. My parents are greatly missed forever.

TABLE OF CONTENTS

Page

LIST OF FIGURES

FIGURE Page

FIGURE Page

FIGURE Page

FIGURE Page

FIGURE Page

FIGURE Page

FIGURE Page

FIGURE Page

FIGURE Page

FIGURE Page

FIGURE Page

FIGURE Page

LIST OF TABLES

1. INTRODUCTION

1.1 Problem Statement and Literature Review

A fundamental issue in the design of steel moment resisting frames is the balance of yielding between the beams and panel zones. Fig. 1.1 illustrates rigid-plastic mechanisms for two limiting cases: (a) plastic hinges in the beams; and (b) plastic hinges in the column panel zones. Shaded areas in these diagrams denote the yielded portions of the frames. By adjusting the relative strength between the beams and panel zones, either of these limiting cases can be achieved in design. A condition that combines these two limiting cases can also be achieved, i.e., a condition where some yielding occurs in both the beams and the panel zones. These three conditions can be referred to as a strong panel zone design (yielding primarily in the beams – Fig. 1.1(a)); a weak panel zone design (yielding primarily in the panel zones – Fig. 1.1(b)); and a balanced panel zone design (yielding shared between beams and panel zones). Which panel zone design option is the best? This question has been addressed in past experimental and analytical studies as well as in building code provisions and design practice. Recommendations from past research and from building codes on panel zone design have often been contradictory, leaving the question of panel zone design without a conclusive answer.

The need to build economical steel structures that are able to resist large

---

This dissertation follows the style of the *Journal of Structural Engineering*.

earthquakes creates a unique design environment. In such an environment, a component is successful if it can withstand a few dozen cycles of loadings from an extremely rare event causing large-scale yielding. To date, a fundamental computational model has yet to be developed to assess the cyclic rupture performance of such components. This investigation seeks to develop a model that provides a quantitative transition between behavior at two length scales: 1) the effects of far-field cyclic plasticity at the metallurgical scale, and 2) the effects of cyclic plasticity at the component scale involving the propagation of small but visible cracks that create a need to update the model in order to account for the damaged component's evolving state. With such a model, fractures can be predicted at moment resisting joints subject to seismic cyclic loading.

1.1.1 Panel Zones in Steel Moment Frames

In the past, panel zone behavior has been widely investigated in both experimental studies and analytical work. Experimental studies including weak panel zones were conducted in the 1970s and 1980s by Krawinkler, Bertero, and Popov (1971 and 1975), Becker (1971), Fielding and Huang (1971), Popov et al. (1985), and Lee (1987). Other experimental studies that were implemented more recently include Engelhardt et al. (2000), Ricles et al. (2002), and Lee et al. (2005a and 2005b). One of the earliest studies of panel zone behavior under cyclic loading was conducted by Krawinkler (1971 and 1978). This study showed that the shear yielding of panel zones results in highly ductile behavior with large and stable hysteretic loops that exhibit a large cyclic inelastic deformation capacity. Further, the panel zone response showed

significant cyclic hardening, which promotes the desirable spread of hinge formation throughout the frame. Based on his study of panel zone behavior, Krawinkler noted that shear distortion of the panel zone resulted in the formation of localized "kinks" at the corners of the panel zone, as shown in Fig. 1.2. These kinks, in turn, caused localized strain concentrations, ultimately leading to the occurrence of fractures in the vicinity of the beam flange groove welds. These fractures are the controlling limit state for joints with weak panel zones. That is, a fracture at or near the beam flange groove welds is ultimately what limits the inelastic deformation capacity of the panel zone. In the case of Krawinkler's tests, these fractures occurred only after a large level of plastic deformation was achieved.

Almost all subsequent studies have demonstrated the finding by Krawinkler that the shear yielding of the panel zone results in "kinks" at the panel zone corners. This finding has led to fundamentally conflicting views of panel zone participation in moment resisting joints in design. On one hand, weak panel zones are highly ductile and should be employed in moment frame design. On the other hand, weak panel zones cause joint fracture, and their use should be limited or completely avoided. A literature review reveals a conflict among investigators on the use of weak panel zones in moment frame design. Ricles et al. (2002) advised the use of strong panel zones. Roeder (2000) recommended a balanced panel zone design, and suggested that attention should be paid to weak panel zones. However, Lee et al. (2005a and 2005b) suggested weak panel zones were desirable and acceptable. While all agreed that panel zones are highly

ductile, varying understandings of the joint fracture caused by weak panel zones have led to the conflicting design recommendations.

1.1.2 Fracture in Steel Moment Frame Joints

The crucial problem in panel zone design is the development of fractures at the beam-column joint. Fractures invariably occur in joints with weak panel zones, although these joints may have withstood large cyclic rotations before the occurrence of fractures. This fact has been observed in many past studies on joints with weak panel zones. In most cases, fractures in joints with weak panel zones were observed at or near the beam flange groove welds. A specimen with a weak panel zone tested by Engelhardt et al. (2000) failed due to a fracture at a beam flange to column flange groove weld, as shown in Fig. 1.3. Prior to the fracture, the specimen sustained a cyclic interstory drift ratio of ± 6%. The occurrence of such fractures has been attributed by many researchers to the "kink" observed at the joints and has led a number of researchers to recommend preventing or limiting the use of weak panel zones in moment frame design. At present, there is currently no fundamental capability to computationally predict these factures. Without such a capacity, a resolution to panel zone design questions is not likely to be achieved.

In order to better understand the fracture of structural steel elements under inelastic cyclic loading, a five-stage progression of damage is proposed (Anderson 1995). This progression will cause a critical fracture of ductile components in steel structures subjected to seismic loads, such as the flange fracture seen in Fig. 1.3. Each

stage represents specific processes of damage accumulation under the combined conditions of large-scale yielding and cyclic deformation.

The five-stage fracture progression is illustrated in Fig. 1.4. The first stage represents the initial processes of damage that cause void nucleation and growth around nonmetallic particles. The second stage represents the processes that cause material separation through void coalescence. The first two stages occur at the metallurgical scale of the component, and models for these processes are often termed micromechanical models. The field quantities of deformation at this length scale are comparatively remote, and the geometric and material representations of the component need not be modified to include the effects of microscopic damage.

The third stage is a transition from microscopic damage to macroscopic fracture, and the prediction of the time elapsed in the third stage processes constitutes the central research questions that will be addressed in this research. At the end of the third stage, small cracks will be visible.

The fourth stage represents the processes of propagation and coalescence of the emergent cracks to form a single dominant crack. The fifth stage represents the process of dominant crack propagation until a significant fracture occurs, such as the fracture of a girder flange as shown in Fig. 1.3. Fourth and fifth stage processes occur at the natural length scale of the component itself. Therefore, the geometric and material representations of the component need to be adjusted to include the changes caused by the progression of damage.

Numerous past studies have formalized our basic understanding and ability to model what we have termed first stage, second stage, and fifth stage processes under the conditions of monotonic loading. To a lesser extent, past studies have also considered fourth stage processes under cyclic loading conditions. Considering all four sets of processes, the majority of past studies have focused on conditions of small-scale yielding, because most engineered components are expected to remain in service for at least tens of thousands of cycles (usually millions of cycles) during their designed life. A comprehensive summary of this body of work can be found in Anderson (1995). The third stage processes are the most important constituent in the overall damage progression, but they are also the least understood.

The work of Kavinde and Deierlein (2004) presents a recent effort in assembling an experimentally-calibrated computational framework to address the progression of damage. Kavinde and Deierlein first presented a review of previous research related to fatigue and fracture mechanics, specifically ductile crack extension. The computational models and experimental procedures resulting from their investigation, however, did not represent a significant departure from existing techniques to assess monotonic loading cases. Kavinde and Deierlein also presented a cyclic loading model. Referring to the five damage progression stages described above, their model considered only the first and second stages explicitly but in a phenomenological manner rather than a mechanistic one, while the behavior relating to the third stage processes was neglected. An effort was made to capture behaviors analogous to the fourth and fifth stage processes. Uniaxial specimens of various configurations were tested, and the specimens were analyzed using

the model. Subsequently the test and model results were compared, and empirical coefficients were adjusted in the model to improve the predictions.

Because cyclic rupture may occur after the component has sustained a small number of loading cycles, the time elapsed in each of the five stages of damage progression needs to be captured accordingly. Each stage consumes a number of cycles according to distinct mechanisms of damage accumulation. Considering that a component may fail by cyclic rupture in 20 cycles, neglecting a stage leads to unfavorably errors in prediction.

The most convenient framework for the cyclic rupture model is one that interfaces with solid finite element models as seamlessly as possible. In this study, a general computational approach that offers a completely seamless interface with solid finite element models and specific models, such as Warp3D (Gullerud et al. 2007), will be investigated. Warp 3D is designed as a research tool for studies in computational fracture mechanics (CFM). Currently, CFM analysis codes lack an ability to correctly analyze the development of fatigue cracks within intact components under cyclic loads. Rather, most CFM analysis codes such as Warp3D are designed to model the progression of preexisting cracks in damaged components. For this framework, an innovative way of predicting low cycle fatigue crack initiation life is developed with the application of artificial neural networks. This method does not depend upon any traditional or established fracture criterion. It looks solely and directly at the time history of local field variables, including but not limited to, stress, strain, displacement, etc. A detailed description of this approach will be given in Section 2.

1.1.3 Computational Fracture Mechanics

CFM is based mostly on calculating integrals of field quantities such as stress and strain. One of the most popular approaches is the J-integral, which was developed by Rice (1968), describing the energy release index as a path-independent contour integral

$$J = \int_{\Gamma} \left(\left(W dx_2 - t \frac{\partial u}{\partial x_1} ds \right) \right), \tag{1-1}$$

where $W(x_1, x_2)$ is the strain energy density, x_1, x_2 are the coordinate directions, $\mathbf{t} = \mathbf{n} \cdot \boldsymbol{\sigma}$ is the traction vector, $\mathbf{n}$ is the normal to the curve Γ, $\boldsymbol{\sigma}$ is the Cauchy stress tensor, and $\mathbf{u}$ is the displacement vector. Another example is also provided by Rice and Tracey (1969), who derived equations for the growth of single cylindrical and spherical voids in an elastic perfectly plastic material. According to his result, the void growth rate for a spherical void can be determined as

$$\frac{dR}{R} = 0.283 \exp\left(\frac{1.5\sigma_m}{\sigma_Y} \right) d\varepsilon_p, \tag{1-2}$$

where R is the instantaneous void diameter, σ_Y is the yield stress, s_m is the mean stress, e_p is the equivalent plastic strain defined by Equation (3), and de_p is its incremental form defined by Equation (1-4).

$$\varepsilon_p = \sqrt{\frac{2}{3} \varepsilon_p^{ij} \cdot \varepsilon_p^{ij}}, \text{ and} \tag{1-3}$$

$$d\varepsilon_p = \sqrt{\frac{2}{3} d\varepsilon_p^{ij} \cdot d\varepsilon_p^{ij}}. \tag{1-4}$$

As proposed above in this study, instead of dealing with integrals of stress and strain, we will look at a more straightforward approach incorporating finite element analyses and artificial neural networks.

1.1.4 Application of Artificial Neural Networks to Engineering Problems

Different from conventional computing techniques, the artificial neural network presents a different computational paradigm in which the solution to a problem is learned from a set of examples (similar to the way the human brain works) rather than from an explicit set of programmed instructions or algorithms (Mathew et al. 2008). The artificial neural network comprises simple elements operating in parallel (Beale et al. 2011). As in nature, the connections between elements largely determine the network function, and the network is trained to perform a particular function by adjusting the values of the connections (synaptic weights) between elements. Fig. 1.5 illustrates a situation where the network is adjusted, or trained, so that a particular input leads to a specific target output. Two of the most commonly used neural networks are: 1) Back-propagation (BP) network, which is the generalization of the Widrow-Hoff (Widrow and Hoff 1960) learning rule to multiple-layer networks and nonlinear differentiable transfer functions; and 2) the Radial Basis Function (RBF) network, which is often used to perform a complex pattern classification task. A detailed description of the two networks can be found in Haykin (1999).

Artificial neural networks have proved to be a powerful and versatile soft-computing method that is efficient in modeling complex linear and non-linear relationships on the basis of experimental data in a number of engineering fields (Hyland

and Fry 1999, Jadid and Fairbairn 1996, Hyland 1995, Wei et al. 2010, and Patela et al. 2011). A scheme of a competitive array of replicators (neural networks) was proposed by Hyland and Fry (1999). They pointed out that while the speed with which a system can be identified or re-identified is limited by the speed of any given replicator, a much faster convergence can be achieved by using a competitive array, as shown in Fig. 1.6. The "comparator" is a neural network that computes, for each replicator in the bank, the mean-square output error (the difference between the replicator output and the actual system output, y). The comparator then chooses the "winning" replicator (the one with the smallest error) as the one to provide the overall output of the system, and it permits back-propagated error signals to flow only to the "winning" replicator. Thus, the winner further refines its performance via gradient-descent adaptation, while the "losing" replicators are not permitted to adapt and hold constant. With this approach, there is promise in damage assessment and health monitoring. Therefore, in the current investigation, applying a similar scheme of neural networks to the estimation of cyclic fracture subject to seismic loading appears to be an appropriate logical extension.

In recent years, artificial neural networks have also found their application in the field of fatigue problems for various purposes (Mathew et al. 2008, Pujola and Pintob 2011, Abdalla and Hawileh 2010, Mohanty et al. 2009, and Skallerud and Zhang 2001). Mathew et al. (2008) developed a neural network model to predict the fatigue life of nitrogen-alloyed stainless steel. The fatigue life of both tested and collected data ranged between 2,000 and 10,000 cycles, with a constant strain amplitude of ±0.5% for the tests. Their neural network model could predict fatigue life within a factor of 2 of the

experimental values over the whole range of test temperatures and nitrogen contents. The model was further expanded to predict fatigue life of stainless steel with and without nitrogen, based on both tested and collected data. Results demonstrated that the neural network could predict fatigue life at any test condition within a factor of 2, as shown in Fig. 1.7.

Abdalla and Hawileh (2010) presented a model for predicting the low cycle fatigue life of steel reinforcing bars using neural networks. An RBF topology was used with two additional hidden layers and four neurons in each of these layers. Low-cycle fatigue tests were conducted for an alternative type of steel reinforcing bars subjected to different strain amplitudes at various strain ratios. The fatigue life ranged from 10 to 60 cycles. The neural network prediction of the low-cycle fatigue life of steel reinforcing bars was within ±2 cycles of the experimental results for the majority of the test data, as shown in Fig. 1.8.

Although many researchers have demonstrated success in predicting fatigue life by means of artificial neural networks, there is still no application of neural networks in the field of cyclic fracture estimation. As described above, among the five stages of damage progression, the third stage is the most important and least understood. The ultra-low cycle fatigue life prediction for beam-to-column connections subject to seismic loading based on soft-computing methods such as artificial neural networks is still lacking.

1.2 Outline of This Research

Following this section, Section 2 describes an innovative way of predicting the low cycle fatigue crack initiation life of notched round bars with the application of static artificial neural networks. In Section 3, the time consumed up to the end of each of the three fracture progression stages during the crack initiation process is estimated with the application of dynamic neural networks. The goal of these two sections is to develop a mechanistic model for cyclic rupture based upon the five essential stages of damage progression outlined earlier. A common procedure is that, cyclic large strain axial fatigue tests of notched round bars are performed; detailed fractographic analyses of the specimens including SEM assays of the fracture surfaces are implemented to identify the stages of damage progressions; corresponding finite element analyses of the notched round bar specimens are preformed to obtain the history of local field variables in the vicinity of crack initiation region; artificial neural networks are trained to be capable of correlating the pattern of input (such as stress, strain, displacement) to the time consumed in each damage progression stage. However, in the current investigation, only analytical study is implemented in the lieu of laboratory experiments. A way of developing reasonable synthetic data for the time elapsed in each of the damage progression stages is established so that the training and testing of neural networks can be realized. Once the application of neural networks to crack initiation life estimation is validated, low cycle fatigue experiments of notched round bar specimens can then be designed and implemented accordingly.

Section 4 predicts the low cycle fatigue crack initiation life of real-size beam-to-column moment resisting joint specimens tested by various programs using the static and dynamic neural array established in Section 2 and Section 3, respectively. Section 5 is devoted to the finite element analyses and fatigue performance estimations of newly designed specimens. Section 6 summarizes and concludes this research.

2. FATIGUE CRACK INITIATION LIFE PREDICTION FOR NOTCHED ROUND BARS USING STATIC ARTIFICIAL NEURAL NETWORKS

2.1 Introduction

This section describes an innovative way of predicting low cycle fatigue crack initiation life with the application of artificial neural networks. This method does not depend upon any traditional or established fracture criterion. Rather, it looks solely and directly at the time history of local field variables, including but not limited to, stress, strain, displacement, etc.

First, a competitive neural array is established, comprising various types of artificial neural networks that function differently. Then, finite element analyses of 30 notched round bar models, which are the analytical objective of this section and the next, are conducted, and the simulation results are extracted to form the inputs for either a single neural network or a competitive neural array. The element that has the maximum damage accumulation potential is identified, and the time elapsed to initiate a crack is predicted and compared with its true synthetic answer. Finally, this new procedure is further verified by investigating the impact of varying the sampling and number of input cases for training.

2.2 Competitive Neural Array

As described in Section 1, the competitive neural array is a powerful tool to create neural images of unknown nonlinear dynamic systems. In the present application,

the array is used to correlate patterns from an input vector of time history fields from a solid finite element model with an output fatigue crack initiation life.

Referring to Fig. 2.1, the competitive array comprises several different BP networks and one Probabilistic Neural Network (PNN) serving as the Comparator and Recorder (C/R). The input vector can include any number and combination of related and unrelated components such as stress and strain, material identification, nodal displacements, etc. During training, the C/R receives both the input vector and a "known" output vector. The C/R compares the known solution with the output from each member BP network and determines which is providing the least error against the known output. The C/R then passes the error differencing information back to the "best" BP network allowing it to readjust its synaptic weights and try to provide an even better answer. In the situation illustrated in Fig. 2.1, only BP network (2) is receiving a back propagation signal and being allowed to improve. The other networks are not permitted to adapt and hold constant until the next input comes in. After a sufficiently diverse matrix of training scenarios, each BP network is conditioned to respond in an optimum manner to a given input vector. Furthermore, the C/R is trained to identify which BP network is best for a given input vector. Thus, the array is ready for implementation.

During operation, however, the input vector will first pass to the C/R so that the best BP network for this given input is identified in advance. For the case illustrated in Fig. 2.2, the best network is BP network (2) again, and it will be the only one that is allowed to give an output.

The competitive neural array described above is realized and established with MATLAB for various purposes in each section. Though there may be different numbers or types of composing networks, the word "array" throughout this dissertation refers to the same competitive neural array whose scheme is described above.

2.3 Finite Element Analysis of Notched Round Bar Models

In lab experiments, steel round bars are often extracted from different materials such as base metal, heat affected zone (HAZ) material, and weld metal in a welding joint specimen for the purpose of calibrating material mechanistic properties. Cyclic fatigue tests of round bars are also often implemented for a shorter time and with less effort than those of real-size structural components. Because of its geometric simplicity in computational analyses, round bars are usually chosen to be the basic analytical unit. Moreover, in order to better capture the location of crack initiation, a notch is sometimes intentionally added. The investigation of predicting low cycle fatigue crack initiation life starts with notched round bars as the analytical objective by taking advantage of these simplicities.

A total of 30 notched bar finite element models are first made in pre- and post-processing software ABAQUS/CAE and then analyzed in ABAQUS. The model matrix is listed in Table 2.1. Three steel grades, AP50, AP70, and AP110, are selected. Detailed material properties are described by Kavinde and Deierlein (2004). Each round bar model has a notch with a radius of either 1mm or 2mm. Due to their symmetric geometry, 2-D axisymmetric solid elements (CAX8) are employed, and only half of the axisymmetric cross section is needed. A sample finite element mesh of models with

different notch radii is shown in Fig. 2.3(a) and Fig. 2.3(b), respectively. The total length of the round bars is assumed to be 60mm, and thus the models have a distance of 30mm from top to bottom. The minimum element size is 0.1mm, which is believed to be fine enough for the consideration of field variable gradients. The total number of nodes ranges from approximately 5200 to 7800, and that of elements ranges from 1500 to 2500.

The lower end of the model is the center cross section of notched round bars, and the nodal displacement along this line is fully constrained. The upper end is subject to a fixed-amplitude cyclic displacement loading. Five nominal strain amplitudes, 0~0.6%, 0~0.8%, 0~1.0%, 0~1.2%, and 0~1.4%, are chosen, indicating that the upper end has a cyclic displacement of 0~0.18mm, 0~0.24mm, 0~0.30mm, 0~0.36mm, and 0~0.42mm, respectively, while the bottom end is fixed. All models are subject to a total of 10 loading cycles, which are supposed to cover the whole time elapsed to initiate a crack at the notch. Detailed information regarding making up the synthetic data of fatigue life is given in Section 2.6. The displacement loading is applied and released quasi-statically, given that 4 seconds are allowed for each cycle of loading. The combined hardening rule (ABAQUS 2009), which is considered to be appropriate to simulate steel cyclic hardening, and the Von Mises yield criterion are used.

A sample contour of Von Mises stress, when the model is fully stretched during the first loading cycle, is plotted in Fig. 2.4(a) and Fig. 2.4(b), for a 1mm and 2mm notch radius, respectively. The time history of field variables of certain elements are extracted

from ABAQUS output in several different ways for the application of neural systems in the following sections.

2.4 The Most Critical Element to Initiate a Crack

Almost certainly, if a notched round bar specimen is perfectly manufactured and the loading is perfectly applied during lab testing, a crack will initiate from the notch root. This underlying fact is not judged by any rule or criterion of fracture mechanics, because the notch root area is where the maximum stress concentration and maximum strain concentration occurs. This area has the highest damage accumulation potential. Therefore, the current investigation begins with simulating the fatigue life of notched round bars for the following reasons: the location of crack initiation is obvious, and raw data of local field history is conveniently accessible from finite element analyses. Derivation of formulas such as integrals of stress history oven strain is no longer necessary, and artificial neural networks will function in their way according to the purpose of the problem to be solved.

The purpose of letting artificial neural networks determine the most critical element is this: if in other circumstances, the crack initiation location for a given specimen to be tested is unknown, will neural networks be able to provide a reliable estimation based on what it has learned from other known cases? In order to address this question, four elements in the vicinity of the notch root, as shown in Fig. 2.5, are selected to be the candidates of each of the models that will initiate a crack. The element at the notch root, Element α in Fig. 2.5, is numbered a random integer from 1 to 4 so that the investigation is unbiased, i.e. neural networks are not “cheating” by obtaining the

same element order when it is trained. In other words, a neural network will make a prediction based on what it receives from the input and its corresponding output numbering, rather than knowing the winning element only by its numbering.

The field histories of non-zero stress components, σ_{xx}, σ_{yy}, σ_{xy}, and σ_{zz}, non-zero strain components, ε_{xx}, ε_{yy}, ε_{xy}, and ε_{zz}, and average nodal displacements in the x and y direction are first collected from ABAQUS output for each of the four candidate elements in each model. In ABAQUS nonlinear plastic analysis, the solver first picks a random arc length and attempts to find a converged solution. If failed, it does this again and iterates this process until a convergence is reached. Therefore, the history of field variables may always consist of unequal time intervals, and no two models have exactly the same history segments. However, artificial neural networks require that the input vector of different cases must have the same subdivision of the whole time history, though the time consumed in each interval does not have to be equal. For easier processing and proper functioning of neural networks, the history of all ten field variables are interpolated to a total of 200 fixed time intervals of 0.2 second (the total time is 4 seconds per cycle multiplied by 10 cycles) using the Piecewise Cubic Hermite Interpolating Polynomial ("pchip" function in MATLAB). The "pchip" function is believed to be most suitable for shape-preserving interpolation for nonsmooth data (Hanselman and Littlefield 2005). A sample comparison between the original and interpolated stress history is plotted in Fig. 2.6, which shows no great scattering between the two. It is also very important to notice that this interpolation process does not

compromise the principle of directly employing the raw data of local field variables. Rather, it is solely a shift in sampling the history, to clear a way around the block.

A screen copy of a Microsoft Excel spreadsheet containing the inputs described above is given in Fig. 2.7. All input vectors have a dimension of 40×1, comprising 10 field variables for 4 elements in the vicinity of the notch root. Outputs for these input vectors are an integer between 1 and 4, depending on its number assignment of Element α. During training, for a given model, input vectors at each of the 201 time instants have the same output numbering, provided that only the static artificial neural networks are investigated in this section. A difference between static and dynamic neural networks will be narrated in Section 3.2. A group of 20 models selected at random is used as the training sets for neural networks, and the other 10 are to be predicted.

A total of four different schemes of neural networks are employed to demonstrate that artificial neural networks are capable of identifying the most critical element in a finite element model in a variety of ways. The first two schemes are of a single Learning Vector Quantization (LVQ) network and a PNN, respectively. The other two schemes are competitive arrays. Both of the arrays have a PNN as C/R, one with four BP networks having one hidden layer of 4, 5, 6, and 7 neurons and the other with four Generalized Regression Neural Networks (GRNNs) having a spread rate of 1, 2, 3 and 4. Detailed information of these terminologies and networks are provided in Neural Network Toolbox User's Guide (Beale et al. 2011). MATLAB has an embedded function ready to use for each type of network in its Neural Network Toolbox. The

number of neurons and the spread rates are picked up randomly to make each competitive network distinct.

After they are trained with 20 cases selected at random, the neural systems take the inputs from the other 10 models and produce an output for each input vector. The MATLAB program developed for this research regulates that among all outputs of the 201 instants of each model, the integer that has the maximum appearance will be the winning element numbering of this model. Further examination of the results finds that all cases have almost the same output integer at every time instant, indicating that neural networks are very confident in picking up the right answers.

The prediction results provided by the single LVQ, the single PNN, the BP-PNN array, and the GRNN-PNN array are plotted in Fig. 2.8, Fig. 2.9, Fig. 2.10, and Fig. 2.11, respectively. All of the four figures have 10 red diamonds, but some are overlapped by others, allowing only four diamonds to be seen from the plot. All of the diamonds on these figures represent Element α, indicating that these four neural schemes are all capable of picking up the element that accumulates the most damage among the four. The conclusion is that artificial neural networks are working very well in predicting the location where a crack is most inclined to initiate, if it is well trained with accurate knowledge.

2.5 Recognition of a Potential Pattern among Analytical Models

In Table 2.1, the 30 notched round bar models are categorized into six groups by three grades of steel and two notch radii. This pattern of grouping is very straight-forward for general purposes. However, if the low cycle fatigue life or the fatigue

fracture problem is under consideration, this taxonomy makes no sense since empirical evidence has shown that only the variation of local field variables matters. The intent of this section is to test whether neural networks still preserve workability if it is provided with ambiguous information.

Inputs are the time history of non-zero stress and strain components and two displacement components of Element α in each model, exactly the same as those used in the previous section, except that the field history of the other three elements is not taken into consideration. Outputs are integers from 1 to 6, depending on the steel grade and notch radius of each model. For example, the 5 models in the column "AP50, R=1mm" in Table 2.1 have the type number 1, and those in column "AP110, R=2mm" are of type 6. During training, for each model, input vectors at every time instant have the same corresponding output type number. In operational mode, the integer that has the maximum appearance will be the type number of the model being predicted.

Again, 20 cases are randomly selected for training, and the other 10 for predicting. The single PNN and the BP-PNN array constructed in Section 2.4 are used. This time, the predicted output result for 201 instants of each notched round bar model is scattered. The MATLAB program still picks up the type number that appears the most in each case, and its comparison with the correct answer is plotted in Fig. 2.12 and Fig. 2.13 for the single PNN and the BP-PNN array, respectively. Both neural schemes fail to recognize the fake pattern that is made up intentionally, as is expected, and this fact further reveals that artificial neural networks are intelligent in filtering the provided information.

2.6 Prediction of Low Cycle Fatigue Crack Initiation Life

As described in Section 1, in a five-stage fracture propagation process, an emergent crack will become visible at the end of Stage III, and the main goal of this study is to estimate the time elapsed before this happens, or in other words, to predict the time needed to create a visible crack in an initially undamaged component subjected to a fatigue loading. Herein we define the fatigue crack initiation life as the time elapsed from the beginning of cyclic loading until the existence of an emergent crack. If implementing lab experiments, a certain rule or standard could be defined to count the cycles elapsed up to the crack initiation, such as when a 1mm crack is observed. However, in this present investigation, only analytical study is carried out. A way of developing reasonable synthetic data for crack initiation lives needs to be found so that the training and testing of neural networks can be realized. Once the application of neural networks to crack initiation life estimation is validated, low cycle fatigue experiments of notched round bar specimens can then be designed and implemented accordingly. In this section, fatigue crack initiation life will be evaluated as a whole, including the first three stages of fracture progression. Further predictions for each stage will be investigated in Section 3.5.

Based on a series of specimens tested in Japan (Long 2006), a relationship between the whole fatigue life (initiation plus propagation, N_f) and the local plastic strain amplitude (ε_{pr}) was established as follows:

$$\varepsilon_{pr} = 1.345 N_f^{-0.630} \tag{2-1}$$

First, the synthetic whole fatigue life of the 30 notched round bar models is calculated by

substituting the plastic strain range of Element α during the first loading cycle into Eq. (2-1). Given an empirical fact that the crack initiation accounts for approximately 15% to 30% of the total fatigue life, the synthetic initiation life for these models is obtained by multiplying a factor of 18% to its whole fatigue life. The choice of 18% is arbitrary, and the resultant initiation lives of all 30 models happen to be within 10 cycles, which is a satisfactory number of loading cycles for finite element analyses. This choice also answers the question left in Section 2.3 why 10 cycles of loading are applied.

Moreover, if integers are used in cycle counting, differentiating each round bar model is difficult, because all 30 models have an initiation life between 1 (actually 3) and 10. There must be at least two models that have the same initiation life. Thus, instead of counting cycles, the elapsed time is directly used to record the initiation life, with 1 cycle equaling to 4 seconds, which is the loading time of each cycle. The total loading time is now 40 seconds, and each model has its own initiation life from, theoretically, 0.2 to 40 seconds (a total of 200 time intervals).

Another issue that needs to be solved before we move forward is that the time history of field variables consists of 201 time instants while crack initiation life is only one number. There is no way for neural networks to correspond 201 input vectors to a single number. Therefore, a so-called fatigue damage index is proposed herein and will be used throughout this dissertation. The assumption is made, in this section only, that all three stages of fracture propagation within the crack initiation progress have an equal allocation of time that is elapsed. This is to say, for example, if the initiation life of a certain model is 30 seconds, Stage I, II, and III will each cost 10 seconds. Then, an index

of unity is specified when and after the initiation life is reached, and that of zero is given at the beginning of loading. The index number 0 is held constant for several time instants until the end of Stage I. In the example above, 0 is the output index of the input vectors that have a time coordinate less than 10 seconds. After this, a new index, 0.3, is provided and holds constant until the end of Stage II, which is 20 seconds in the same example, followed by 0.6, until 30 seconds. Now each of the 201 input vectors has an output damage index. Again, the index numbers 0, 0.3, 0.6, and 1 are otherwise arbitrary except that their ascending sequence indicates a stepwise damage accumulation progress explicitly. Each notched round bar model now has a series of 201 output indices consisting of a portion of 0's, 0.3's, 0.6's and 1's, depending on the stage of crack propagation that has been reached.

Inputs are the time histories of non-zero stress and strain components and two displacement components of Element α in each model, and outputs are the fatigue damage indices. First, a single GRNN is employed with 25 cases selected at random for training and the other 5 for testing. The comparison between predicted and expected initiation life is plotted in Fig. 2.14. A single BP is then tested after being trained by 25 cases, and the prediction result is provided in Fig. 2.15. Additionally, with the application of the BP-PNN array constructed in Section 2.4, three groups of simulations are performed. In the first group, all three trials have 25 cases selected at random for training and the remaining 5 for prediction, but their samplings are different. Similarly, the other two groups also consist of trials with different samplings, while the number of cases for training is 20 and 15, and the number for testing is 10 and 15, respectively. The

comparisons between prediction and expectation are plotted in Figs. 2.16 ~ 2.18, for the first group, Figs. 2.19 ~ 2.21, for the second group, and Figs. 2.22~2.24, for the last group. The Mean Square Error (MSE) of each test is also calculated and listed on the corresponding plot.

The simulation made by the single network, as shown in Fig. 2.14 and Fig. 2.15, has an MSE of approximately 58, roughly meaning that the average error of the five predicted cases is almost 8 seconds, the equivalent of two loading cycles. In comparison, the first group of trials made with the array is also trained by 25 input sets but results in a much lower average MSE of 16, the equivalent of one loading cycle. The comparison of prediction results leads to the conclusion that the introduction of the competitive neural array promotes neural networks' simulation capability.

For the first group of trials made with the array, the MSE of their prediction ranges from 11 to 22. Though not perfect, compared with the other two groups, the prediction made by the first group is still satisfactory and acceptable. The first group's predictions have different accuracy, because each is trained by certain 25 input sets and no two sets are of exactly the same sampling. However, even if two trials with identical training cases are ordered for a given array, they will almost still generate diverged predictions for identical unknown cases, because the simulation made by neural networks is basically a stochastic process. An evidence of this matter of fact will be provided in Section 3.6. The purpose of making three distinct trials with the same number of cases for training herein is to gain more confidence on the application of

neural networks to fatigue life estimation by changing the sampling of training and testing cases.

Figs. 2.16~2.24 also point out that the accuracy of the predictions produced by the array decreases as the number of cases used for training decreases. Though one may argue that the average MSE is very large in the last group of trials because of a significant number (15) of models being predicted, the fundamental cause is actually that the array is less tuned when there are only 15 input sets in the training process.

2.7 Summary

In this section, a competitive neural array comprising various types of neural networks is established to estimate fatigue crack initiation life. Then, the investigation starts with finite element analyses of notched round bar models, followed by extracting their history of local field variables, such as stress, strain, and nodal displacements, as the input vectors for neural networks. Results show that neural networks are capable of predicting the location that is most inclined to initiate a crack, as well as estimating the time elapsed to cause this initiation to a satisfactory extent.

3. FRACTURE PROGRESSION ESTIMATION OF NOTCHED ROUND BARS MADE OF DIFFERENT MATERIALS USING DYNAMIC ARTIFICIAL NEURAL NETWORKS

3.1 Introduction

In this section, the time consumed up to the end of each of the three fracture progression stages during the crack initiation process is estimated with the application of dynamic neural networks. The investigation is wholly based on synthetic data that is specifically designed, and significant conclusions will be drawn to provide useful recommendations to experiment designs and tests.

This section starts with a general comparison between static and dynamic neural networks. Then, two types of steel-like materials are created so that material identification information can be added to the input vectors for neural networks. After finite element models of notched round bars made of the new materials are analyzed, a competitive array comprising dynamic neural networks is established and examined. The time elapsed by the end of every stage is evaluated based on the synthetic allocation of the total initiation life assigned to each model. Finally, the impact of the number of input cases for training on the prediction accuracy is examined.

3.2 Comparison of Static and Dynamic Neural Networks

"The prototypical use of a static neural network (e.g., multilayer perceptron, radial-basis function network) is structural pattern recognition. In contrast, temporal

pattern recognition requires processing of patterns that evolve over time, with the response at a particular instant of time depending not only on the present value of the input but also on its past values," (Haykin 1999). In the current investigation, fatigue crack initiation is basically a damage accumulation process in which an emergent crack is formed over time from the nucleation of embedded voids. Therefore, the history of local field variables is actually following a temporal, rather than structural, pattern. Though static neural networks perform promising predictions, as shown in Section 2, dynamic networks are more suitable, especially when more analytical cases are being predicted and the problem becomes more complex, such as distinguishing the three fracture progression stages.

In order to make a general comparison of the prediction accuracy associated with static and dynamic neural networks, the BP-PNN array established in Section 2.4 is employed as the static array. The BP networks in this array are substituted by Focused Time-Delay Neural Networks (FTDNNs), having one hidden layer of the same number of neurons as the BP networks to establish a dynamic array. Out of the 30 notched round bar models analyzed in Section 2.3, a group of 25 are selected at random and used as the training cases for both arrays. The results predicted for the 5 remaining cases are plotted in Fig. 3.1 and Fig. 3.2 for the static array and the dynamic array, respectively. Fig. 3.2 shows a much closer agreement between the expected and predicted values of crack initiation lives, demonstrating that the problem under study possesses a temporal pattern, and the application of dynamic neural networks is more appropriate in estimating fatigue crack initiation lives.

3.3 Finite Element Analysis of Bars Made of Synthetic Materials

One of the most convenient features of using neural characteristics for fatigue evaluations is that any number and combination of related and unrelated components can be included in the input vector. This versatility is important because different materials such as weld metal and base metal usually display vastly different fatigue properties. Moreover, other manufacturing details of a moment resisting joint, including the weld metal toughness and the connection type (such as Welded Unreinforced Flange Welded web and Welded Flange Bolted web), also have an impact on its seismic performance and can be included in the input vector. The functionality of neural networks trained by input vectors, consisting of other related information besides local field variables, is examined by developing two types of synthetic material. The influence of the existence of material identification information on promoting/destroying networks' simulation capabilities are not investigated in this study and will be suggested for further research. Rather, the objective is to look for a feasible way for neural networks to function after adding this information to the input.

In this attempt, two types of quasi-steels are developed which have the following distinctions from the prototype steels (Type A): the elastic stiffness (Young's modulus) of one quasi-steel (Type B) is halved, and the strain hardening of the other (Type C) is doubled. Here, the prototype is designated to the three grades of steels introduced in Section 2.3. Fig. 3.3 plots a sample of nominal stress – nominal strain constitutive relationships of the three types of material, one authentic and two synthetic.

Finite element models of notched round bars made of the two types of newly-created materials are then analyzed, given that all other conditions, except the definition of material properties, are the same as the models analyzed in Section 2.3. The time history of non-zero stress and strain components and two displacement components of Element α (shown in Fig. 2.5) in each model is extracted, and a pool of 90 cases is ready for implementation in neural network simulations.

3.4 Dynamic Neural Array and its Input and Output

In addition to the ten components already contained in the input vectors, an eleventh component, the material identification, also needs to be included. Using a type denotation of "A", "B", or "C" is inherently reasonable because vectors/matrices can comprise a combination of numbers and strings in almost any computer language. However, the calculation of numbers and strings can never be mixed. Instead, in MATLAB, each character will first be converted to its corresponding ASCII code before a vector containing a string is numerically calculated. Therefore, the representation of the material identification is arbitrary as long as it is identifiable among others, because no matter what string is used, this representation will be converted to a number. Then, to comply with the fluctuating displacements that the top end of the model is subject to, a series of material identification indices is established for each of the three materials being used and for every time instant of each loading cycle. Table 3.1 lists these indices, which are, again, otherwise arbitrary, except that their waveform looks similar to the one plotted in Fig. 2.6 and that all materials are defined by a mutually distinct series of

indices. Now, the input vector at each time instant has a material identification index as the eleventh component, and this vector can be written as

$$\mathbf{p} = [\sigma_{xx}\ \sigma_{yy}\ \sigma_{xy}\ \sigma_{zz}\ \varepsilon_{xx}\ \varepsilon_{yy}\ \varepsilon_{xy}\ \varepsilon_{zz}\ u_x\ u_y\ I_m]^T.$$

For a given notched round bar model, the whole history of its input vectors will then be

$$[\mathbf{p}(1)\ \mathbf{p}(2)\ \mathbf{p}(3)\ \ldots\ \mathbf{p}(201)].$$

Among other choices of dynamic neural networks, the FTDNN is well suited to time-series predictions. The FTDNN is a back-propagation feedforward network with a tapped delay line at the input. A detailed description of the FTDNN, or sometimes also referred to as the Focused Time Lagged Feedforward Network, is provided by Haykin (1999). If several models are to be trained in one FTDNN, the network is presented with a concurrent set of sequences (Beale et al. 2011), and the history of input vectors of, for example, three models need to be formatted in the following way:

$$\{[\mathbf{p}_1(1)\ \mathbf{p}_2(1)\ \mathbf{p}_3(1)]\ [\mathbf{p}_1(2)\ \mathbf{p}_2(2)\ \mathbf{p}_3(2)]\ \ldots\ [\mathbf{p}_1(201)\ \mathbf{p}_2(201)\ \mathbf{p}_3(201)]\}.$$

Each element of the above cell array is a matrix of concurrent vectors that correspond to the same point in time for each sequence (Beale et al. 2011). Different from static neural networks that treat each input vector independently, dynamic networks have to be trained by an input cell array format so that the concurrent sequences of each input case will have a tapped delay line memory of the same order.

To design the synthetic data of the time consumed in all three stages of the fracture progression, the fatigue crack initiation lives of all 90 models are obtained first in the same way as described in Section 2.6. Then, each fracture stage is assigned an allocation percentage, and this allocation is made different for each material, as listed in

Table 3.2. Referring to Table 3.2, if, for example, an emergent crack appears at the 11th time instant, a notched round bar made of the prototype steel (type "A") will have a series of fatigue damage index outputs of

$$[0_{(1)}\ 0\ 0\ 0.3\ 0.3\ 0.3\ 0.6\ 0.6\ 0.6\ 0.6\ 1\ 1\ 1\ 1\ \ldots\ 1_{(201)}],$$

and bars made of the other two quasi-steels (types "B" and "C") will have a series of outputs of

$$[0_{(1)}\ 0\ 0.3\ 0.3\ 0.3\ 0.3\ 0.3\ 0.3\ 0.3\ 0.6\ 0.6\ 1\ 1\ 1\ 1\ \ldots\ 1_{(201)}], \text{ and}$$

$$[0_{(1)}\ 0\ 0\ 0\ 0\ 0\ 0.3\ 0.3\ 0.6\ 0.6\ 0.6\ 1\ 1\ 1\ 1\ \ldots\ 1_{(201)}],$$

respectively. The indices of 0's, 0.3's, 0.6's, and 1's have the same features described in Section 2.6. They provide a way of capturing the stepwise procedure of fracture progression as well as distinguishing the models made of different materials.

To comply with the format of the inputs trained in one FTDNN, the output indices also need to be configured accordingly. The whole history of outputs for a given model has the form of

$$[t(1)\ t(2)\ t(3)\ \ldots\ t(201)],$$

where the t's are the fatigue damage indices that are numbers (0, 0.3, 0.6, or 1) rather than vectors. The cell array of outputs of three models that are trained in one FTDNN has the layout of

$$\{[\ t_1(1)\ t_2(1)\ t_3(1)]\ [\ t_1(2)\ t_2(2)\ t_3(2)]\ \ldots\ [\ t_1(201)\ t_2(201)\ t_3(201)]\ \}.$$

A dynamic competitive neural array is then established and will be applied towards the end of this dissertation. The array consists of a PNN as the C/R, and a total of 4 competitive FTDNNs that all have two hidden layers of neurons. Table 3.3 lists the

number of neurons in the hidden layers and the number of time delays selected for each FTDNN. These FTDNNs are made mutually distinct so that a sufficiently diverse matrix of training scenarios is realized by a comprehensive variety of neural networks.

In preliminary dynamic array training trials, it occasionally appears that, after being trained by a certain number of input cases, one of the 4 FTDNNs becomes the winning network that is allowed to be readjusted for almost all of the remaining cases. As a result, the C/R is not able to function properly in operational mode in the two following aspects: for a given input to be predicted, the C/R may identify an inappropriate network because of the frequent appearance of the winning network during the C/R training; or it may pick up a network that has never been trained. Therefore, in addition to the scheme developed for the static neural array, one more route is designed. The flow chart for this new scheme is illustrated in Fig. 3.4. It is regulated that when the ratio of the number of input cases trained by an FTDNN over the total number of input cases is equal to or greater than 80%, the corresponding FTDNN is trained again by all input cases and will be the only one used for operation. The choice of threshold value for this ratio is also arbitrary, as long as uncommon circumstances can be filtered by this hurdle.

The addition of the extra route to the original array scheme does not alter the preference of the competitive array to a single network. Rather, the competitive array becomes more inclusive. For the group of 90 notched round bar models under investigation, their local field history displays similar, though not exactly the same, patterns mainly because they are all made of steel-like materials. Depending on the

sequence in which each input case is presented to the array (and this sequence is always random), either a network is sufficiently trained in a very early stage in the training process that it is suited to all remaining cases, or minor differences in the pattern are first detected and several networks take the responsibility for a certain number of input cases. In contrast, if another group of input cases with vastly diverged patterns is presented, this extra route may never be utilized.

Finally, the dynamic competitive array with a newly designed scheme is developed, and its input and output are prepared in an appropriate format. A wide variety of trials are to be carried out and evaluated in Sections 3.5 and 3.6.

3.5 Prediction of the Time Consumed up to the End of Each Stage

The first series of trials is associated with 85 input cases selected at random for training and the remaining 5 cases for predictions. A total of 3 trials are implemented, and no two trials have exactly the same set of input cases for training or for predictions. In each trial, the time instant corresponding to the first appearance of the output index of 0.3 is when the first stage of the crack initiation progression ends. Similarly, the first appearance of 0.6 and 1 will then be the end of stage II and stage III, respectively. These simulation results are compared with their expected synthetic values and depicted in Figs. 3.5~3.7 for the first trial, Figs. 3.8~3.10 for the second trial, and Figs. 3.11~3.13 for the last trial. The MSE of every prediction is also provided in these plots. The prediction results scatter among each trial mainly because different cases are being predicted. The average MSE of the predictions made for the whole initiation life (the end of Stage III) is approximately 36, indicating an average error of roughly 6 seconds,

which is basically satisfactory. A predominant trend is that the MSEs associated with the predictions made for the first two stages are smaller than those for the initiation life. This may be caused by the fact that the time consumed up to the end of Stage II is within 15 seconds for most cases. A group of smaller numbers is prone to be predicted with a lower MSE.

Under the same principle, three more series of trials are performed with 80 input cases selected at random for training and the other 10 for prediction, 75 cases for training and 15 for prediction, and 60 for training and 30 for prediction. Their corresponding results are provided in Figs. 3.14~3.22, Figs. 3.23~3.31, and Figs. 3.32~3.40, respectively. Similarly, the MSEs of the first two stages' predictions are smaller than the initiation life's MSEs. The MSE average becomes higher when more cases are predicted, which may be accounted by the fact that fewer cases are available for training. Also note that the MSEs are all within 30 in Figs. 3.13, 3.19, and 3.31, where there are 5, 10, and 15 cases for prediction, respectively. Therefore, a further examination of the impact of input volume on the performance of the dynamic array is needed.

3.6 Impact of the Total Number of Input Cases for Training

First, a new trial is executed in the following steps: a total of five cases is selected at random for prediction; the dynamic array is trained by the first five cases in the pool of the remaining 85 cases; the initiation life of the five cases selected in the first step is predicted, and its MSE is recorded; the dynamic array is returned to its original, untrained status and then trained by the first six cases in the pool of 85 cases; the five cases selected in the first step are predicted again, and the MSE is recorded; this iteration

keeps processing until the raw dynamic array is trained by all 85 cases. After the first trial is complete, the process repeats with the same sets of cases for prediction applying the same procedure beyond the first step. In other words, two identical trials with the same 5 cases for prediction are practiced, and the MSE records are plotted in Fig. 3.41 and Fig. 3.42. The two plots are not identical, indicating that the simulation made by neural networks is basically stochastic. Both of them show a significant decrease in the MSE when the number of training cases reaches around 40.

Similarly, two identical trials are conducted for a situation when 10, 15, or 30 cases are predicted. Their MSE records are illustrated in Figs. 3.43 and 3.44, Figs. 3.45 and 3.46, Figs. 3.47 and 3.48, respectively. Again, two identical trials with the same sets of predicting cases never preserve repeatability.

From Figs. 3.41~3.48, it is observed that the MSE level becomes relatively stable if the dynamic array is trained by at least 40~50 input cases. This finding provides a significant reference to the testing matrix design of notched round bar specimens that will be the subject of experiment soon after this study. If finally concluded that the dynamic array trained by the local field history of notched round bar models is capable of evaluating the fatigue performance of real-size moment resisting joints to a satisfactory extent, it is recommended that a total of approximately 50 specimens made of different materials be tested. It is also suggested that the experiment results substitute the synthetic data of elapsed time so that the dynamic array can be better calibrated. The experiments of notched round bars should follow the same loading pattern as for the real-size joint specimens, because all of the 90 cases under study are subject to constant-

amplitude cyclic tensional loading. Otherwise, a more diverse testing matrix should be designed. Additional array trainings are also necessary in this case.

For an unknown case that is to be predicted, the statistic of MSEs almost makes no sense. Whether the MSE level holds stable or not, the prediction of a given case is either approximately right or wrong. Therefore, a certain number of trials should be allowed, and other statistical tools may be employed to filter irrational outliers and average the reasonable. An effort of such attempt is demonstrated in Section 4.

3.7 Summary

In addition to the 30 models created in Section 2, 60 more notched round bar models made of synthetic materials are analyzed, and the history of their local field variables is extracted. After assigning a series of indices for each material, input vectors consisting of 11 components at every time instant of all 90 cases are prepared in a proper format for processing in FTDNNs. Then, a dynamic competitive array with a newly designed scheme is developed, and the time elapsed up to the end of each of the three fracture progression stages during the crack initiation process is estimated. The influence of the number of training input cases on the prediction accuracy is also examined. MSEs associated with the predictions made for the first two stages are found to be much smaller than those for the initiation life, and the predictions made for the initiation life are satisfactory. Around 50 notched round bar specimens are recommended for use in future experiments, given that the loading pattern is similar to the pattern for real-size moment resisting joints.

4. LOW CYCLE FAGITUE LIFE ESTIMATION OF PAST TESTED SPECIMENS

4.1 Introduction

This section aims to predict the low cycle fatigue crack initiation life of real-size beam-to-column moment resisting joint specimens tested by various programs using the static and dynamic neural array established in Section 2 and Section 3, respectively. The predictions are compared with their experimental results, and significant conclusions will be drawn.

First, finite element analyses of notched bar models subject to stepwise increasing amplitude cyclic strain loading are conducted. The time history of local field variables is extracted for several elements in the vicinity of the notch root. Second, the static neural array is trained to identify the element that has the most potential to initiate a fatigue crack. The dynamic array is trained to predict the time elapsed up to the formation of a crack at this element, based on the synthetic fatigue crack initiation life that is specifically developed. Then, 8 tested real-size beam-to-column moment joint specimens are selected from several published papers based on three criteria. Finite element analyses of these specimens subject to monotonic loading are implemented. The local field history in the region where the controlling fatigue crack is first observed is extracted from the analytical results of cyclic hierarchical finite element analyses. Finally, by inputting the local field history of these specimens, the fatigue crack initiation life is predicted by the trained neural arrays.

4.2 Finite Element Analysis Subject to Varying Amplitude Loading

The sensitivity of artificial neural networks to loading patterns is indicated by the failure of a preliminary trial using the dynamic array trained by round bar models subject to constant amplitude cyclic loading to predict the fatigue life of a real-size joint specimen subject to stepwise increasing amplitude. Therefore, a new set of finite element analyses of notched round bar models are implemented, applying cyclic stepwise increasing amplitude strain loading.

Fig. 4.1 illustrates the basic mode of cyclic loading, and Table 4.1 details the number of cycles at each strain amplitude. This mode is proportional to the loading protocol specified in SAC/BD-97/02 (SAC 1997). The selection of this load style will be further discussed in Section 4.4. Applying a magnification factor of 1 to 10 to the basic mode, a total of 10 loading histories are designed. With three grades of steel, AP50, AP70, and AP110, and two notch radii, 1mm and 2mm, a matrix of 60 analytical cases is made and listed in Table 4.2.

In this series of finite element analyses, the loading is applied quasi-statically. It is assumed that the strain loading rate is fixed at 0.025% per second for the basic mode, and 0.25% per second for the loading history with a magnification factor of 10. In this way, the total time specified in every analysis is the same, which is approximately 680 seconds. The total number of analysis steps is 85, corresponding to the 42 cycles in Table 4.1.

The choice of these strain amplitudes is not arbitrary. The local field histories in the vicinity of the notch root are estimated to be comparable with the field histories in

the region that initiates a fatigue crack in real-size specimens so that artificial neural networks are trained accordingly. Unless the neural array is provided with necessary and relevant knowledge, accurate predictions cannot be realized.

4.3 Training of the Neural Arrays

There are two stages in the training process. First, the static array comprising four BP competitive networks and a PNN comparator, which is developed in Section 2.4, is trained to detect the element that has the most potential to initiate a fatigue crack. As is shown in Fig. 2.5, again, four elements near the vicinity of the notch root are selected as the candidates. By assigning a random number (between 1 and 4) to the four elements in each of the 60 cases, the array is capable of identifying the "winning" element depending on their local field histories rather than on the numberings. Second, the dynamic array comprising 10 competitive FTDNNs and a PNN comparator is trained to predict the fatigue crack initiation life. Parameters used in the 10 FTDNNs are provided in Table 4.3. The extra route in the flow chart described in Section 3.4 is also employed to account for uncommon incidents.

The objective of Section 4 is to correlate notched round bar models with tested real-size moment joint specimens in the means of neural networks. An important issue has to be solved before such a trial is conducted. For the notched round bars, the loading is applied vertically, resulting in a predominant stress/strain component in the y direction. In contrast, for almost all experiments of joint specimens, the load is applied horizontally, and the predominant stress/strain component of the elements in the fracturing region is in the x direction. Moreover, since no torsion is applied to the bars,

the stress components, σ_{13} and σ_{23}, and the strain components, ε_{13} and ε_{23}, are always zero. If the neural arrays are trained directly by the local field histories of the round bars, the predictions made for the real-size specimens will be highly questionable. In order for the neural arrays to overcome this difficulty, the stress/strain histories need to be converted from their original basis to a randomly chosen basis while the state of the stress/strain is kept. In other words, the state of the stress/strain is represented by another group of components for a random basis by linear transformations so that the network training is coordinate independent. Notice that altering the representation of a stress/strain state does not conflict with the original idea of employing the raw data of local field histories.

The displacement components in the input vectors also have a similar issue. For the round bars, the notch root has almost no displacement at all, especially in the horizontal direction, but the fracturing region of moment joints always experiences a large extent of horizontal displacements that mostly comprise rigid motion. Therefore, the displacements in the notch root area also need to be transformed, so that the neural network simulation is also rigid motion independent.

In a Cartesian coordinate system, the total displacement of a point after a combined transformation comprising a rigid translation, a rotation, and a nodal displacement due to external loading is calculated as

$$\mathbf{\Delta}_{\mathbf{C}} = \mathbf{T} + R\mathbf{D} + \left(R - I\right)\mathbf{X}, \tag{4-1}$$

where $\mathbf{T} \equiv \begin{bmatrix} x_T & y_T & z_T \end{bmatrix}^T$ is the rigid translation vector, $\mathbf{D} \equiv \begin{bmatrix} dx & dy & dz \end{bmatrix}^T$ is the nodal displacement output from finite element analysis, $\mathbf{X} \equiv \begin{bmatrix} x_o & y_o & z_o \end{bmatrix}^T$ is the coordinate of the point, I is the three-dimension identity matrix and R is the rotation matrix. Detailed derivation of Eq. (4-1) is provided in Appendix C. The rotation matrix is the product of the three basic rotation matrices,

$$R = R_x R_y R_z \tag{4-2}$$

where R_x, R_y, and R_z correspond to the rotation about x, y, and z axis, respectively (as shown in Fig. C.5 ~ C.7), and are calculated as

$$R_x = \begin{bmatrix} 1 & 0 & 0 \\ 0 & \cos\theta_x & -\sin\theta_x \\ 0 & \sin\theta_x & \cos\theta_x \end{bmatrix}, \tag{4-3}$$

$$R_y = \begin{bmatrix} \cos\theta_y & 0 & \sin\theta_y \\ 0 & 1 & 0 \\ -\sin\theta_y & 0 & \cos\theta_y \end{bmatrix}, \tag{4-4}$$

$$R_z = \begin{bmatrix} \cos\theta_z & -\sin\theta_z & 0 \\ \sin\theta_z & \cos\theta_z & 0 \\ 0 & 0 & 1 \end{bmatrix}. \tag{4-5}$$

Transformation of stresses and strains depends solely on the rotation. According to the tensor transformation rule, an alternative representation of a stress tensor and strain tensor is

$$S' = RSR^T, \tag{4-6}$$

and

$$E' = RER^T, \tag{4-7}$$

respectively, where

$$S \equiv \begin{bmatrix} \sigma_{11} & \sigma_{12} & \sigma_{13} \\ \sigma_{21} & \sigma_{22} & \sigma_{23} \\ \sigma_{31} & \sigma_{32} & \sigma_{33} \end{bmatrix}, \tag{4-8}$$

and

$$E \equiv \begin{bmatrix} \varepsilon_{11} & \varepsilon_{12} & \varepsilon_{13} \\ \varepsilon_{21} & \varepsilon_{22} & \varepsilon_{23} \\ \varepsilon_{31} & \varepsilon_{32} & \varepsilon_{33} \end{bmatrix} \tag{4-9}$$

A total of 9 transformations are made for each round bar model, and the parameters selected for each transformation is listed in Table 4.4. Including the original coordinate, each of the 60 input cases is represented in 10 different ways, and 600 cases are created for training the dynamic array.

Now, the input vectors at each time instant are formatted properly, and comprise 15 components, of which 6 are stresses, 6 are strains, and 3 are displacements. The synthetic outputs are developed based on the following two formulas:

$$\varepsilon_r = 0.295 N^{-0.538} \tag{4-10}$$

$$D = \sum_i \frac{n_i}{N_i} \tag{4-11}$$

Equation (4-11) is proposed by a group of Japanese scholars (Miki et al. 1981) and correlates the fatigue crack initiation life to the local strain amplitude in the loading direction, which is $\varepsilon_{r,22}$ in this case. Equation (4-12) is the Palmgren-Miner's rule (Liu et al. 2005), which is also called the rainflow counting method. This method assumes that the effect of each cycle is independent, and its damage index is a linear

accumulation of each cycle. D is the damage index, n_i is the number of cycles corresponding to the ith block of constant strain amplitude, and N_i is the number of cycles to failure at this amplitude, calculate by Eq. (4-11). When D reaches 1, a crack is considered to initiate, so this index can be directly used as the output at each time instant. Note that the 10 different representations of each of the 60 round bar models have the same synthetic outputs.

All 600 cases are employed for training the dynamic array. Both the static and the dynamic arrays are well trained for their own goal and are prepared to predict the test results of real-size moment resisting joint specimens.

4.4 Selection of Tested Beam-to-Column Moment Joint Specimens

The selection of tested real-size moment resisting joint specimens from published papers is based on the following three criteria, and each criterion is provided with a detailed description of its purpose.

Criterion 1: The failure mode of the specimen is low cycle fatigue fracture.

Generally, there are three limit states in experiments of real-size beam-to-column moment resisting joint specimens: the occurrence of a fatigue fracture, local buckling resulting in a significant loss of capacity, and reaching a story drift corresponding to the limit of the test setup. The last limit state is associated with unusual situations and is of no research interest. Other than the last limit state, all moment joints with a weak panel zone and some with a balanced panel zone are failed by the first limit state, while joints with a strong panel zone and some with a balanced panel zone are controlled by the second limit state.

In the current investigation, most efforts contribute to the prediction of cyclic ruptures, and only the joints with a failure due to fatigue cracks are within the scope of this research. Although neural networks may be able to predict the fatigue life of joints with a strong panel zone, they have to be organized and trained in a different way, because the failure of these joints is caused by the loss of stability rather than pure fatigue fractures. The decision to end the fatigue test of joints with a strong panel zone is also subjective. Moreover, the finite element analysis of strong-panel joints stalls when local buckling occurs, usually at a drift ratio of 3~4%. After the program stalls, the analysis of strong-panel joints subject to monotonic loading may be followed by a "RESTART" analysis in ABAQUS, however, this brings a huge inconvenience to the analyses subject to cyclic loading especially when there are 85 analysis steps. This problem may call for further independent research.

Criterion 2: There must be a clear indication of when and where the controlling fracture is first observed.

The time elapsed up to the initiation of a crack is the objective of this study. Without such information, there is no way to judge the accuracy of the predictions made by the neural arrays. Similarly, the location of the crack initiation is also essential since the finite element analyses could focus on that region with refined mesh.

Criterion 3: The cyclic loading of the experiment is similar to the SAC loading protocol.

As discussed in Section 4.2, neural networks are sensitive to loading patterns. However, this is not to say that neural networks are not able to recognize different loading patterns. Before it is confirmed that the transition from round bar models to real-

size joint specimens can be realized, no more complexity should be assigned to the current investigation. Therefore, all joint specimens should experience similar loading histories.

In experiments, especially those carried out after 1997, the SAC loading protocol (SAC 1997) is the most commonly used loading pattern, and the maximum number of specimens that experience similar loading histories may be selected from published papers. This also explains why the stepwise increasing amplitude cyclic loading that are proportional to the protocol are imposed to the notch round bars in Section 4.2.

Complying with the above three criteria, a total of 8 specimens are found from more than 100 relevant papers. Table 4.5 lists the researchers, denotation, column shape, girder shape, and, if there is any, doubler plate thickness of each specimen. Although three specimens have a doubler plate in their panel zone, they are still categorized as having a weak-panel joint. The cyclic drift ratio of specimens tested by Lee et al. (2005) was kept at ±4% after two cycles of ±3% were finished, and loadings for all the others (Engelhardt et al. 2000, Kim et al. 2010, and Ricles et al. 2002) followed the SAC loading protocol.

Coincidentally, for all 8 specimens, the controlling fracture initiated in the center portion of the interface between a beam flange and the groove weld, either on the top side of a top flange or on the bottom side of a bottom flange, i.e. the tension side of a tension flange. (It will be shown in Section 4.5 that compression stress can be found on the inner side of a tension flange.) For example, the fracture images of specimens DBBWWPZ and CR2 are provided in Fig. 4.2 and Fig. 4.3, respectively. This finding

further demonstrates that the selected specimens are of the same type, and their fatigue performance will be judged by a certain scheme of neural array.

In order to confirm that the panel zone of all specimens is not stronger than girders, finite element analyses of these joints subject to a monotonic loading are carried out. First order reduced integration shell (S4R) elements are employed. The number of nodes, the number of elements, and the minimum element size are listed in Table 4.6, as are those for global models. Material properties are specified as close as possible to the ones described in the papers. If detailed strain hardening information is not provided, a linear hardening is assumed, and likewise, if elongation is not described, a final strain of 0.15 is approximated. Von Mises yielding criteria and isotropic hardening are employed.

A drift ratio limit of ±10% is set in all analyses. Figs. 4.4 ~ 4.10 plot the Von Mises stress contour of all specimens when they are pushed to this limit. For all models, the ABAQUS program does not stall, indicating the difficulty associated with cyclic analyses of strong-panel joints is not present. In every figure, the column is zigzagged because of the large shear deformation constrained in the panel, and the column flange does not remain normal to the beam flange, implying a crack may initiate from the welding corner.

4.5 Hierarchical Finite Element Analysis

In order to acquire local field histories in the fracturing region, hierarchical finite element analyses are conducted using the submodeling technique in ABAQUS. First, the whole (global) model is analyzed subject to cyclic loading applied at the top end of the column. For specimens CR1, CR2, CR3, and CR5, after ±3% drift ratio cycles are

finished, constant ±4% drift cyclic loading are kept until a total of 42 cycles are reached. For all the others, the SAC loading protocol is applied until two cycles of ±10% drift ratio are completed, and the total number of cycles is also 42, corresponding to 85 analysis steps. The total time span is assumed to be the same as indicated in Fig. 4.1, and the loading rate is approximately 0.75% drift ratio per second. Then, the intermediate local model that contains the fracturing region is analyzed, and the boundary conditions are extracted from the analytical result of the global model. Finally, the sublocal model is analyzed by applying the boundary conditions extracted from the result of the local model.

The global models are the same as the models subject to the monotonic loading in Section 4.4. The local and sublocal models employ second order reduced integration solid (C3D20R) elements, which are proved to prevent numeric problems of both shearlocking and hourglassing (Sun 2006). The number of nodes, the number of elements, and the minimum element size for each specimen are listed in Table 4.4. The hierarchical ABAQUS models are illustrated in Figs. 4.11 ~ 4.33. Material properties are specified in the same way as described in Section 4.4, except combined hardening is employed, and cyclic hardening developed by Kavinde and Deierlein (2004) is added.

In the analyses subject to monotonic loading, all specimens can reach a drift ratio of ±10% without any difficulty, but this does not hold true when cyclic loading is applied. The strain hardening in the panel zone may cause the girder to buckle locally. Generally, this will not be the case in experiments because the beam flange already fractures before buckling occurs. The stall of the analyses also happens later than the

corresponding instant when the controlling fracture is observed in experiments. Therefore, the full history of local field variables up to the crack initiation is still preserved.

The column tip load verses column tip drift ratio relationship of each specimen is plotted for analyses subject to the monotonic loading and analyses subject to cyclic loading in Figs. 4.34 ~ 4.40. For the analyses subject to cyclic loading, only the peak load – peak drift ratio of each cycle in the positive sense is plotted for easier comparisons. It is clear to see that by introducing cyclic hardenings, the loading capacity is promoted.

Figs. 4.41 ~ 4.48 depict the contour of normal stress in the longitudinal direction of the girder (σ_{22} for SP2 and σ_{11} for all the others) for the sublocal model of each specimen when it is fully loaded for the last time. Due to the excessive local bending of the girder flange near the fracturing corner, even compressive stresses appear on the inner side of a tension flange. This finding agrees with the study conducted by Engelhardt et al. (2000).

4.6 Prediction of Low Cycle Fatigue Crack Initiation Life

Figs. 4.49 ~ 4.56 plot the contour of the Von Mises stress for the sublocal model of each specimen when it is fully loaded for the last time. The welding region between the girder flange and the column flange has a very high stress concentration. Also noticed is that in almost all specimens, the welding that connects the shear tab and the column flange also attracts a large amount of stress at the corner of the weld access hole. This agrees with the findings described in some of the papers, that a visible crack was

observed at the top or bottom edge of the shear tab. However, since this crack never propagated and the specimen suffered no strength degradation, it is not a controlling fracture. The focused region is only the center portion of the girder flange welding.

A zoomed-in view of the Von Mises stress contour of the sublocal model of CR1 is provided in Fig. 4.57, which also shows the four elements that are chosen as the candidates of initiating a fatigue crack. The choice of these four elements is solely based on experiment observations that identify this region as critical, rather than on any traditional fracture mechanics criterion regarding Von Mises stress. If computing resources permit, all elements in the welding region can be selected as candidates and the trained static neural array will still identify the element that has the most potential to initiate a fatigue crack. For all other specimens, the four candidates are chosen in the same way as for CR1.

As indicated in the previous section, the analysis of the global model may stall before ±10% drift ratio is reached. In order to make all predicted cases have the same span of field histories, for those specimens that the analysis stalls before experiencing 42 loading cycles, the local field variables recorded during the last successful loading cycle are repeated until the 85^{th} time instant is reached.

As indicated in Section 3.6, simulations made by artificial neural networks are stochastic. Two identical trials of training-prediction may generate diverse results. In order to overcome this disadvantage, first, the training-prediction process is repeated 30 times. The training is based on the 600 cases described above, and the predictions are made for the 8 tested specimens. Then, two incidents of predictions -- all 8 specimens

having a predicted fatigue crack initiation life of 0 or 680 seconds (corresponding to the end of the 42 loading cycles) -- are defined as an irrational outlier, given that their occurrences are not frequent. Among all 30 predictions, around 3 such incidents are found, and their results are neglected. Finally, all remaining prediction results are averaged, and the average value is compared with its corresponding true value recorded in experiments. Fig. 4.58 illustrates this comparison. Apparently, a significant error exists for some of the specimens, because so many uncertainties, such as strain hardening and welding toughness, are embedded in the whole process all the way up from the beginning. On the other hand, a relatively acceptable estimation can also be seen for other specimens, indicating the current investigation is at least meaningful. It is anticipated that, if low cycle fatigue tests of round bars that are directly cut out from real-size joint specimens are carefully carried out, and if the finite element analyses of real-size specimens are well calibrated, the fatigue performance of these specimens will be estimated accurately by the neural arrays.

To conclude, this is the first time that the fatigue performance of a real-size structural component is estimated from that of a much smaller composing element using the dynamic competitive neural array. Besides other uncertainties, although the synthetic data based on tests done in Japan is independent from the test results of joint specimens, the dynamic array still performs well. Ideally, fatigue tests of all weak panel zone and some balanced panel zone specimens can be waived and replace by low cycle fatigue tests of notched round bars, which will save both physical and financial efforts.

Moreover, a great number of future research topics may be suggested. First, neural network predictions made for specimens subject to mixed patterns of cyclic loading may be investigated. Second, for those specimens that fail to be analyzed for the whole loading cycles, the local field histories can be linearly mapped so that the predictions will only depend on the available span of loading histories. This will also require a more comprehensive scheme of network trainings. Last, although the fatigue tests of those joint specimens cannot be repeated, the finite element analyses can always be replicated with different material properties. If a lower and higher bound of material strain hardenings are specified for each specimen, more points will be plotted in Fig. 4.58, and a confidence interval may be found.

4.7 Summary

In this section, the low cycle fatigue crack initiation life of real-size beam-to-column moment resisting joint specimens tested by various programs is predicted. It is the first time that the fatigue performance of a real-size structural component is estimated from that of a much smaller composing element using the dynamic competitive neural array. Although far from perfect, the estimations made by neural arrays are satisfactory. The fatigue performance of real-size beam-to-column specimens will be estimated accurately if a matrix of round bar specimens are designed and tested under cyclic loading. A larger impact of this investigation is that, fatigue tests of all joints with a weak panel zone and some with a balanced panel zone may be waived in the future.

5. FINITE ELEMENT ANALYSIS AND LOW CYCLE FATIGUE LIFE ESTIMATION OF NEWLY DESIGNED SPECIMENS

5.1 Introduction

A peer research team at the University of Texas at Austin has designed a matrix of 10 steel beam-to-column moment resisting joint specimens which are being tested at the University of Minnesota's Multi-Axial Subassemblage Testing (MAST) Laboratory, a member of the George E. Brown, Jr. Network for Earthquake Engineering Simulation (NEES). This section is devoted to the finite element analyses and fatigue performance estimations of these specimens.

First, the design of the specimens is briefly discussed. Then, finite element analyses of the specimens subject to cyclic loading specified by the SAC loading protocol are conducted in ABAQUS. Manufacturing imperfections are considered, and quasi-static analyses with an adaptive automatic stabilization scheme are implemented. In addition, hierarchical finite element analyses are carried out, and the local field histories in the region of welding connections are obtained. Finally, the low cycle fatigue crack initiation life of the specimens with a weak panel zone is predicted.

5.2 Newly Designed Specimens

Table 5.1 lists all 10 specimens designed by the University of Texas group, and Fig. 5.1 depicts the test setup plan. Figs. 5.2 ~ 5.3 provide photos of the test setup in the laboratory. The specimens are categorized into three sets: the deep column set

(Specimens 1 ~ 3), the jumbo column set (Specimens 4 ~ 7), and the small column set (Specimens 8 ~ 10). In the first set, the only difference among the three specimens is the thickness of the panel zone. In the second set, Specimens 4 ~ 6 differ according to panel zone thickness, while Specimen 7 has cover plates attached to the beam flanges. In the last set, varying axial loads in the column are designed for identical specimens.

Specimen 7 has a Bolted Flange Plate (BFP) moment connection, and all the other specimens have a Welded Unreinforced Flange – Welded web (WUF-W) connection. As indicated in Table 5.1, Specimens 3 and 6 are designed as moment joints with a strong panel zone, Specimens 2 and 5 are designed with a balanced panel zone, and the others are those with a weak panel zone.

5.3 Finite Element Analysis Subject to Cyclic Loading

5.3.1 Finite element models

For all analyses described in this section, four-node reduced integration shell (S4R) elements are employed, and the number of nodes, the number of elements, and the minimum element size are listed in Table 5.2, as are those for global models.

In the laboratory, braces need to be installed to provide lateral constraints to tested specimens, as shown in Figs. 5.1 ~ 5.3. These boundary conditions are realized in two different ways in the finite element models: 1) rigid surfaces are created to simulate the braces, and the contact between steel shape edges and these surfaces are frictionless so that the braces only provide out-of-plane support, allowing the specimens to freely slide within the braces; and 2) when the specimens are in their original unloaded position, the nodes on the braced portions of the shape edges are constrained from

moving laterally in *z* direction. The finite element models of these two cases are provided in Fig. 5.4. Moreover, specimens designed with an axial load in the column are also analyzed for the case when the axial load is not present. Thus, for Specimens 1 ~ 3, each specimen is analyzed in four different conditions (with and without braces, with and without axial load). When the axial load is not present, Specimens 9 and 10 are the same as Specimen 8, therefore each of Specimens 8 ~ 10 are only analyzed in two conditions (with and without braces). No axial load has been designed for Specimens 4 ~ 7, and these specimens are also analyzed in two conditions (with and without braces). The horizontal column tip loads follow the SAC loading protocol.

At the time when this dissertation is almost accomplished, the University of Texas group has just finished testing Specimens 8 ~ 10 and Specimen 4. In order to make the prediction of all specimens' hysteresis behavior as accurate as possible, the material property is calibrated according to the test result of Specimen 8. A yield strength of 415MPa (60ksi) is chosen, and multi-linear post-yield hardening is determined after several trials. The comparison between the finite element analysis result and the test result will be provided below. The Von Mises rule is chosen as the yielding criteria for steel, and nonlinear kinematic hardening is specified.

Fabrication imperfections are mostly, among other reasons, caused by unbalanced heat induction during the welding procedure and may substantially morph the original geometry of real-size subassemblage specimens. Since imperfections are always randomly formed and located, a widely used method of incorporating imperfections in finite element analyses is to assume that they have the same shape of

the lowest bucking modes and that their magnitudes are proportional to a combination of these modes. Detailed information can be found in ABAQUS (2009). Before the cyclic quasi-static analyses of all specimens, a linear elastic analysis of the buckling modes is prerequisite. An example (Specimen 1) of the lowest buckling mode, which is the first mode in the positive sense, is shown in Fig. 5.5. In this case, a certain magnitude of horizontal force is applied to the column tip along the positive x direction. If a negative x direction force is applied, a symmetric mode shape will appear where the top flange and upper web of the left beam buckle, as well as the bottom flange and lower web of the right beam. In order to take all possible buckling modes in the close vicinity of the panel zone into account, the first 4 mode shapes are equally weighted with a uniform proportional factor and combined to be the geometric imperfection of the corresponding specimen. By adding a command line referring to the result of the linear buckling analysis, geometric imperfections are prescribed in the ABAQUS input file for quasi-static analyses. In this study, imperfections whose maximum magnitude equals 10% of the beam web thickness are assumed.

Beam local buckling invariably occurs when a large drift is posed, and the loss of stability due to buckling may unfavorably stall the finite element analysis. ABAQUS provides an automatic mechanism for stabilizing unstable quasi-static problems through the automatic addition of volume-proportional damping to the model (ABAQUS 2009). In this series of cyclic analyses, the adaptive automatic stabilization scheme is used.

5.3.2 Analysis results

The load – drift ratio hysteresis loops of all specimens analyzed in different conditions are plotted in Figs. 5.6 ~ 5.15. Almost all specimens display a much larger loop when the braces are replaced by freezing the lateral freedom of the relevant nodes. Further investigation of ABAQUS message files indicates that the analyses with the existence of braces are terminated due to the unacceptable contact penetration error. In other words, the plastic deformation developed in one or some of the beam flanges in a loading step prevents the specimens sliding through the braces any more when the load is reversed in the following step. In finite element analysis, this limit is rigorous because almost no penetration is allowed between elements in contact. However, in the laboratory, braces are not absolutely rigid, and a low level of friction between the specimens and the braces is also present. Although the inclusion of braces in the finite element models preserves a closer simulation of laboratory setups, as a substitutive approach, constraining the lateral freedom of the relevant nodes provides a better perspective of the hysteresis behavior without sacrificing global accuracy. The discussion made below will only consider the results of the analyses without braces.

The comparisons between ABAQUS simulation results and test results for Specimens 8, 9, 10, and 4 are illustrated in Figs. 5.16 ~ 5.19, respectively. As mentioned above, the material property of steel is calibrated based on a trial and error process until the simulated hysteresis loop of Specimen 8 is close enough to the test result, as shown in Fig. 5.16. Figs. 5.17 ~ 5.19 also exhibit a high extent of agreement between the simulation and the test, indicating the calibrated material property is realistic. Simulations made for Specimens 8 ~ 10 exhibit a delayed strength softening compared

with experiment results, which may be caused by a lower extent of geometry imperfection that has been assumed.

As shown in Figs. 5.6 ~ 5.8, tensile force in the column plays a role in promoting the horizontal load carrying capacity of moment joints as well as elongating the hysteresis loop. As opposed to the P-delta effect, a larger horizontal column tip load is needed to push the specimens to the same drift when a tensile load exists in the column. In other words, the resultant bending moment due to the tensile force in the positive y direction is counteracting the moment due to the horizontal load in the positive x direction, resulting in a great promotion of the loading capacity. In addition, when the specimen is about to be pushed over, the pulling force in the column holds its weight to prevent the collapse. These findings are also repeated in Figs. 5.13~ 5.15. Specimens 9 and 10 have a greater loading capacity than Specimen 8 by applying tensile force in the column.

Figs. 5.6 ~ 5.15 also demonstrate that almost all specimens display a strength hardening in the first several loading cycles until degradation occurs at various drift ratios associated with beam local buckling. It is observed from these figures that beam local buckling occurs at 6% drift ratio for Specimen 1, 3% for Specimens 2 and 3, 6% for Specimen 5, 5% for Specimen 6, 8% for Specimen 8, 7% for Specimen 9, and 8% for Specimen 10. No noticeable strength degradation is found in the hysteresis loop of Specimens 4 and 7. Further comparisons indicate that the specimens with a weak panel zone (such as Specimens 1, 4, and 7) yield at a lower load level and perform a longer strength hardening, while those with a strong panel zone (such as Specimens 3 and 6)

yield at a higher load level, presumably followed by strength softening after a 2~3% drift ratio is reached. Another finding is that attaching a cover plate to girder flanges (Specimen 7) does not significantly increase the loading capacity, because the fuse is the weak panel zone.

Figs. 5.20 ~ 5.39 plot the Von Mises stress contour of all the specimens on their deformed shape when 4% drift ratio is reached and when the specimens are in their final loading cycle. Magnified views of the panel zone region are also illustrated. Clearly, at 4% drift ratio, yielding is mostly constrained within the panel zone of Specimens 1, 4, 7, 8, 9, and 10, and no buckling is observed. On the contrary, more yielding occurs in the beams of Specimens 2, 3, and 6, and both sides of the beams have buckled. Specimen 5 displays a balanced yielding of the panel and the girder at 4% drift ratio. Except Specimens 4 and 7, all specimens display beam buckling in their final loading stage. Portions of the columns of Specimens 1, 2, 3, 9, and 10 also yield resulting from stress concentration caused by the bending stress coupled with the tensile normal stress. Figs. 5.40 ~ 5.42 are photos of Specimens 8, 9, and 10, respectively, in the laboratory when the experiment was finished. The location of beam buckling matches that of the ABAQUS simulation result, indicating a good agreement between the analysis and the test.

The histories of column tip displacement contributions from the panel zone, the beams, and the columns of each specimen are calculated following the equations derived by Jones (2000) and plotted in Figs. 5.43 ~ 5.56. Specifically, the displacement components due to plastic deformations of the whole joint, the panel zone, the beams,

and the columns are plotted in Fig. 5.47, Fig. 5.49, Fig. 5.51, and Fig. 5.53 for Specimens 4, 5, 6, and 7, respectively. Figs. 5.43 ~ 5.56 demonstrate that, Specimens 4 and 7 have a weak panel zone, and Specimens 2, 3, and 6 have a strong panel zone. Specimens 1, 5, 8, 9, and 10 may have a balanced panel zone, and a further investigation of the contributions from each component of these specimens will be conducted below. Notice that the straight lines adjacent to the vertical axis penetrating the envelope of Figs. 5.43(a), 5.55(a), and 5.56(a) denote the contributions from the panel zone of Specimens 1, 9, and 10, respectively, when the specimens' drift ratio is greater than 8%. At this time, their column tip displacements are mainly caused by the large ductile deformations in the beams while the stability of the joints being held by the axial force in the column. This large drift (8% of the column's height) is not likely to be achieved in experiments. Figs. 5.46 and 5.47 show that Specimen 4's column tip displacement is mostly contributed by the panel zone, and plastic deformation is predominant. On the contrary, as illustrated in Figs. 5.50 and 5.51, a major source of Specimen 6's displacement falls in the beams, indicating Specimen 6 has a strong panel zone.

Following the above calculations, the evolutions of the displacement contribution percentage of the panel zone, the beams, and the columns when the corresponding drift ratio is first reached in the positive sense are plotted in Figs. 5.57 ~ 5.66 for all specimens. After Specimen 5 yields at 3% drift ratio, its panel zone and beams exhibit balanced contributions to the total column tip displacement. However, when beam local buckling occurs at 6% drift ratio, the contribution from the beams becomes predominant. Similar trends can also be observed on both Specimens 9 and 10 that exhibit balanced

yielding between the panel zone and the beams before beam local buckling is present. After yielding, the contribution from the panel zone of Specimens 1 and 8 surpasses the contribution from the beams, until the contribution from the beams becomes the highest when beam local bucking happens. The contribution from the beams of Specimens 2, 3, and 6 and the contribution from the panel zone of Specimens 4 and 7 are overwhelming through the whole loading history.

5.4 Hierarchical Finite Element Analysis

In order to acquire local field histories in the supposed fracturing region and perform neural array predictions, hierarchical finite element analyses are conducted for Specimens 1, 4, and 7. It is assumed that, due to welding difficulties, the bottom side of one of the bottom flanges of the girder may initiate a fracture in the fusion region. Global, local, and sublocal models are made accordingly and illustrated in Figs. 5.67 ~ 5.74. Geometrical symmetry is utilized to lower the total number of elements, given that during most of the time of cyclic loading, the beams remain unbuckled. Second order reduced integration solid (C3D20R) elements are used, and the number of nodes, the number of elements, and the minimum element size are listed in Table 5.2. Material properties are the same as described in Section 5.3.

Figs. 5.75 ~ 5.77 depict the contour of normal stress in the longitudinal direction of the girder (σ_{11}) for the sublocal model of the three specimens during a loading cycle of 4% drift ratio. Due to the excessive local bending of the beam flange near the kinking corner, even compressive stresses appear on the top side of the bottom flange.

Figs. 5.78 ~5.80 depict the Von Mises stress contour of the sublocal model of the three specimens during a loading cycle of 4% drift ratio. The welding region between the girder flange and the column flange has a high stress concentration, especially in the center portion of the bottom side of the beam flange.

5.5 Prediction of Low Cycle Fatigue Crack Initiation Life

Following the procedure narrated in Section 4.6, the fatigue crack initiation life of Specimens 1, 4, and 7 is predicted by the trained neural arrays and recorded in Table 5.3. It is predicted that the crack initiation of Specimen 4 occurs when the specimen is in its first loading cycle of 5% drift ratio. In the laboratory the first crack was found after the first cycle of 4% drift ratio at the east beam top flange, and the corresponding photo is provided in Fig. 5.81. Then, subsequent cracks were observed at the bottom flange of both east and west beams after the second cycle of 6% drift ratio, as shown in Figs. 5.82 and 5.83. The photo of the final fracture of the east beam bottom flange is given in Fig. 5.84. The prediction made for Specimen 4 is very close to the experiment result, indicating the competitive neural array developed and trained in Section 4.6 functions very well. The accuracy of the prediction will be promoted when the finite element analyses of the round bars and the moment joint specimens are calibrated by the results of material tests that will be implemented in the near future.

The predictions made for Specimens 1 and 7 provide a reference of the loading cycles under focus during experiments and will be compared with test results to further validate the application of neural networks to fatigue performance estimations.

5.6 Summary

In this section, finite element analyses of newly designed specimens are preformed, the strength of their panel zone is identified, and the fatigue performance of the specimens with a weak panel zone is predicted. Comparisons demonstrate that, tensile force in column plays a role in promoting the horizontal load carrying capacity of moment joints as well as preventing the joints from collapsing. The moment joints with a weak panel zone display a stable post-yielding strength hardening with the column tip displacement mainly contributed by panel zone plastic shear. The joints with a strong panel zone reach their ultimate strengths at a lower drift, followed by strength degradation, and their column tip displacement is due mostly to beam plastic deformation. The fatigue crack initiation life of three weak-panel specimens is predicted and the prediction made for one of the specimens has been validated by experiment.

6. CONCLUSION

6.1 Summary and Conclusions

This dissertation presents an innovative way of predicting low cycle fatigue crack initiation life with the application of artificial neural networks.

Following literature reviews and problem statements, a competitive neural array comprising various types of neural networks is established in Section 2 to estimate fatigue crack initiation life. Then, the investigation starts with the finite element analyses of notched round bar models, followed by extracting their history of local field variables, such as stress, strain, and nodal displacements, as the input vectors for neural networks. Results show that neural networks are capable of predicting the location that is most inclined to initiate a crack, as well as estimating the time elapsed to cause this initiation to a satisfactory extent.

In addition to the 30 models created in Section 2, 60 more notched round bar models made of synthetic materials are analyzed in Section 3, and the history of their local field variables is extracted. After assigning a series of indices for each material, input vectors consisting of 11 components at every time instant of all 90 cases are prepared in a proper format for processing in FTDNNs. Then, a dynamic competitive array with a newly designed scheme is developed, and the time elapsed up to the end of each of the three fracture progression stages during the crack initiation process is estimated. The influence of the number of training input cases on the prediction accuracy

is also examined. MSEs associated with the predictions made for the first two stages are found to be much smaller than those for the initiation life, and the predictions made for the initiation life are satisfactory. Around 50 notched round bar specimens are recommended for use in future experiments, given that the loading pattern is similar to the pattern for real-size moment resisting joints.

In Section 4, the low cycle fatigue crack initiation life of real-size beam-to-column moment resisting joint specimens tested by various programs is predicted. It is the first time that the fatigue performance of a real-size structural component is estimated from that of a much smaller composing element using the dynamic competitive neural array. Although far from perfect, the estimations made by neural arrays are satisfactory. The fatigue performance of real-size beam-to-column specimens will be estimated accurately if a matrix of round bar specimens are designed and tested under cyclic loading. A larger impact of this investigation is that, fatigue tests of all joints with a weak panel zone and some with a balanced panel zone may be waived in the future.

In Section 5, finite element analyses of newly designed specimens are preformed, the strength of their panel zone is identified, and the fatigue performance of the specimens with a weak panel zone is predicted. Comparisons demonstrate that, tensile force in column plays a role in promoting the horizontal load carrying capacity of moment joints as well as preventing the joints from collapsing. The moment joints with a weak panel zone display a stable post-yielding strength hardening with the column tip displacement mainly contributed by panel zone plastic shear. The joints with a strong

panel zone reach their ultimate strengths at a lower drift, followed by strength degradation, and their column tip displacement is due mostly to beam plastic deformation. The fatigue crack initiation life of three weak-panel specimens is predicted and the prediction made for one of the specimens has been validated by experiment.

6.2 Suggestions for Future Research

A number of future research topics may be suggested from this dissertation. First, neural network predictions made for specimens subject to mixed patterns of cyclic loading may be investigated. Second, for real-size moment joint specimens that fail to be analyzed for the whole loading cycles, the local field histories can be linearly mapped so that predictions will only depend on the available span of loading histories. This will also require a more comprehensive scheme of network trainings. Moreover, the finite element analyses can be replicated for real-size moment joint specimens with different material properties. If a lower and higher bound of material strain hardenings are specified for each specimen, more points will be plotted in Fig. 4.61, and a confidence interval may be found. In addition, for predicting the fatigue performance of the newly designed real-size moment joint specimens, it is recommended that a total of approximately 50 notched round bars directly cut out from the real-size specimens be tested, so that the dynamic array can be better calibrated by experimental results of round bars. Detailed fractographic analyses should be performed on the round bar specimens including scanning electron microscope (SEM) assays of the fracture surfaces, therefore the first three stages of the fracture progression is expected to be differentiated in the experiments. Last, a different training – prediction scheme may be

developed for moment joints with a strong panel zone, given that the failure of these joints is defined by the same extent of capacity loss.

REFERENCES

ABAQUS (2009). *ABAQUS Analysis User's Manual Version 6.9-EF,* Dassault Systèmes Simulia Corp., Providence, RI.

Abdalla, J. and Hawileh, R. (2010). "Modeling and simulation of low-cycle fatigue life of steel reinforcing bars using artificial neural network." *Journal of the Franklin Institute*, 348(7), 1393-1403.

Anderson, T. L. (1995). *Fracture Mechanics: Fundamentals and Applications*, 2nd Edition., CRC Press, Inc., Boca Raton, FL.

Beale, M. H., Hagan, M. T., and Demuth, H. B. (2011). *Neural Network Toolbox User's Guide*, The MathWorks, Inc., Natick, MA.

Becker, E. R. (1971). "Panel zone effect on the strength and stiffness of rigid steel frames." *Research Report*, Mechanical Laboratory, University of Southern California, Los Angeles, CA.

Engelhardt, M. D., Fry, G. T., Jones, S. L., Venti, M. J., and Holliday, S. D. (2000). "Behavior and design of radius cut reduced beam section connections." *Report No. SAC/BD 00/17*, Sac Joint Venture, Sacramento, CA.

Fielding, D. J. and Huang, J. S. (1971). "Shear in steel beam-to-column connections." *Welding Journal*, 50(7), 313-326.

Gullerud, A., Koppenhoefer, K., Roy, A., RoyChowdury, S., Walters, M., Bichon, B., Cochran, K., Carlyle, A., and Dodds, R. H., Jr. (2007). *WARP3D-Release 15.7: 3-D Dynamic Nonlinear Fracture Analysis of Solids Using Parallel Computers and Workstations*, Department of Civil Engineering, University of Illinois at Urbana-Champaign, Urbana, IL.

Hanselman, D. C. and Littlefield, B. L. (2005). "Cubic Splines." *Mastering MATLAB 7*, Pearson/Prentice Hall, Upper Saddle River, NJ, 340-342.

Haykin, S. (1999). *Neural Networks: A Comprehensive Foundation*, 2nd Edition, Pearson/Prentice Hall, Upper Saddle River, NJ.

Hsiao, J. K., Schultz, W., Petersen, T., and Vaicik, S. (2008). "Computation of story drifts considering panel zone deformations for multistory steel moment frames

with welded flange plate connections." *The Structural Design of Tall and Special Buildings*, 17(2), 419-443.

Hyland, D. C. (1995). "Adaptive neural control for flexible aerospace systems: progress and prospects." *Proceedings of the 10th IEEE International Symposium on Intelligent Control*, Monterey, CA, Aug. 27-29.

Hyland, D. C. and Fry, G. T. (1999). "A neural-genetic hybrid approach for optimizing structural health monitoring systems." *Proceedings of the 2nd International Workshop on Structural Health Monitoring*, Palo Alto, CA, Sep. 8-10., 800-811.

Jadid, M. N. and Fairbairn, D. R. (1996). "Neural-network applications in predicting moment-curvature parameters from experimental data." *Engineering Applications of Artificial Intelligence*, 9(3), 309-319.

Jones, S. L. (2000). "An analysis procedure to facilitate performance-based design of steel moment frame buildings with reduced beam section joints." Ph.D. Dissertation, Department of Civil Engineering, Texas A&M University, College Station, TX.

Kanvinde, A. M. and Deierlein, G. G. (2004). "Micro simulation of earthquake-induced fracture in steel structures." *Report No. 145*, The John A. Blume Earthquake Engineering Center, Department of Civil and Environmental Engineering, Stanford University, Palo Alto, CA.

Kim, T., Kim, U., and Kim, J. (2010). "Collapse resistance of unreinforced steel moment connections." *The Structural Design of Tall and Special Buildings*, Early View (Online Version of Record published before inclusion in an issue), DOI: 10.1002/tal.636.

Krawinkler, H., Bertero, V. V., and Popov, E. P. (1971). "Inelastic behavior of steel beam-column subassemblages." *Report No. EERC 71/07*, University of California, Berkeley, CA.

Krawinkler, H., Bertero, V. V., and Popov, E. P. (1975). "Shear behavior of steel frame joints." *Journal of the Structural Division*, ASCE, 101(11), 2317-2336.

Krawinkler, H. (1978). "Shear in beam-column joints in seismic design of steel frames." *Engineering Journal*, AISC, 42(4), 189-213.

Lee, D., Cotton, S. C., Hajjar, J., Dexter, R. J., and Ye, Y. (2005a). "Cyclic behavior of steel moment-resisting connections reinforced by alternative column stiffener details I. connection performance and continuity plate detailing." *Engineering Journal*, AISC, 5(3), 82-91.

Lee, D., Cotton, S. C., Hajjar, J., Dexter, R. J., and Ye, Y. (2005b). "Cyclic behavior of steel moment-resisting connections reinforced by alternative column stiffener details II. panel zone behavior and doubler plate detailing." *Engineering Journal*, AISC, 5(3), 215-238.

Lee, S. J. (1987). "Seismic behavior of steel building structures with composite slabs." *Doctoral Dissertation*, Department of Civil Engineering, Lehigh University, Bethlehem, PA.

Liu, W., Liang, Z., and Lee, G. C. (2005). "Low-cycle bending fatigue of steel bars under random excitation. Part II: design considerations." *Journal of Structural Engineering*, ASCE, 131(6), 919-923.

Long, X. (2006). "Fatigue strength of butt-welded joints with under-matched filler metals under cyclic plastic strain." Master Thesis, Department of Civil Engineering, Tokyo Institute of Technology, Tokyo, Japan.

Mathew, M. D., Kim, D. W., and Ryu, W. S. (2008). "A neural network model to predict low cycle fatigue life of nitrogen-alloyed 316L stainless steel." *Material Science and Engineering*, 474(1-2), 247-253.

Miki, C., Nishimura, T., Tanabe, H, and Nishikawa, K. (1981). "Study on estimation of fatigue strengths of notched steel members." *Proceedings of JSCE (Japan Society of Civil Engineers)*, 316, 153-166.

Mohanty, J. R., Verma, B. B., Parhi, D. R. K., and Ray, P. K. (2009). "Application of artificial neural network for predicting fatigue crack propagation life of aluminum alloys." *Computational Materials Science and Surface Engineering*, 1(3), 133-138.

Patela, M., Lala, S. K. L., Kavanagha, D., and Rossiterb, P. (2011). "Applying neural network analysis on heart rate variability data to assess drive fatigue." *Expert Systems with Applications*, 38(6), 7235-7242.

Popov, E. P., Amin, N. R., Louie, J. C., and Stephen, R. M. (1985). "Cyclic behavior of large beam-column assemblies." *Earthquake Spectra*, 1(2), 201-237.

Pujola, J. C. F. and Pintob, J. M. A. (2011). "A neural network approach to fatigue life prediction." *International Journal of Fatigue*, 33(3), 313-322.

Rice, J. R. (1968). "A path independent integral and the approximate analysis of strain concentration for notches and cracks." *Journal of Applied Mechanics*, 35(2), 379-386.

Rice, J. R. and Tracey, D. M. (1969). "On the ductile enlargement of voids in triaxial stress fields." *Journal of the Mechanics and Physics of Solids*, 17(3), 201-217.

Ricles, J. M., Mao, C., Lu, L., and Fisher, J. W. (2002). "Inelastic cyclic testing of welded unreinforced moment connectors." *Journal of Structural Engineering*, ASCE, 128(4), 429-440.

Roeder, C. (2000). "State of the art report on connection performance." *Report No. FEMA-355D*, Federal Emergence Management Agency, Washington, DC.

SAC (1997). "Protocol for fabrication, inspection, testing, and documentation of beam-column connection tests and other specimens." *Report No. SAC/BD-97/02 Version 1.1*, SAC Joint Venture, Sacramento, CA.

Skallerud, B. and Zhang, Z. L. (2001). "On numerical analysis of damage evolution in cyclic elastic-plastic crack growth problems." *Fatigue & Fracture of Engineering Materials & Structures*, 24(1), 81-86.

Sun, E. Q. (2006). "Shear locking and hourglassing in MSC Nastran, ABAQUS, and ANSYS." *MSC Software Technical Papers*, <http://www.mscsoftware.com /events/vpd2006/na/presentations/tech_papers/27.pdf> (Dec. 1, 2011).

Wei, H. L., Billings, S. A., Zhao, Y. F., and Guo, L. Z. (2010). "An adaptive wavelet neural network for spatio-temporal system identification." *Neural Networks*, 23(10), 1286-1299.

Widrow, B. and Hoff, M. E., Jr. (1960). "Adaptive Switching Circuits." *IRE Western Electric Show and Convention Record*, New York, NY, Part 4, 96-104.

APPENDIX A

FIGURES

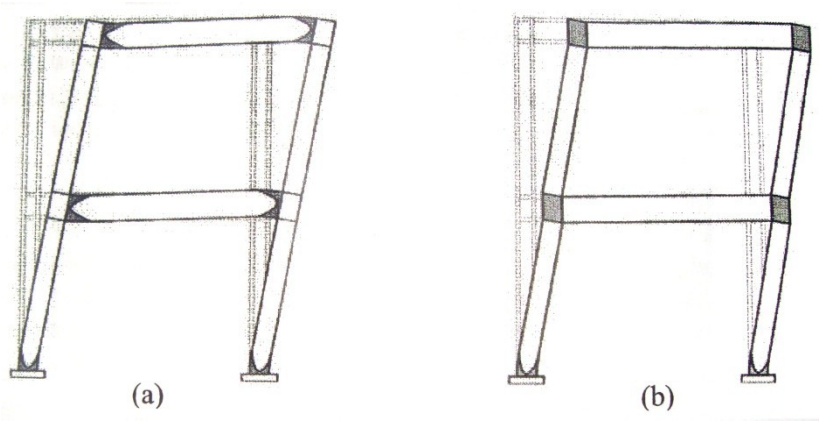

Figure 1.1 Steel moment frames with plastic hinges in (a) beams and (b) panel zones

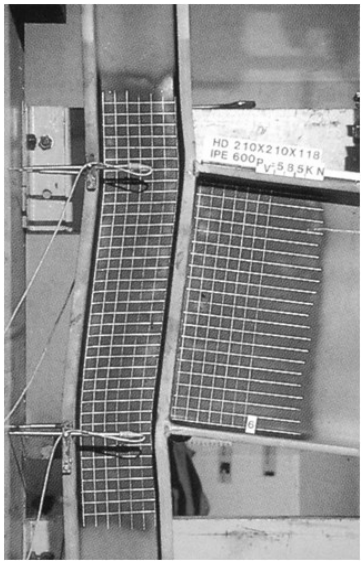

Figure 1.2 Shear distortion of joint with a weak panel zone (Krawinkler 1978)

Figure 1.3 Fracture near beam flange groove welds of a weak panel zone (Engelhardt et al. 2000)

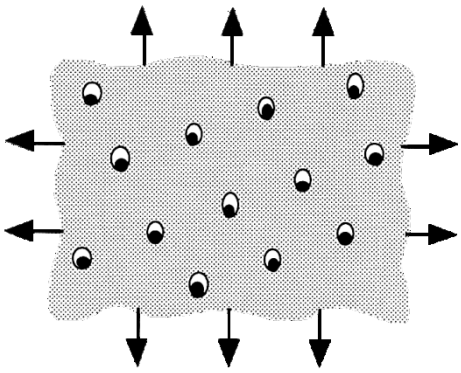

(a) Void nucleation and growth

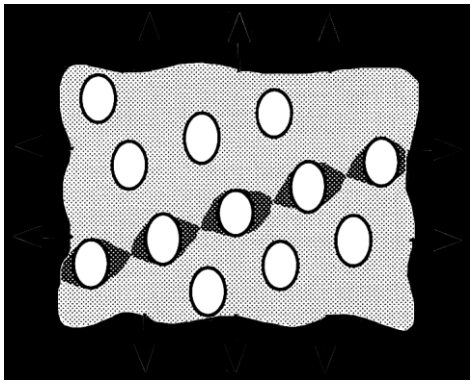

(b) Material separation

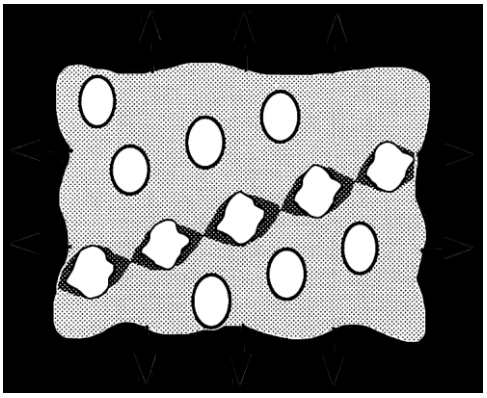

(c) Micro- to macro-scopic crack

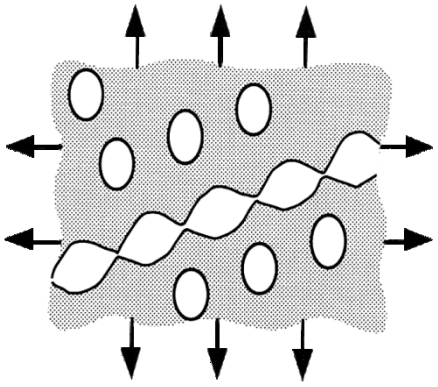

(d) Coalescence of emergent crack

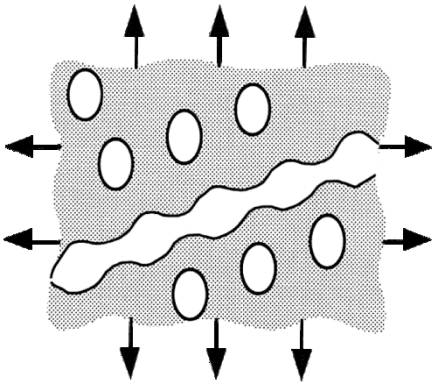

(e) Dominant crack propagation

Figure 1.4 Five-stage fracture progression (Anderson 1995)

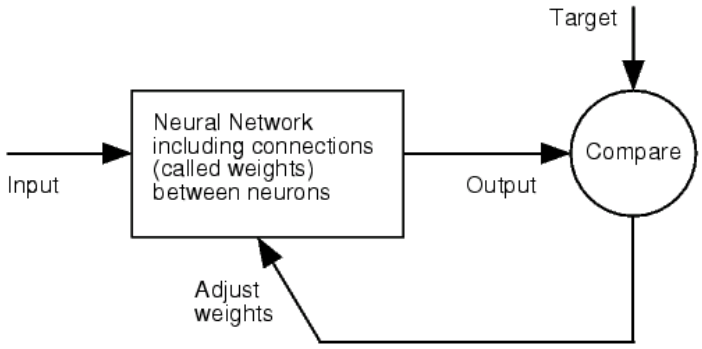

Figure 1.5 Artificial neural networks training loop (Beale et al. 2011)

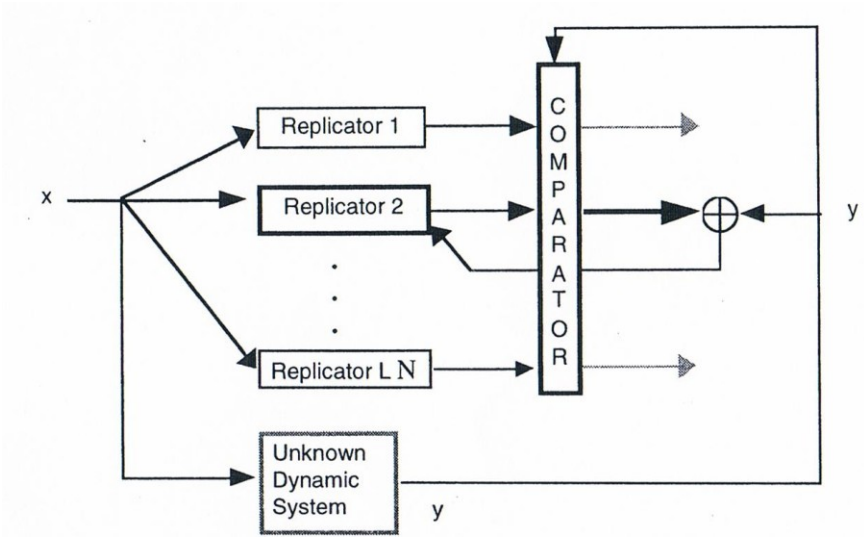

Figure 1.6 Competitive model scheme for rapid system identification (Hyland and Fry 1999)

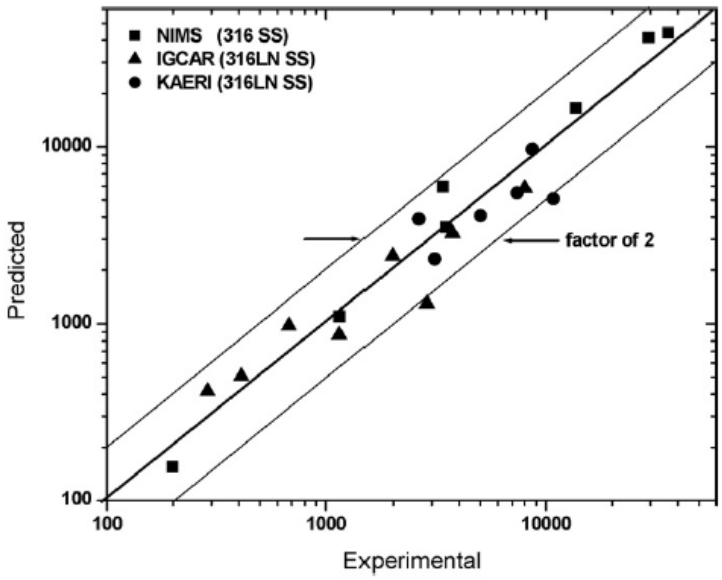

Figure 1.7 Comparison between experimental and predicted fatigue life using artificial neural networks (Mathew et al. 2008)

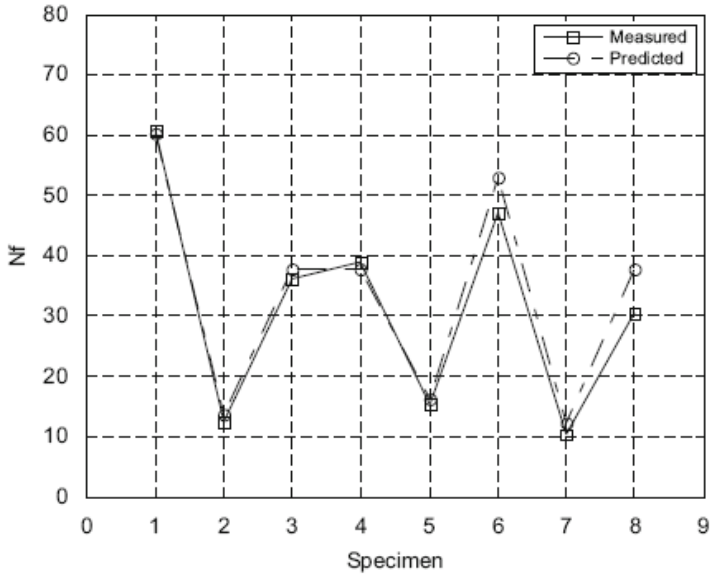

Figure 1.8 Measured and predicted fatigue life of test specimens (Abdalla and Hawileh 2010)

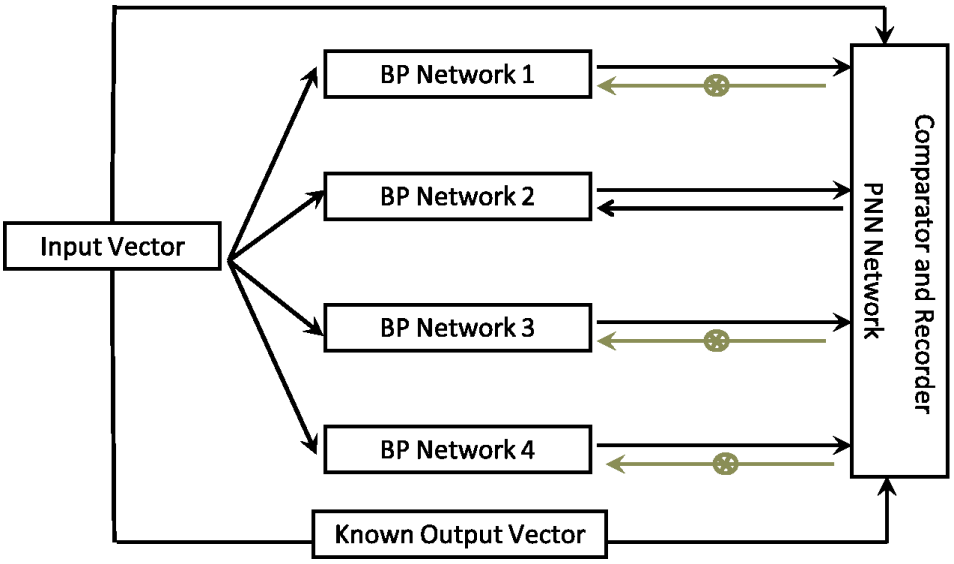

Figure 2.1 Artificial neural network array – training mode

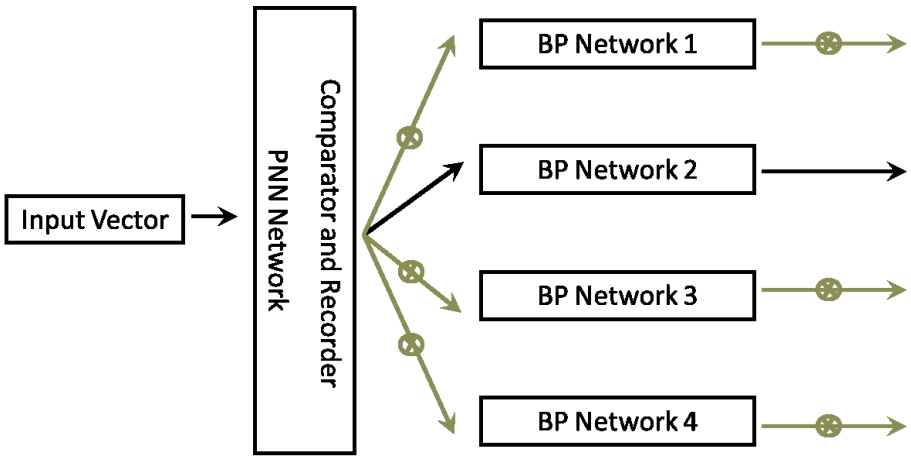

Figure 2.2 Artificial neural network array – operation mode

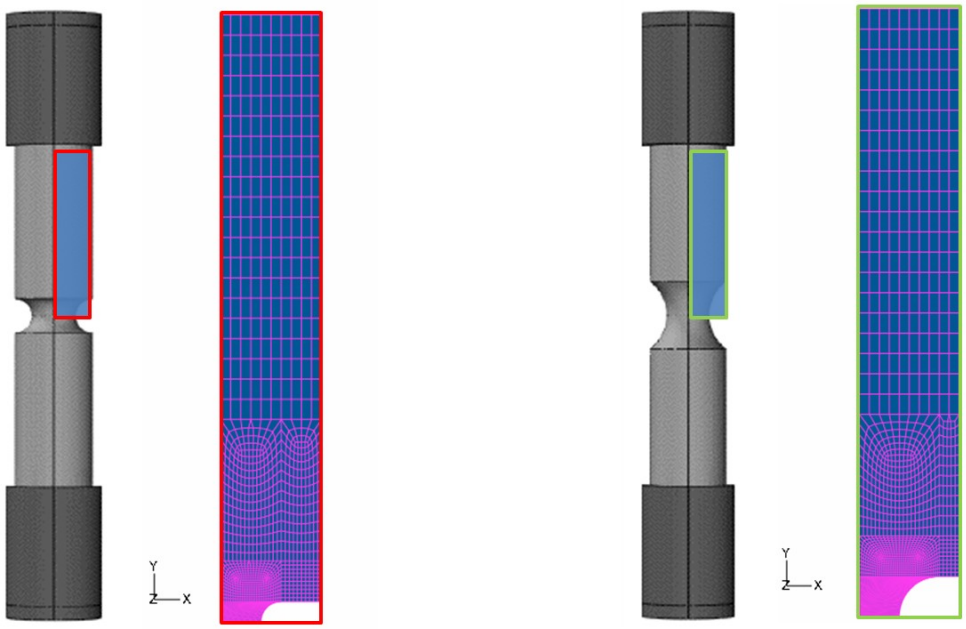

(a) R=1mm (b) R=2mm

Figure 2.3 Finite element models for notched round bars

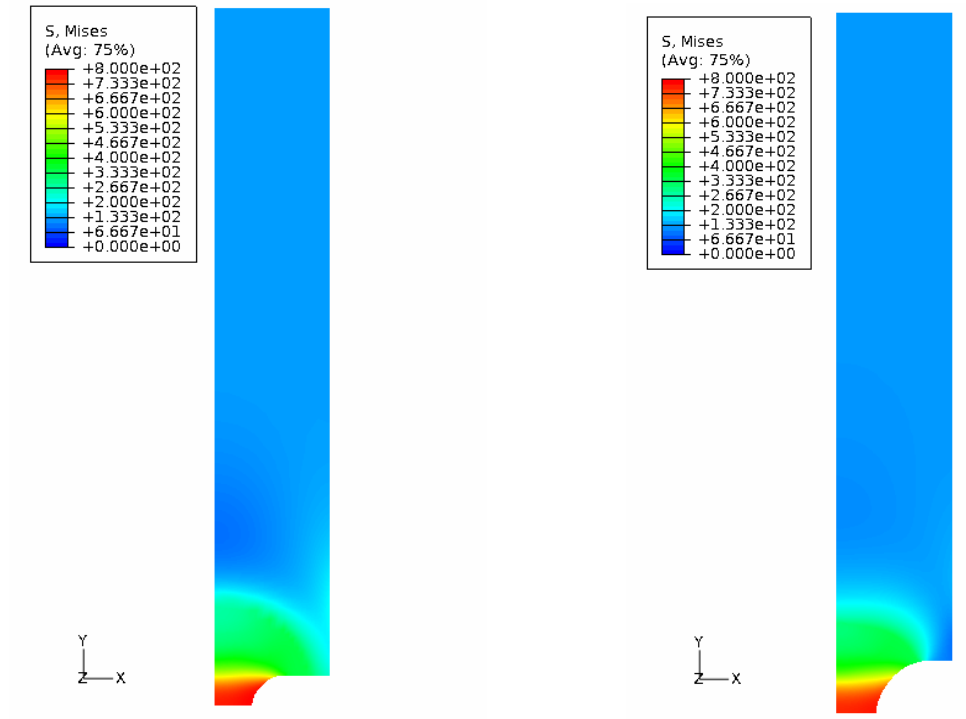

(a) R=1mm (b) R=2mm

Figure 2.4 Von Mises stress contour when the models are fully stretched

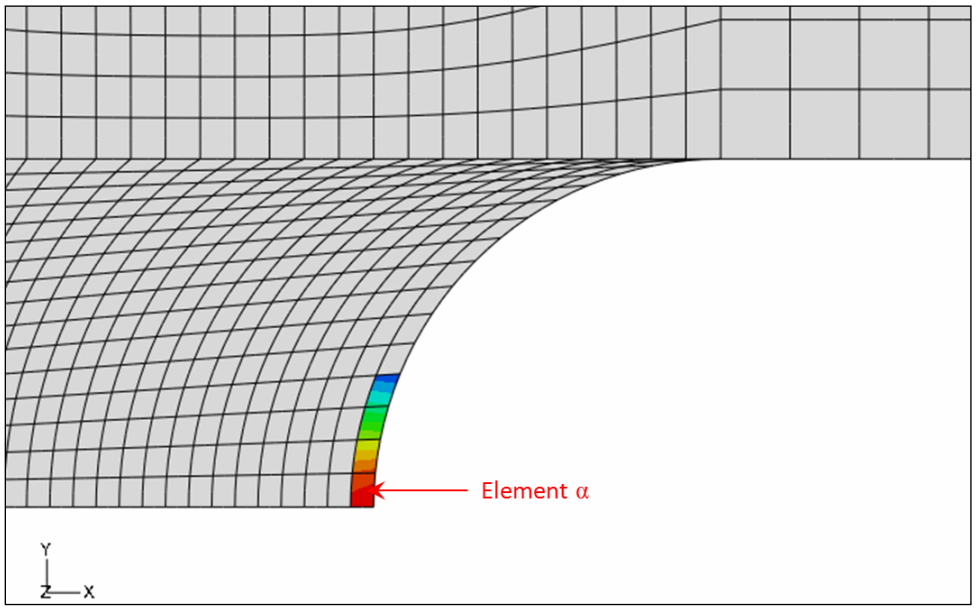

Figure 2.5 The four candidate elements in the vicinity of notch root

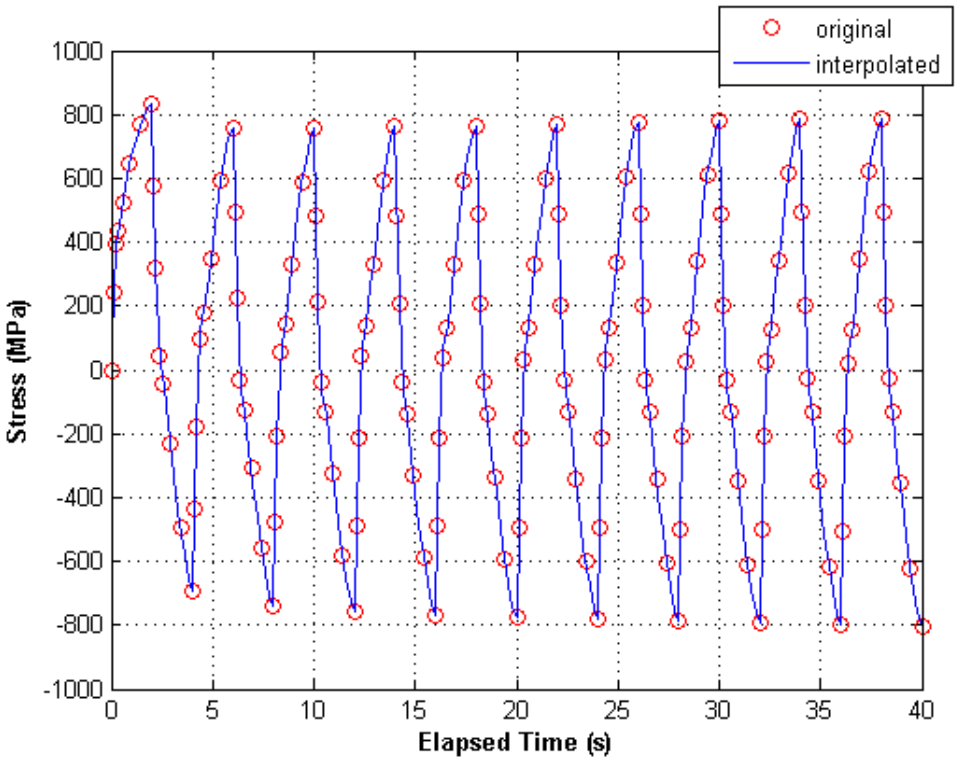

Figure 2.6 Comparison between original and interpolated data

	A	B	C	D	E	F	G	H	I	J	K	L
1		t	0	0.2	0.4	0.6	0.8	1	1.2	1.4	1.6	1.8
2		σxx	0	3.588	5.532	7.172591	8.543247	9.618987	10.32684	10.85893	11.15889	11.24545
3		σyy	0	426.4	520.8	609.9579	679.7672	733.3839	771.6766	801.5424	822.8242	837.4754
4		σzz	0	134.9	95.2	113.1251	129.8346	142.475	149.7482	154.6848	156.9801	155.5992
5		σxy	0	5.259	7.093	8.83611	10.44613	11.96141	13.52036	15.14145	16.81757	18.9801
6	Element α	εxx	0	-0.0059	-0.02371	-0.0423	-0.06166	-0.0816	-0.10219	-0.12343	-0.14496	-0.17152
7		εyy	0	0.008439	0.036467	0.065703	0.095703	0.126347	0.158048	0.190812	0.224293	0.266363
8		εzz	0	-0.00144	-0.01155	-0.02199	-0.03245	-0.04304	-0.05406	-0.06553	-0.07744	-0.09293
9		εxy	0	0.000354	0.001626	0.003093	0.004762	0.006647	0.008875	0.011494	0.014469	0.018834
10		ux	0	-0.0029	-0.02296	-0.04348	-0.06383	-0.0842	-0.10514	-0.12666	-0.14877	-0.17701
11		uy	0	0.000418	0.001829	0.003346	0.004949	0.006634	0.008438	0.010359	0.012379	0.015029
12		σxx	0	8.551	12.03	15.08296	17.66427	19.82992	21.77281	23.54584	25.27297	27.42494
13		σyy	0	421.1	514.4	601.6862	669.6399	721.5362	758.1777	786.6206	806.3883	819.1428
14		σzz	0	136.2	98.11	115.9884	132.5247	145.0713	152.6333	158.0281	160.5777	159.5585
15		σxy	0	46.35	58.62	70.43665	80.55399	89.29404	97.41385	105.1034	112.5887	121.6452
16	Element β	εxx	0	-0.00568	-0.02295	-0.04086	-0.05938	-0.07834	-0.09774	-0.11759	-0.13752	-0.16173
17		εyy	0	0.008173	0.035464	0.06381	0.092741	0.122153	0.152367	0.183407	0.214898	0.254
18		εzz	0	-0.0014	-0.0113	-0.02153	-0.03177	-0.0421	-0.05283	-0.06395	-0.07547	-0.09035
19		εxy	0	0.00311	0.013597	0.025066	0.037468	0.050819	0.065768	0.082415	0.10068	0.12631
20		ux	0	-0.00276	-0.02227	-0.04222	-0.06196	-0.08167	-0.10183	-0.12248	-0.14357	-0.17027
21		uy	0	0.001236	0.005415	0.009902	0.014634	0.019598	0.024891	0.030513	0.036407	0.044107
22		σxx	0	21.32	28.41	34.73348	40.03353	44.56813	48.89332	53.07572	57.34775	63.01022
23		σyy	0	407.9	498.2	580.656	643.906	691.9324	724.9102	750.135	766.7127	775.878
24		σzz	0	139.7	105.3	122.856	138.758	150.7384	158.3501	164.1039	166.8755	166.3691
25		σxy	0	85.45	107.5	128.4431	145.9094	160.7912	174.1856	186.5259	198.2083	211.7863
26	Element γ	εxx	0	-0.00513	-0.02102	-0.03721	-0.05365	-0.07022	-0.08677	-0.10337	-0.1196	-0.13845
27		εyy	0	0.007515	0.032918	0.059013	0.085289	0.111696	0.138329	0.165247	0.192072	0.224453

Figure 2.7 Screen copy of Excel spread sheet containing input vectors for artificial neural networks

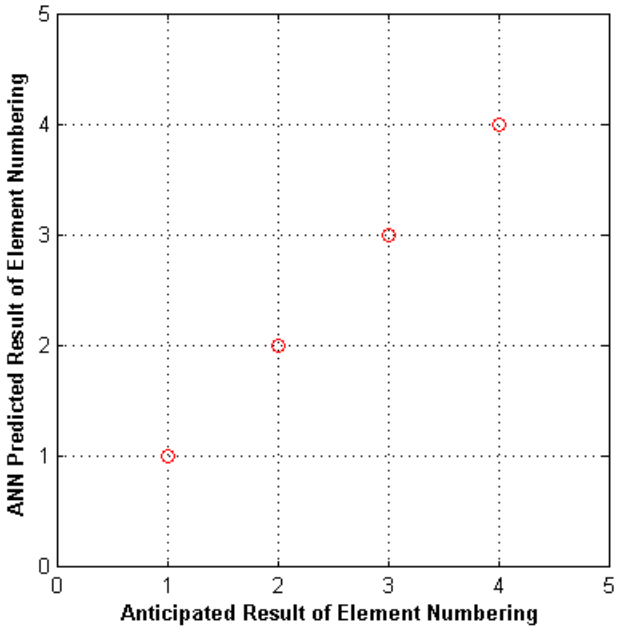

Figure 2.8 Prediction of the element from which crack initiates – LVQ

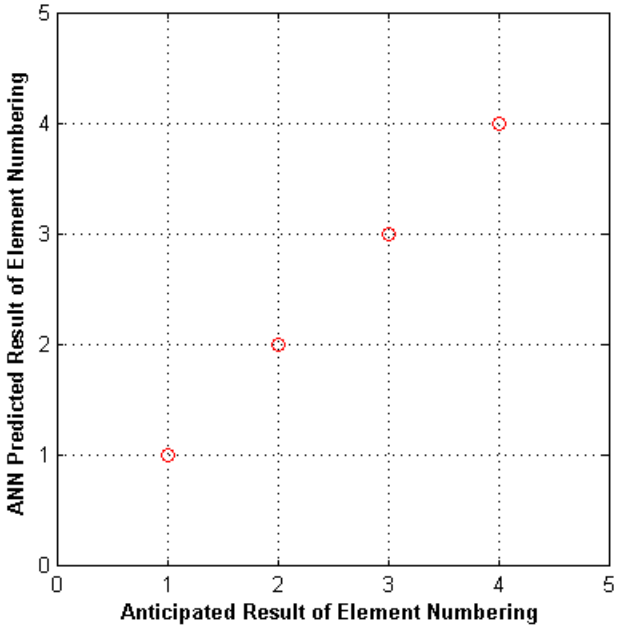

Figure 2.9 Prediction of the element from which crack initiates – PNN

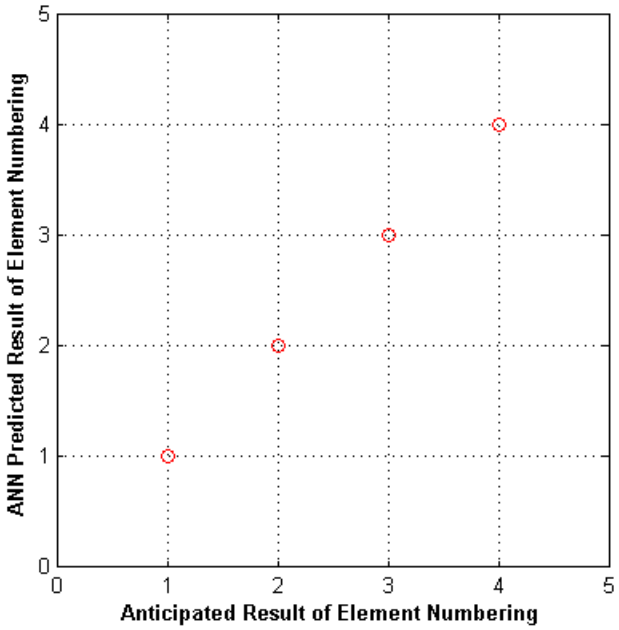

Figure 2.10 Prediction of the element from which crack initiates – BP-PNN array

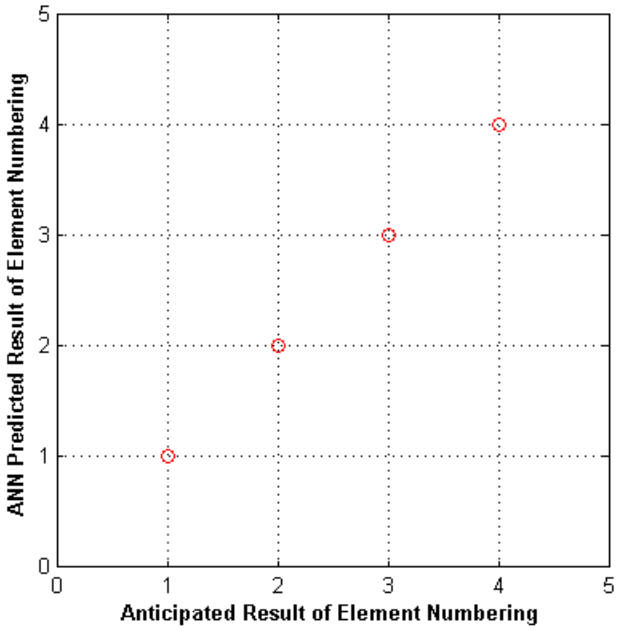

Figure 2.11 Prediction of the element from which crack initiates – GRNN-PNN array

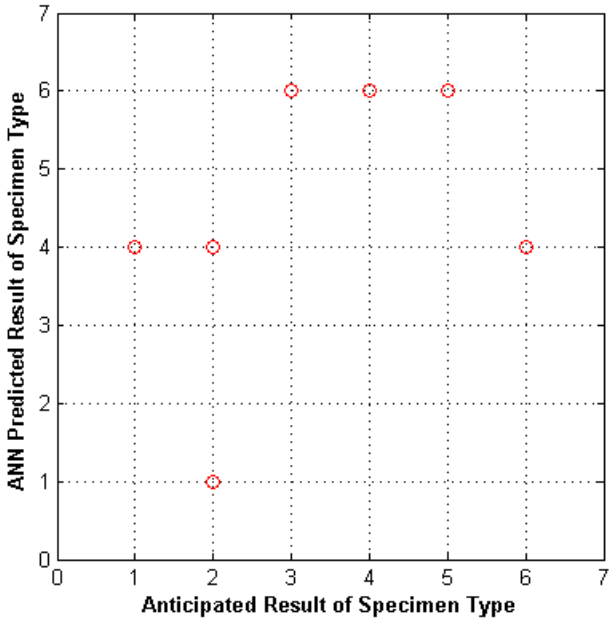

Figure 2.12 Recognition of a ‘fake’ pattern – PNN

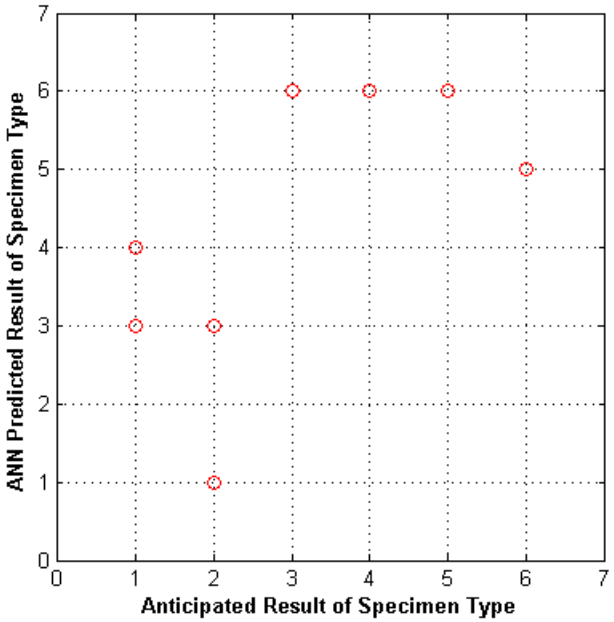

Figure 2.13 Recognition of a ‘fake’ pattern – BP-PNN array

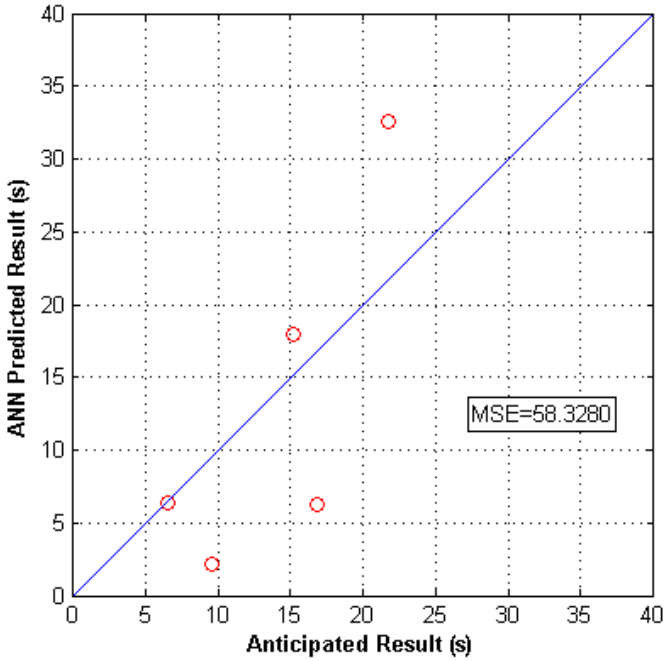

Figure 2.14 Prediction of the fatigue initiation life – GRNN with 25 training cases

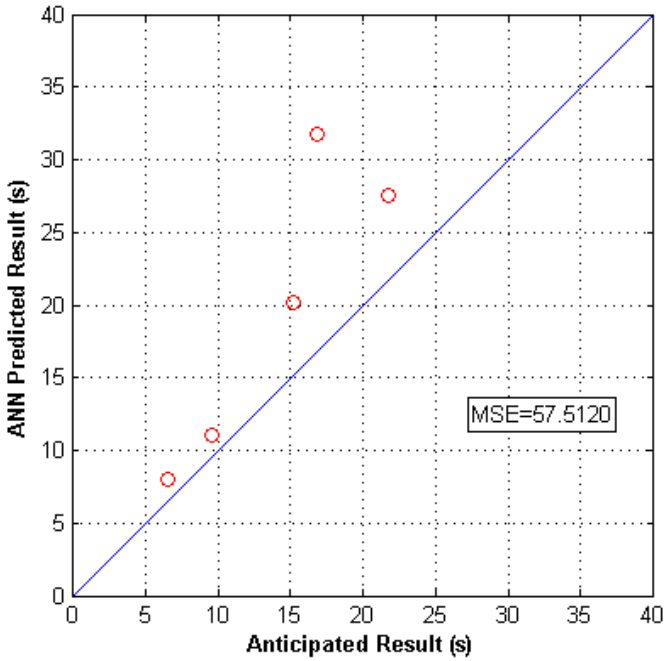

Figure 2.15 Prediction of the fatigue initiation life – BP with 25 training cases

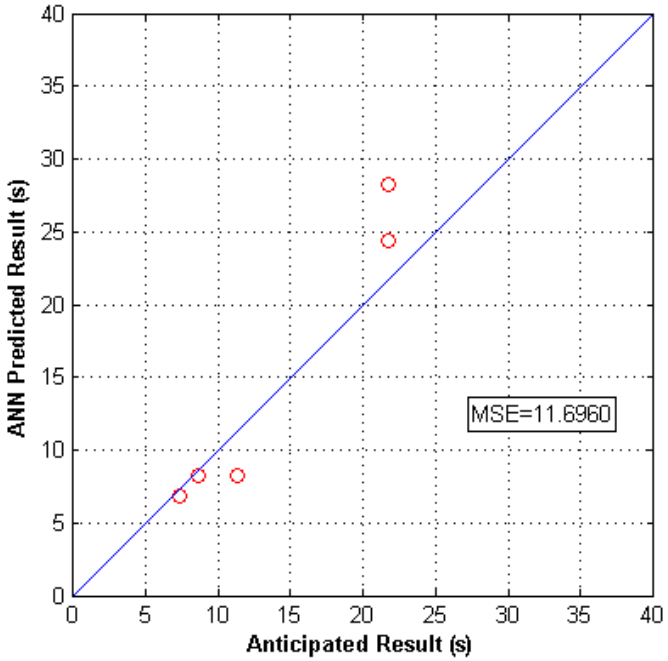

Figure 2.16 Prediction of the fatigue initiation life – BP-PNN array with 25 training cases (Trial 1)

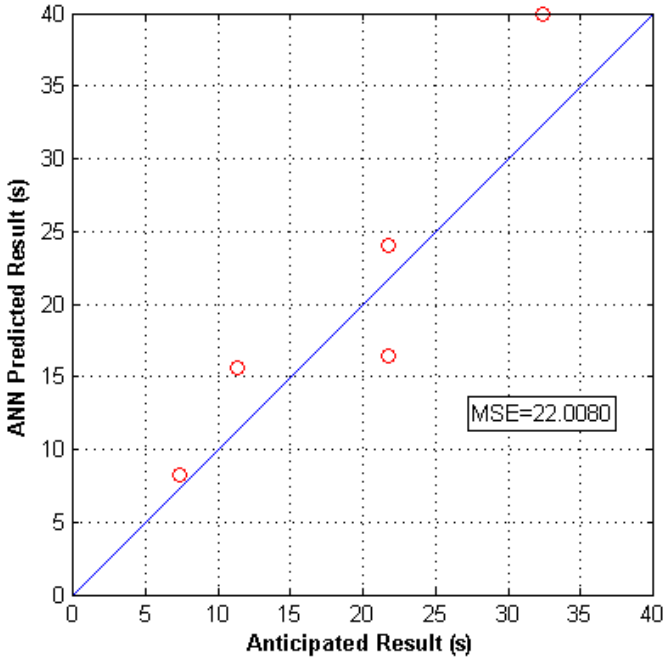

Figure 2.17 Prediction of the fatigue initiation life – BP-PNN array with 25 training cases (Trial 2)

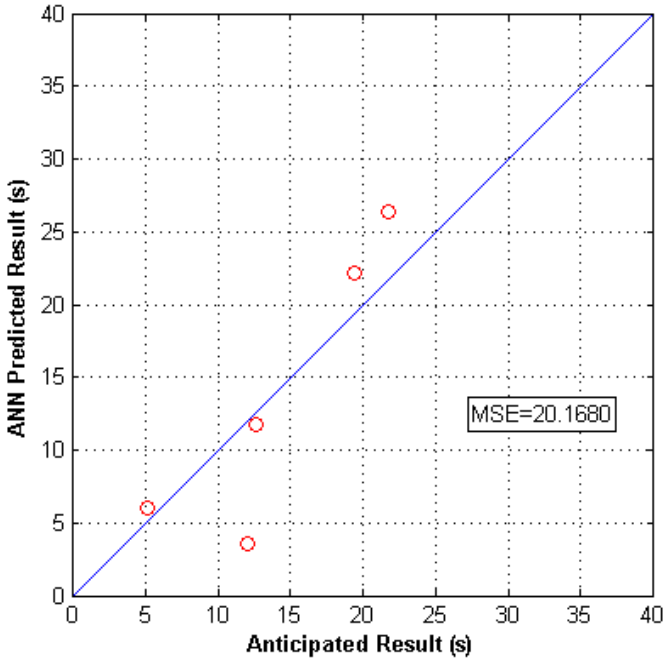

Figure 2.18 Prediction of the fatigue initiation life – BP-PNN array with 25 training cases (Trial 3)

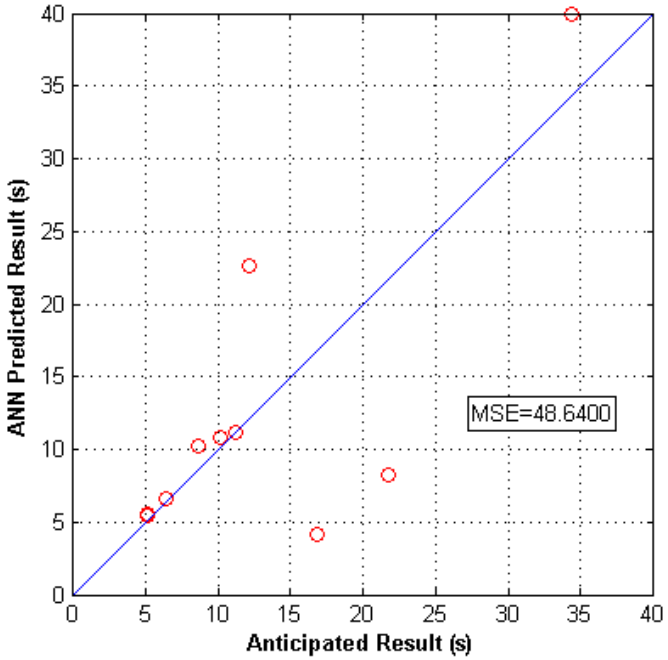

Figure 2.19 Prediction of the fatigue initiation life – BP-PNN array with 20 training cases (Trial 1)

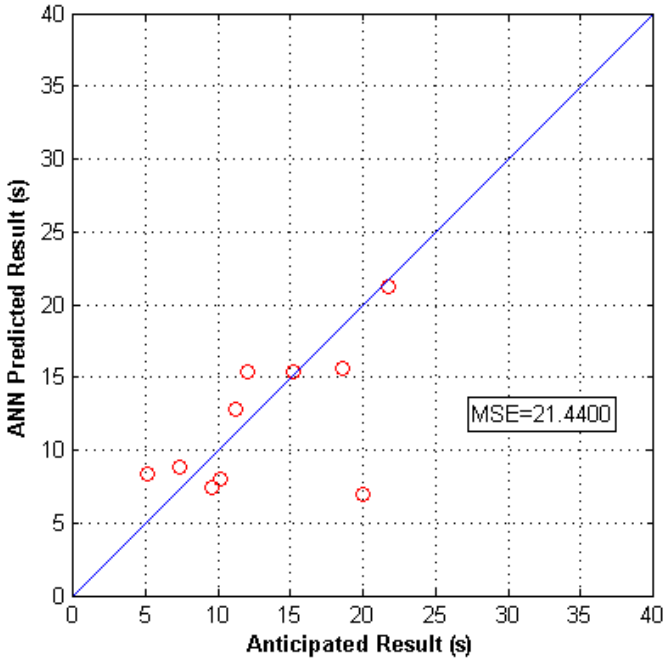

Figure 2.20 Prediction of the fatigue initiation life – BP-PNN array with 20 training cases (Trial 2)

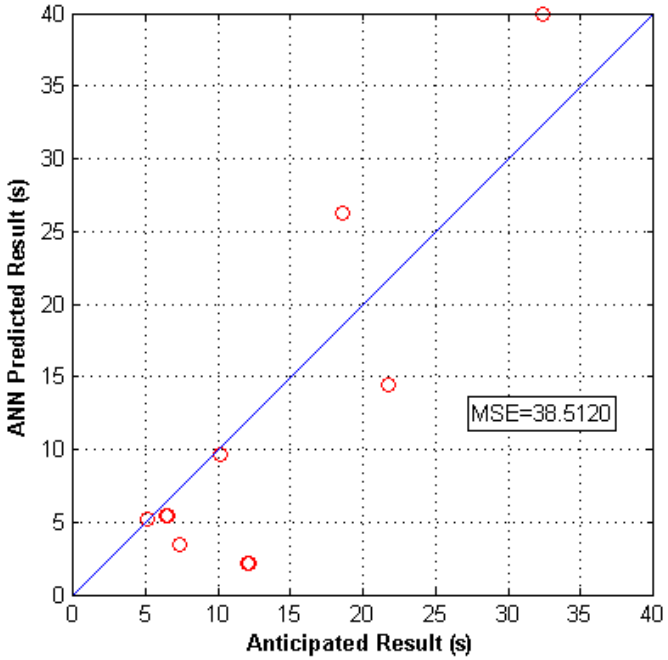

Figure 2.21 Prediction of the fatigue initiation life – BP-PNN array with 20 training cases (Trial 3)

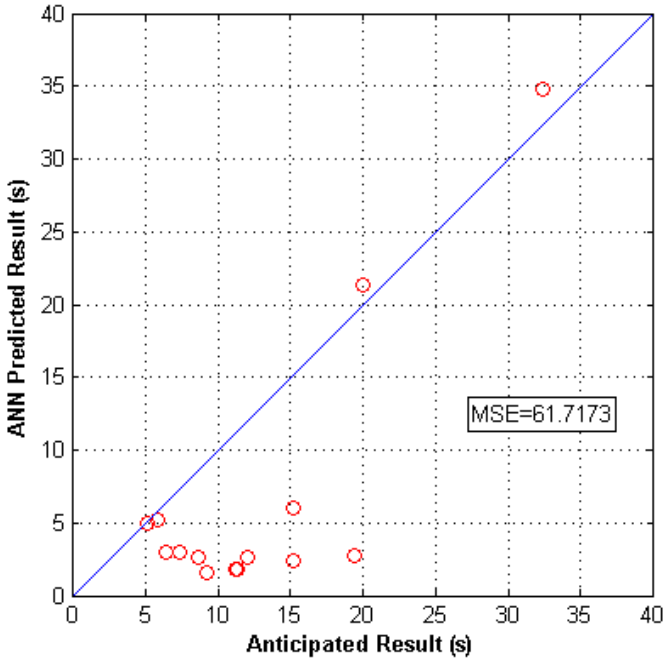

Figure 2.22 Prediction of the fatigue initiation life – BP-PNN array with 15 training cases (Trial 1)

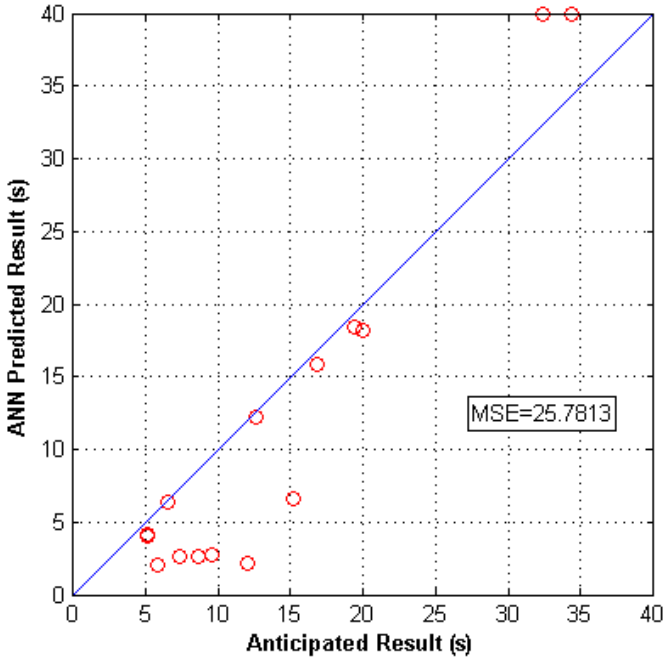

Figure 2.23 Prediction of the fatigue initiation life – BP-PNN array with 15 training cases (Trial 2)

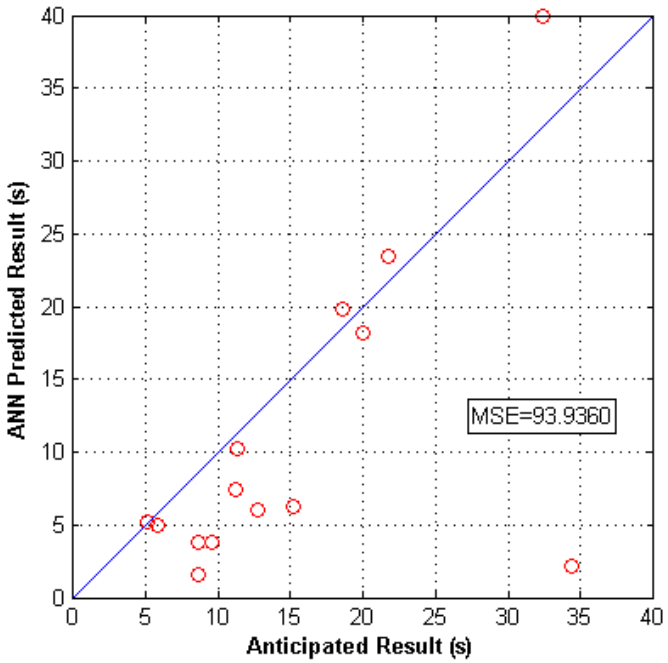

Figure 2.24 Prediction of the fatigue initiation life – BP-PNN array with 15 training cases (Trial 3)

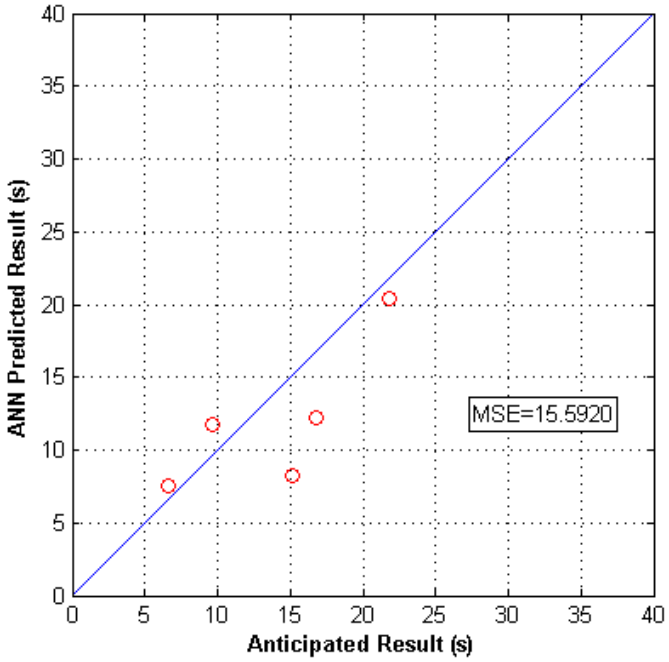

Figure 3.1 Prediction of the fatigue initiation life – a static array

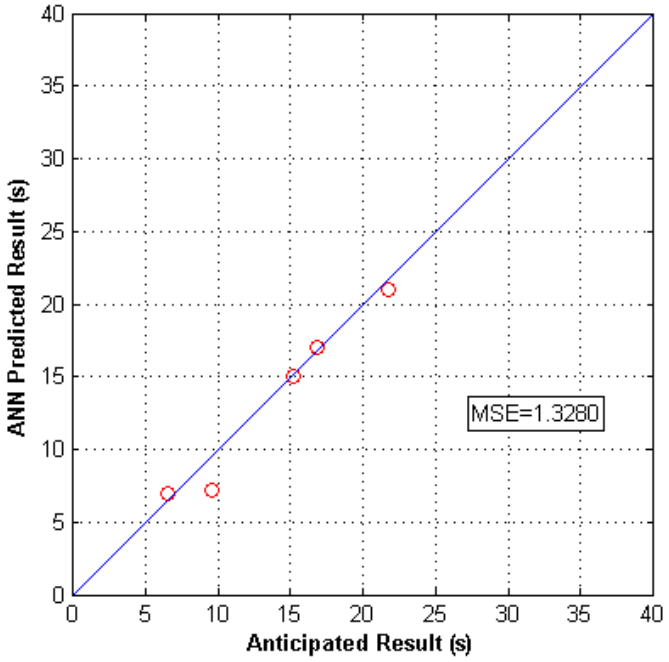

Figure 3.2 Prediction of the fatigue initiation life – a dynamic array

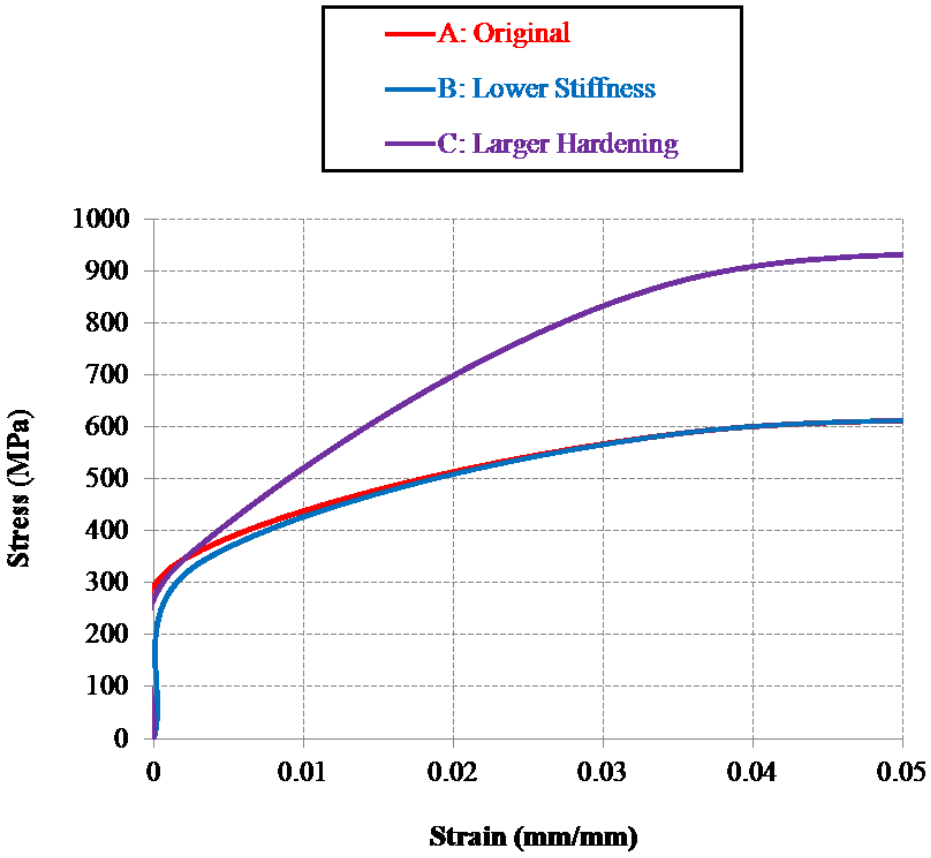

Figure 3.3 Stress-strain constitutive relationships of the three types of steel

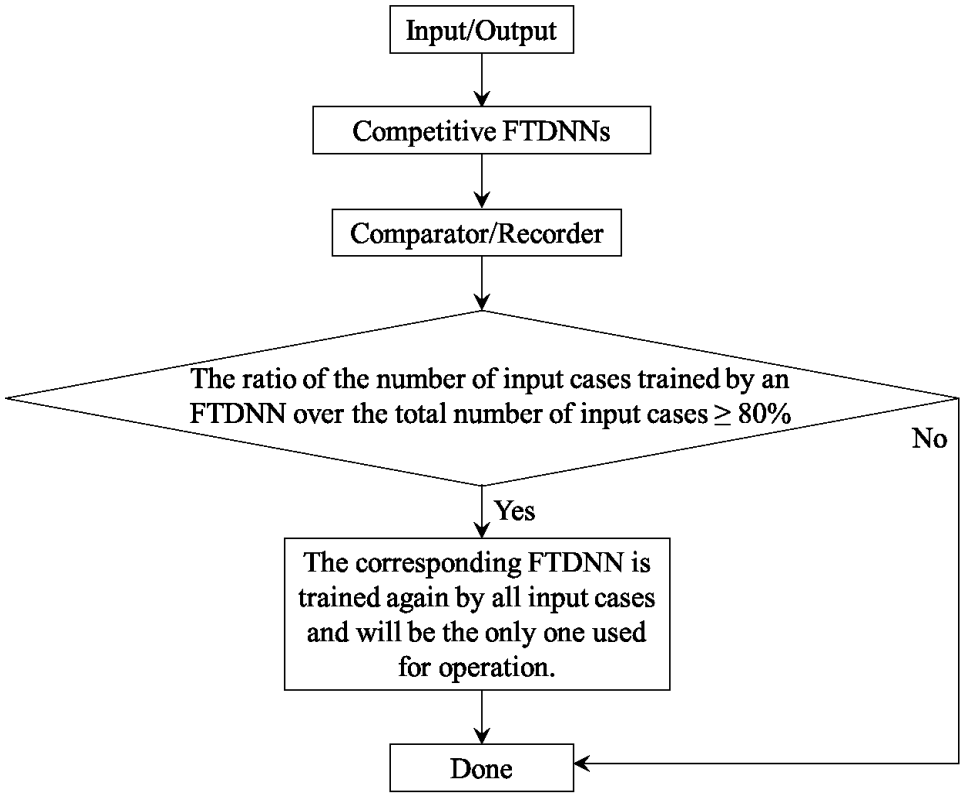

Figure 3.4 Flow chart of the dynamic array

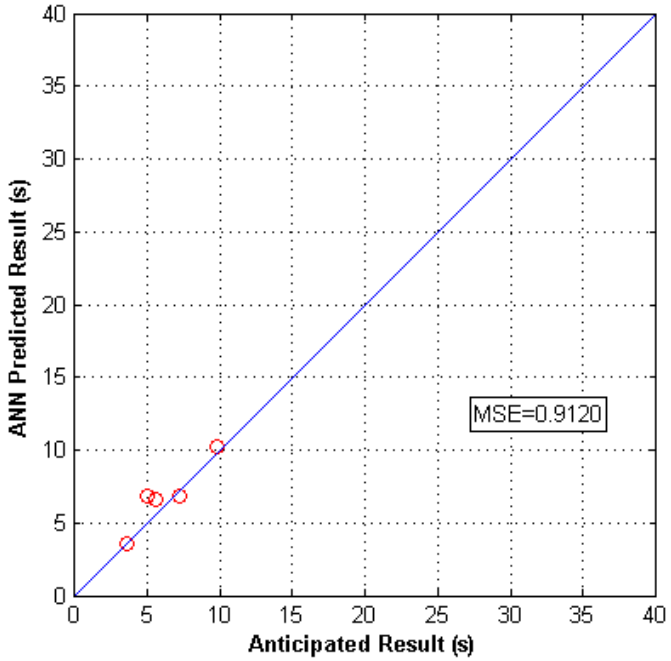

Figure 3.5 Prediction of the time consumed up to the end of Stage I – dynamic array with 85 training cases (Trial 1)

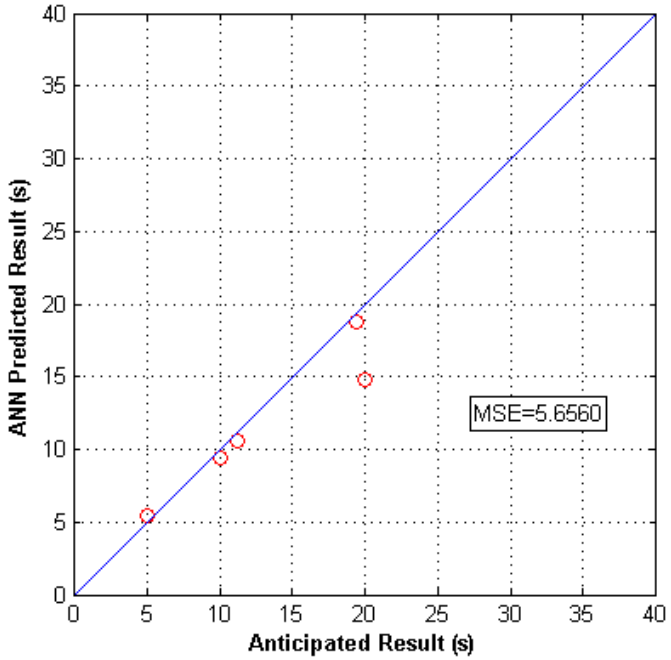

Figure 3.6 Prediction of the time consumed up to the end of Stage II – dynamic array with 85 training cases (Trial 1)

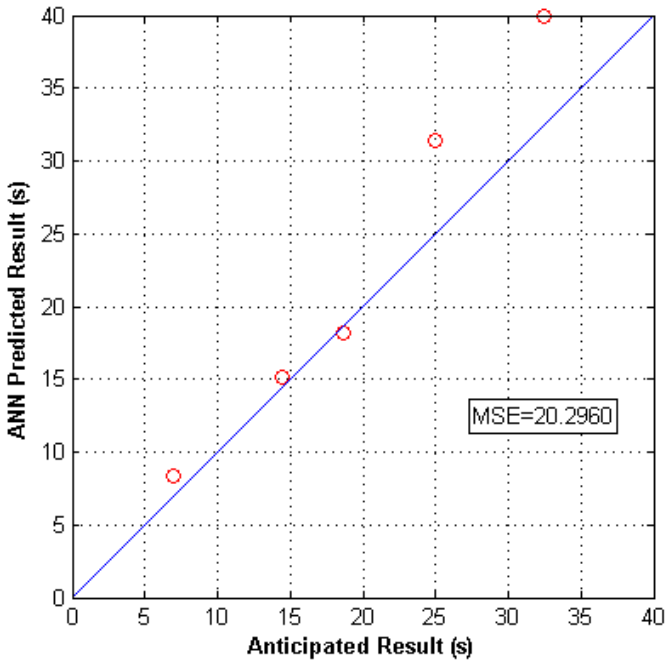

Figure 3.7 Prediction of the fatigue initiation life – dynamic array with 85 training cases (Trial 1)

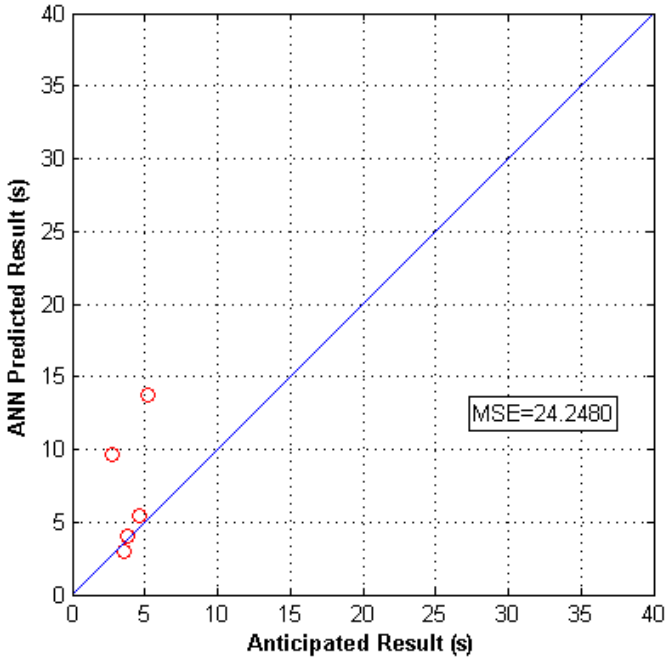

Figure 3.8 Prediction of the time consumed up to the end of Stage I – dynamic array with 85 training cases (Trial 2)

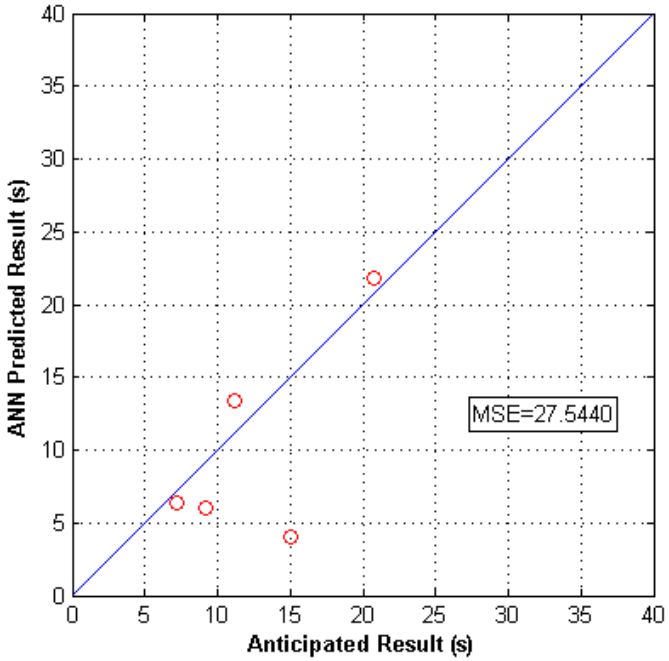

Figure 3.9 Prediction of the time consumed up to the end of Stage II – dynamic array with 85 training cases (Trial 2)

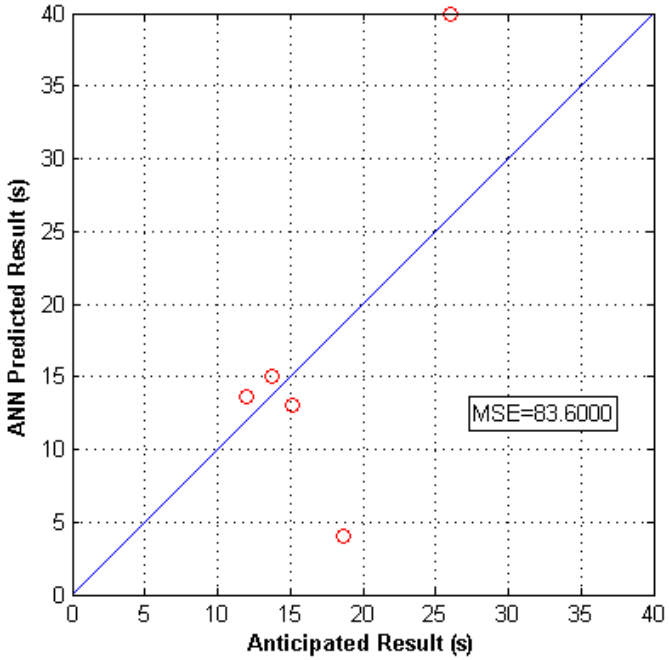

Figure 3.10 Prediction of the fatigue initiation life – dynamic array with 85 training cases (Trial 2)

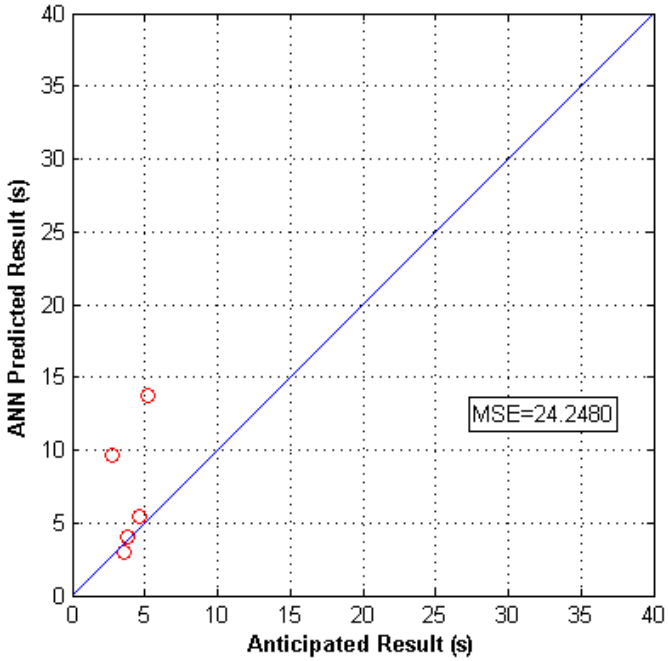

Figure 3.11 Prediction of the time consumed up to the end of Stage I – dynamic array with 85 training cases (Trial 3)

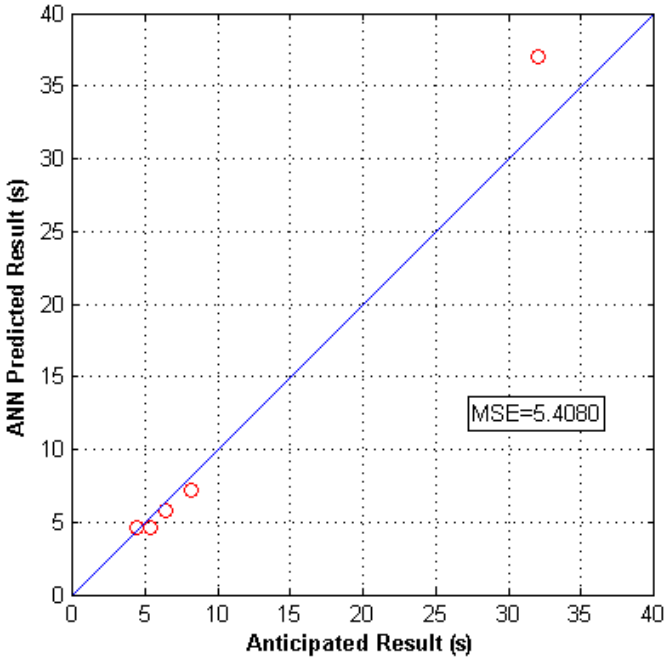

Figure 3.12 Prediction of the time consumed up to the end of Stage II – dynamic array with 85 training cases (Trial 3)

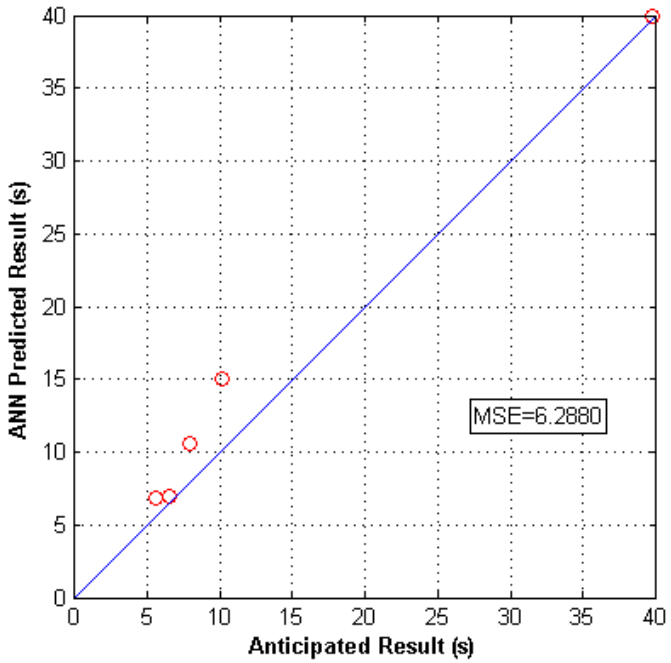

Figure 3.13 Prediction of the fatigue initiation life – dynamic array with 85 training cases (Trial 3)

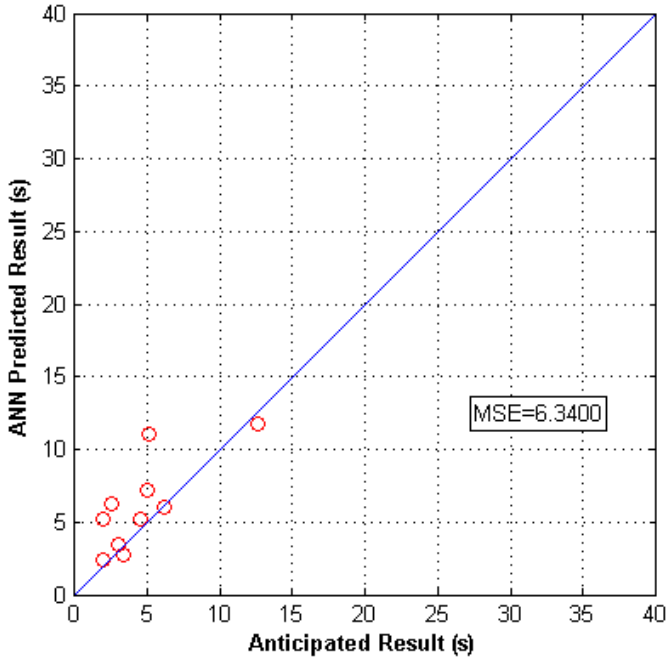

Figure 3.14 Prediction of the time consumed up to the end of Stage I – dynamic array with 80 training cases (Trial 1)

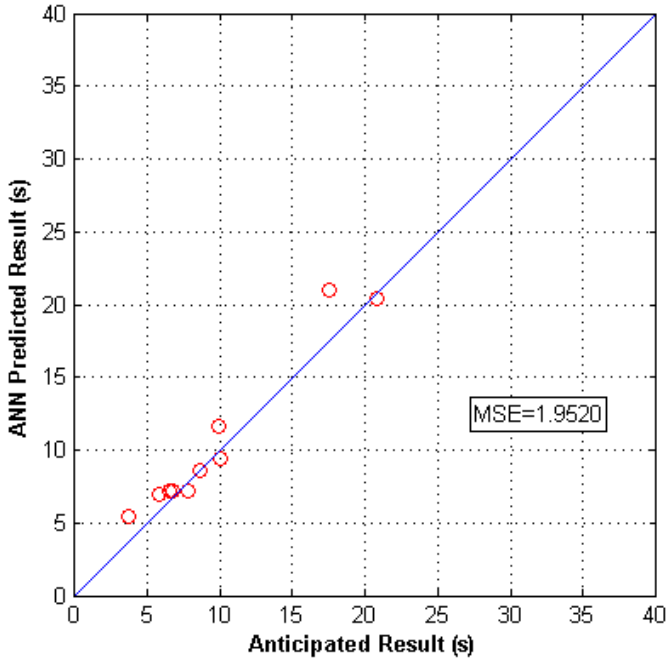

Figure 3.15 Prediction of the time consumed up to the end of Stage II – dynamic array with 80 training cases (Trial 1)

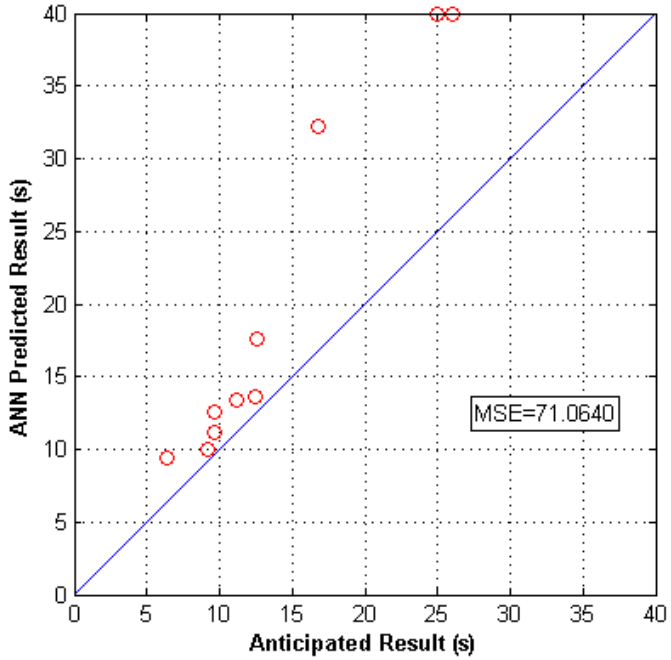

Figure 3.16 Prediction of the fatigue initiation life – dynamic array with 80 training cases (Trial 1)

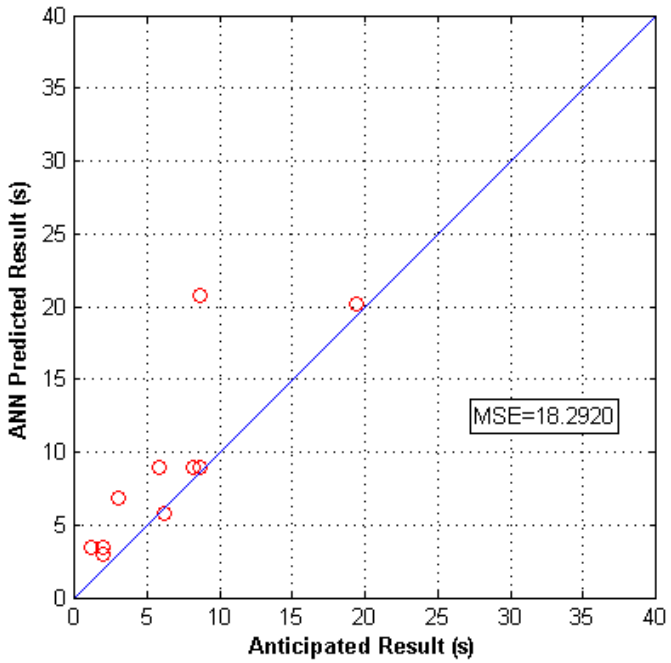

Figure 3.17 Prediction of the time consumed up to the end of Stage I – dynamic array with 80 training cases (Trial 2)

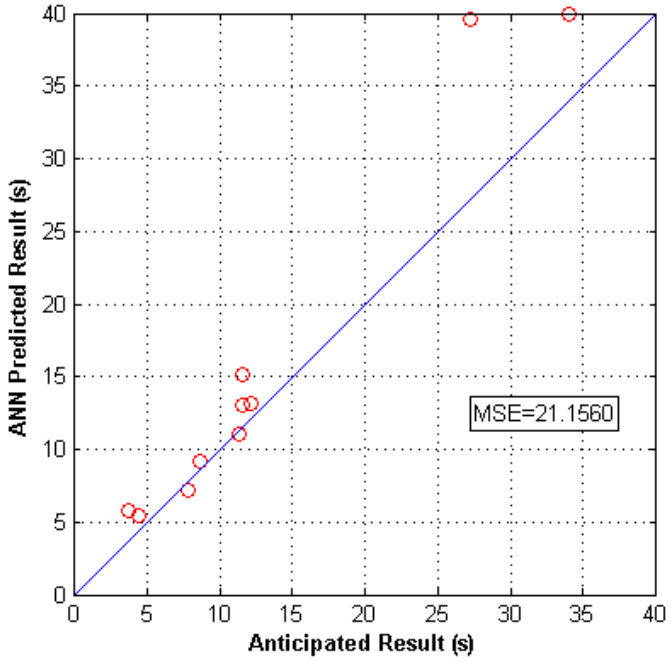

Figure 3.18 Prediction of the time consumed up to the end of Stage II – dynamic array with 80 training cases (Trial 2)

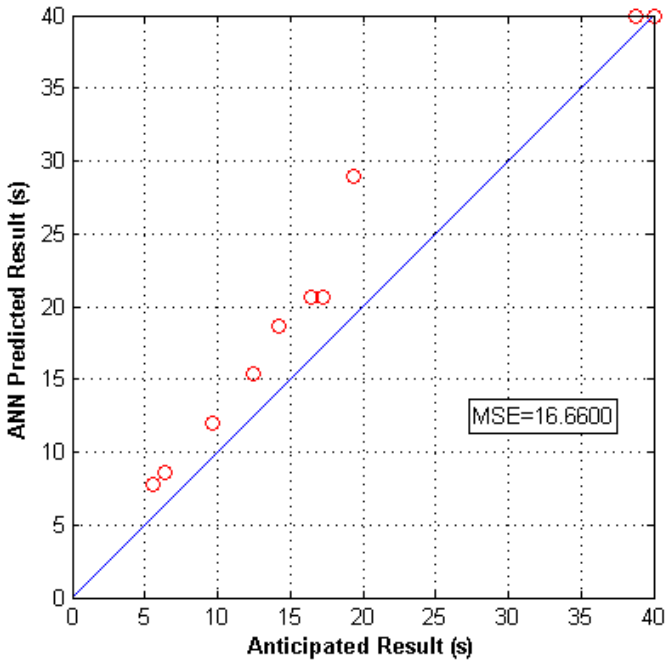

Figure 3.19 Prediction of the fatigue initiation life – dynamic array with 80 training cases (Trial 2)

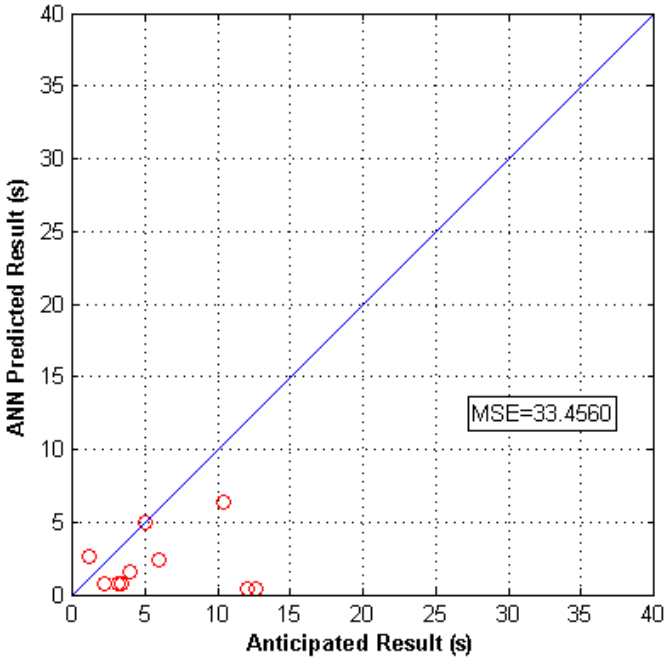

Figure 3.20 Prediction of the time consumed up to the end of Stage I – dynamic array with 80 training cases (Trial 3)

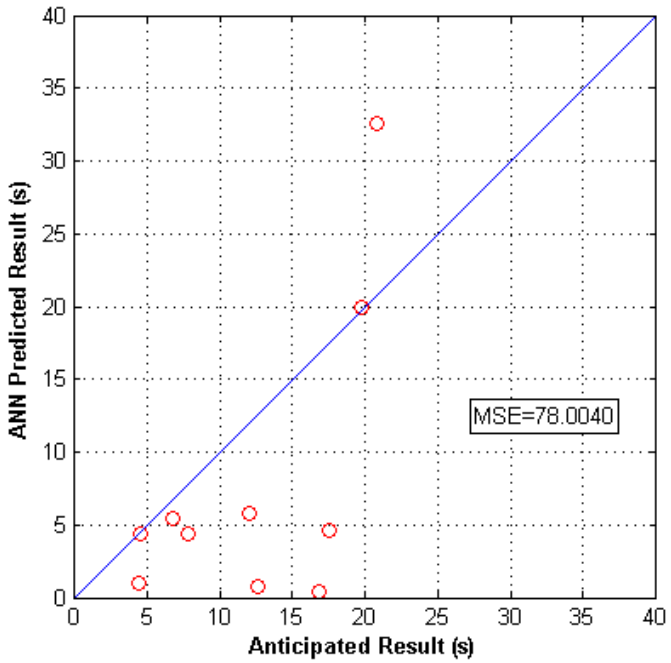

Figure 3.21 Prediction of the time consumed up to the end of Stage II – dynamic array with 80 training cases (Trial 3)

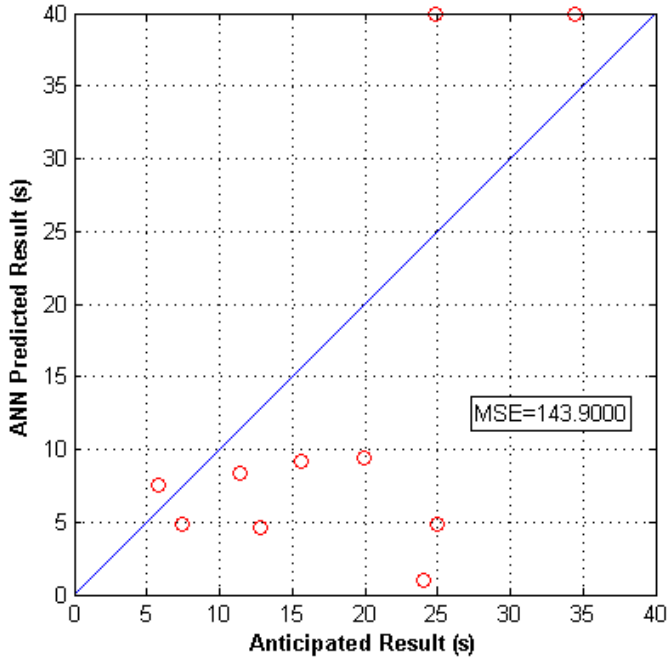

Figure 3.22 Prediction of the fatigue initiation life – dynamic array with 80 training cases (Trial 3)

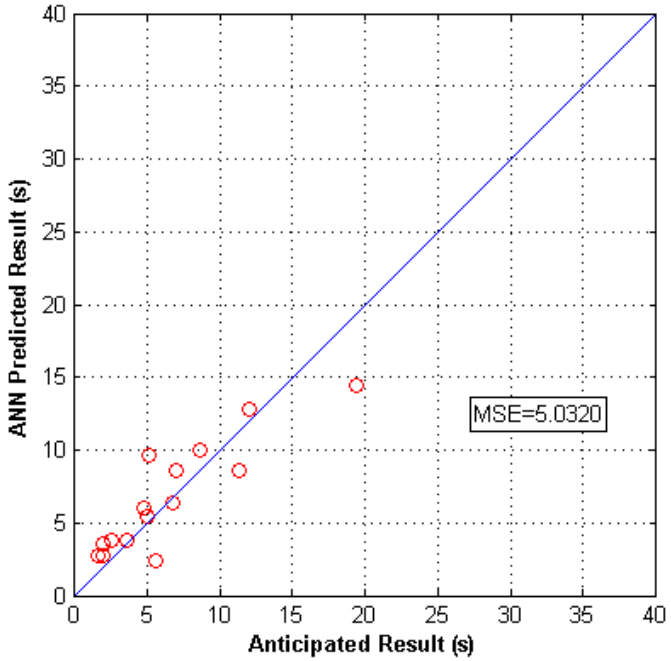

Figure 3.23 Prediction of the time consumed up to the end of Stage I – dynamic array with 75 training cases (Trial 1)

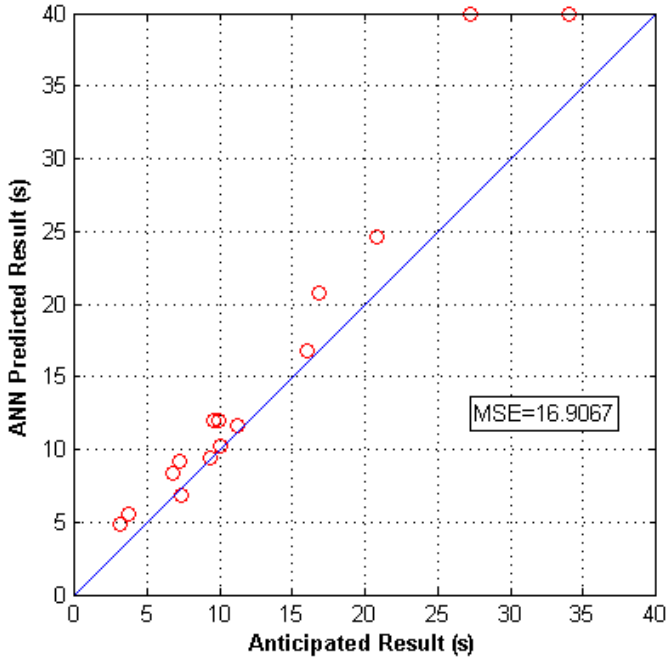

Figure 3.24 Prediction of the time consumed up to the end of Stage II – dynamic array with 75 training cases (Trial 1)

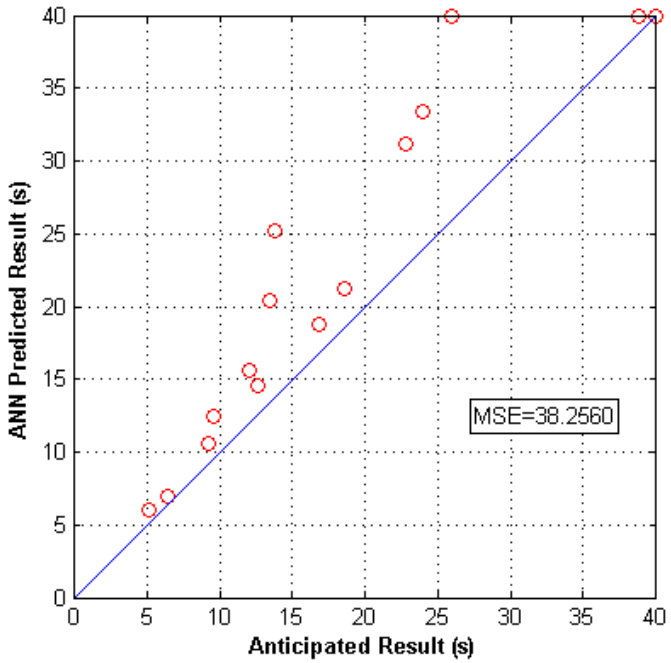

Figure 3.25 Prediction of the fatigue initiation life – dynamic array with 75 training cases (Trial 1)

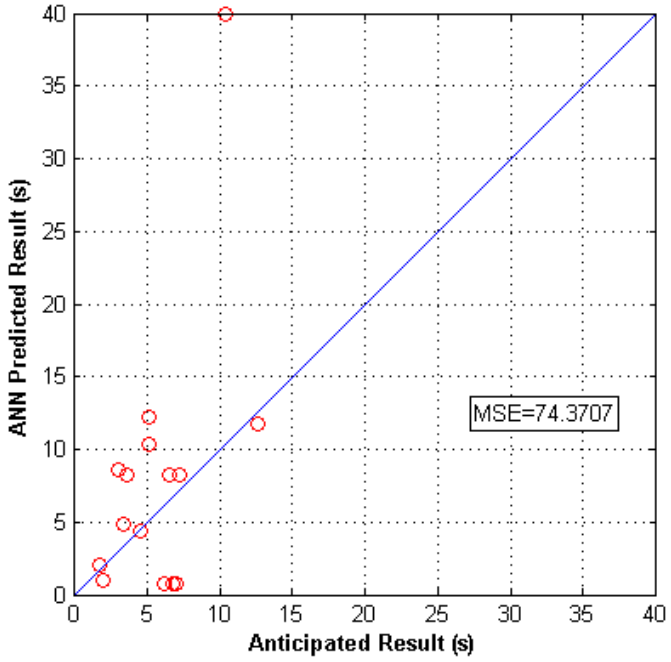

Figure 3.26 Prediction of the time consumed up to the end of Stage I – dynamic array with 75 training cases (Trial 2)

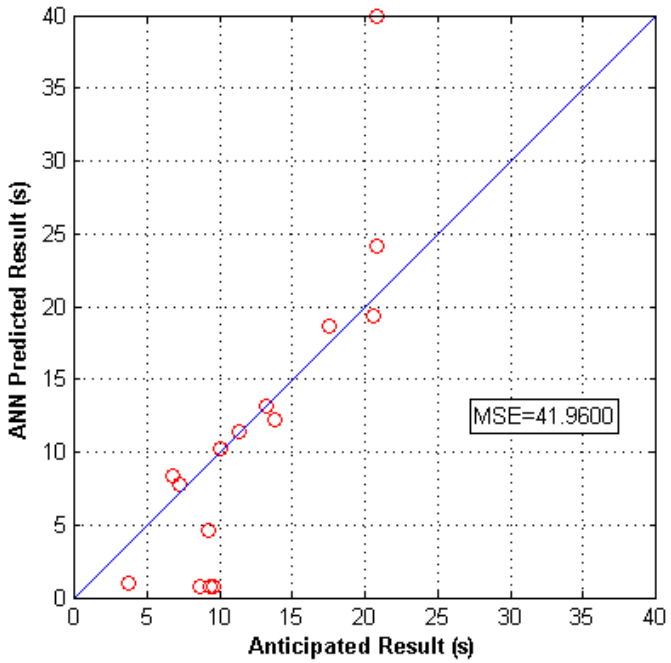

Figure 3.27 Prediction of the time consumed up to the end of Stage II – dynamic array with 75 training cases (Trial 2)

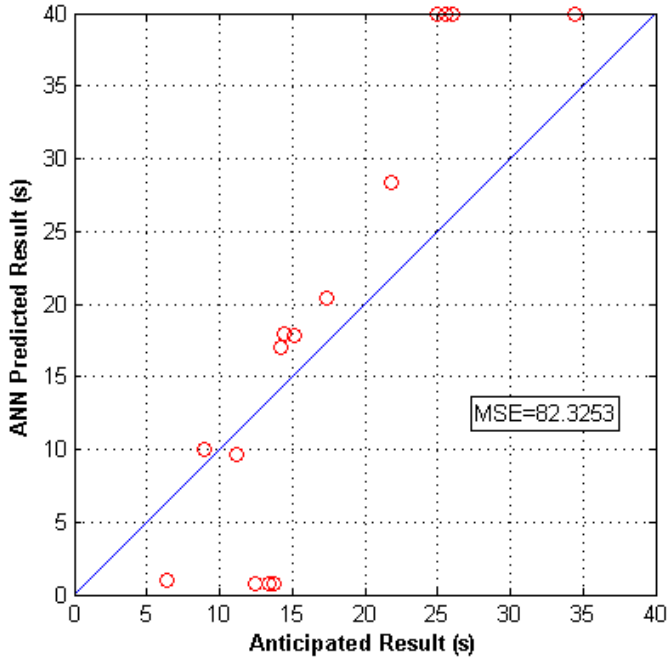

Figure 3.28 Prediction of the fatigue initiation life – dynamic array with 75 training cases (Trial 2)

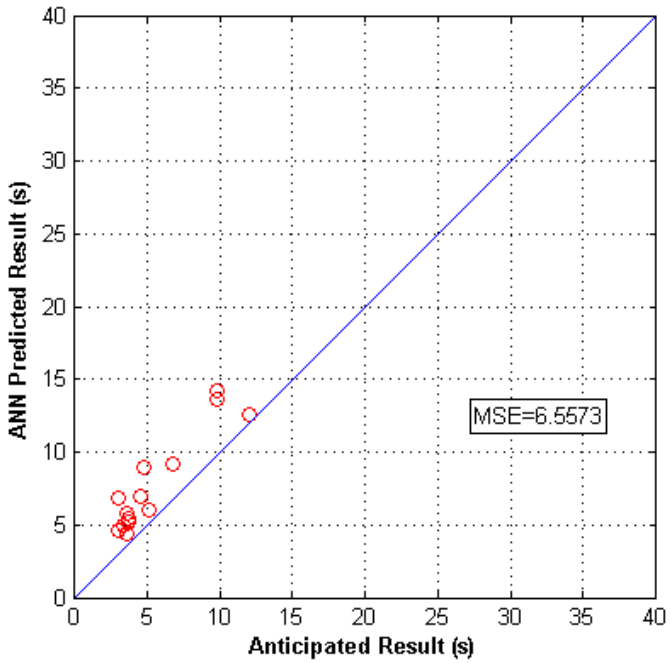

Figure 3.29 Prediction of the time consumed up to the end of Stage I – dynamic array with 75 training cases (Trial 3)

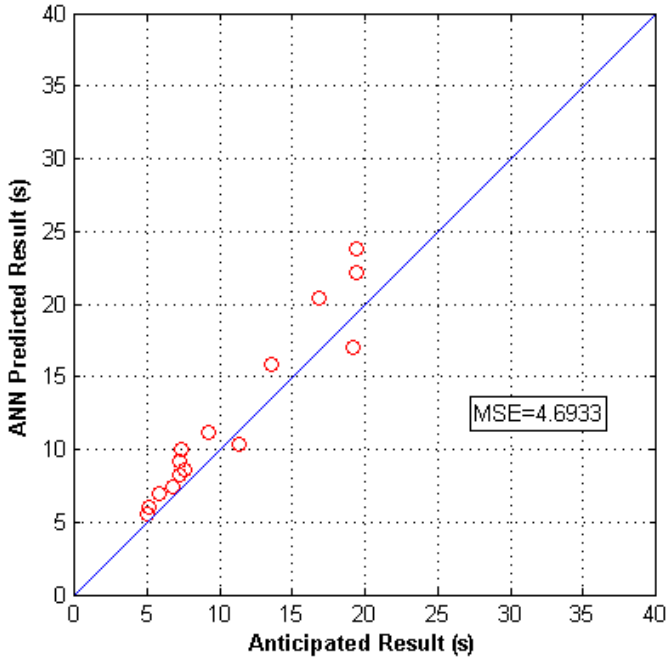

Figure 3.30 Prediction of the time consumed up to the end of Stage II – dynamic array with 75 training cases (Trial 3)

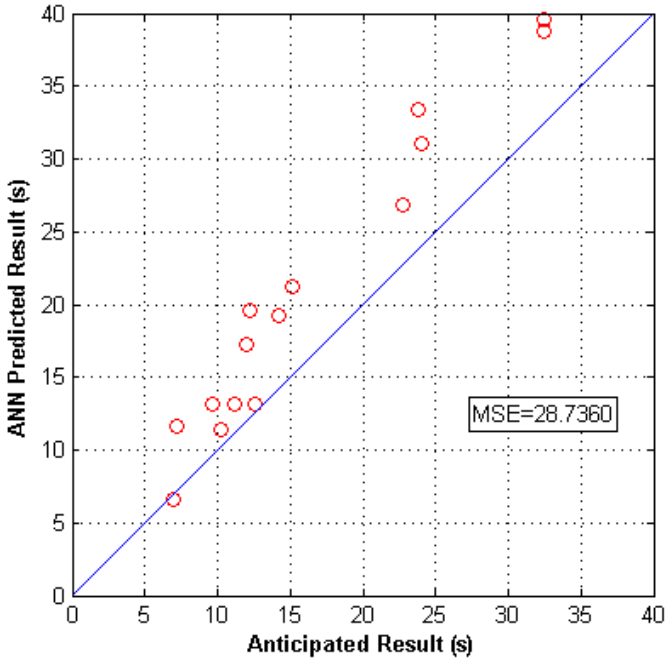

Figure 3.31 Prediction of the fatigue initiation life – dynamic array with 75 training cases (Trial 3)

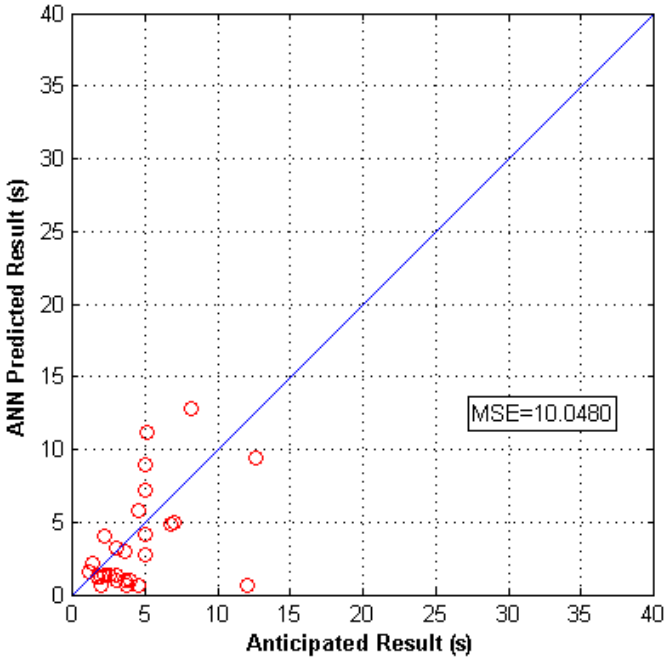

Figure 3.32 Prediction of the time consumed up to the end of Stage I – dynamic array with 60 training cases (Trial 1)

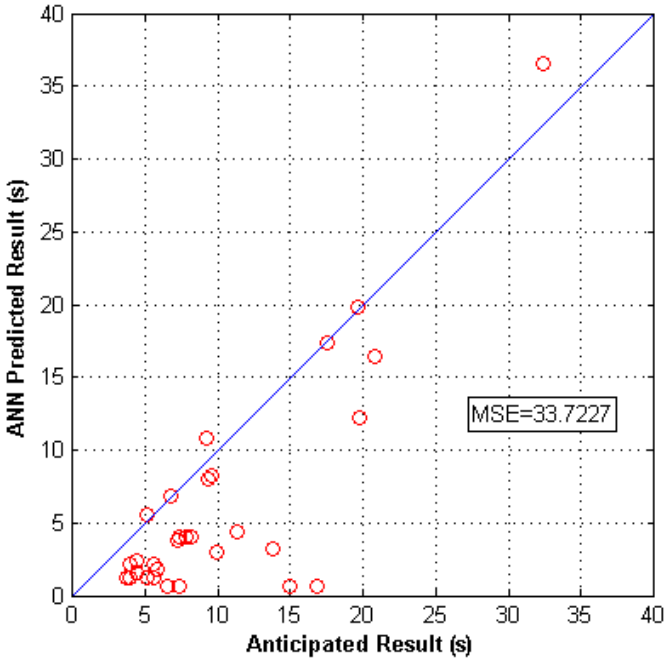

Figure 3.33 Prediction of the time consumed up to the end of Stage II – dynamic array with 60 training cases (Trial 1)

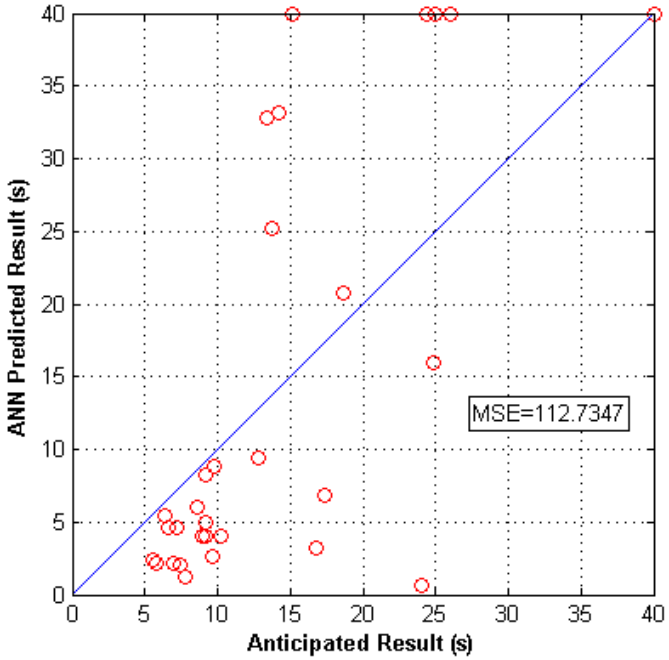

Figure 3.34 Prediction of the fatigue initiation life – dynamic array with 60 training cases (Trial 1)

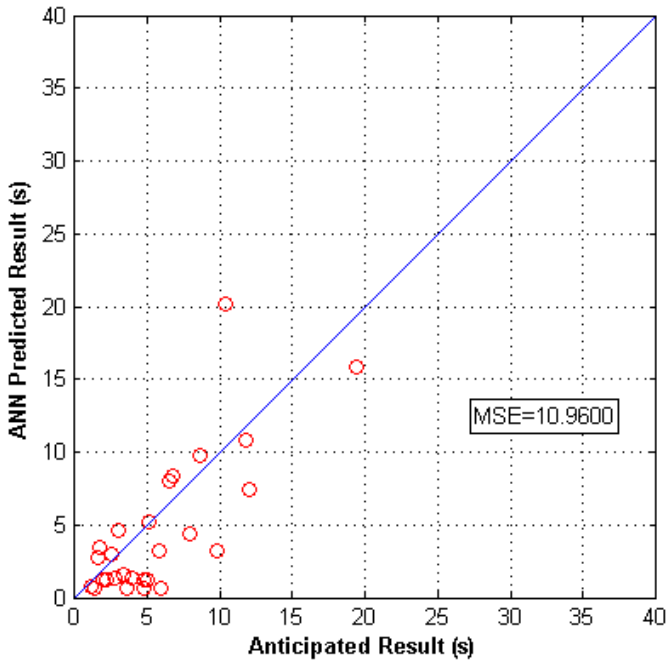

Figure 3.35 Prediction of the time consumed up to the end of Stage I – dynamic array with 60 training cases (Trial 2)

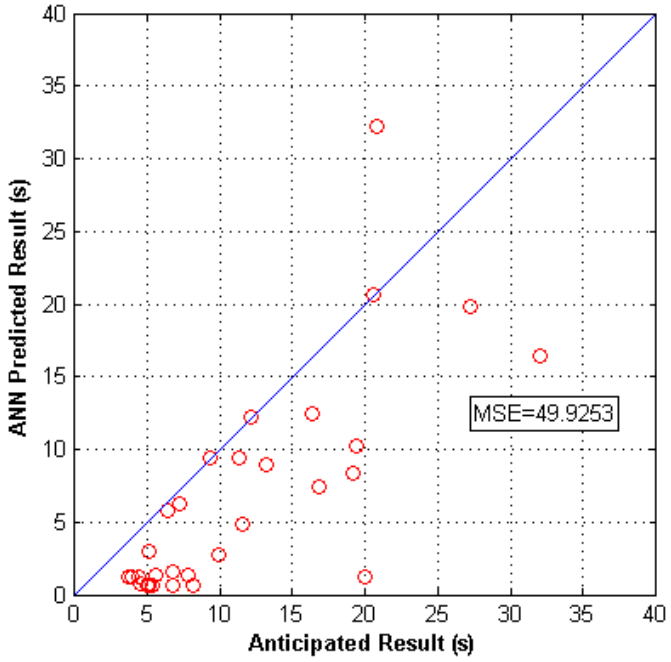

Figure 3.36 Prediction of the time consumed up to the end of Stage II – dynamic array with 60 training cases (Trial 2)

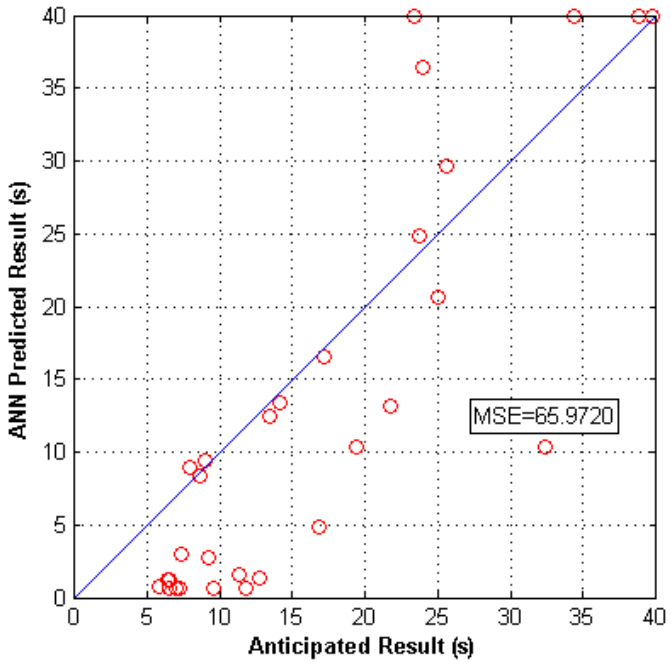

Figure 3.37 Prediction of the fatigue initiation life – dynamic array with 60 training cases (Trial 2)

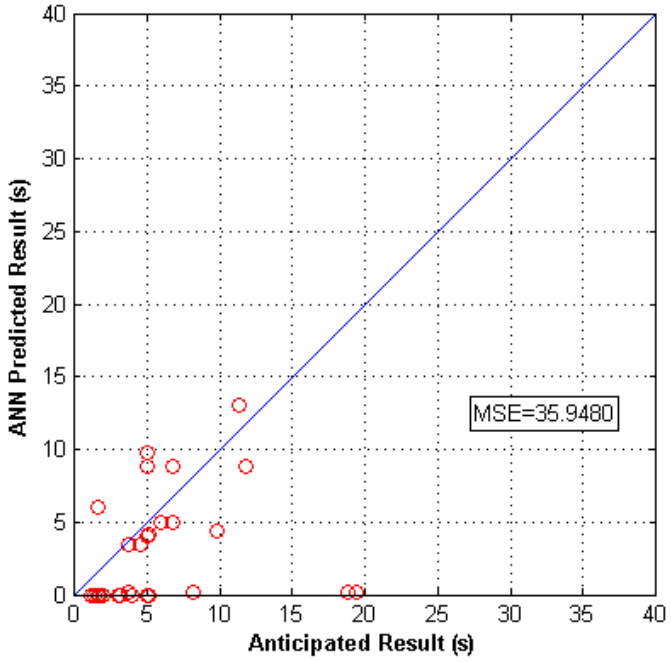

Figure 3.38 Prediction of the time consumed up to the end of Stage I – dynamic array with 60 training cases (Trial 3)

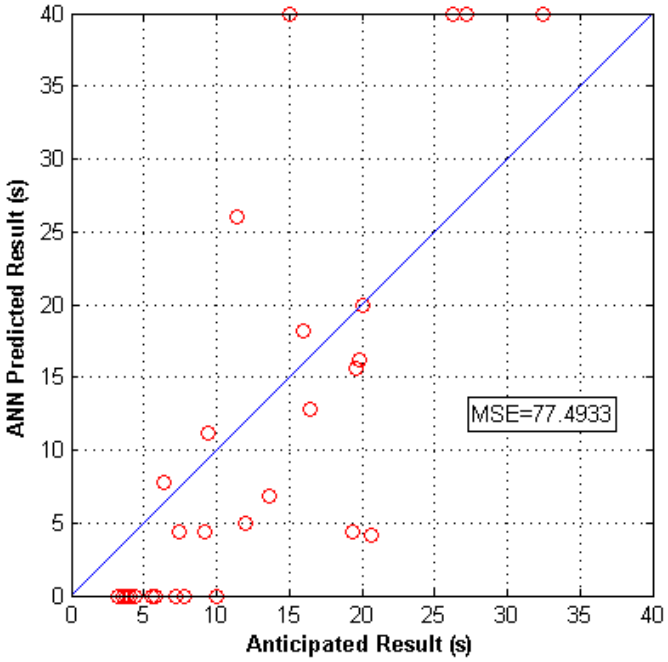

Figure 3.39 Prediction of the time consumed up to the end of Stage II – dynamic array with 60 training cases (Trial 3)

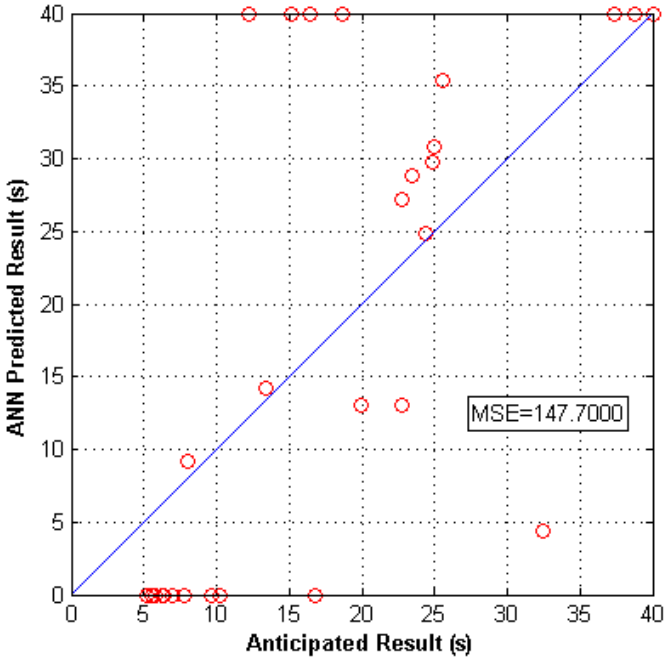

Figure 3.40 Prediction of the fatigue initiation life – dynamic array with 60 training cases (Trial 3)

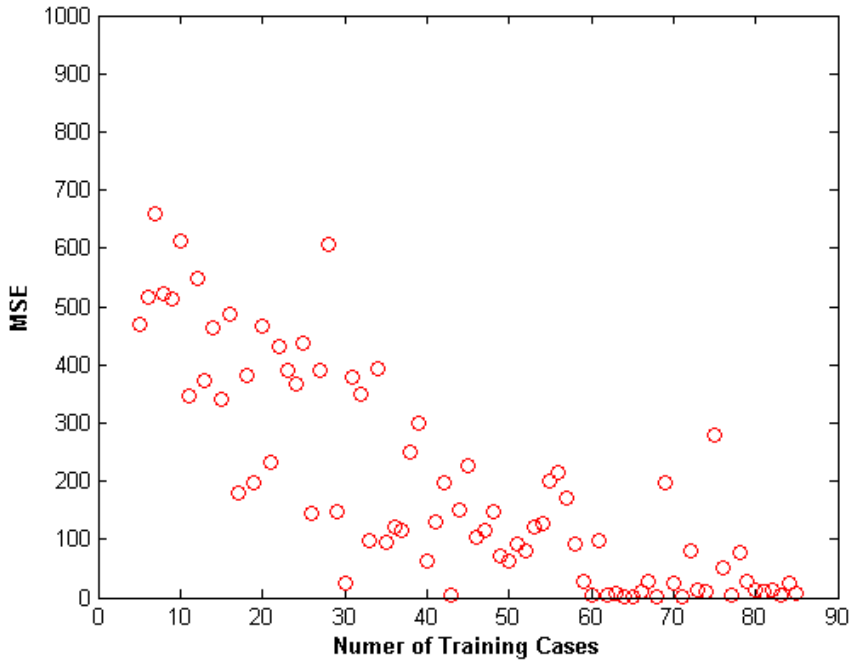

Figure 3.41 Impact of the number of training cases on prediction accuracy when 5 cases are predicted (Trial 1)

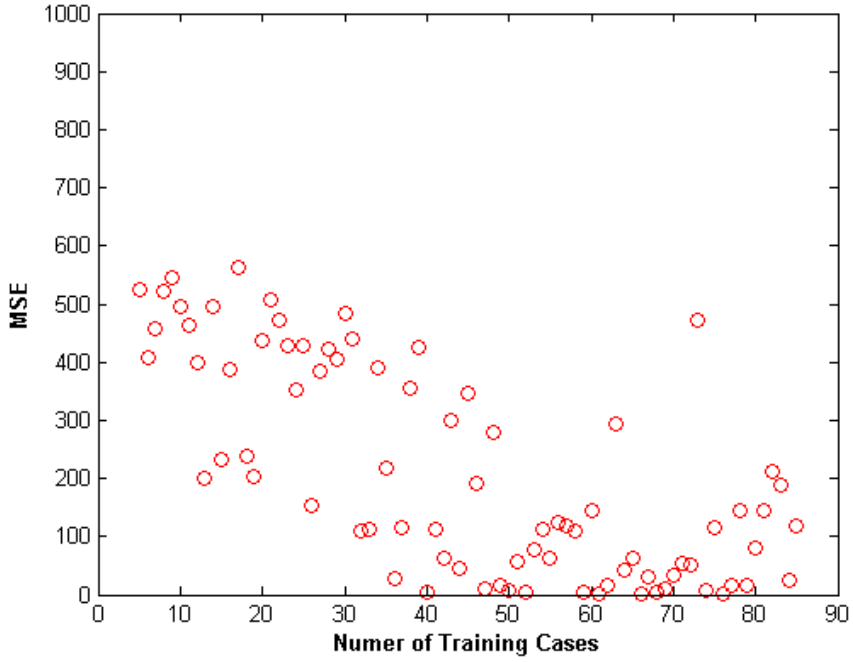

Figure 3.42 Impact of the number of training cases on prediction accuracy when 5 cases are predicted (Trial 2)

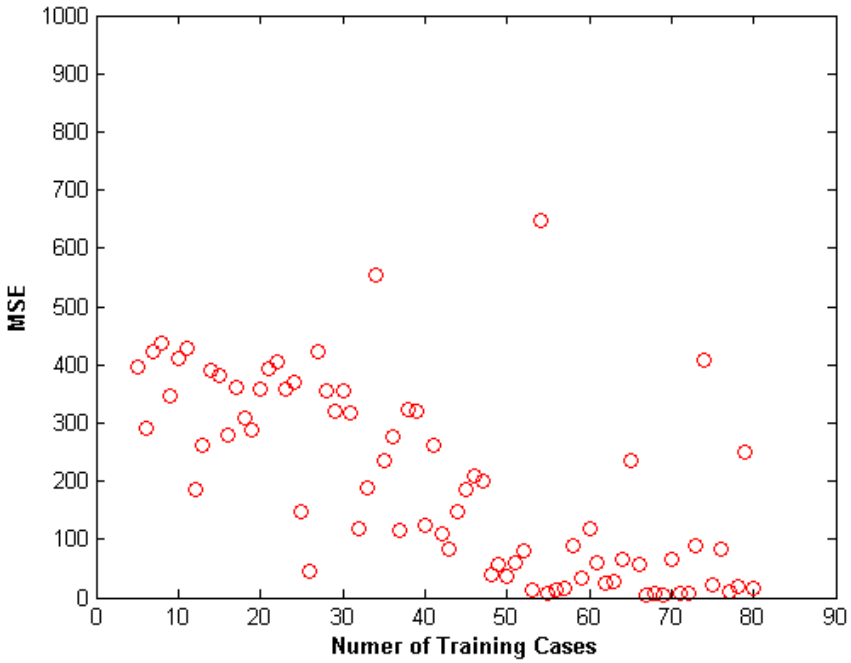

Figure 3.43 Impact of the number of training cases on prediction accuracy when 10 cases are predicted (Trial 1)

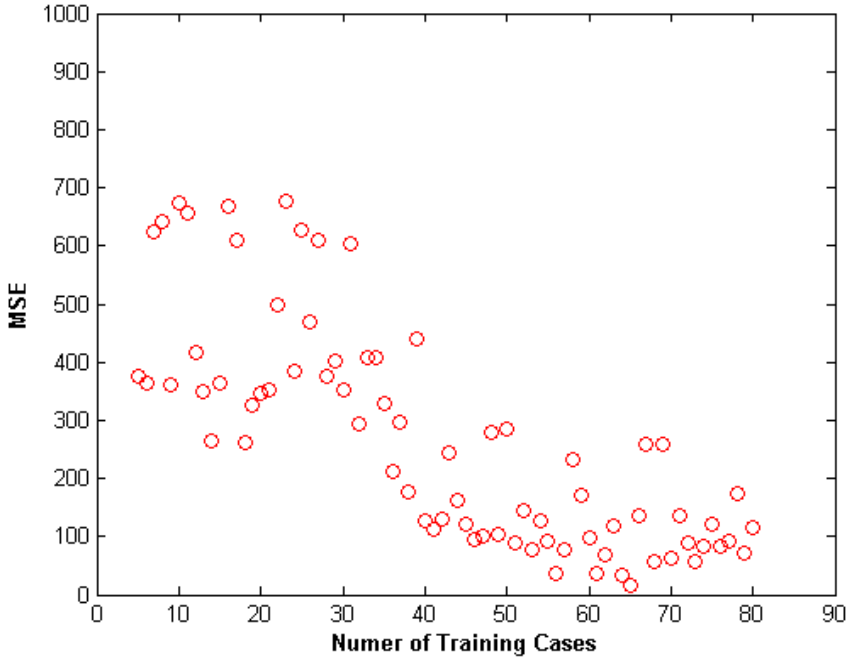

Figure 3.44 Impact of the number of training cases on prediction accuracy when 10 cases are predicted (Trial 2)

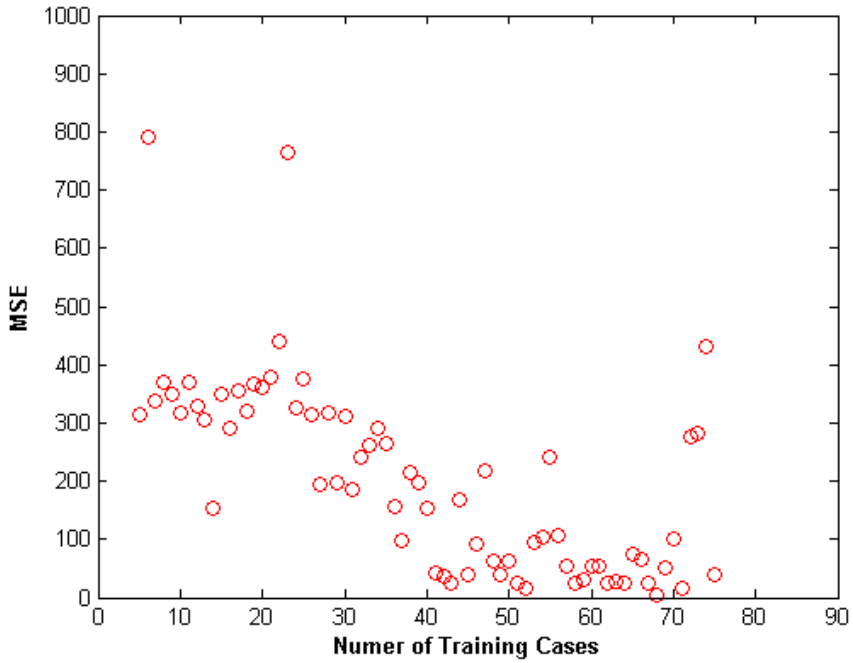

Figure 3.45 Impact of the number of training cases on prediction accuracy when 15 cases are predicted (Trial 1)

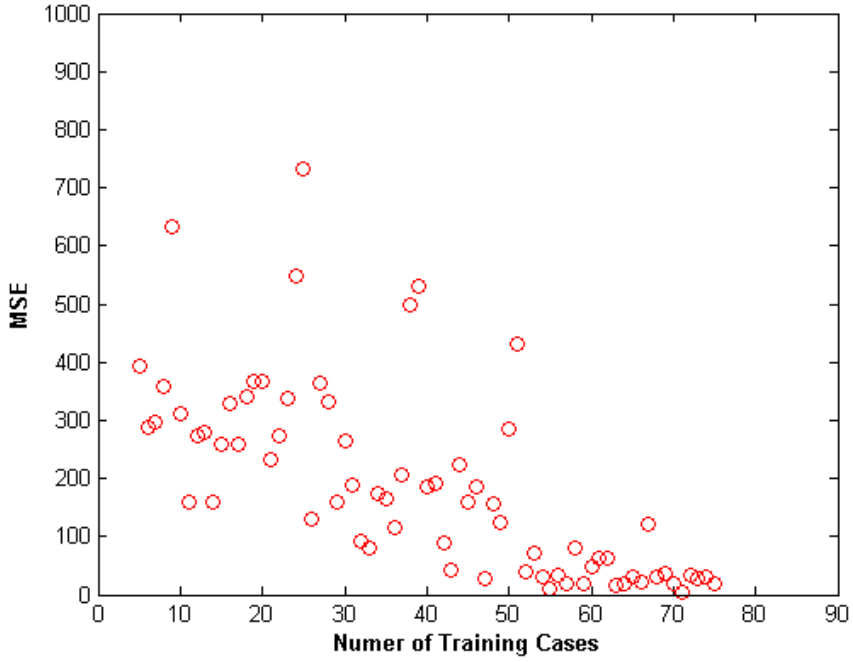

Figure 3.46 Impact of the number of training cases on prediction accuracy when 15 cases are predicted (Trial 2)

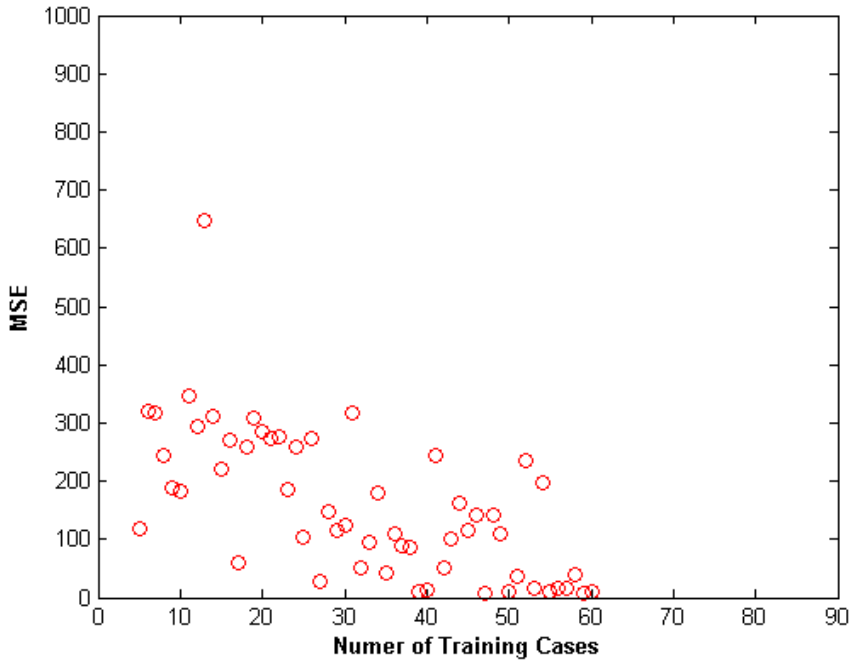

Figure 3.47 Impact of the number of training cases on prediction accuracy when 30 cases are predicted (Trial 1)

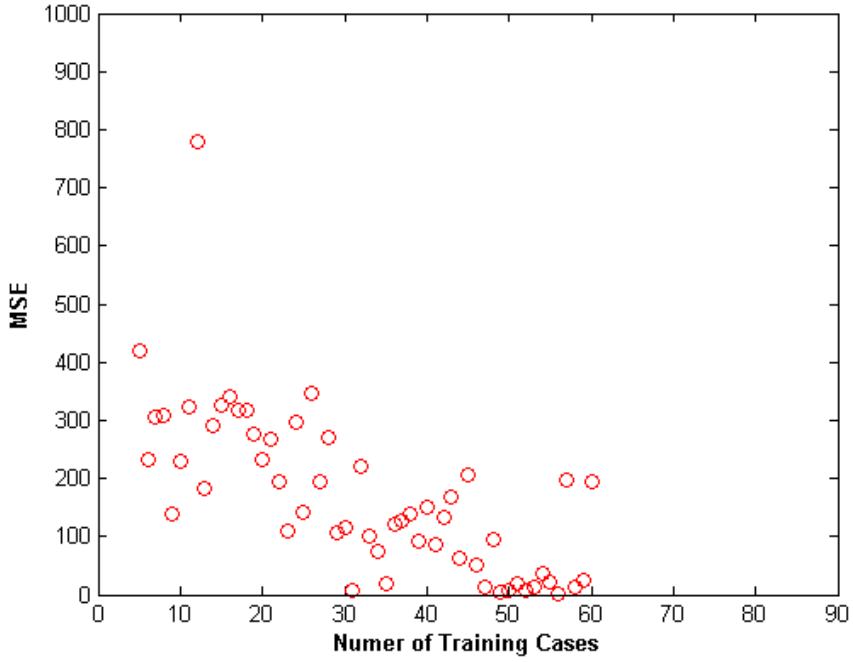

Figure 3.48 Impact of the number of training cases on prediction accuracy when 30 cases are predicted (Trial 2)

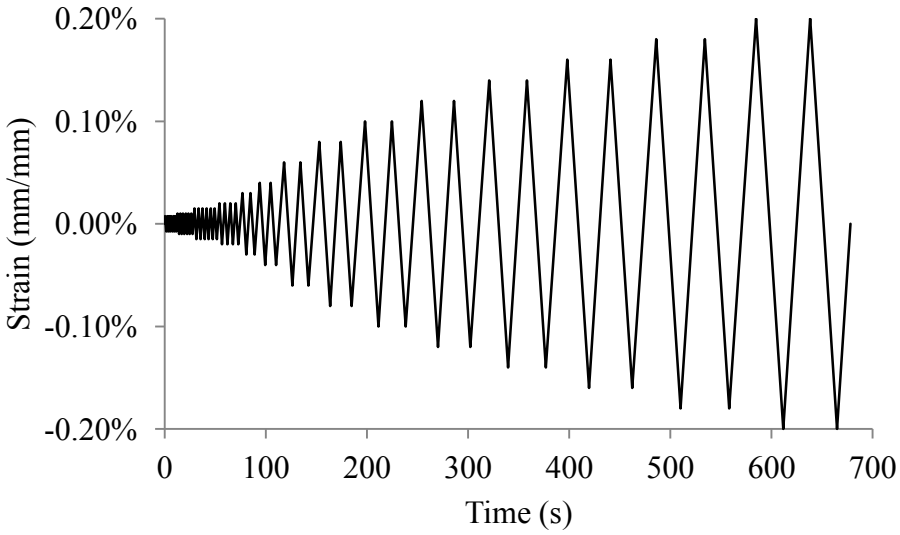

Figure 4.1 The basic loading mode for round bar models subject to stepwise increasing cyclic loads

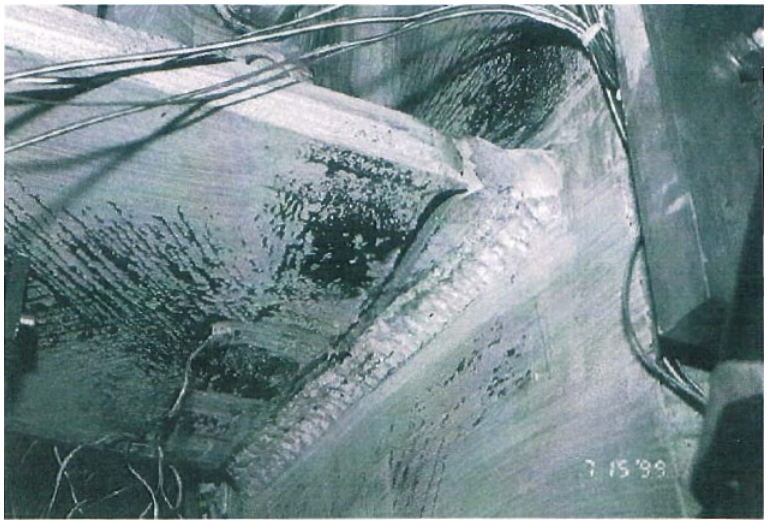

Figure 4.2 Beam flange fracture of DBBWWPZ (Engelhardt et al. 2000)

Figure 4.3 Beam flange fracture of CR2 (Lee et al. 2005(a))

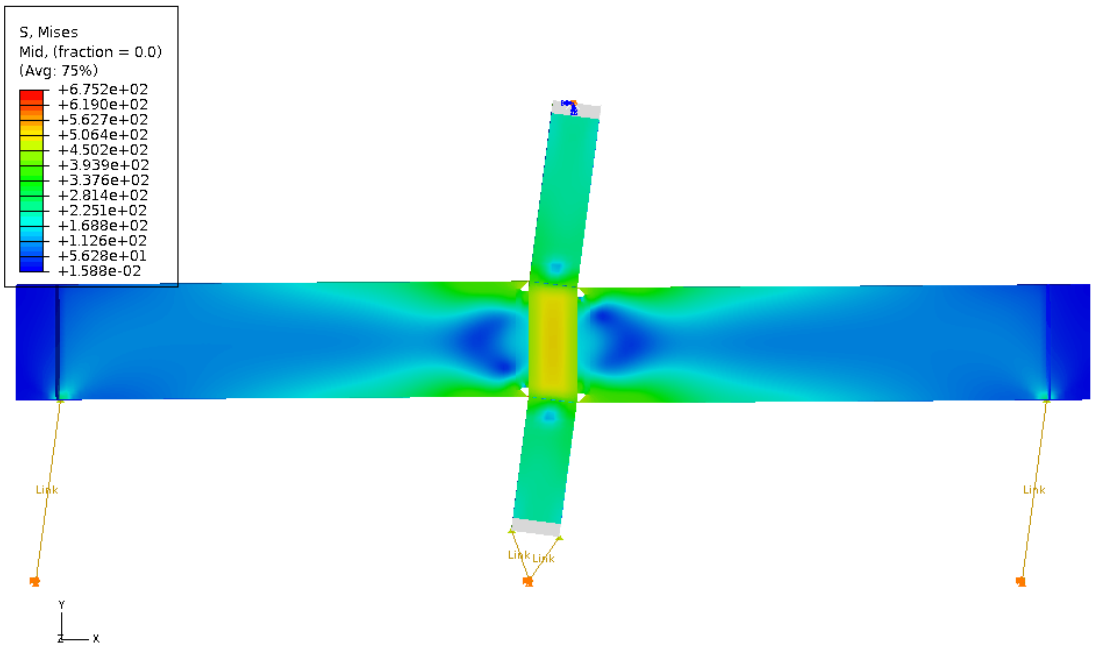

Figure 4.4 Von Mises stress contour of specimen DBBWWPZ subject to monotonic load

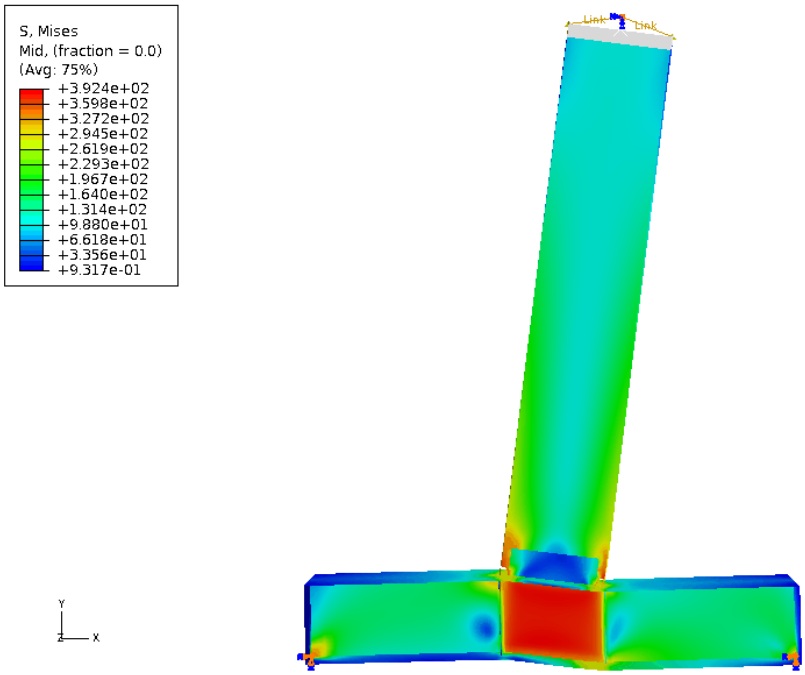

Figure 4.5 Von Mises stress contour of specimen SP2 subject to monotonic load

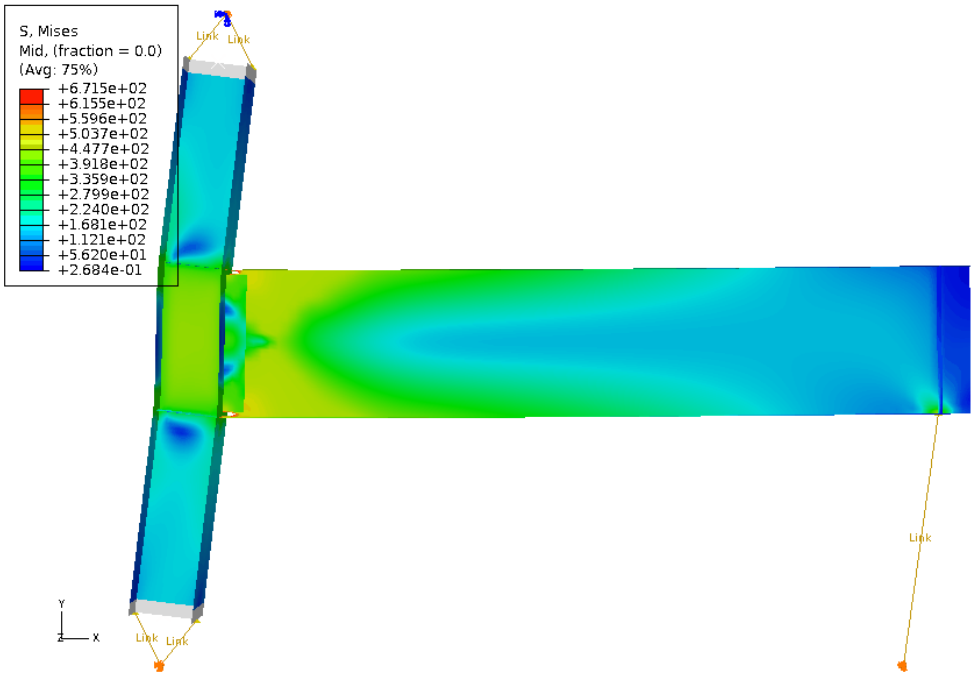

Figure 4.6 Von Mises stress contour of specimens T2 and T3 subject to monotonic load

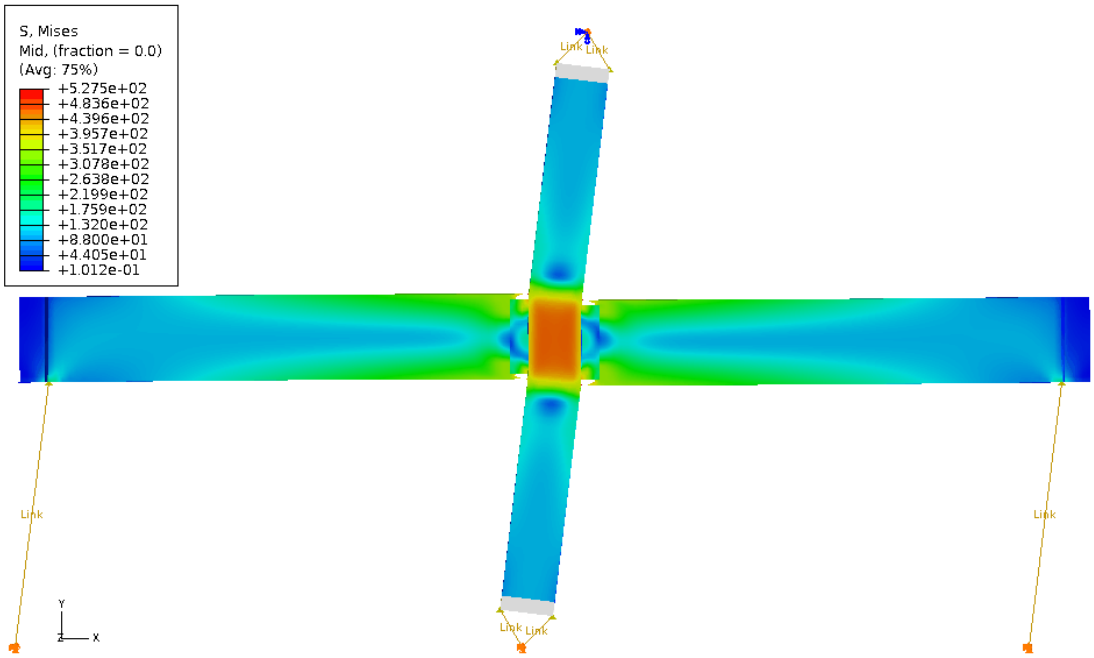

Figure 4.7 Von Mises stress contour of specimen CR1 subject to monotonic load

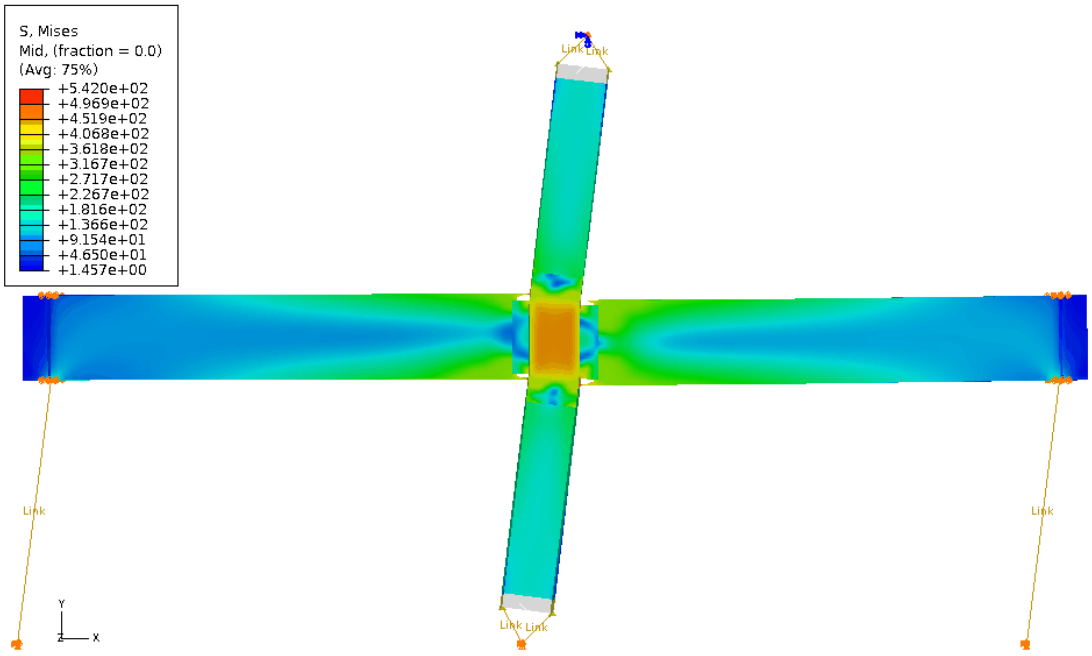

Figure 4.8 Von Mises stress contour of specimen CR2 subject to monotonic load

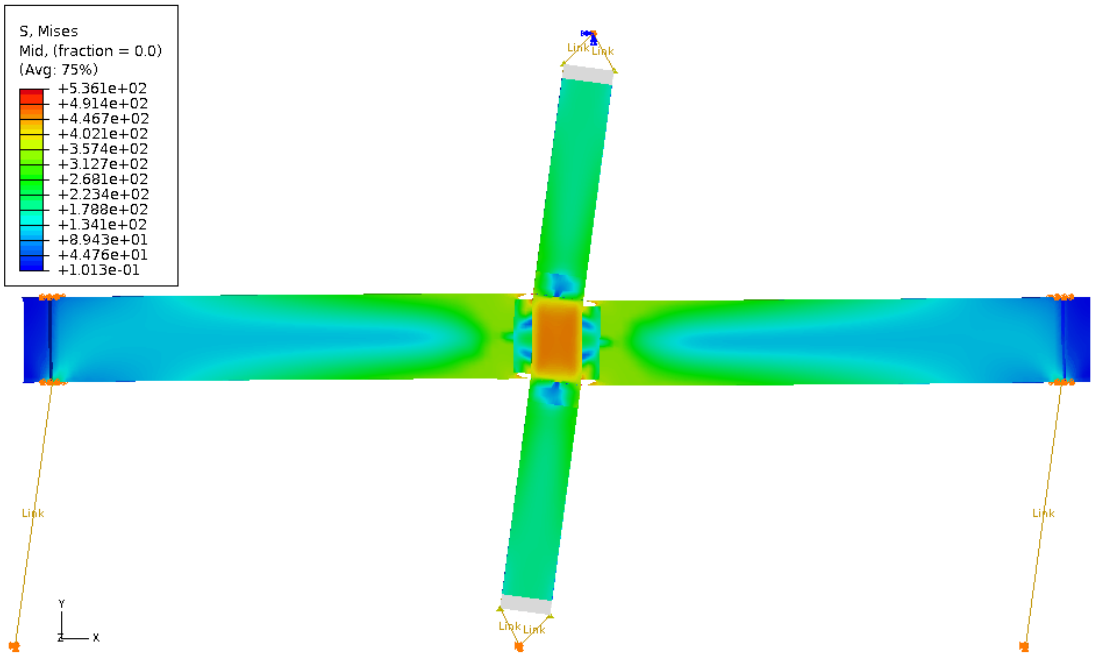

Figure 4.9 Von Mises stress contour of specimen CR3 subject to monotonic load

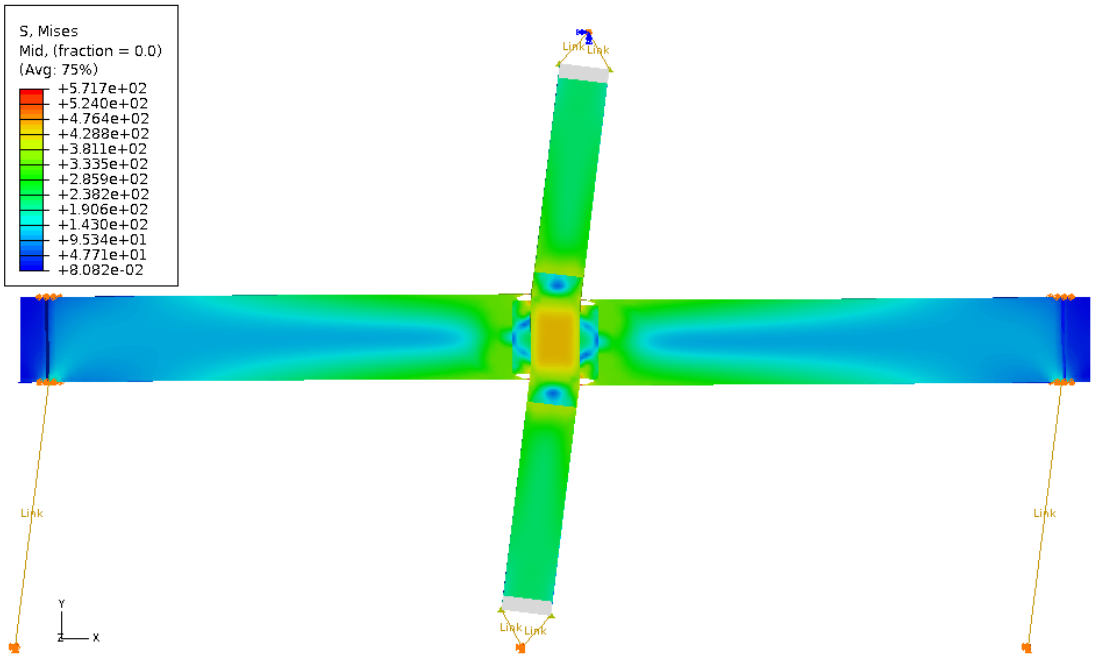

Figure 4.10 Von Mises stress contour of specimen CR5 subject to monotonic load

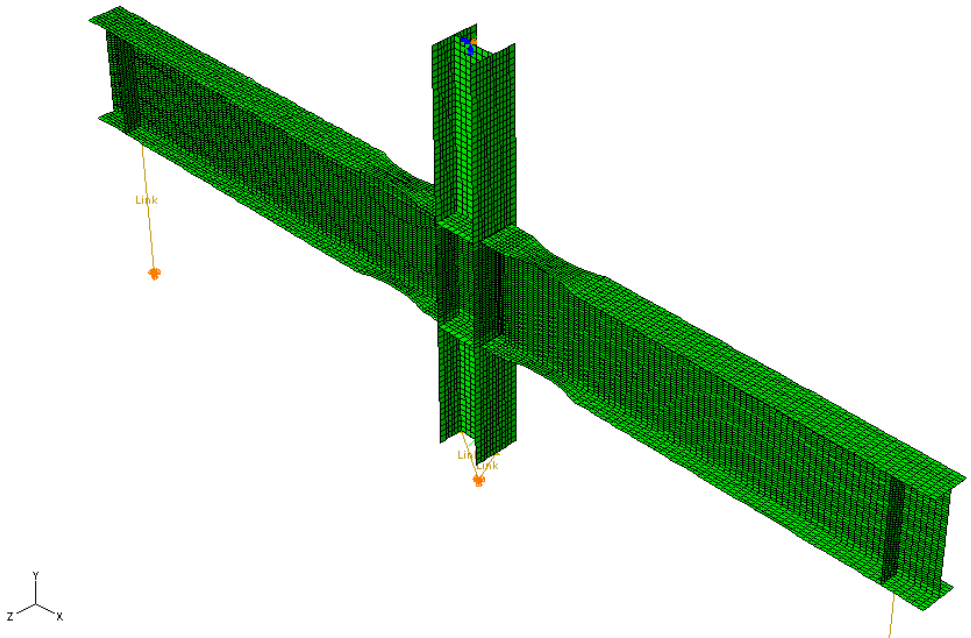

Figure 4.11 Global finite element model of specimen DBBWWPZ

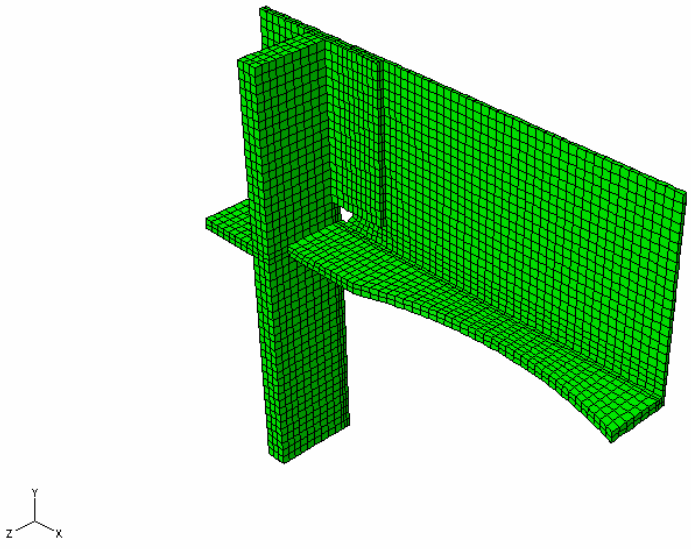

Figure 4.12 Local finite element model of specimen DBBWWPZ

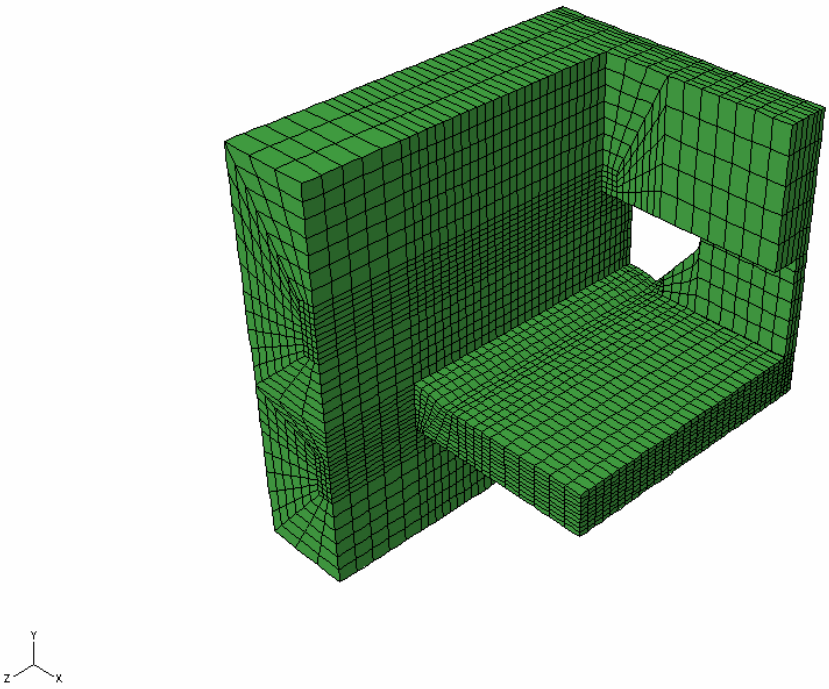

Figure 4.13 Sub-local finite element model of specimen DBBWWPZ

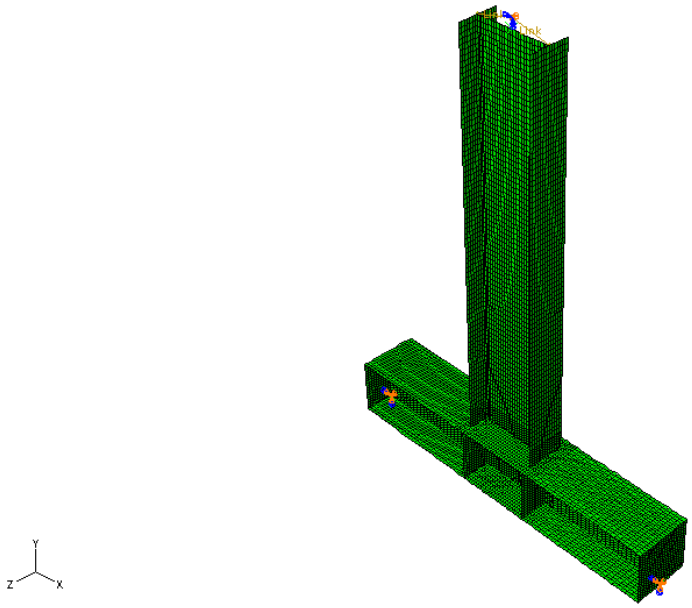

Figure 4.14 Global finite element model of specimen SP2

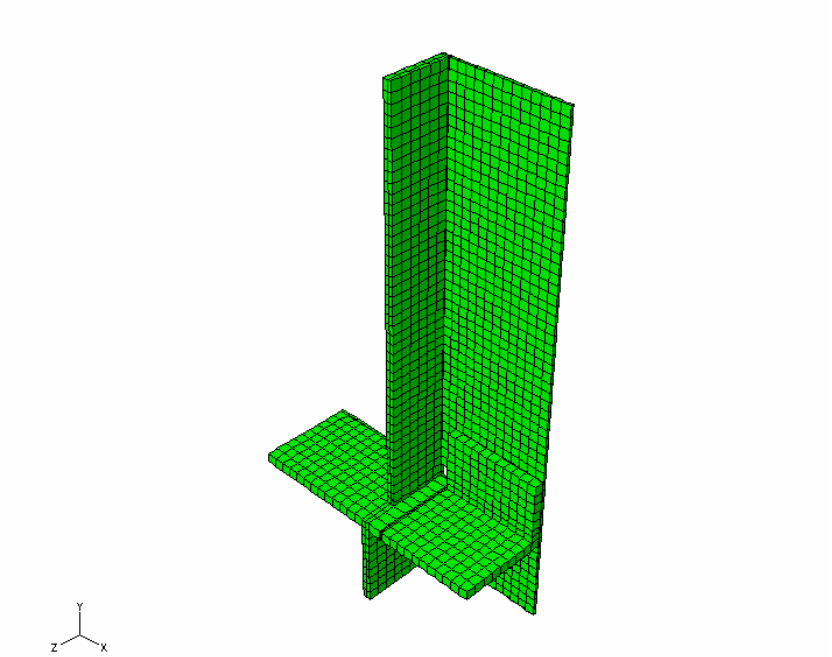

Figure 4.15 Local finite element model of specimen SP2

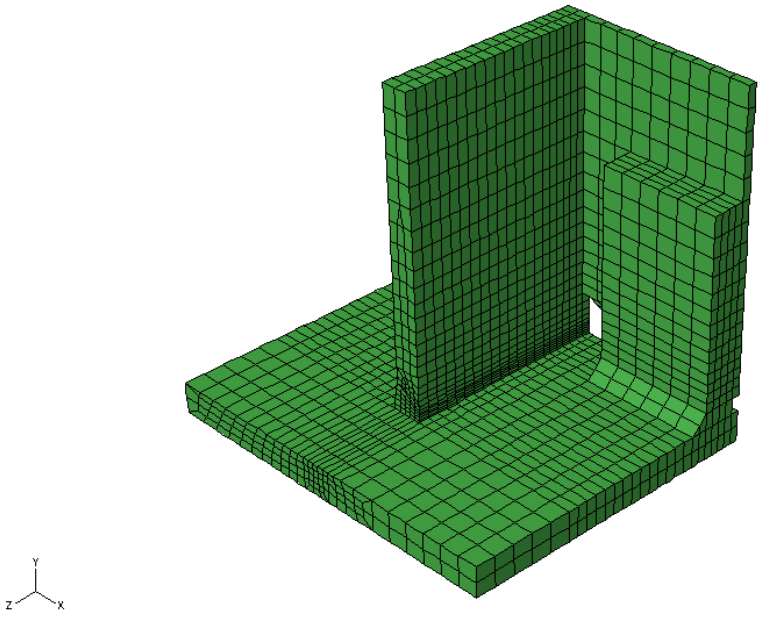

Figure 4.16 Sub-local finite element model of specimen SP2

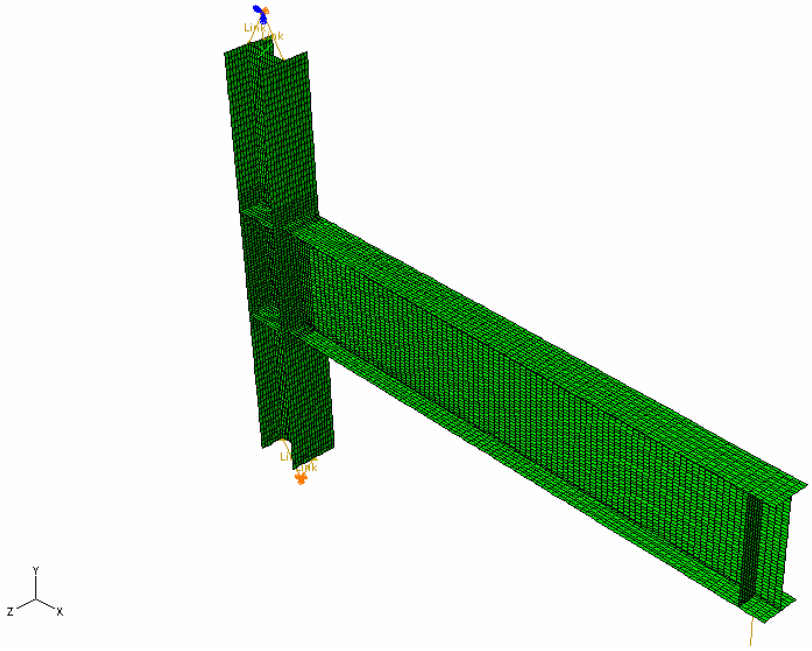

Figure 4.17 Global finite element model of specimens T2 and T3

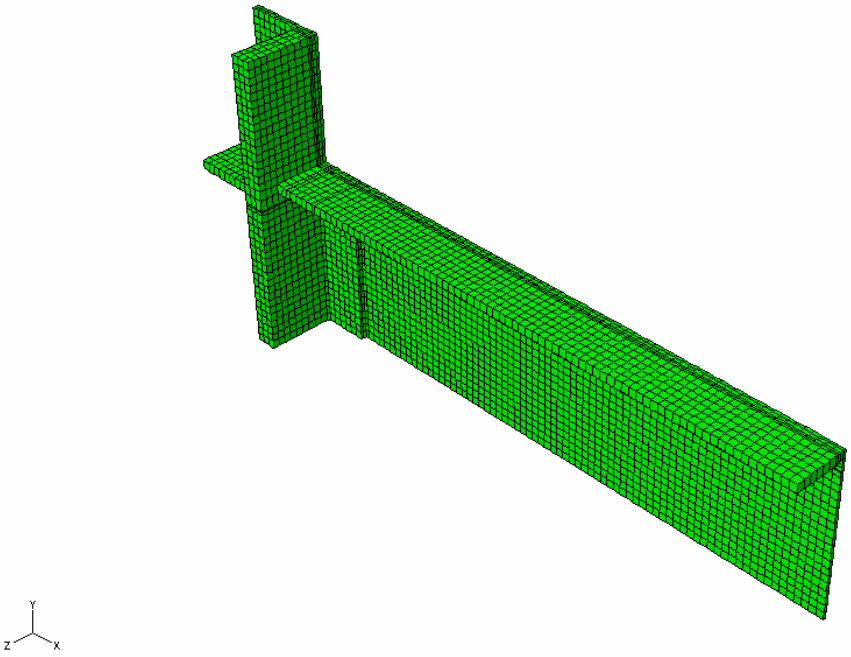

Figure 4.18 Local finite element model of specimen T2

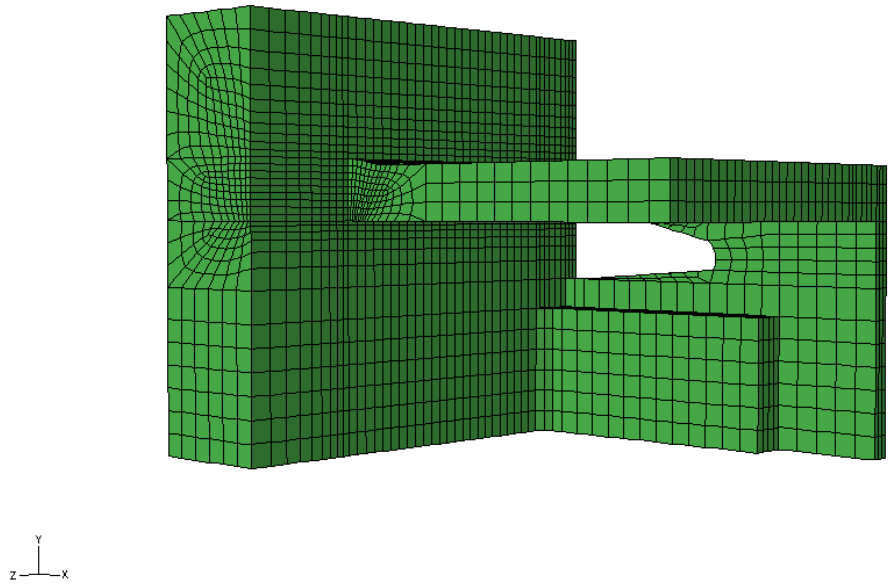

Figure 4.19 Sub-local finite element model of specimen T2

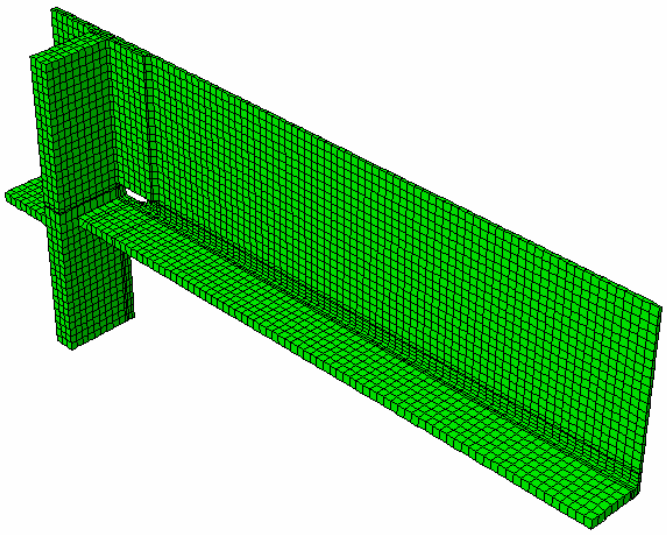

Figure 4.20 Local finite element model of specimen T3

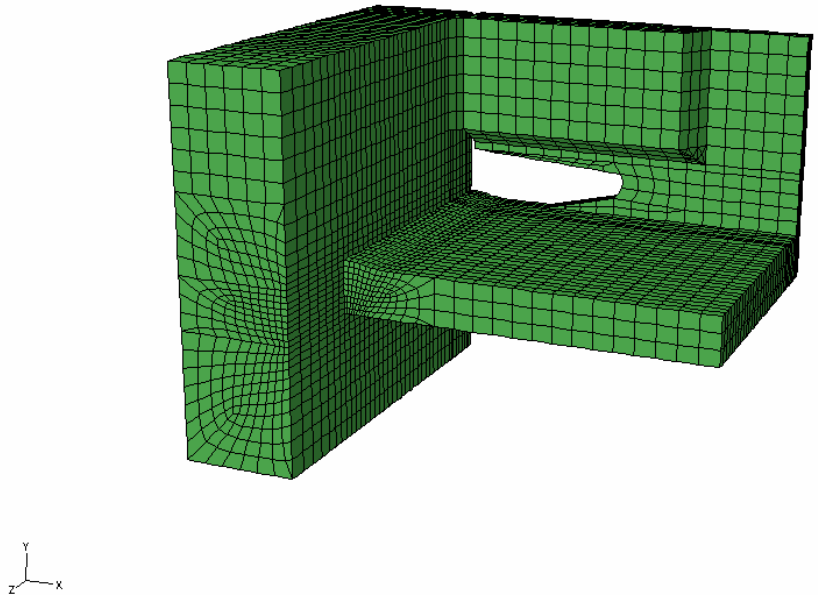

Figure 4.21 Sub-local finite element model of specimen T3

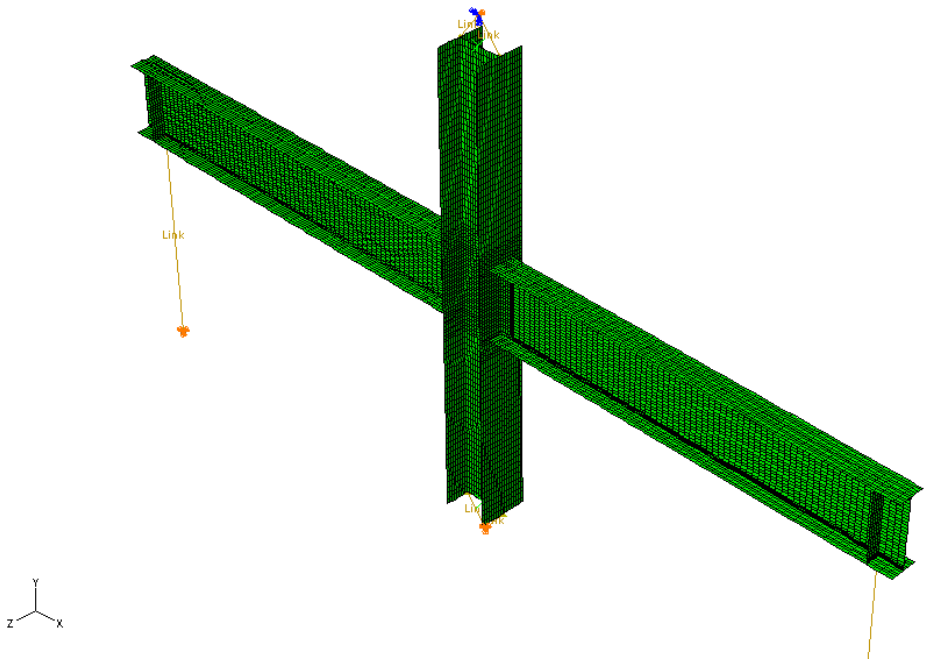

Figure 4.22 Global finite element model of specimen CR1

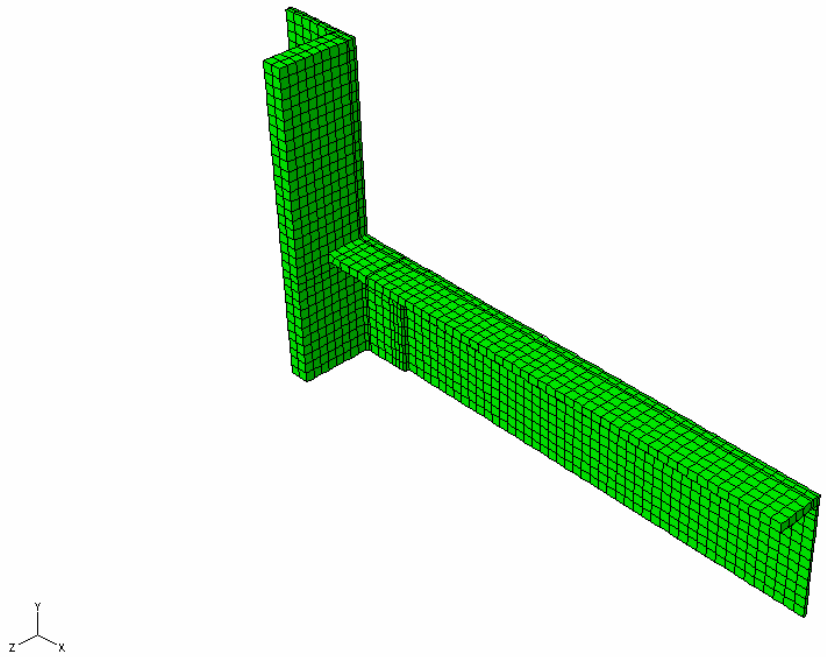

Figure 4.23 Local finite element model of specimen CR1

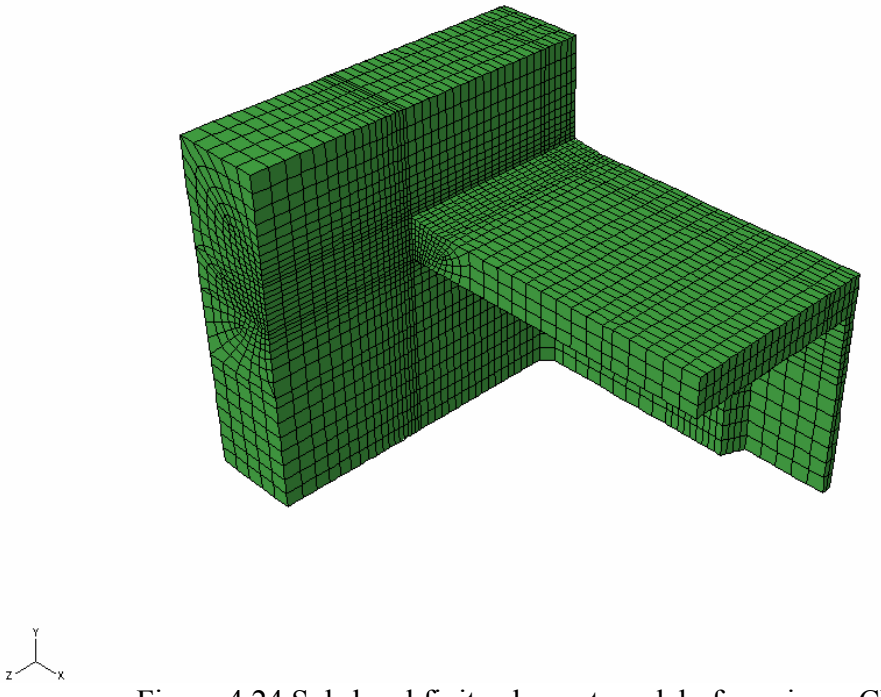

Figure 4.24 Sub-local finite element model of specimen CR1

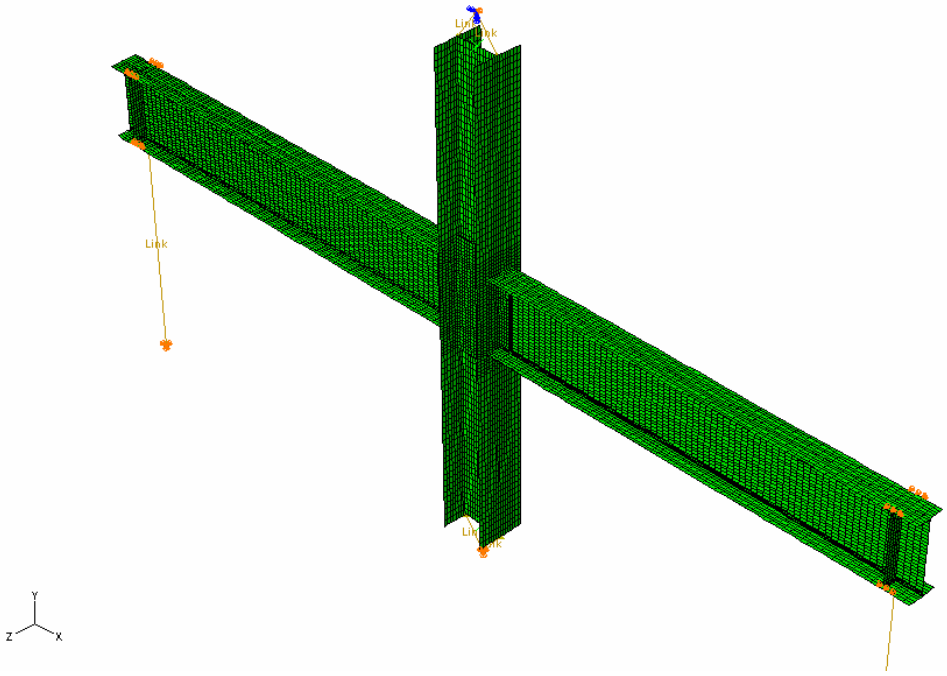

Figure 4.25 Global finite element model of specimen CR2

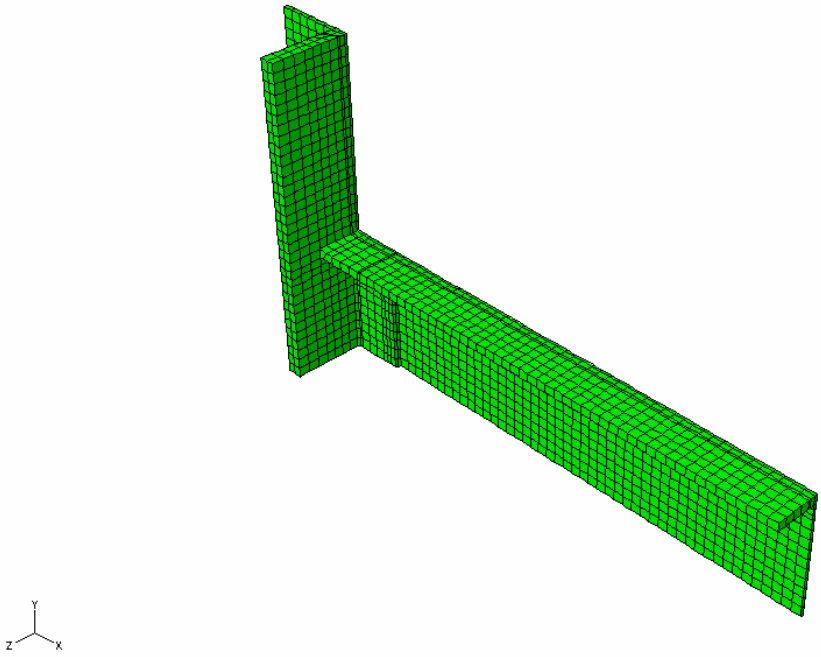

Figure 4.26 Local finite element model of specimen CR2

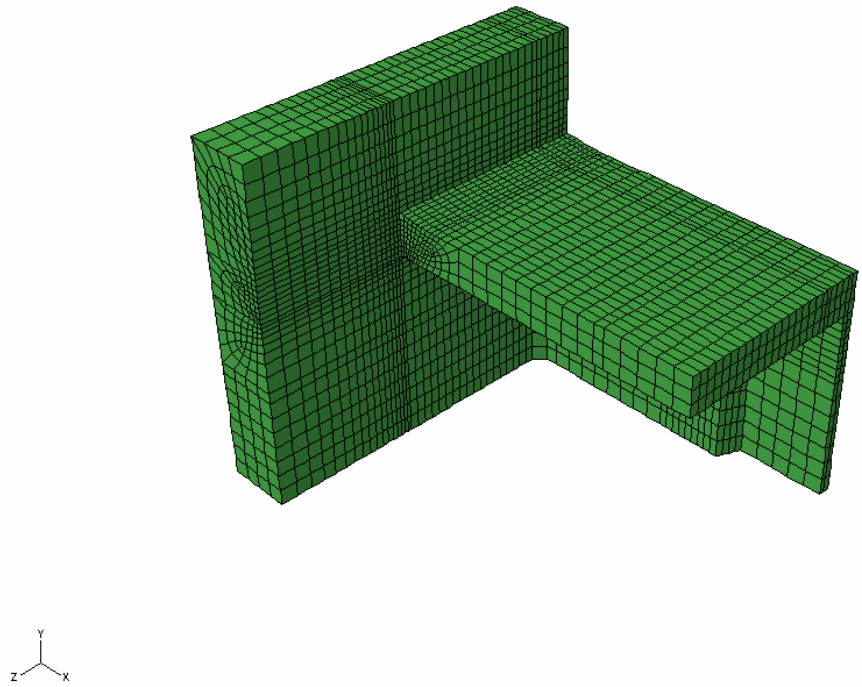

Figure 4.27 Sub-local finite element model of specimen CR2

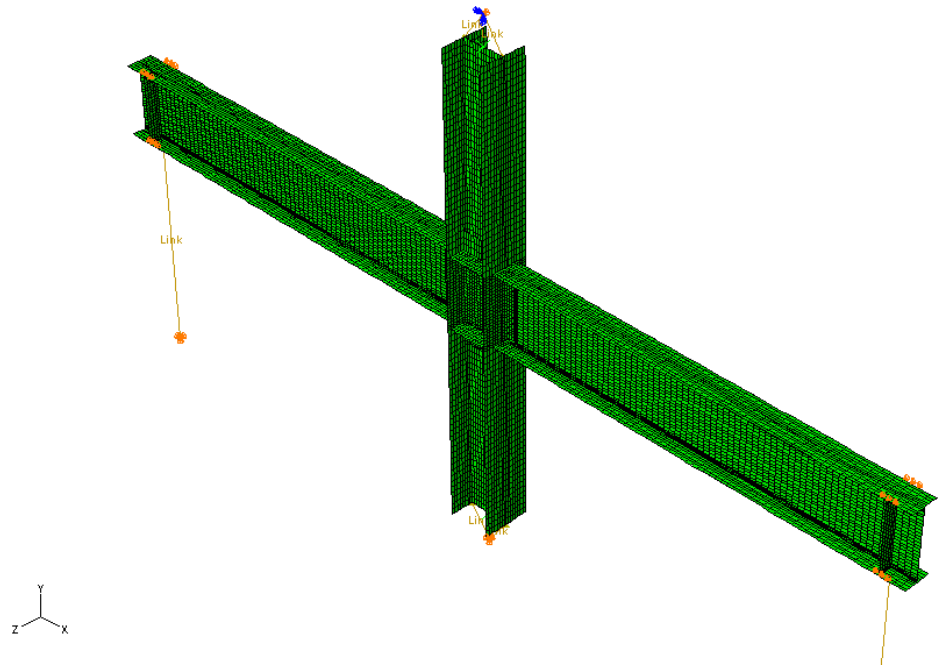

Figure 4.28 Global finite element model of specimen CR3

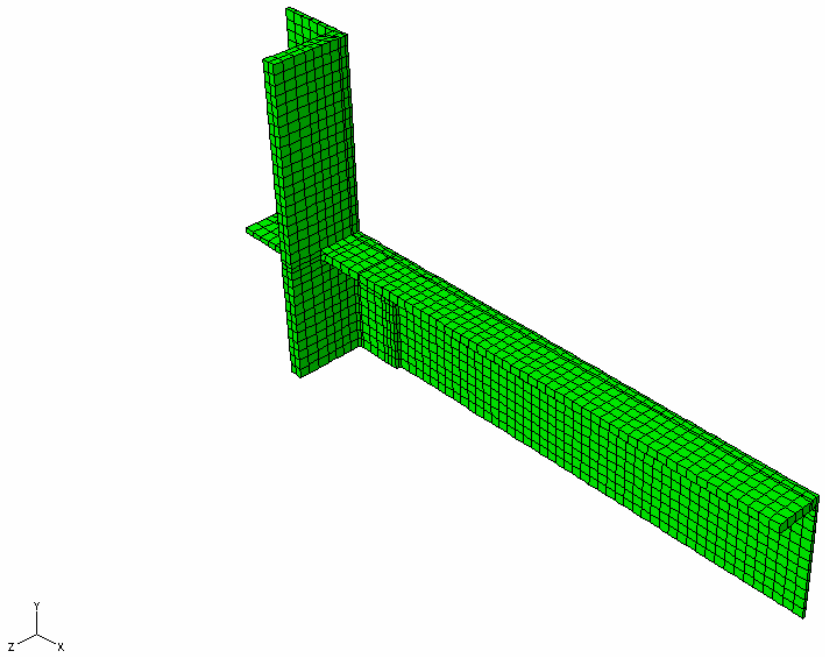

Figure 4.29 Local finite element model of specimen CR3

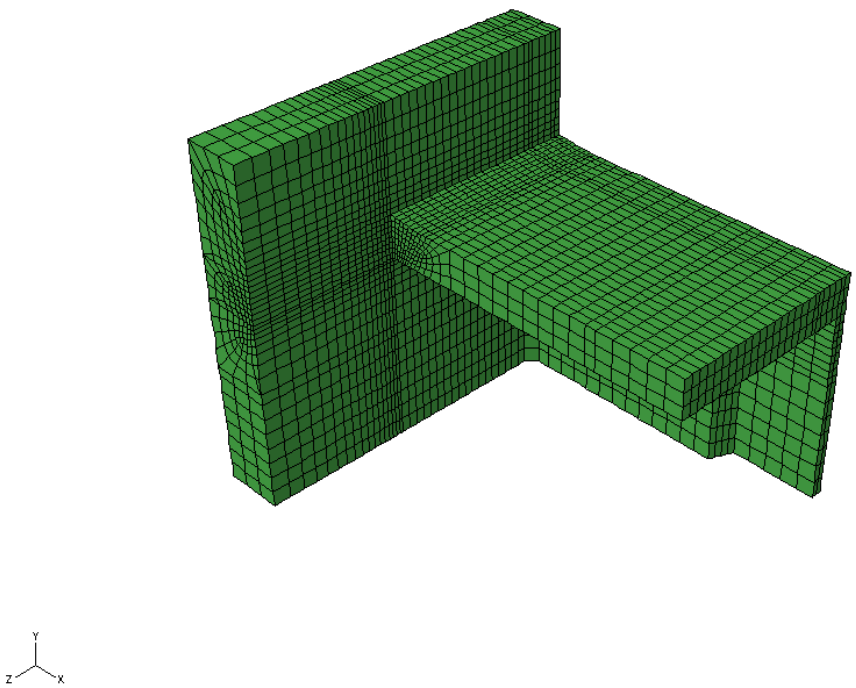

Figure 4.30 Sub-local finite element model of specimen CR3

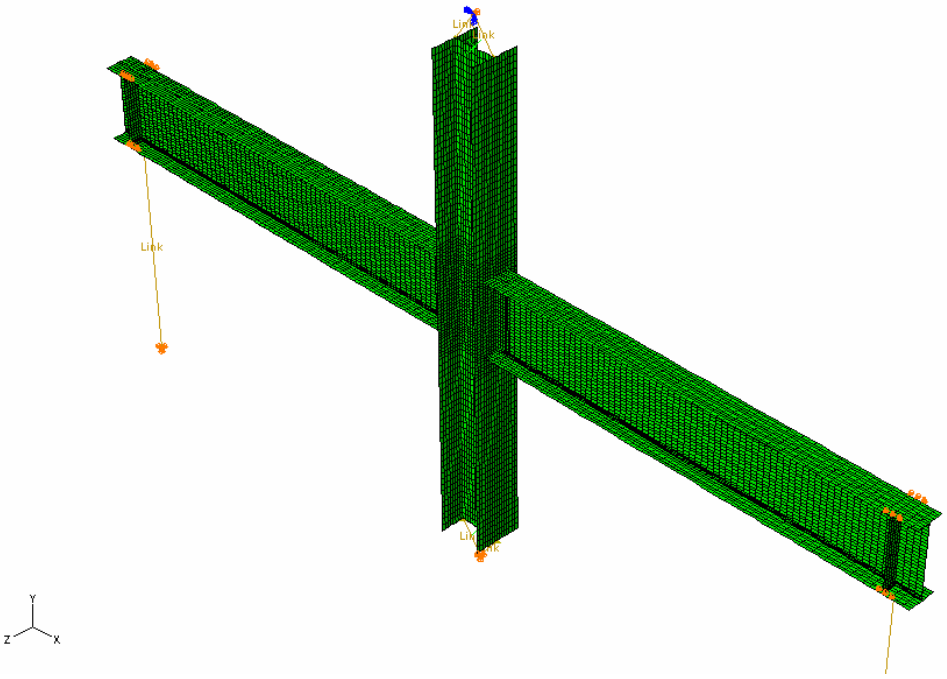

Figure 4.31 Global finite element model of specimen CR5

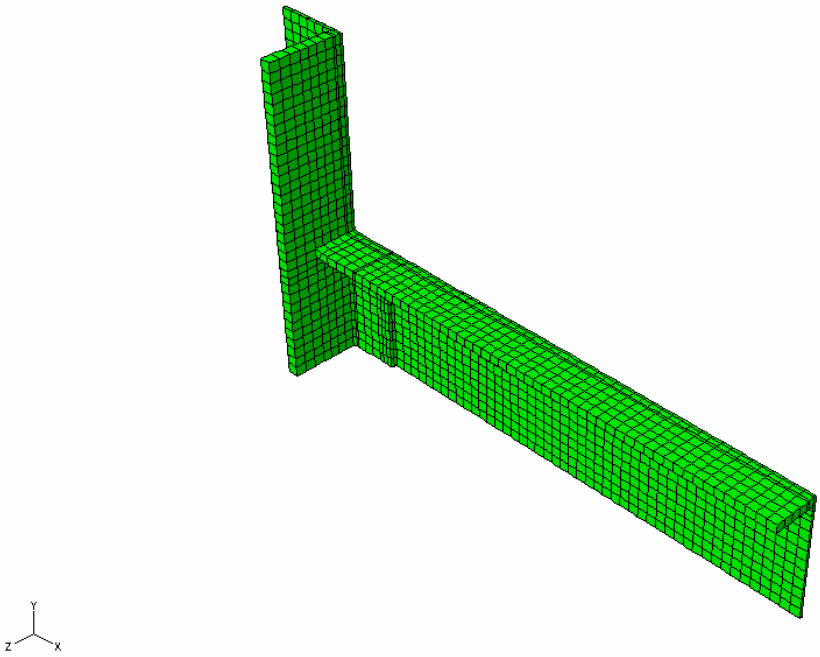

Figure 4.32 Local finite element model of specimen CR5

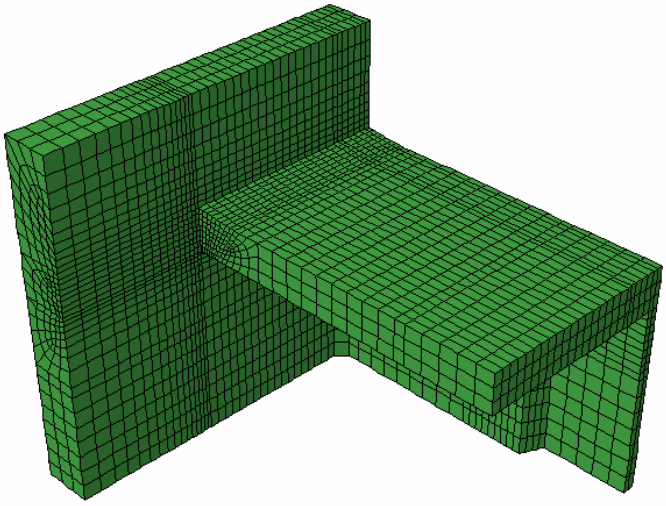

Figure 4.33 Sub-local finite element model of specimen CR5

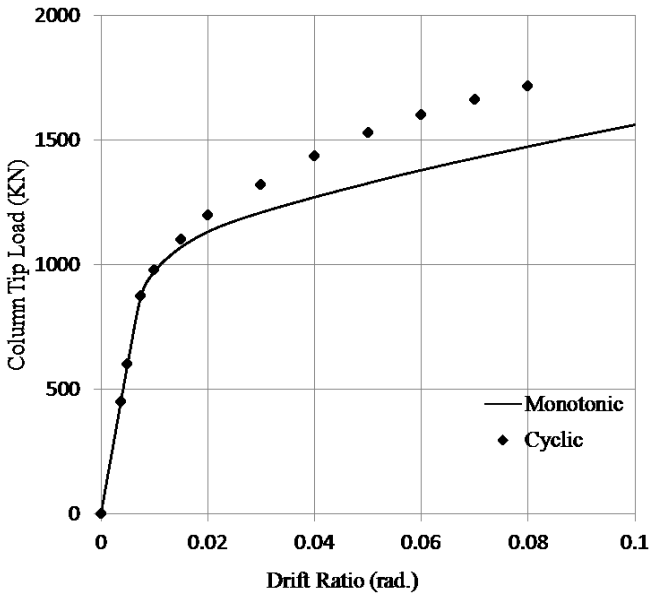

Figure 4.34 Comparison of load - drift ratio relationships subject to monotonic and cyclic loads – specimen DBBWWPZ

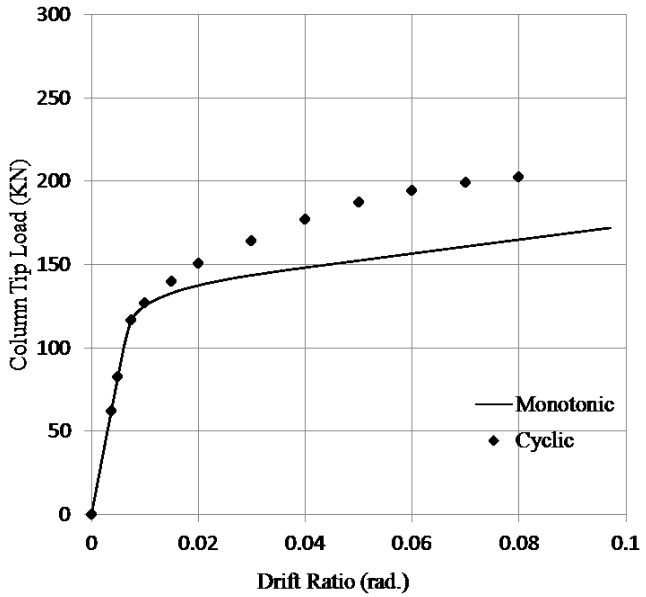

Figure 4.35 Comparison of load - drift ratio relationships subject to monotonic and cyclic loads – specimen SP2

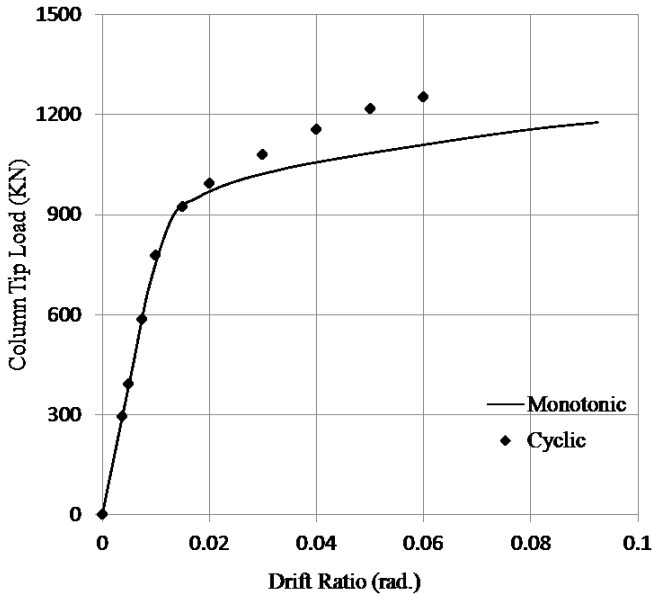

Figure 4.36 Comparison of load - drift ratio relationships subject to monotonic and cyclic loads – specimens T2 and T3

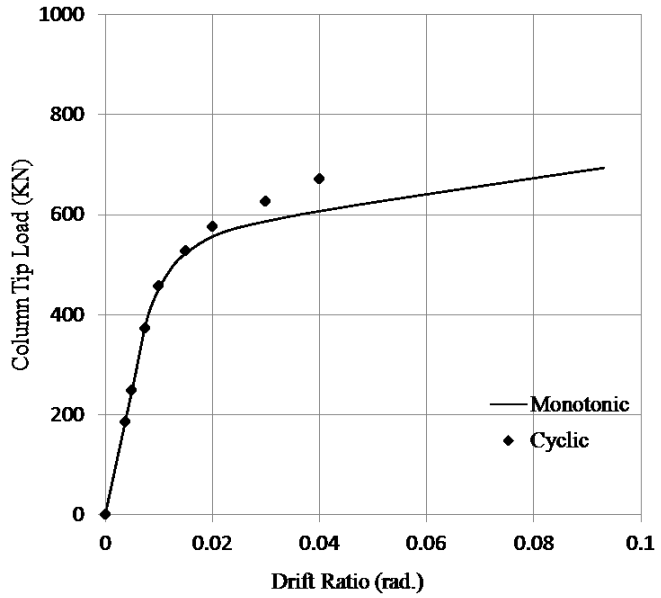

Figure 4.37 Comparison of load - drift ratio relationships subject to monotonic and cyclic loads – specimen CR1

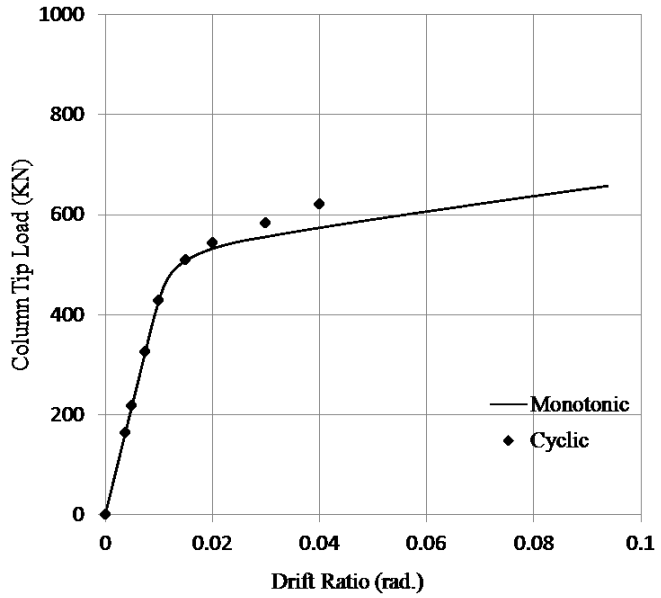

Figure 4.38 Comparison of load - drift ratio relationships subject to monotonic and cyclic loads – specimen CR2

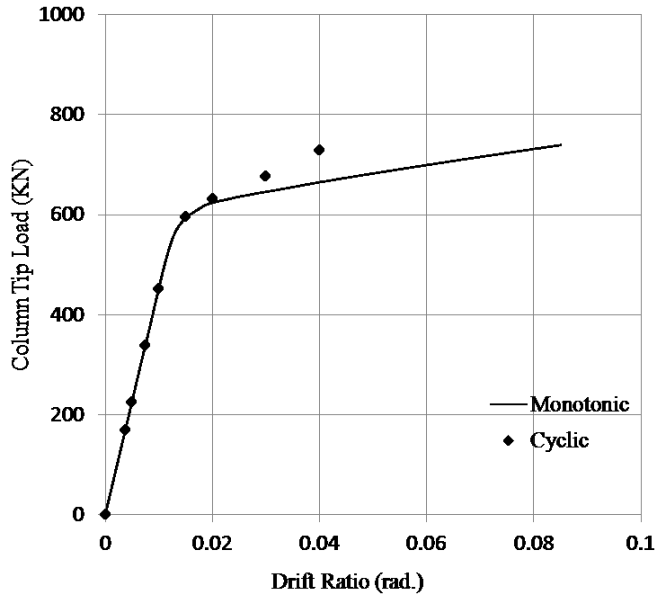

Figure 4.39 Comparison of load - drift ratio relationships subject to monotonic and cyclic loads – specimen CR3

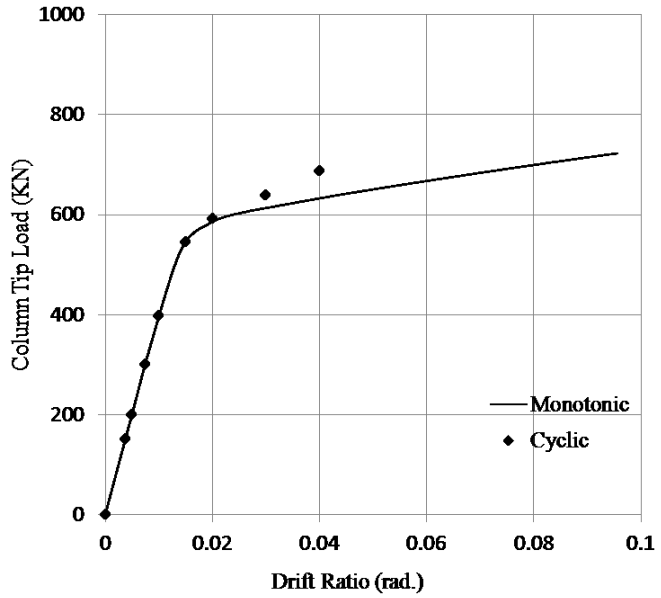

Figure 4.40 Comparison of load - drift ratio relationships subject to monotonic and cyclic loads – specimen CR5

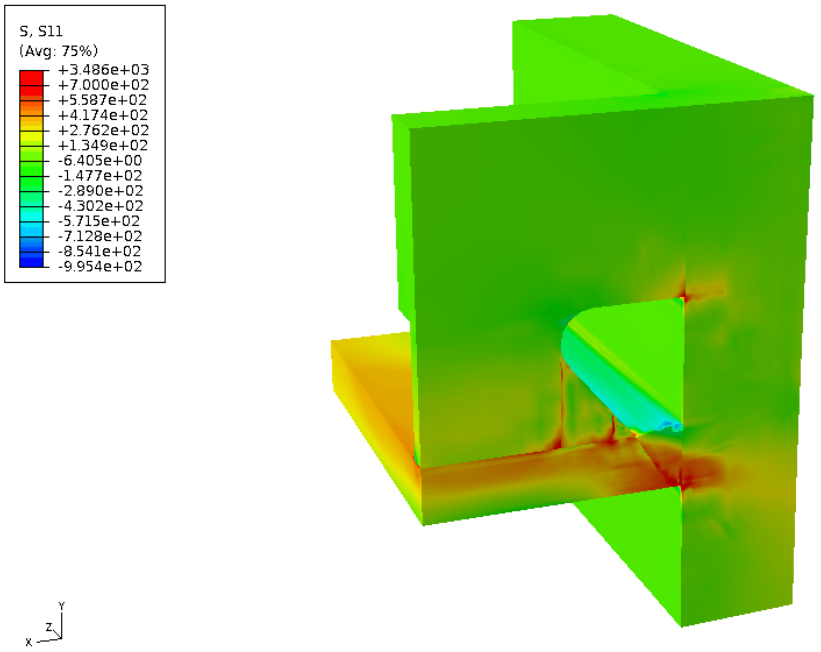

Figure 4.41 Contour of normal stress in the longitudinal direction – DBBWWPZ sub-local model

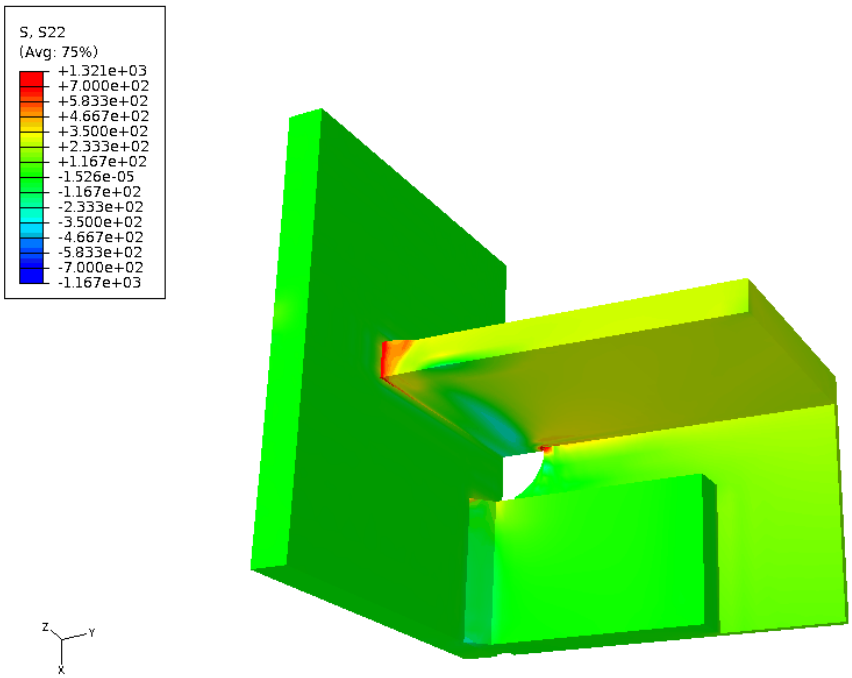

Figure 4.42 Contour of normal stress in the longitudinal direction – SP2 sub-local model

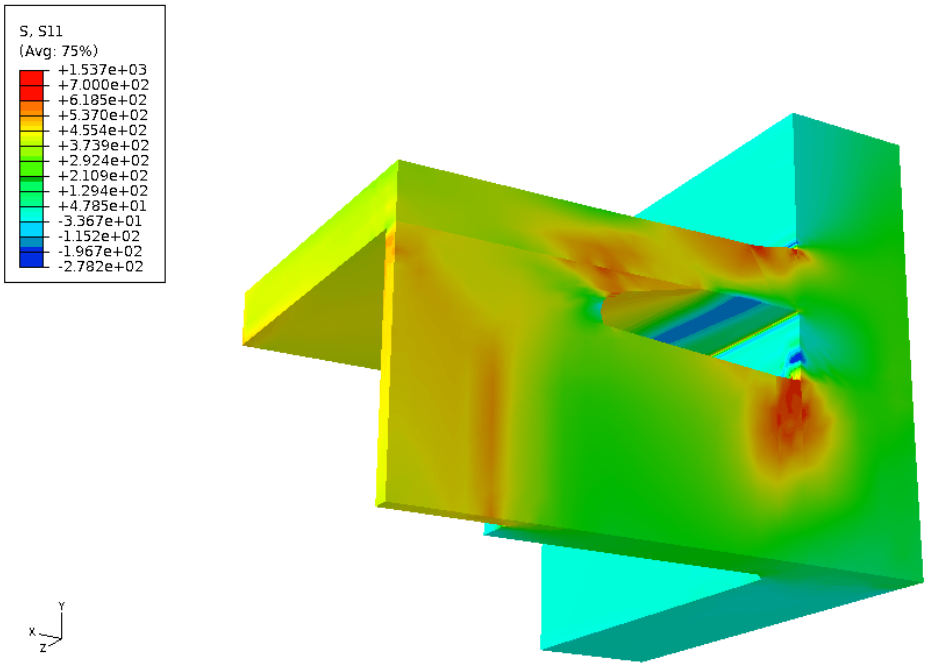

Figure 4.43 Contour of normal stress in the longitudinal direction – T2 sub-local model

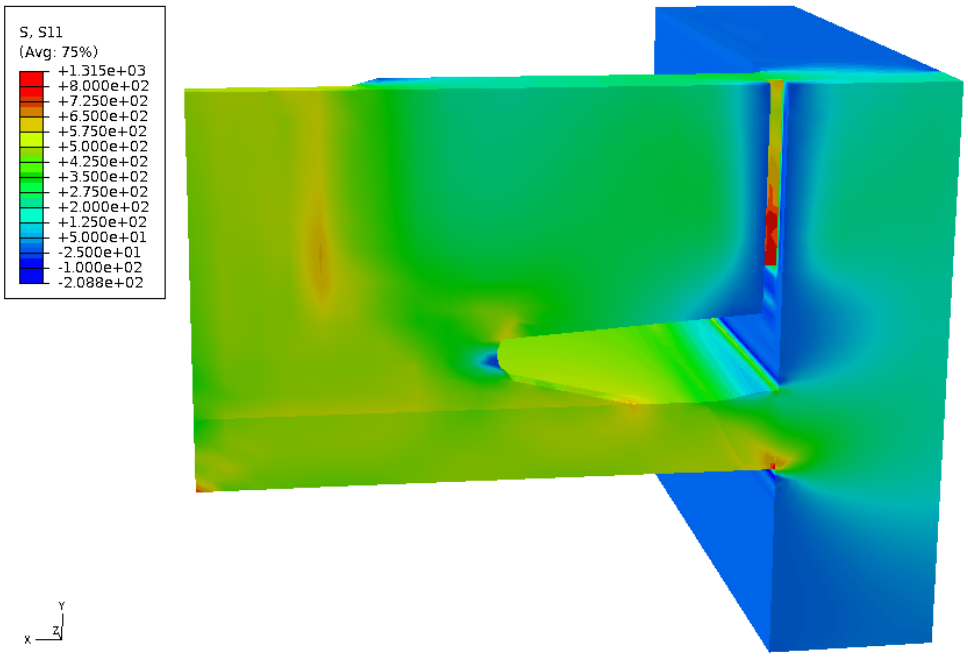

Figure 4.44 Contour of normal stress in the longitudinal direction – T3 sub-local model

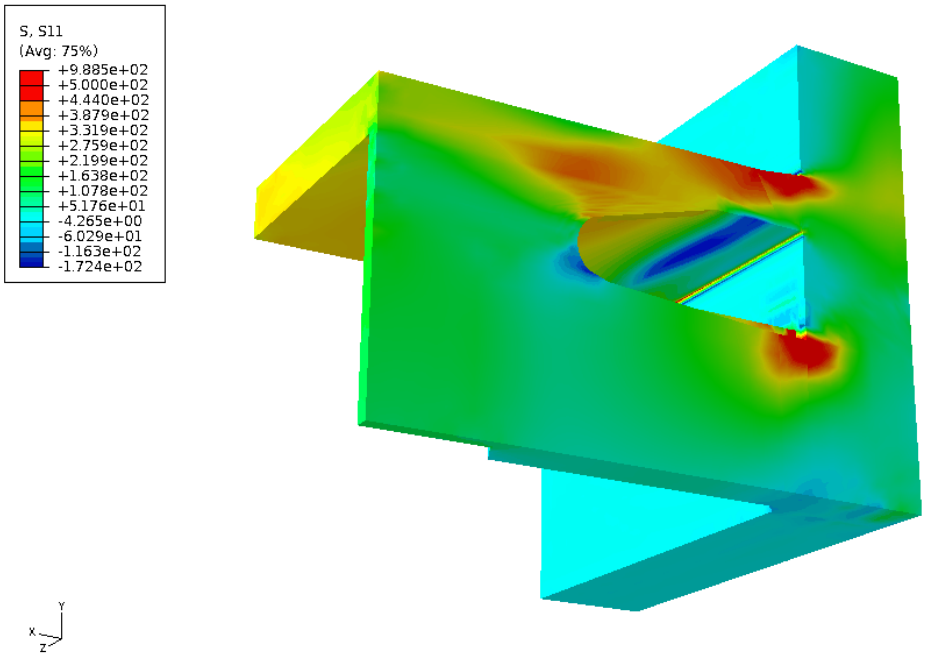

Figure 4.45 Contour of normal stress in the longitudinal direction – CR1 sub-local model

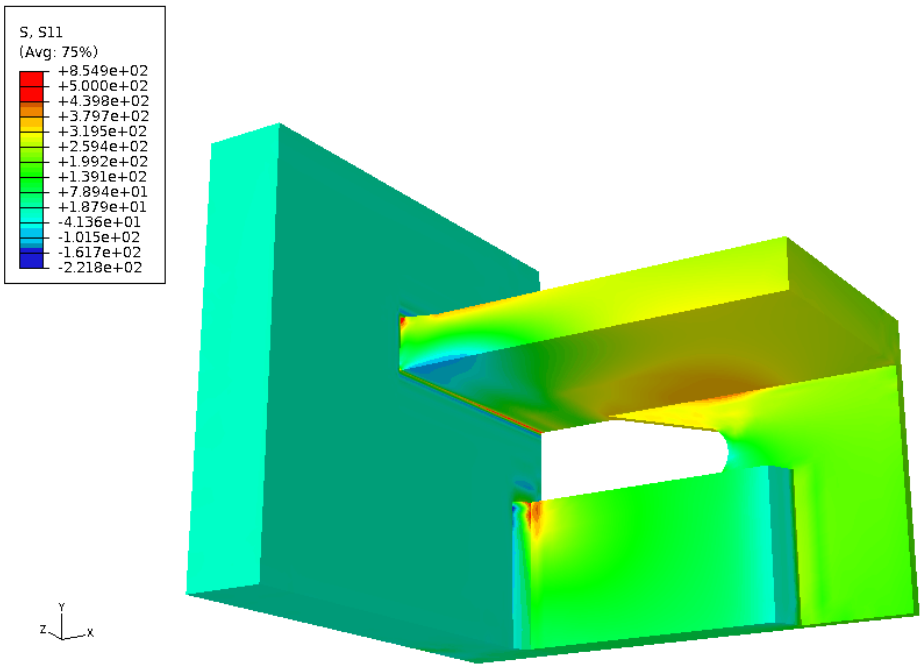

Figure 4.46 Contour of normal stress in the longitudinal direction – CR2 sub-local model

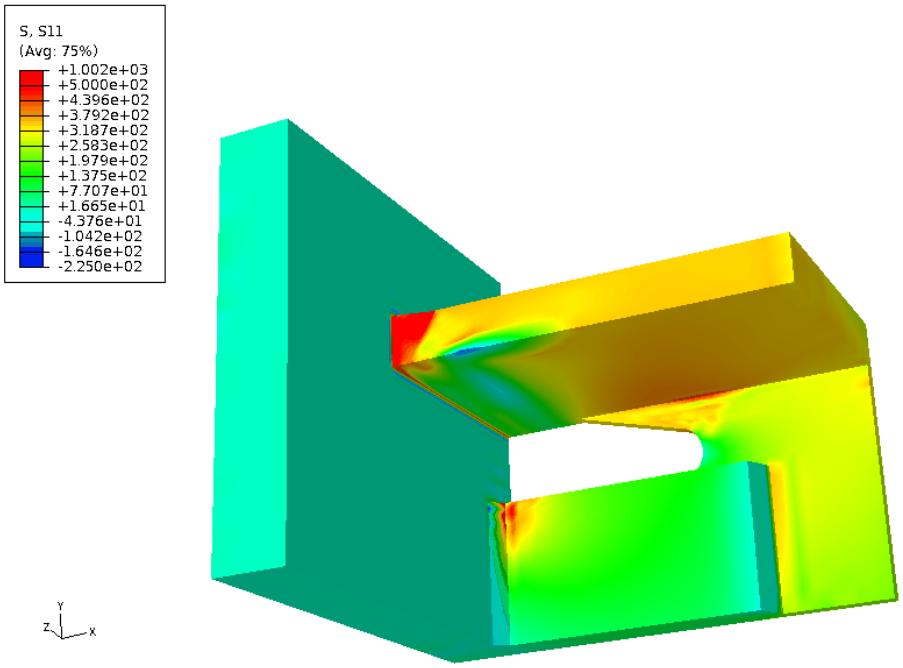

Figure 4.47 Contour of normal stress in the longitudinal direction – CR3 sub-local model

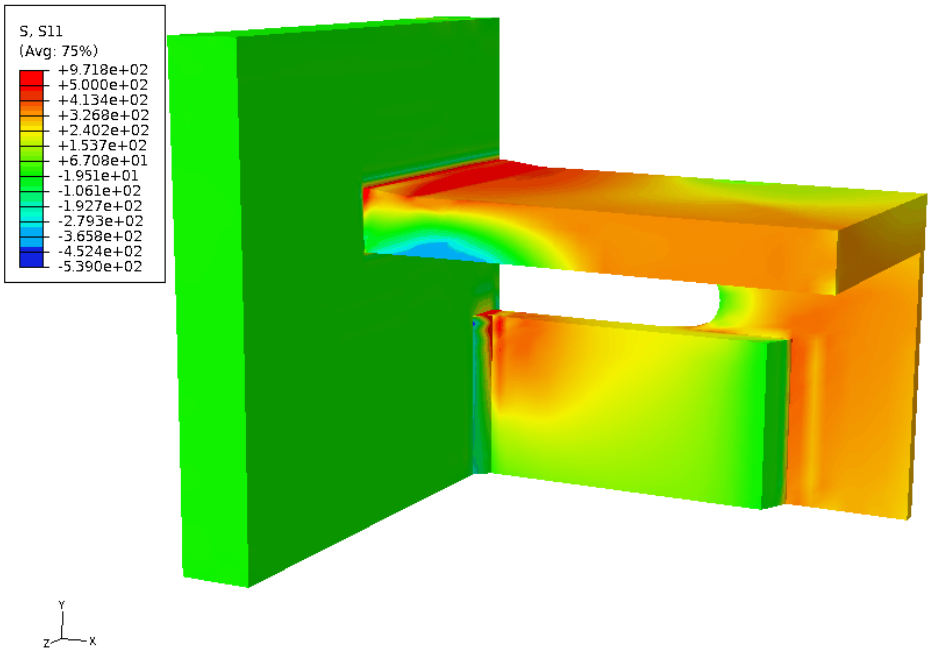

Figure 4.48 Contour of normal stress in the longitudinal direction – CR5 sub-local model

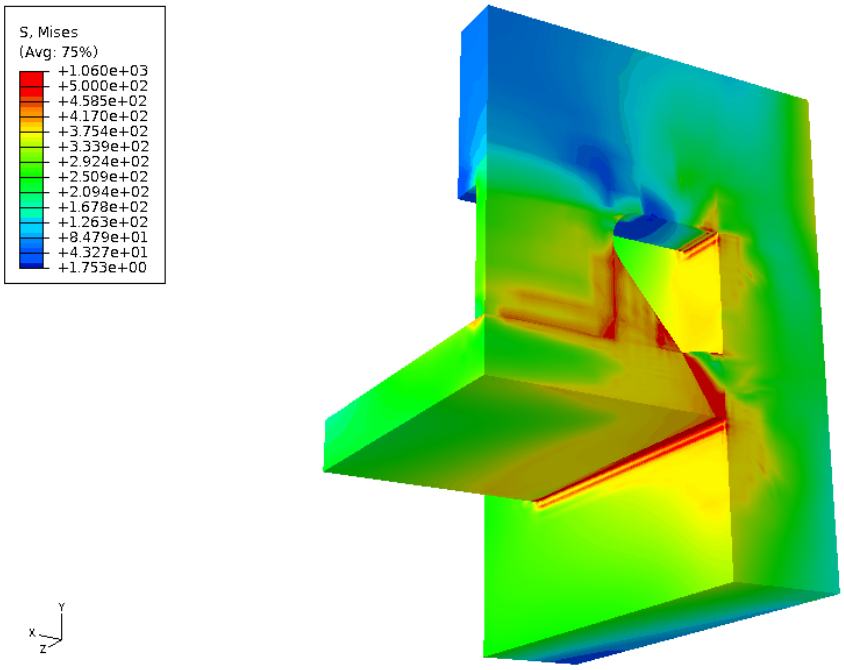

Figure 4.49 Von Mises stress contour – DBBWWPZ sub-local model

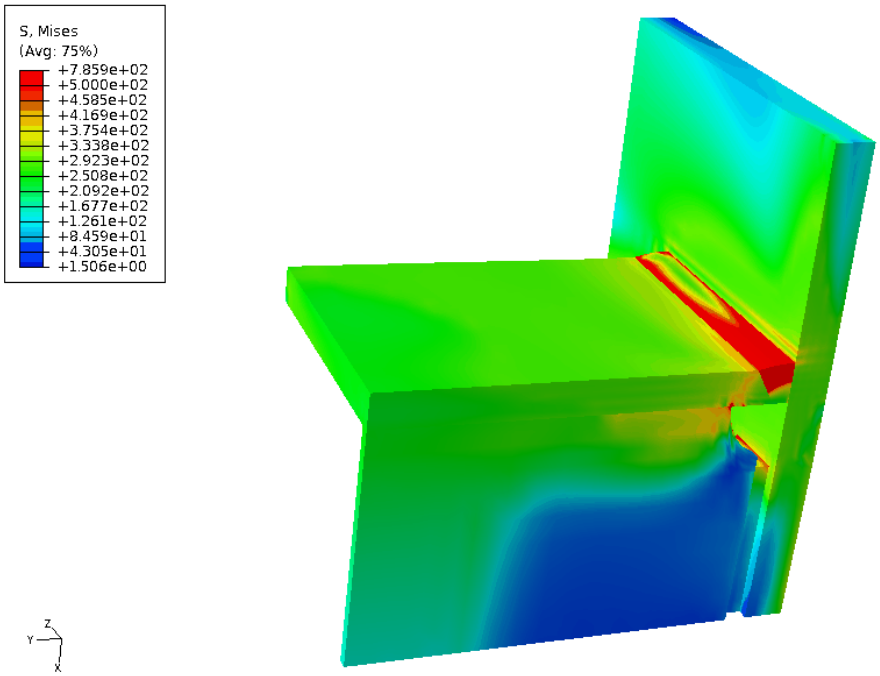

Figure 4.50 Von Mises stress contour – SP2 sub-local model

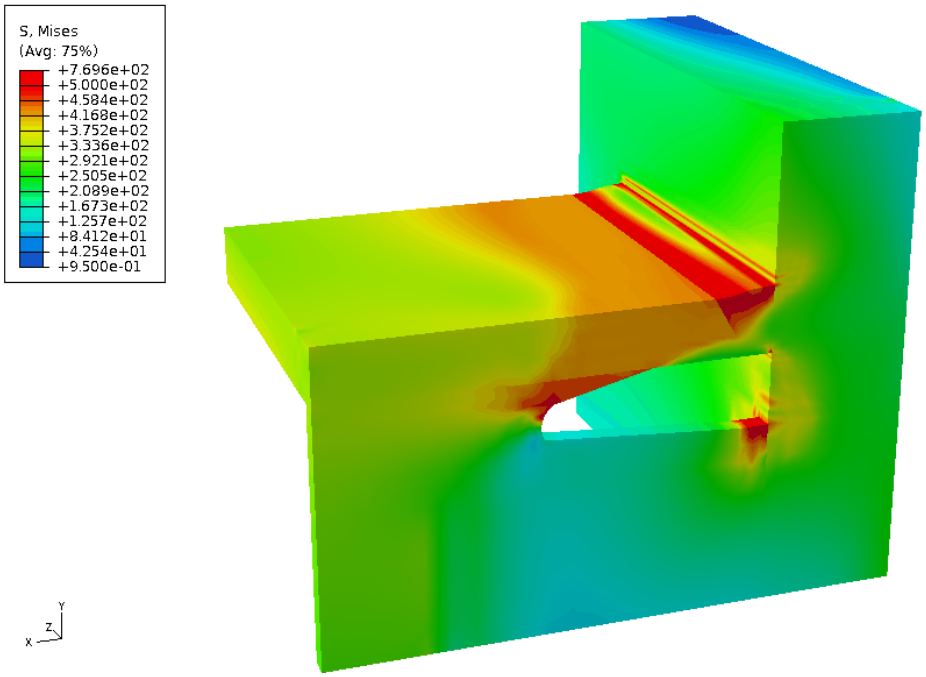

Figure 4.51 Von Mises stress contour – T2 sub-local model

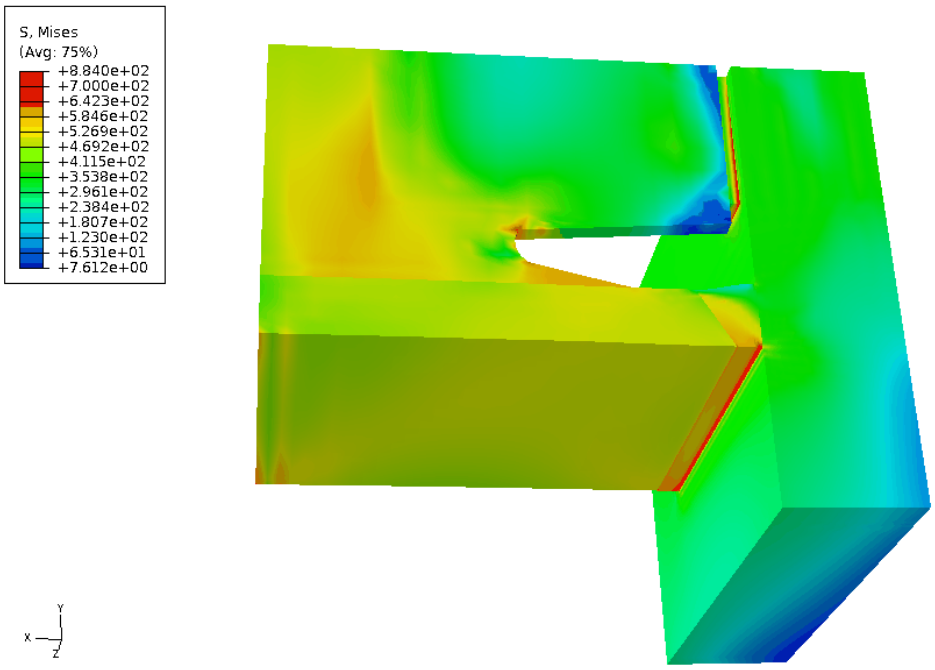

Figure 4.52 Von Mises stress contour – T3 sub-local model

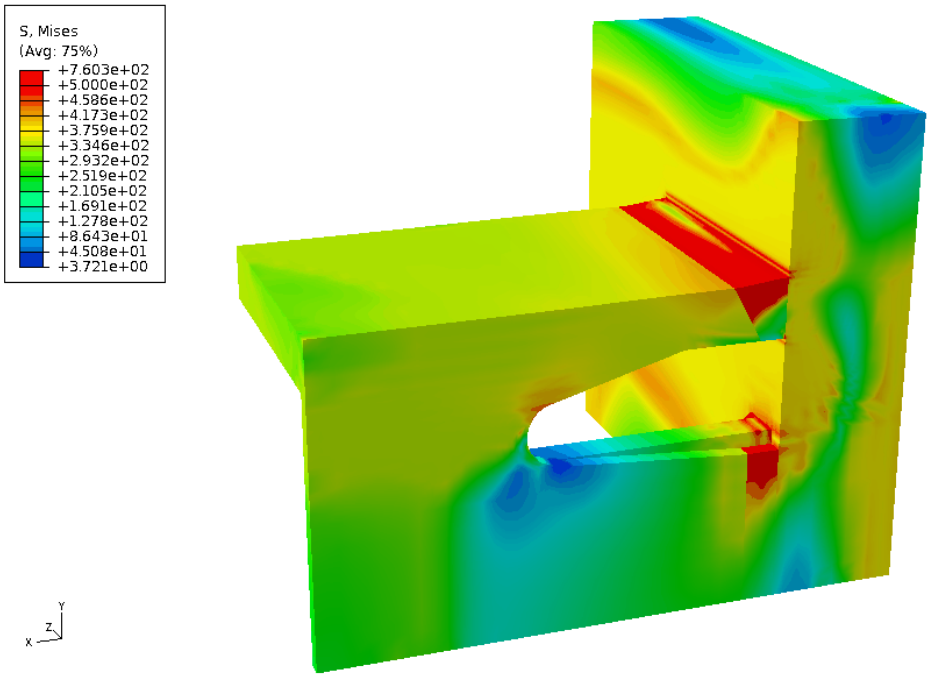

Figure 4.53 Von Mises stress contour – CR1 sub-local model

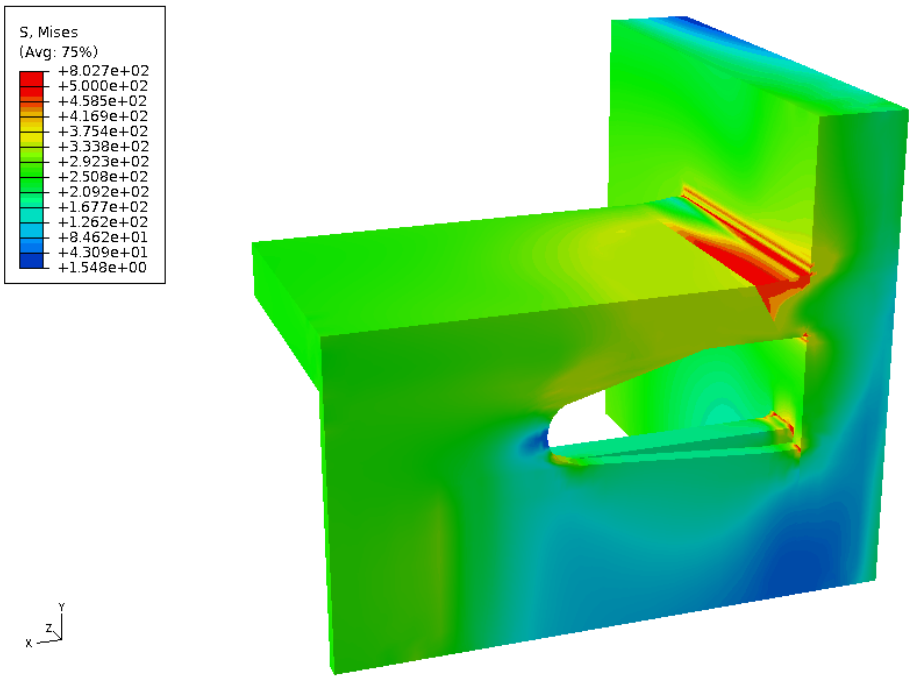

Figure 4.54 Von Mises stress contour – CR2 sub-local model

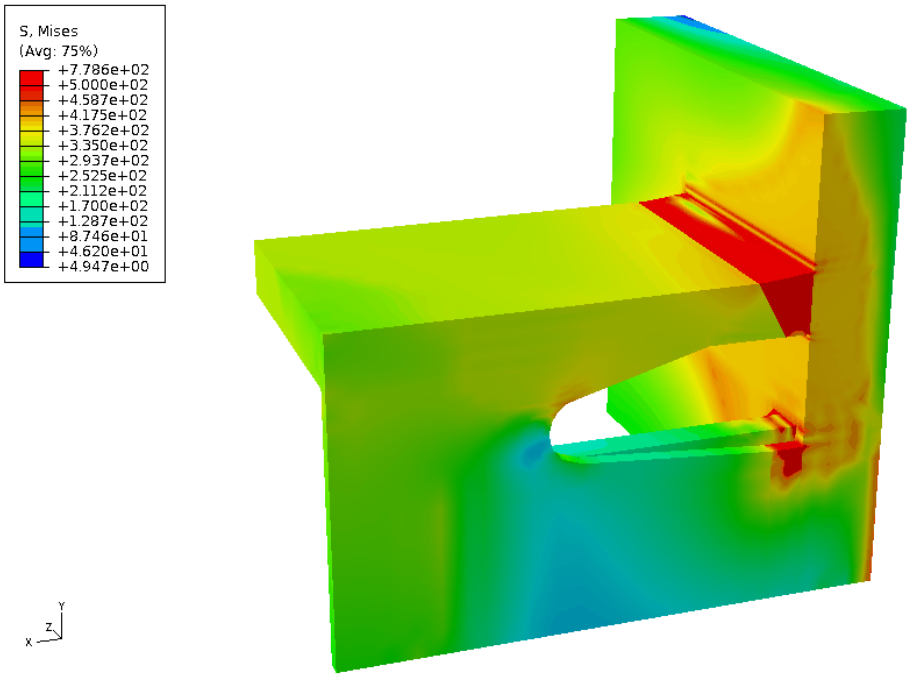

Figure 4.55 Von Mises stress contour – CR3 sub-local model

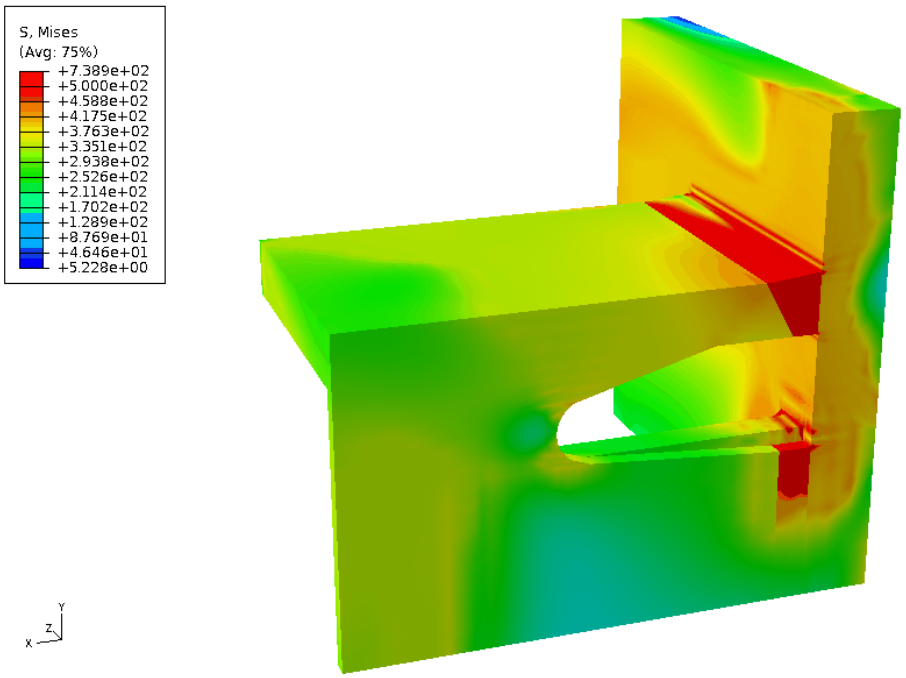

Figure 4.56 Von Mises stress contour – CR5 sub-local model

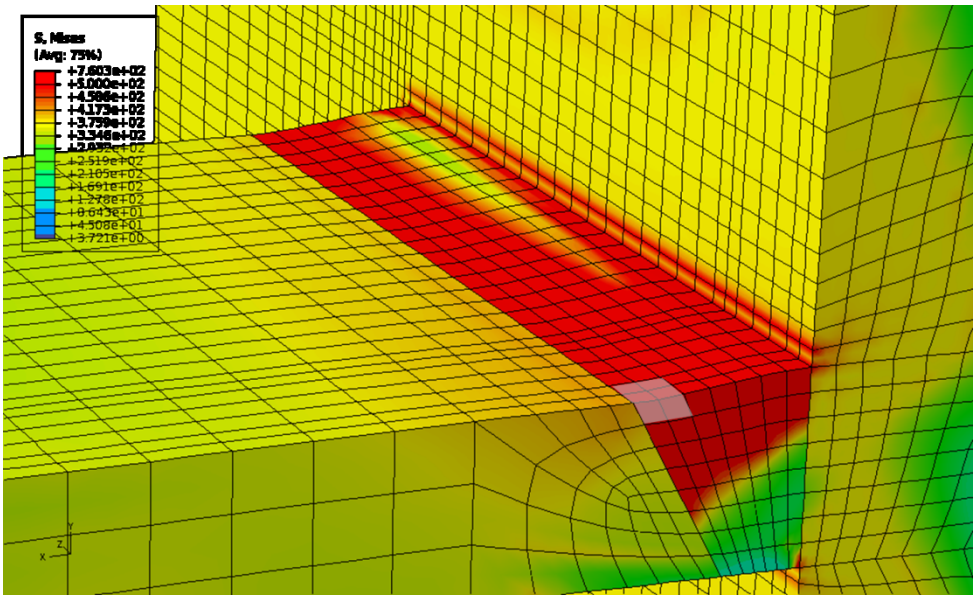

Figure 4.57 Four elements assumed as the candidates of crack initiation location

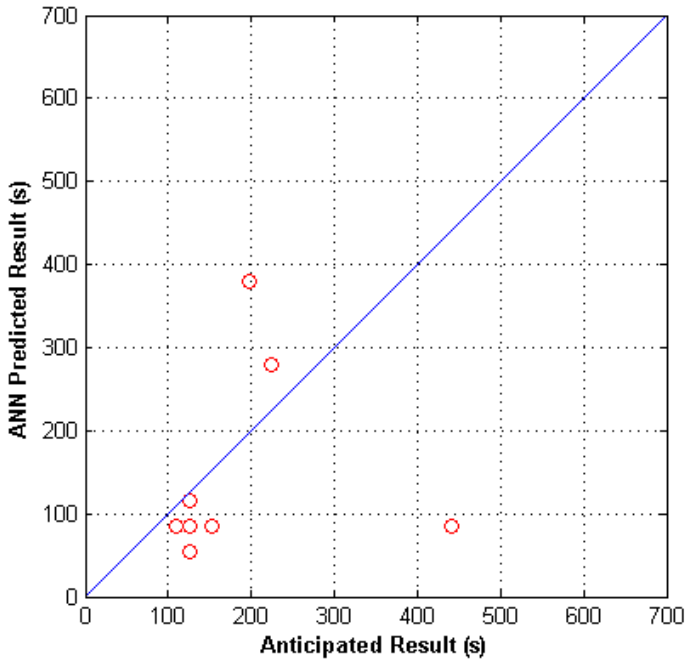

Figure 4.58 Competitive neural array predictions of fatigue crack initiation life of tested specimens

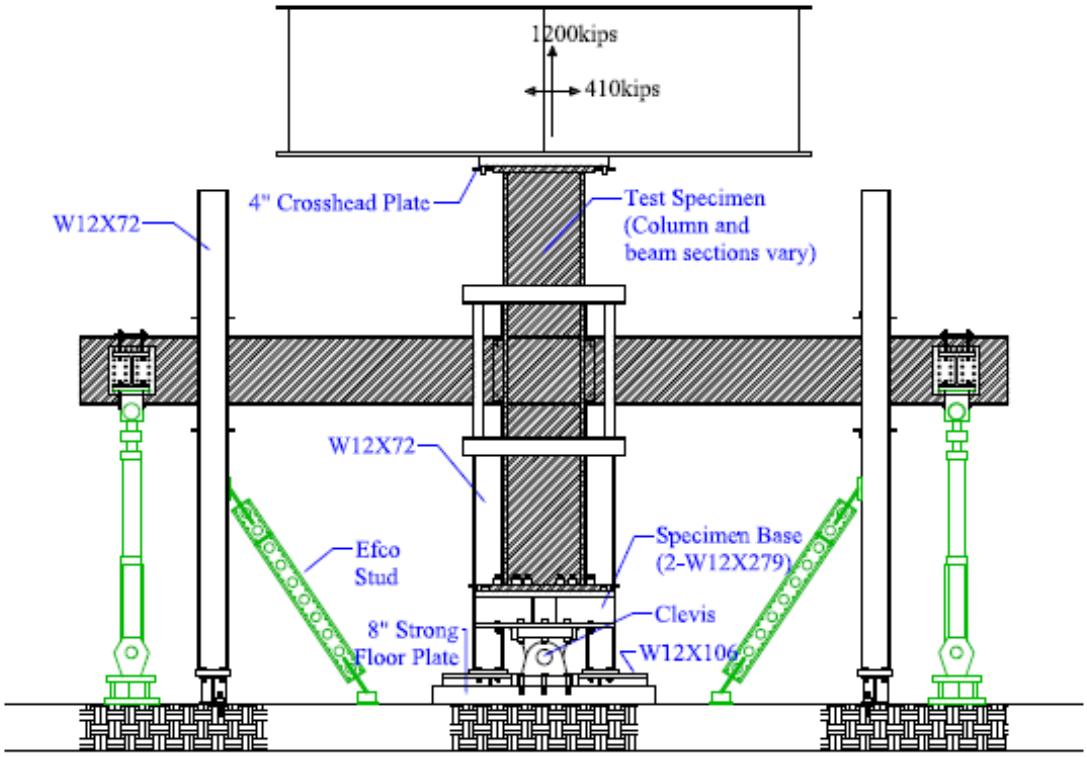

Figure 5.1 Test setup plan of newly designed specimens

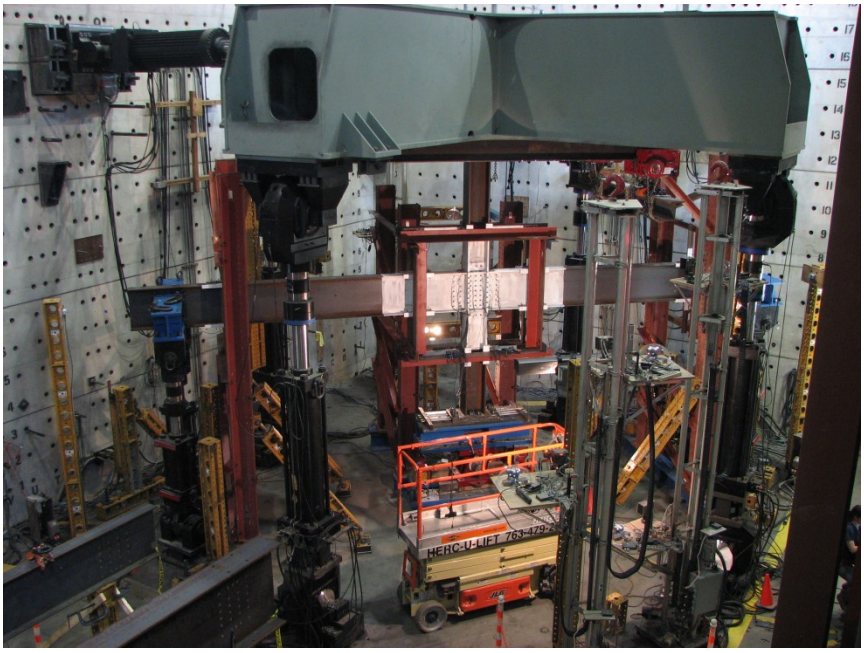

Figure 5.2 Test setup of Specimen 8 in the laboratory – global view

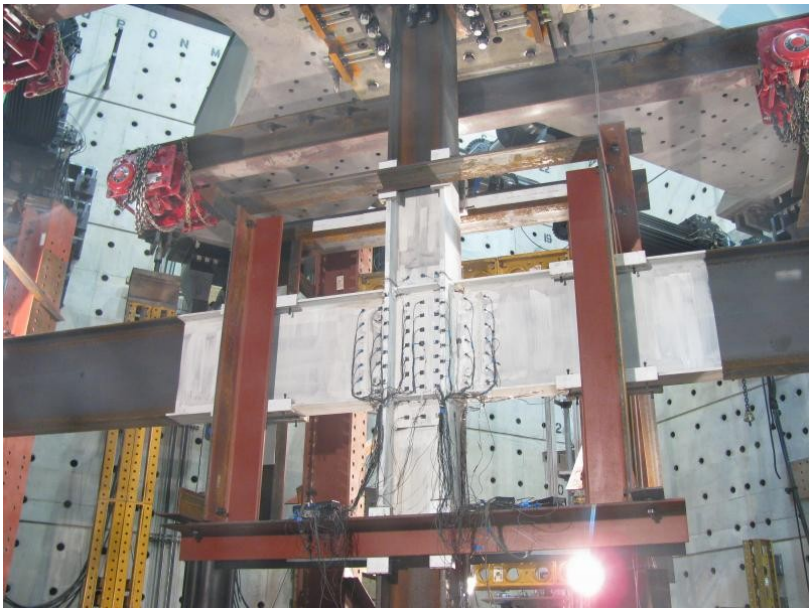

Figure 5.3 Test setup of Specimen 8 in the laboratory – magnified view

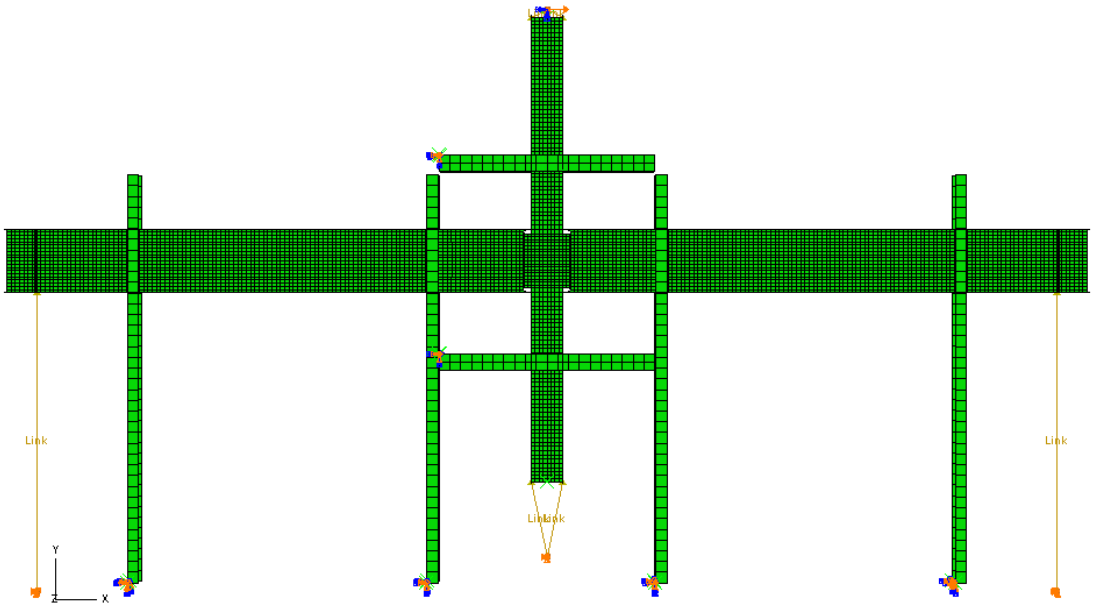

(a) with braces

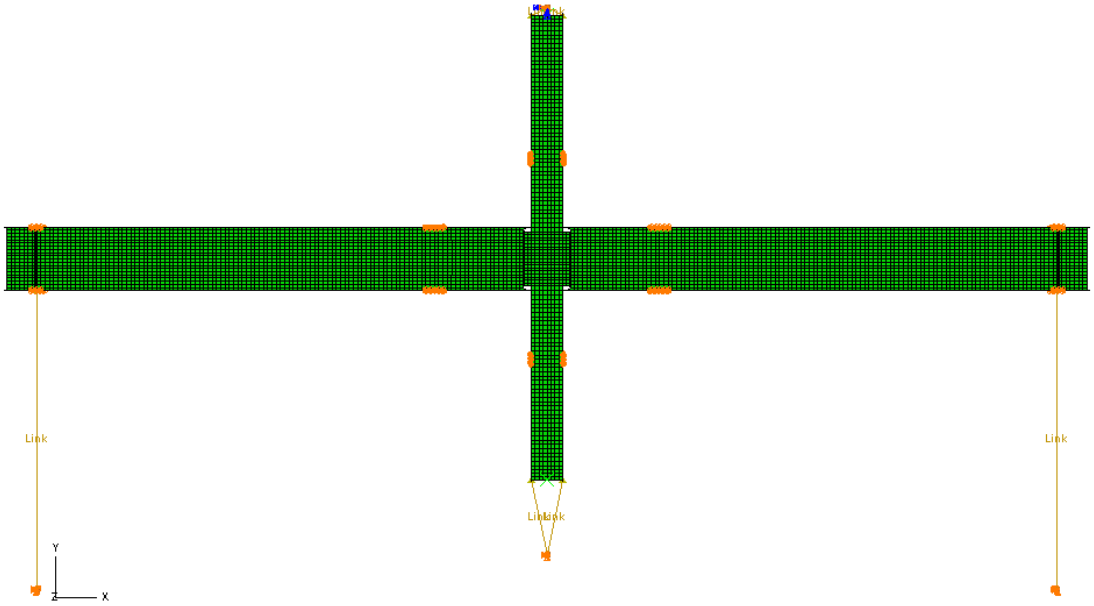

(b) without braces

Figure 5.4 Global finite element models of Specimens 8 ~ 10

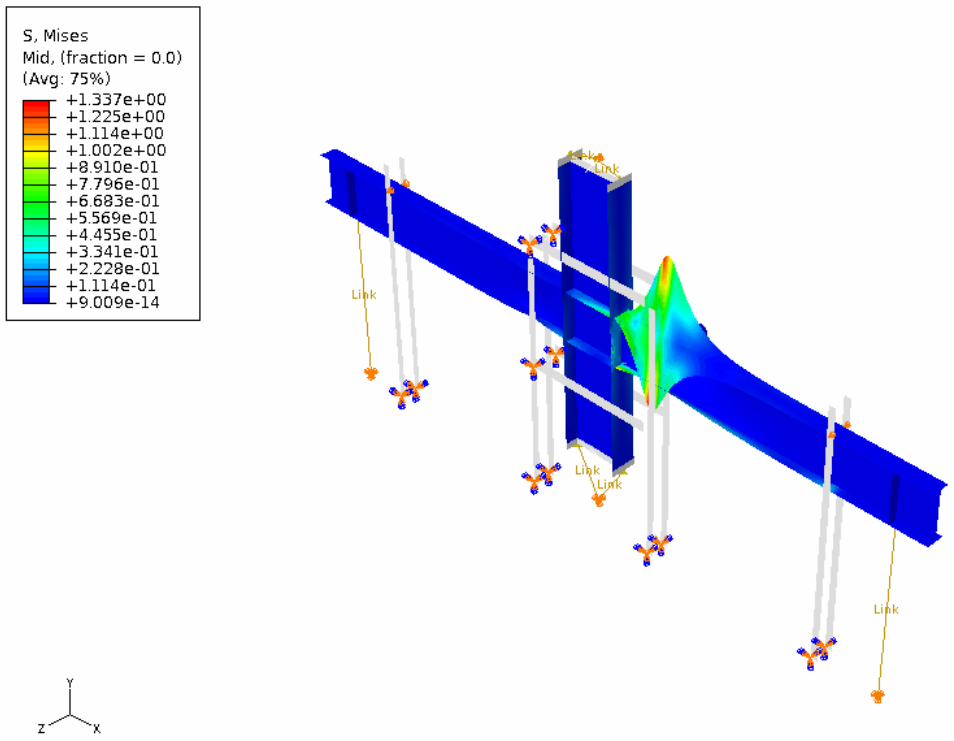

Figure 5.5 Shape of first buckling mode of Specimen 1 – positive sense

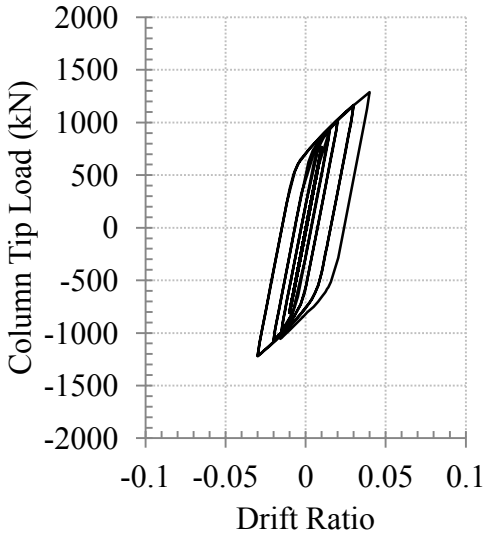

(a) with braces, with axial load

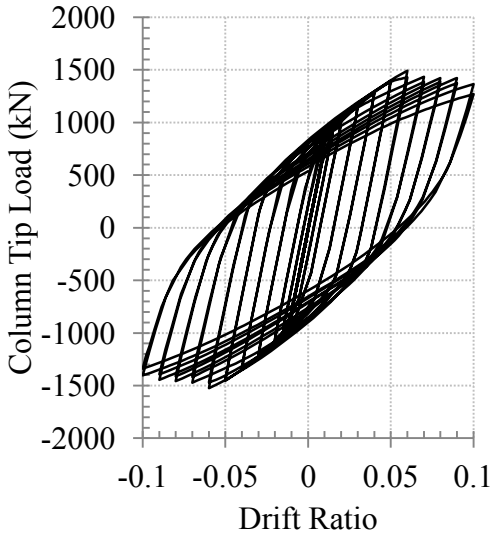

(b) without braces, with axial load

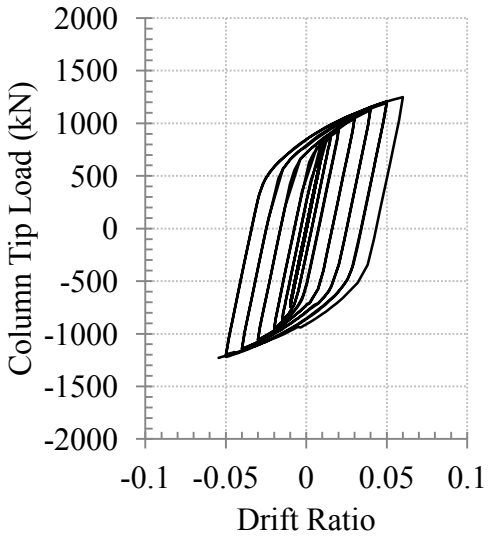

(c) with braces, without axial load

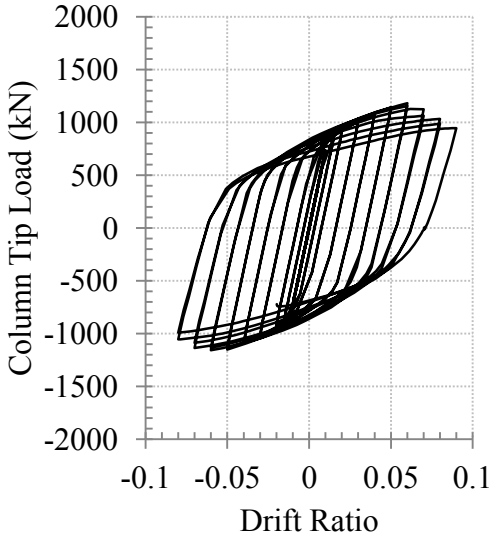

(d) without braces, without axial load

Figure 5.6 Load – drift ratio hysteresis loop of Specimen 1

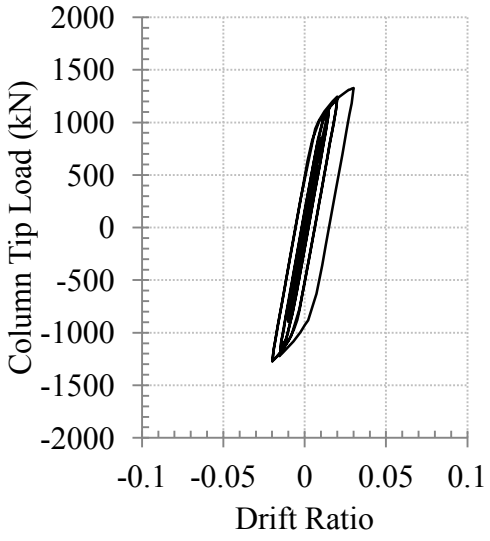

(a) with braces, with axial load

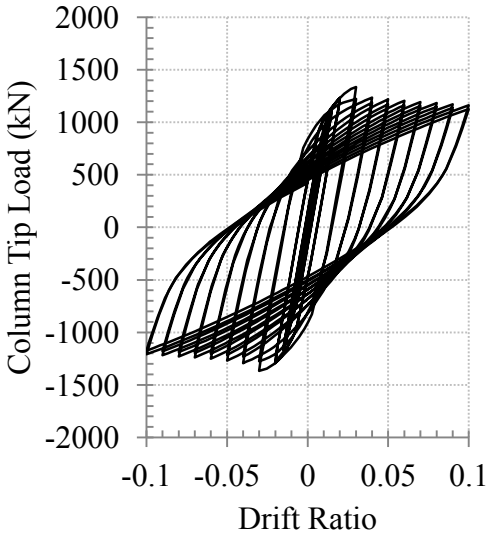

(b) without braces, with axial load

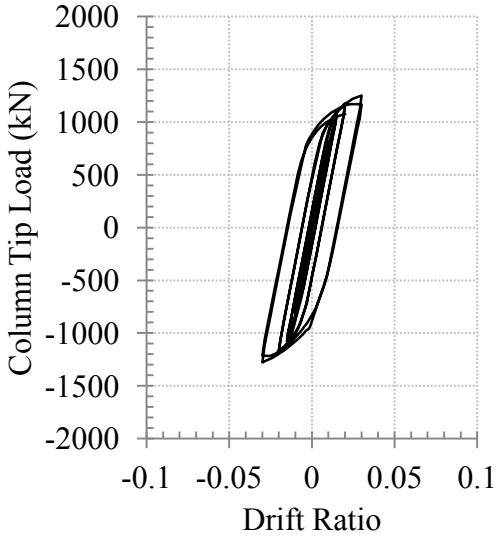

(c) with braces, without axial load

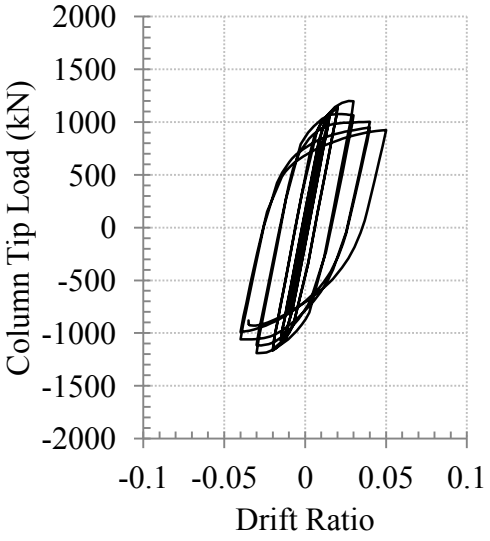

(d) without braces, without axial load

Figure 5.7 Load – drift ratio hysteresis loop of Specimen 2

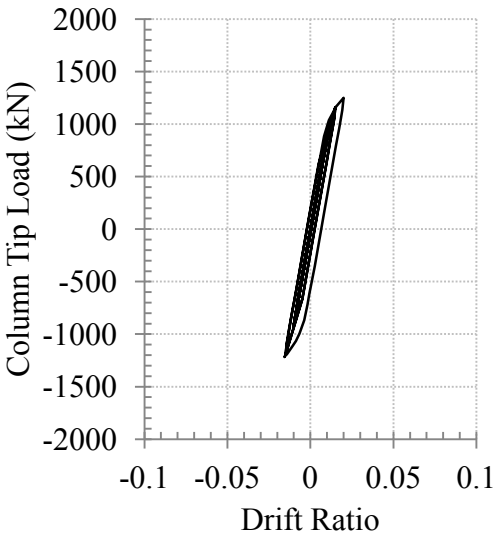

(a) with braces, with axial load

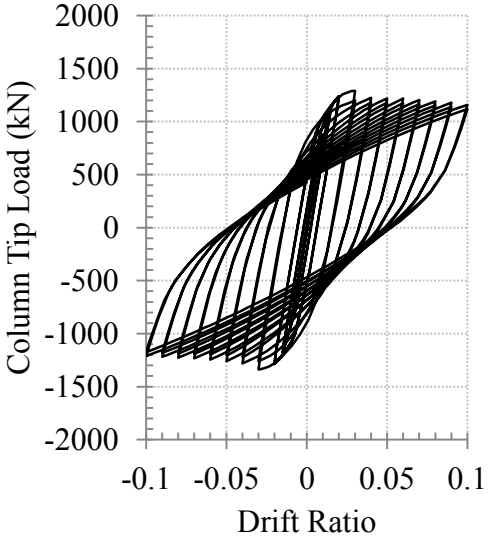

(b) without braces, with axial load

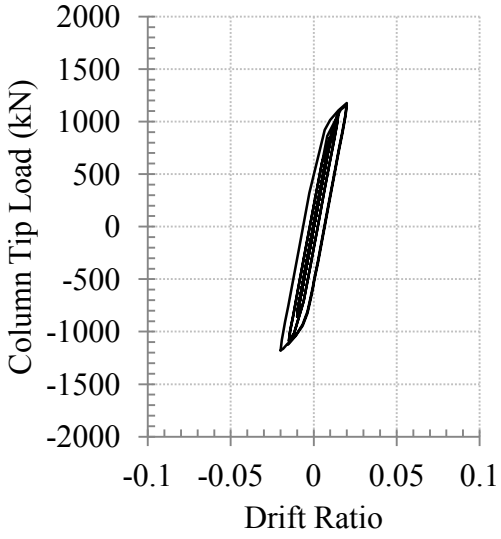

(c) with braces, without axial load

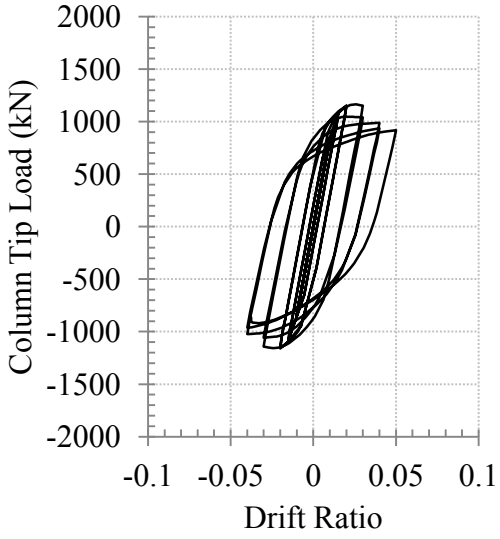

(d) without braces, without axial load

Figure 5.8 Load – drift ratio hysteresis loop of Specimen 3

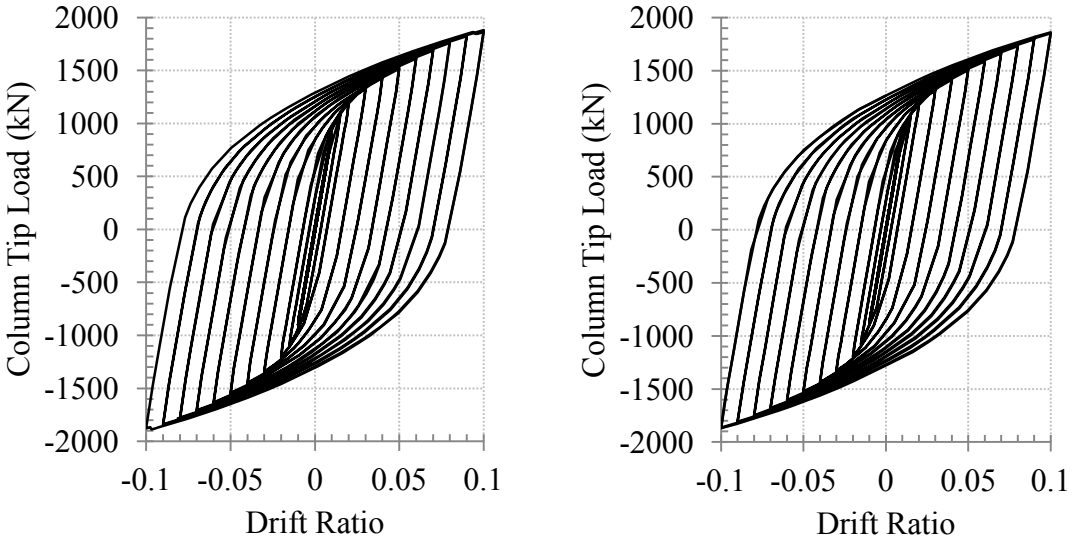

(a) with braces (b) without braces

Figure 5.9 Load – drift ratio hysteresis loop of Specimen 4

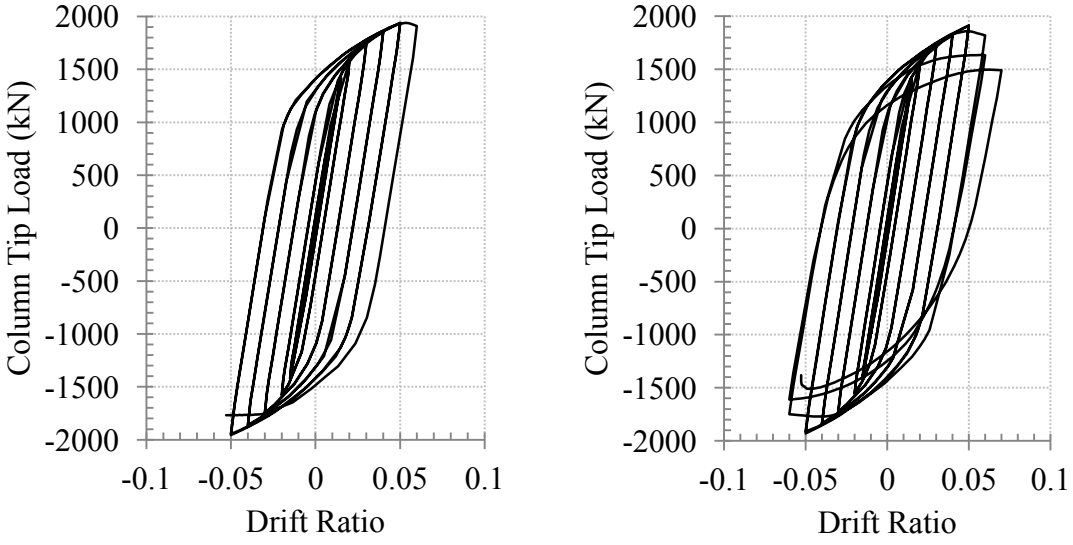

(a) with braces (b) without braces

Figure 5.10 Load – drift ratio hysteresis loop of Specimen 5

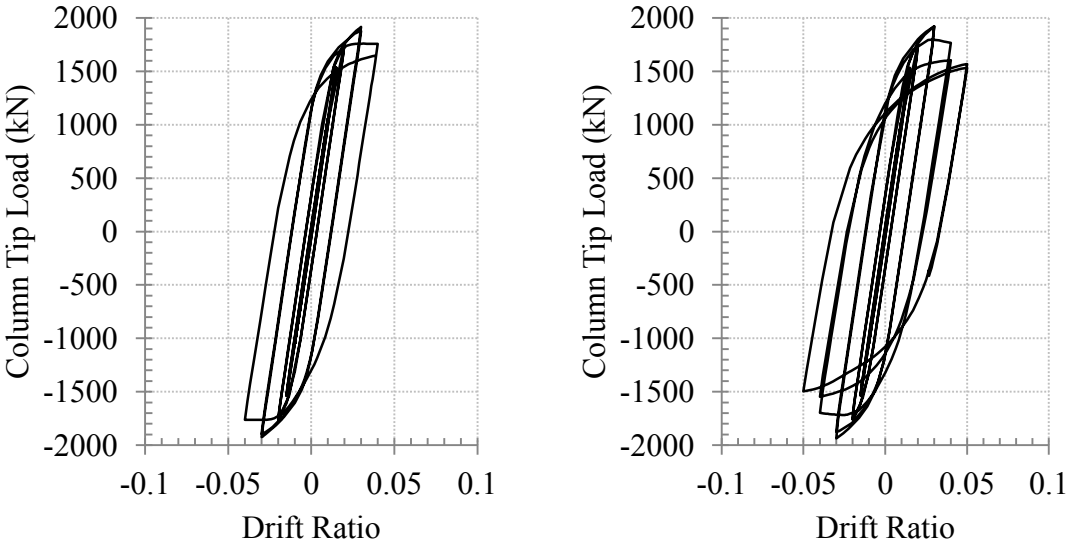

(a) with braces (b) without braces

Figure 5.11 Load – drift ratio hysteresis loop of Specimen 6

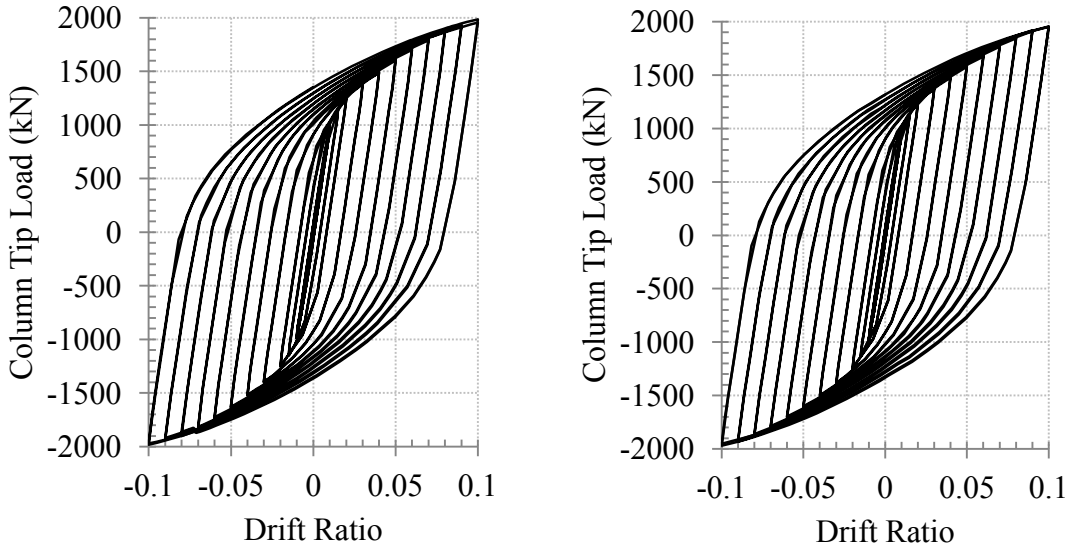

(a) with braces (b) without braces

Figure 5.12 Load – drift ratio hysteresis loop of Specimen 7

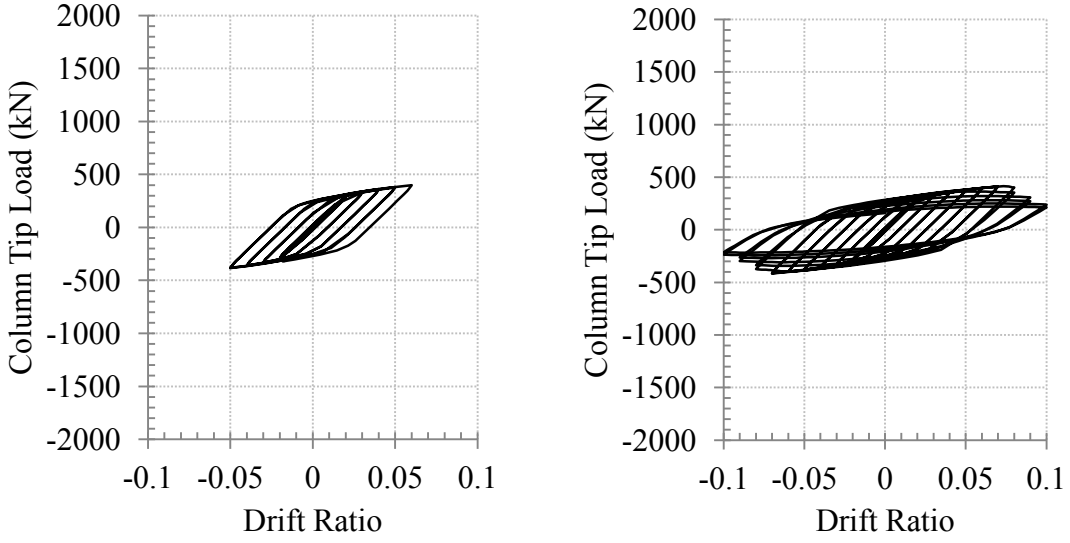

(a) with braces (b) without braces

Figure 5.13 Load – drift ratio hysteresis loop of Specimen 8

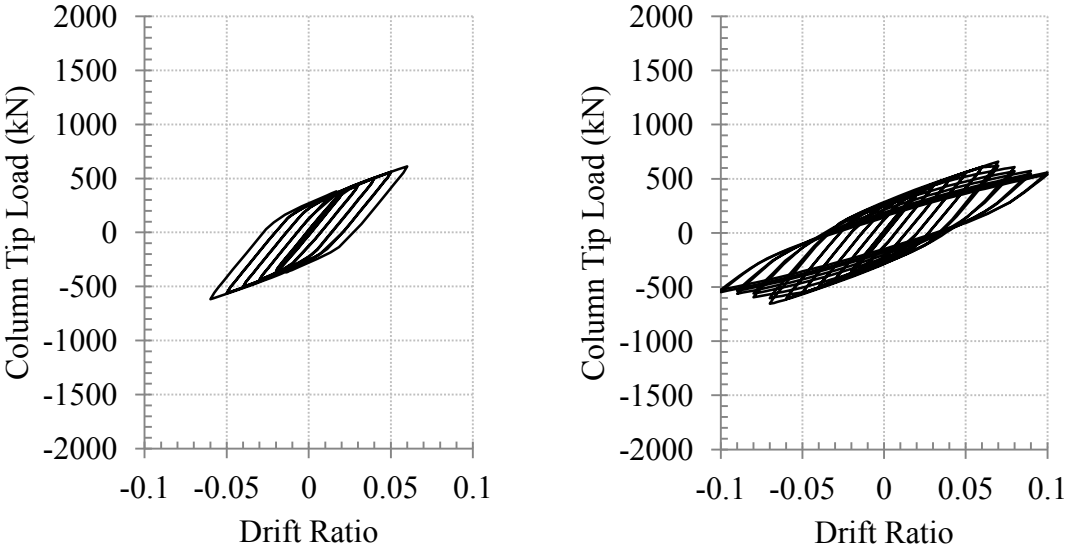

(a) with braces (b) without braces

Figure 5.14 Load – drift ratio hysteresis loop of Specimen 9

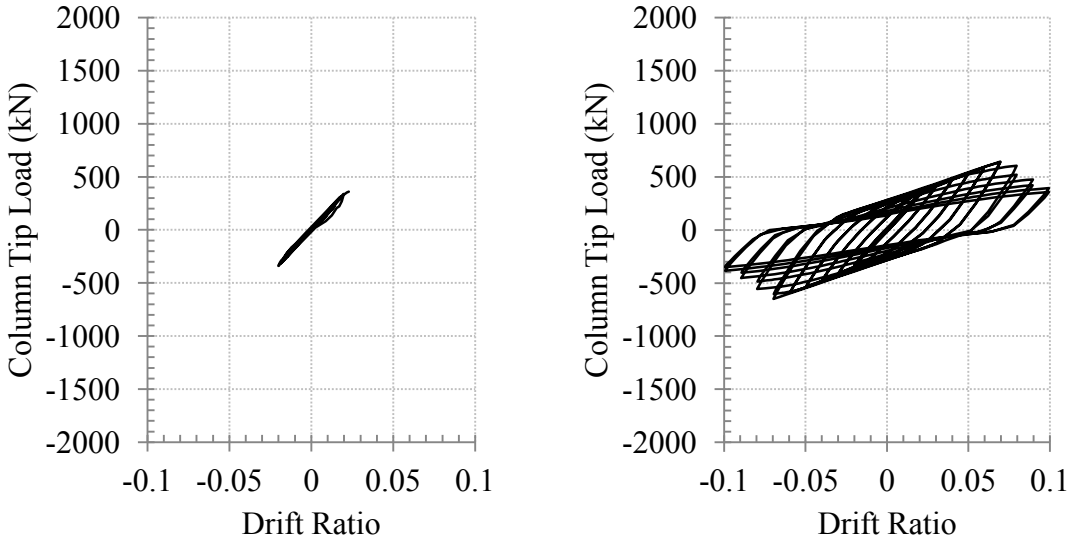

(a) with braces (b) without braces

Figure 5.15 Load – drift ratio hysteresis loop of Specimen 10

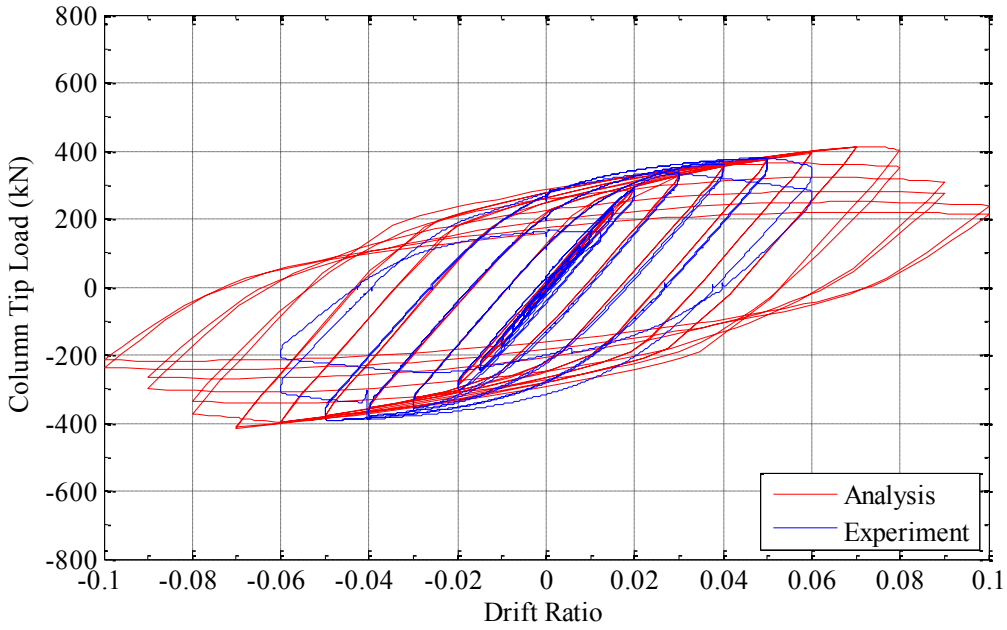

Figure 5.16 Comparison of analytical and experimental results of Specimen 8

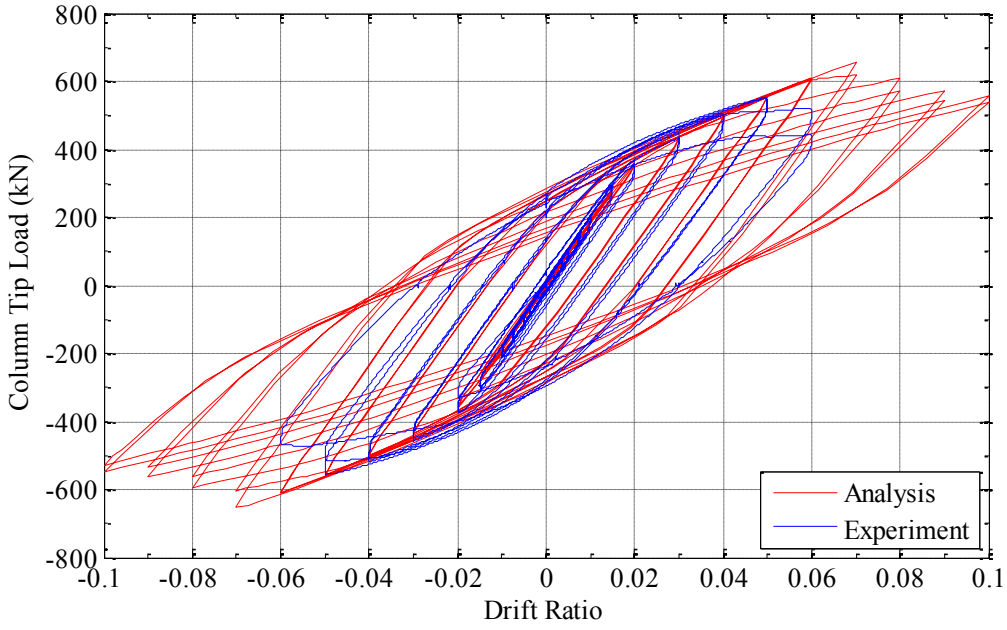

Figure 5.17 Comparison of analytical and experimental results of Specimen 9

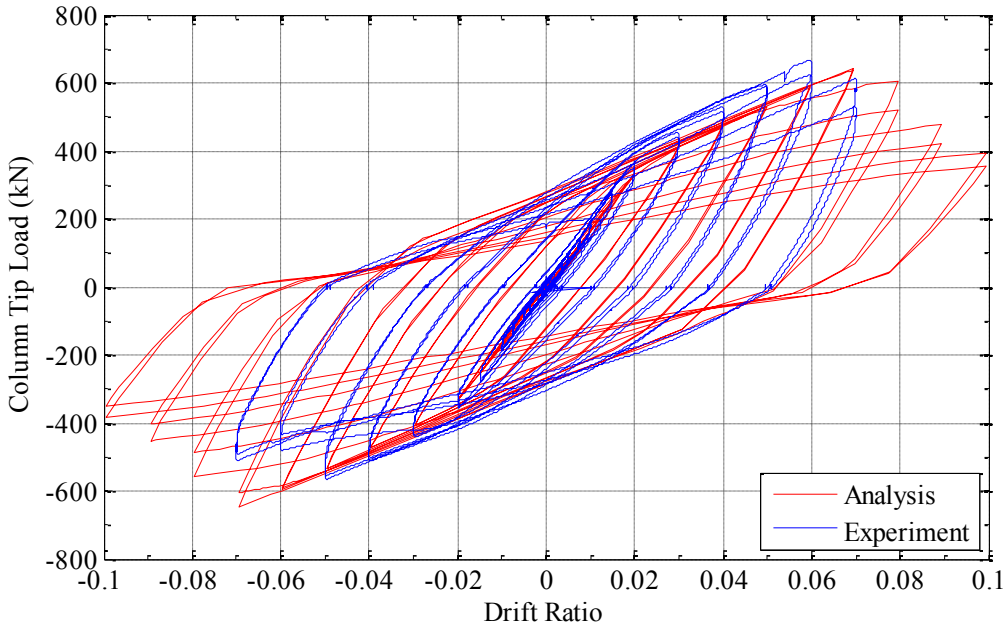

Figure 5.18 Comparison of analytical and experimental results of Specimen 10

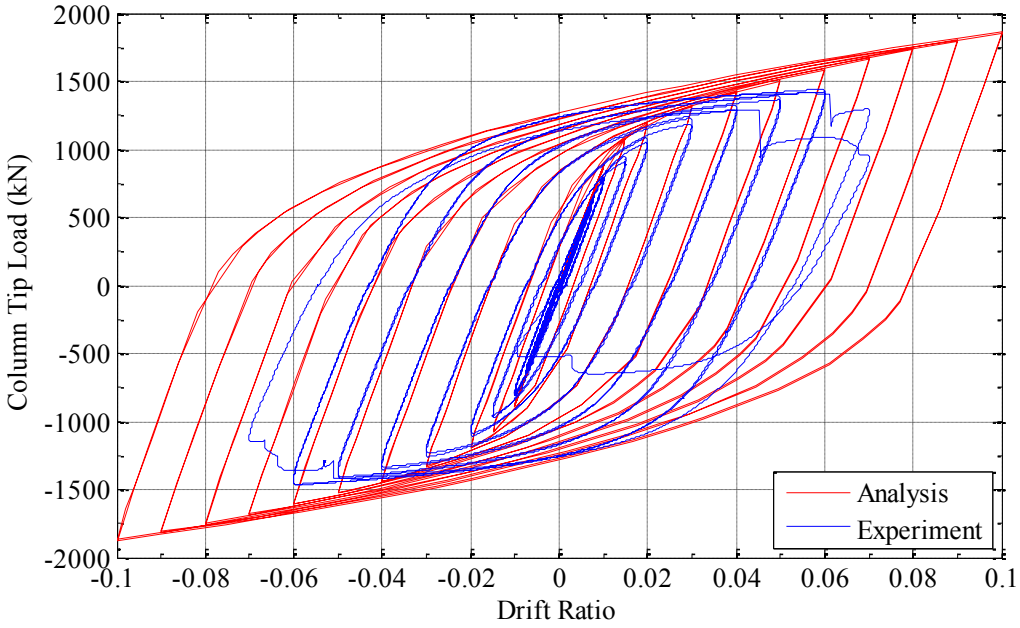

Figure 5.19 Comparison of analytical and experimental results of Specimen 4

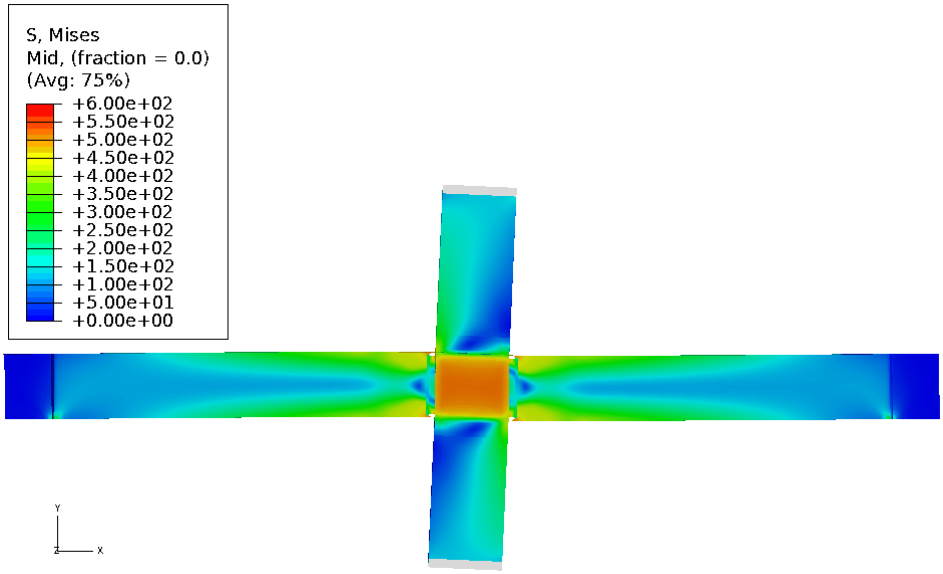

(a) Global view

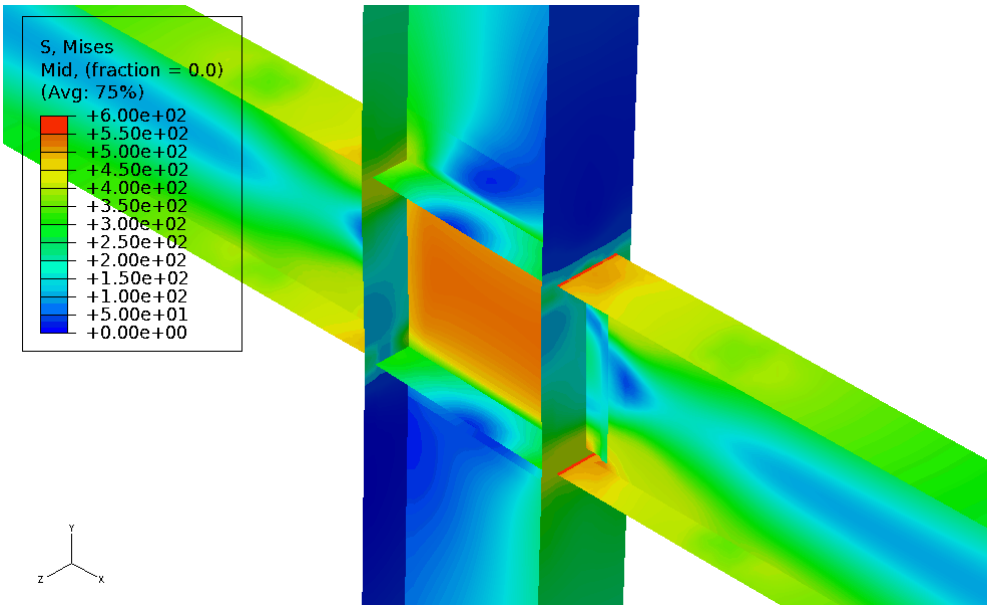

(b) Magnified view

Figure 5.20 Von Mises stress contour of Specimen 1 at 4% drift ratio

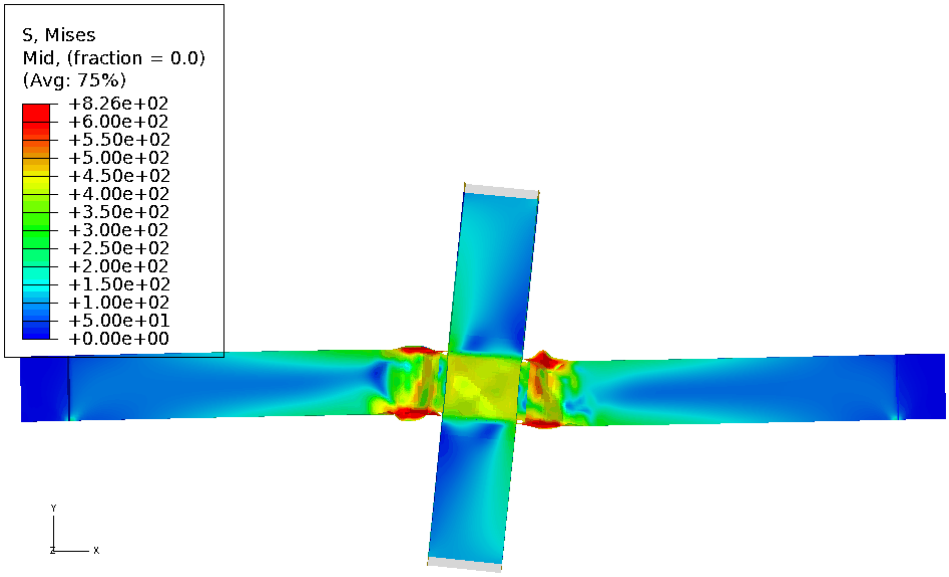

(a) Global view

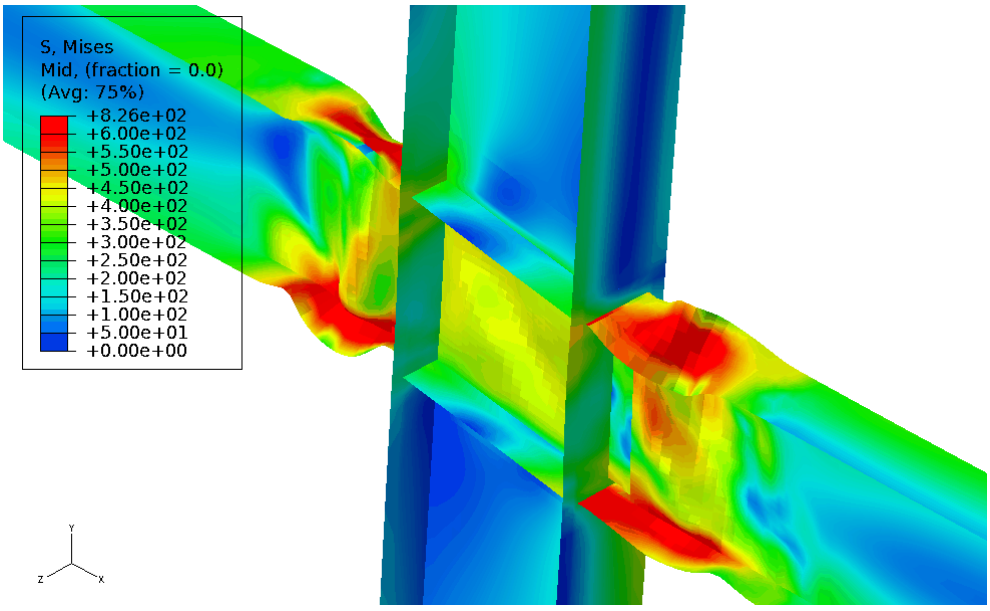

(b) Magnified view

Figure 5.21 Von Mises stress contour of Specimen 1 at 10% drift ratio

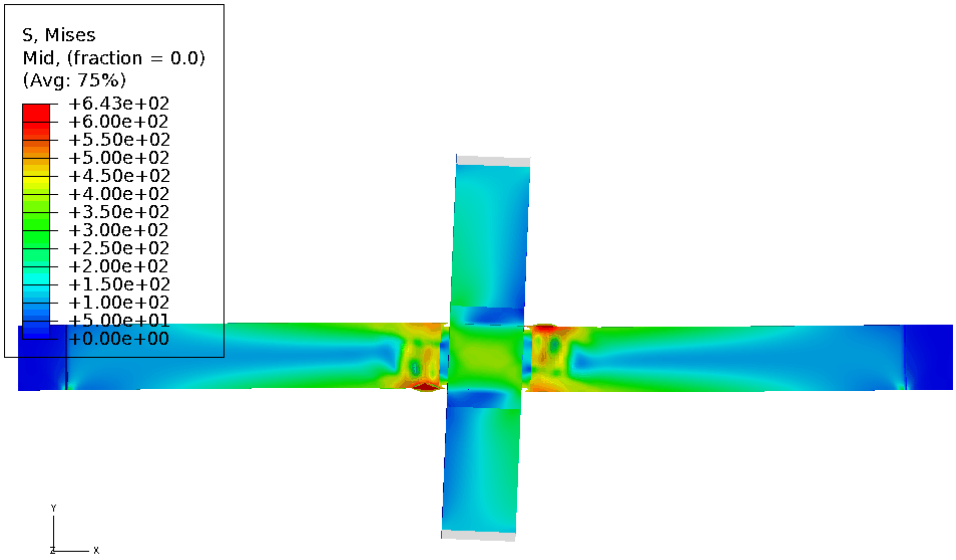

(a) Global view

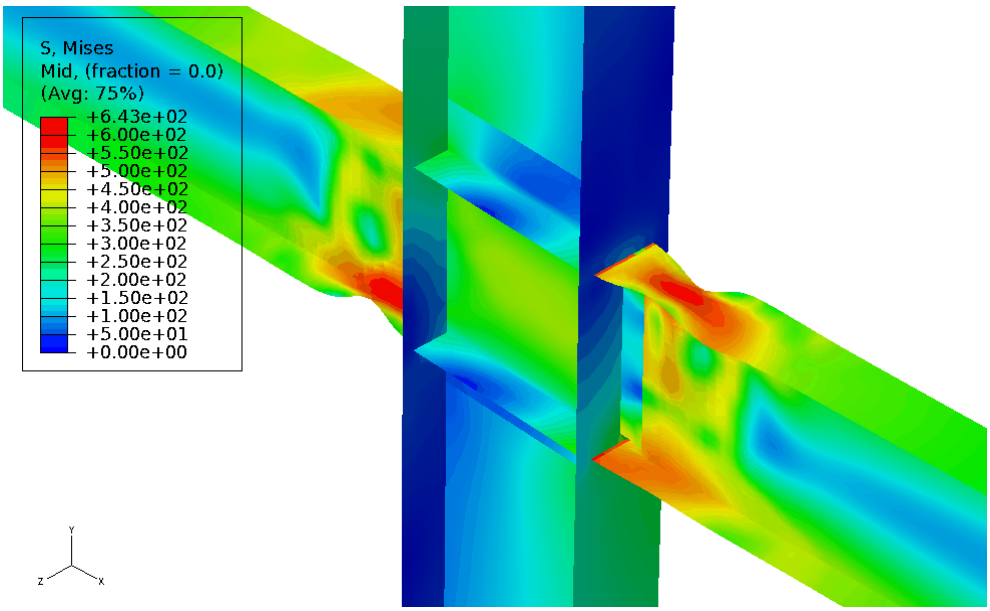

(b) Magnified view

Figure 5.22 Von Mises stress contour of Specimen 2 at 4% drift ratio

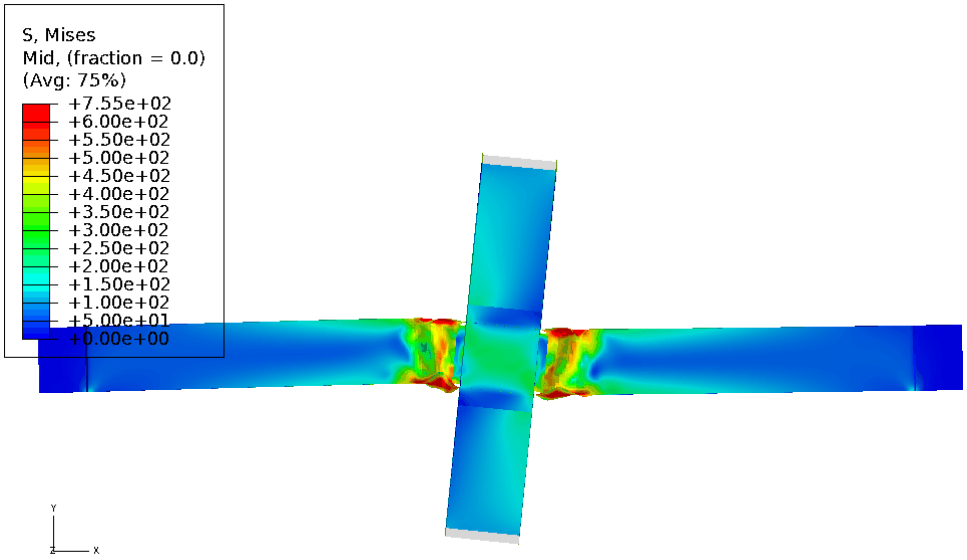

(a) Global view

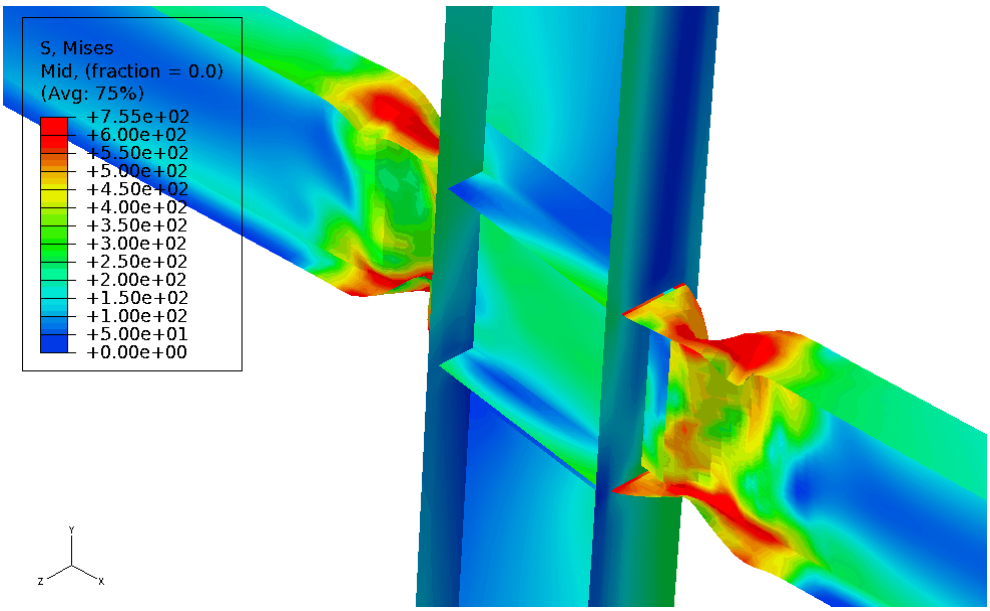

(b) Magnified view

Figure 5.23 Von Mises stress contour of Specimen 2 at 10% drift ratio

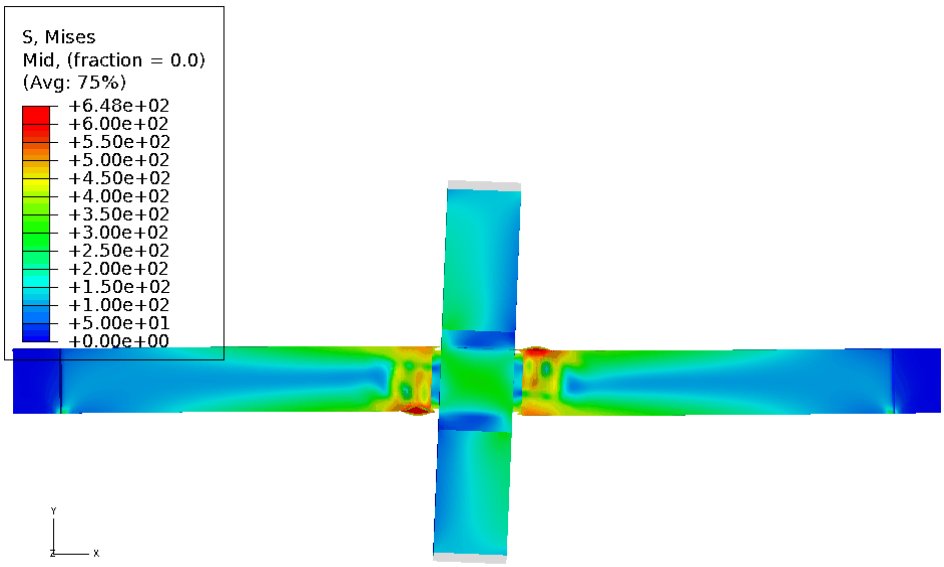

(a) Global view

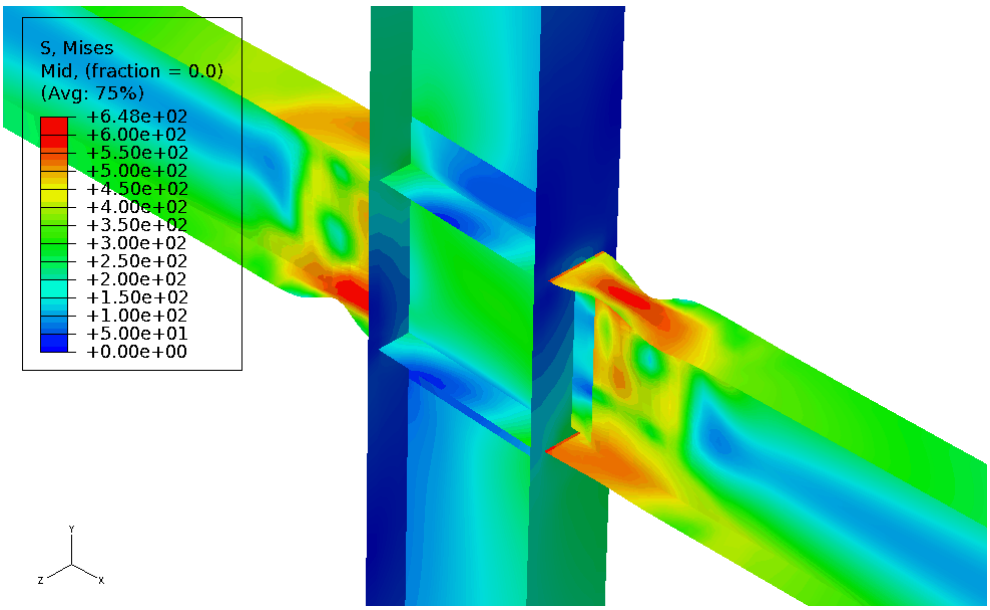

(b) Magnified view

Figure 5.24 Von Mises stress contour of Specimen 3 at 4% drift ratio

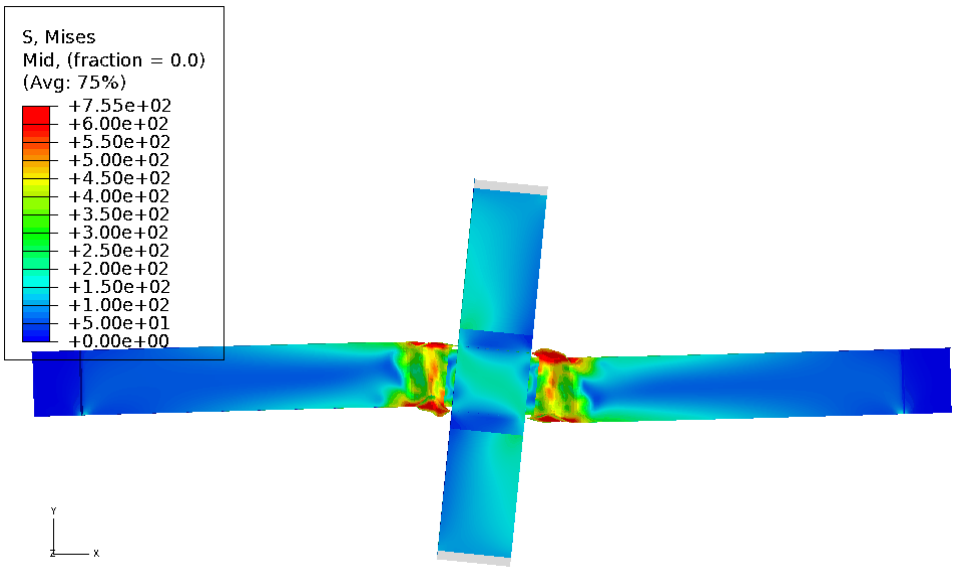

(a) Global view

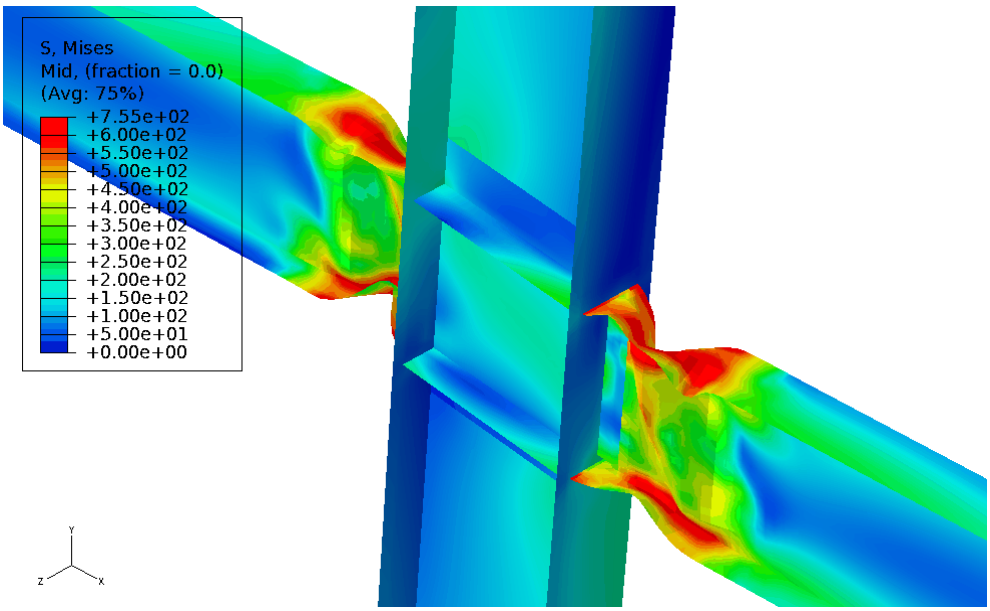

(b) Magnified view

Figure 5.25 Von Mises stress contour of Specimen 3 at 10% drift ratio

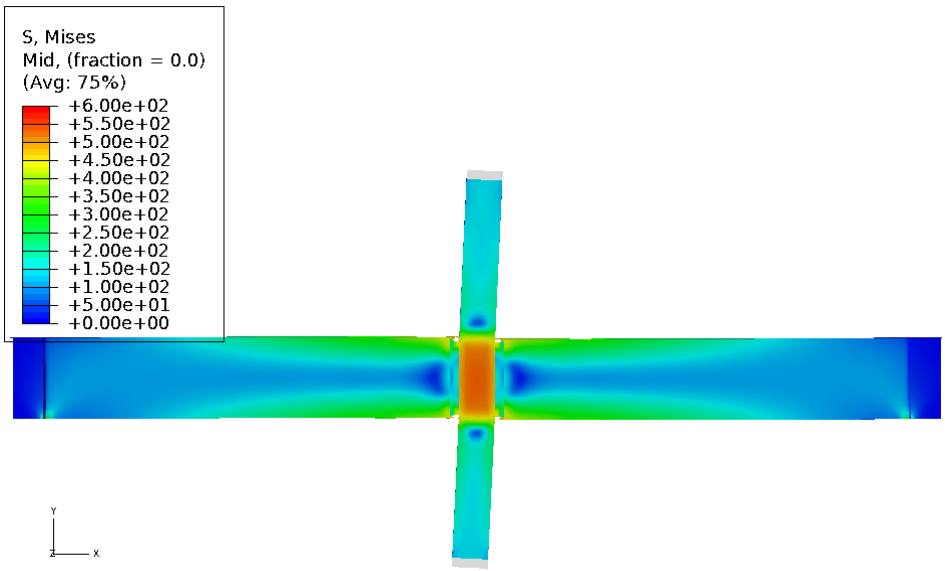

(a) Global view

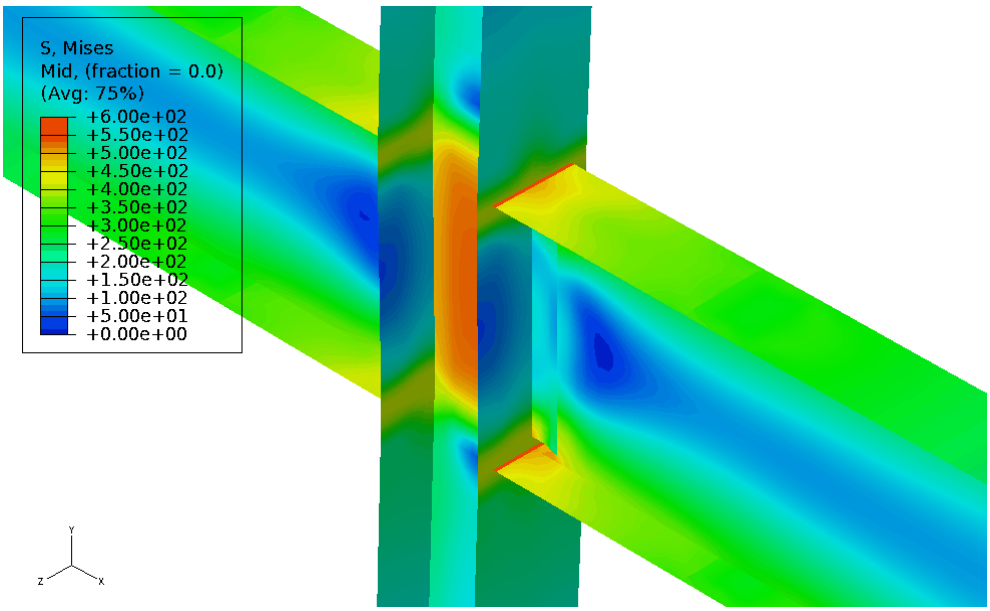

(b) Magnified view

Figure 5.26 Von Mises stress contour of Specimen 4 at 4% drift ratio

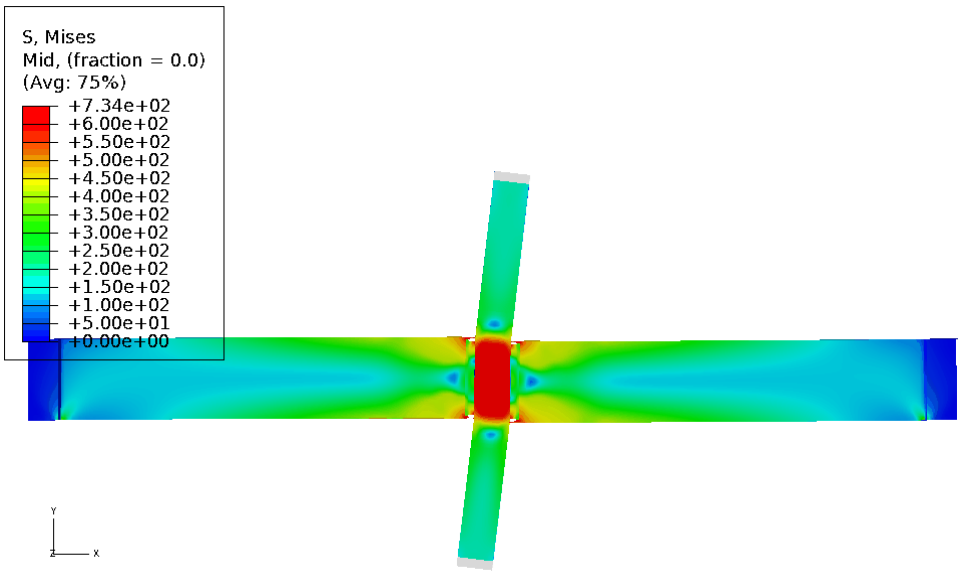

(a) Global view

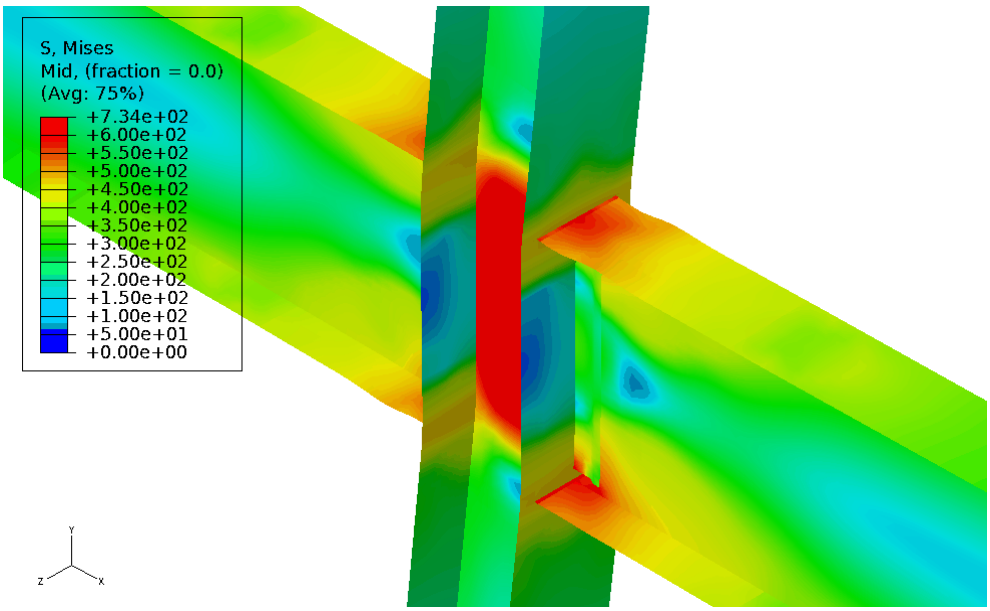

(b) Magnified view

Figure 5.27 Von Mises stress contour of Specimen 4 at 10% drift ratio

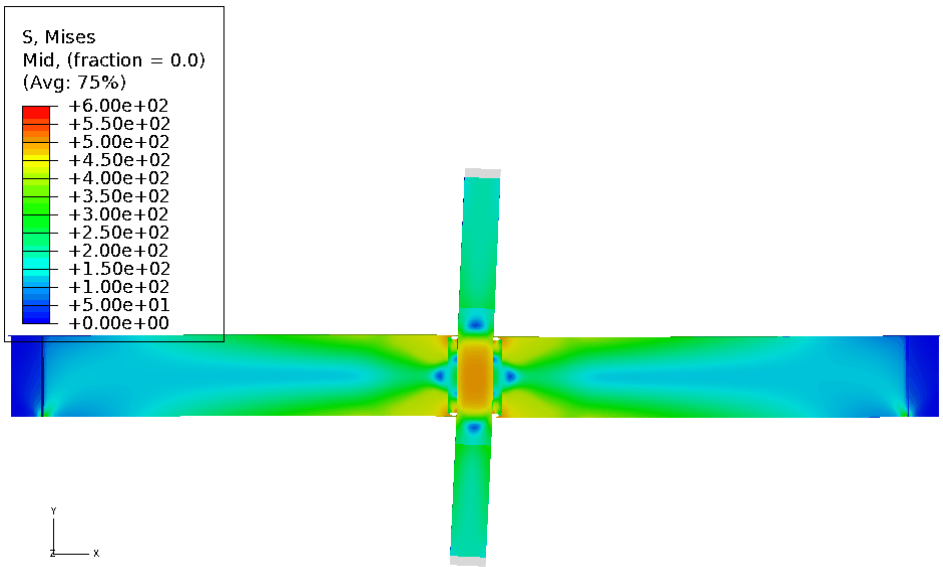

(a) Global view

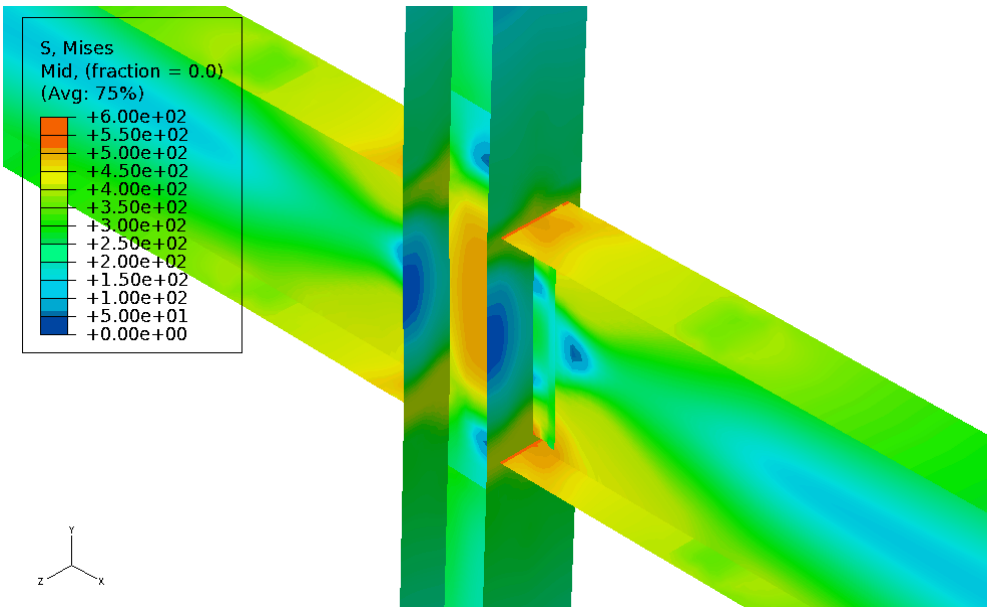

(b) Magnified view

Figure 5.28 Von Mises stress contour of Specimen 5 at 4% drift ratio

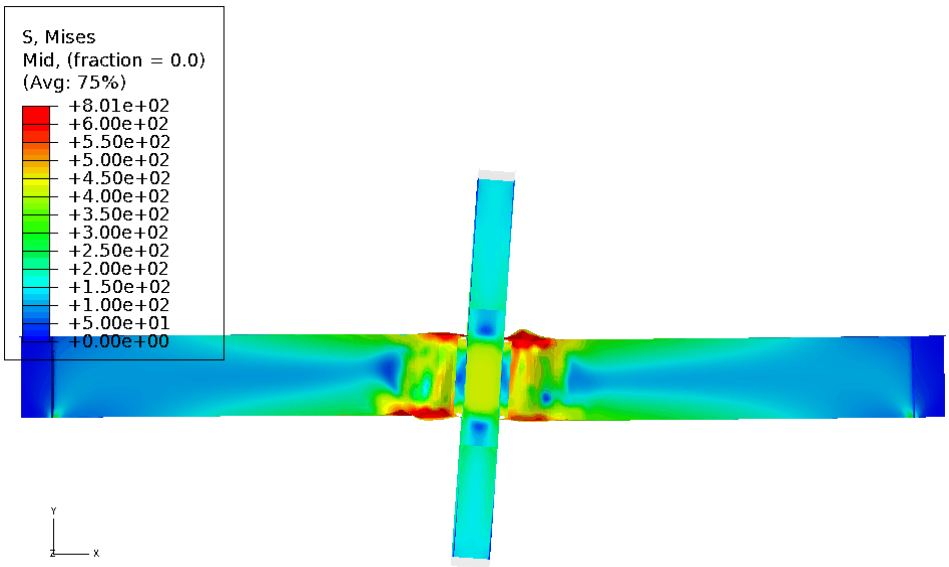

(a) Global view

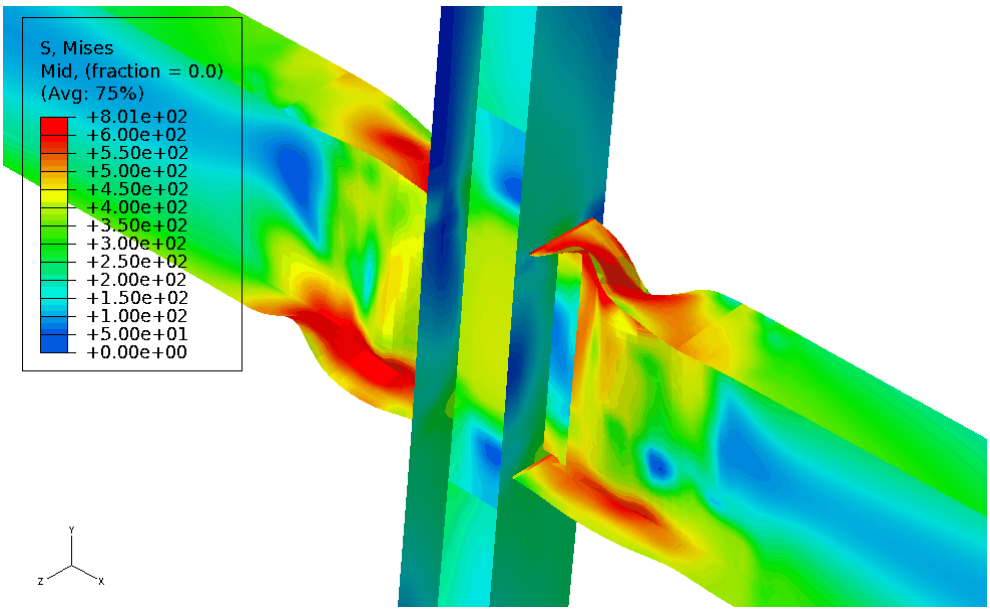

(b) Magnified view

Figure 5.29 Von Mises stress contour of Specimen 5 at 6% drift ratio

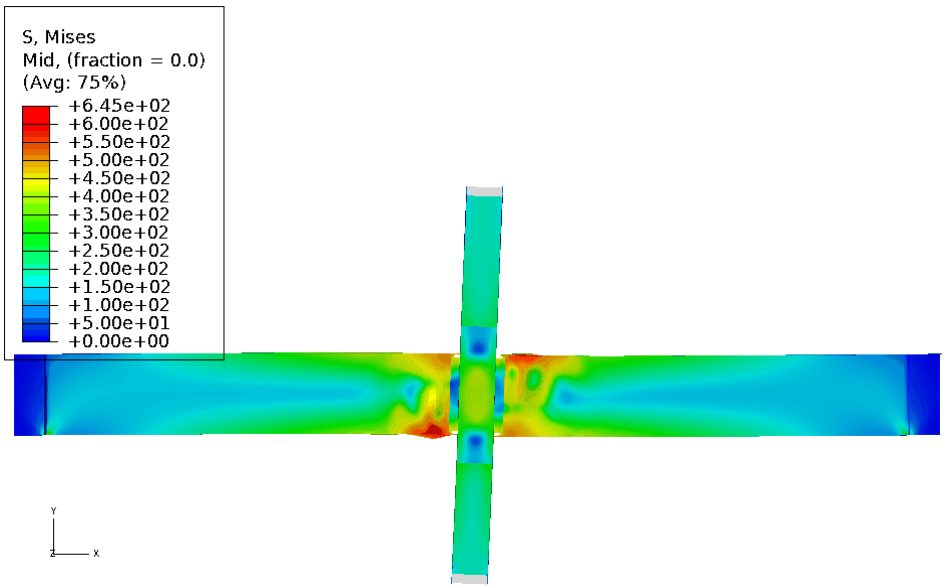

(a) Global view

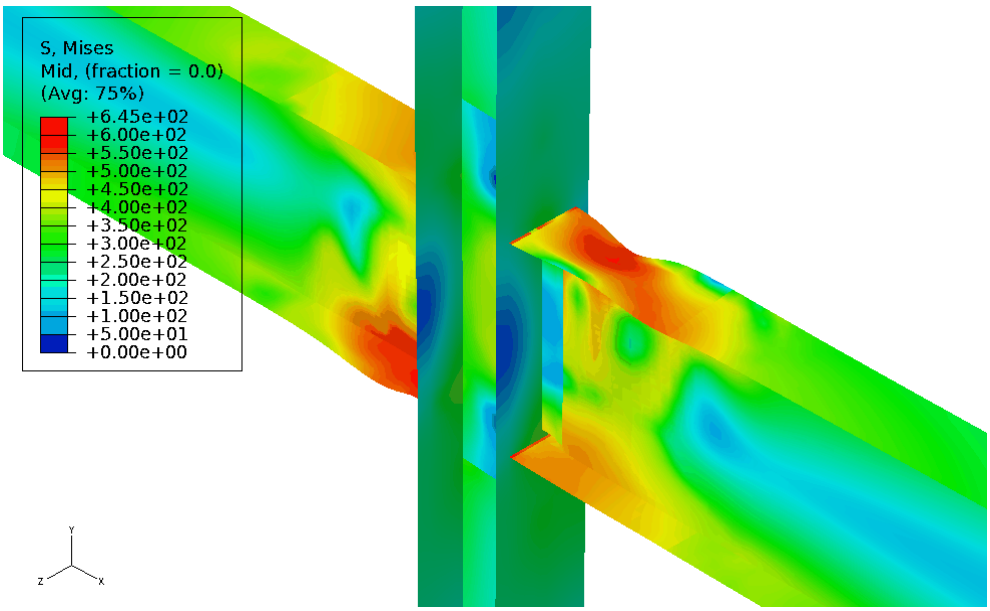

(b) Magnified view

Figure 5.30 Von Mises stress contour of Specimen 6 at 4% drift ratio

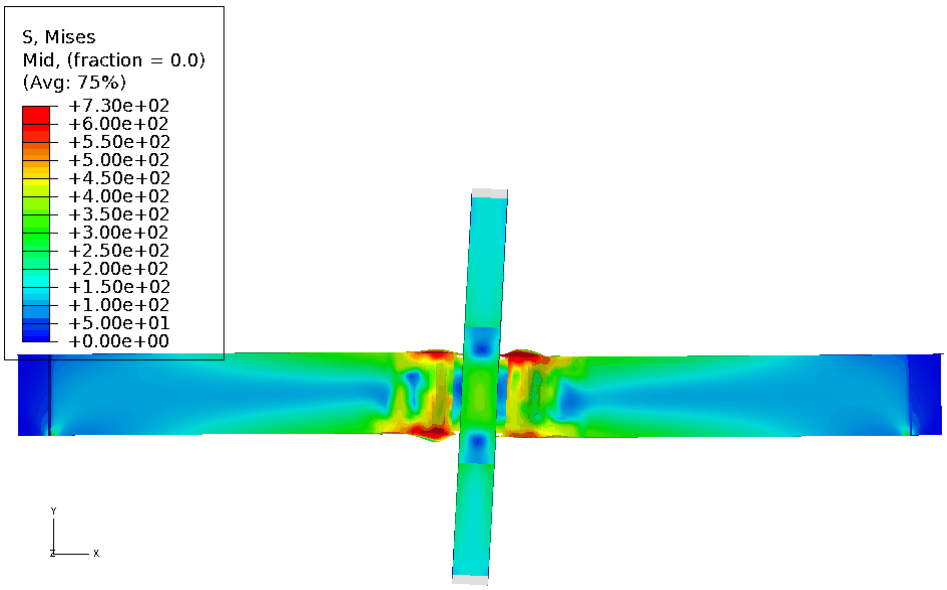

(a) Global view

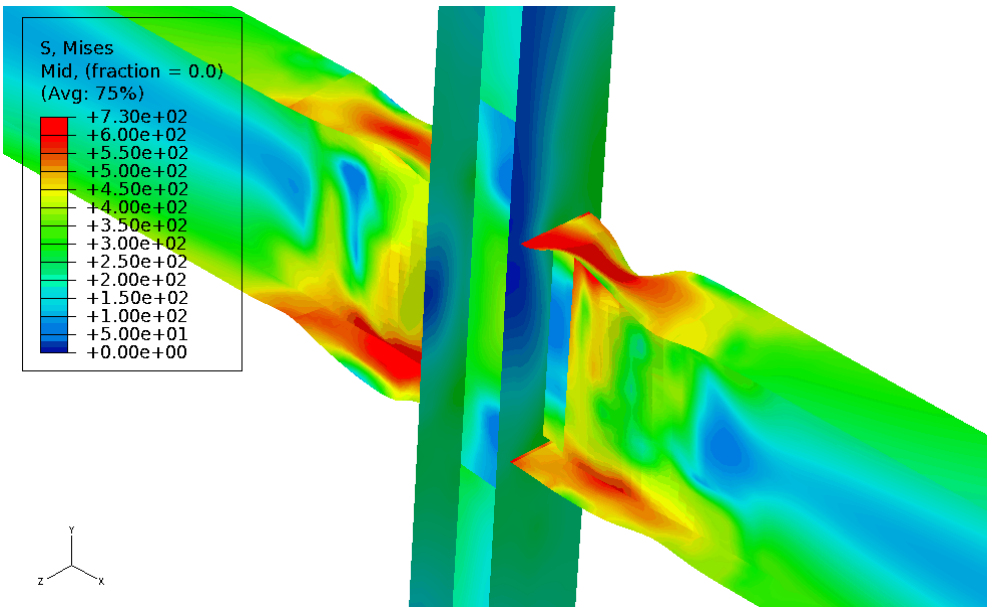

(b) Magnified view

Figure 5.31 Von Mises stress contour of Specimen 6 at 5% drift ratio

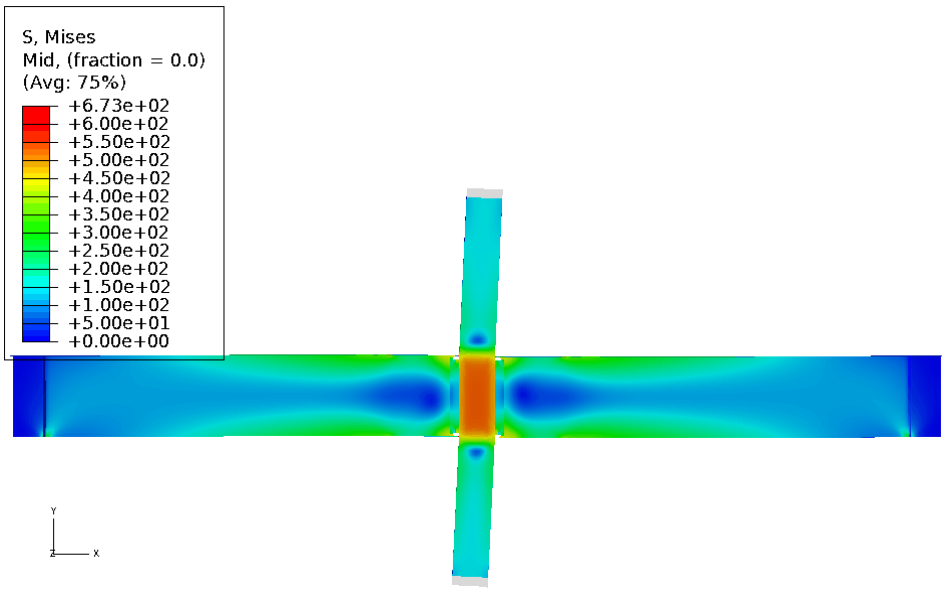

(a) Global view

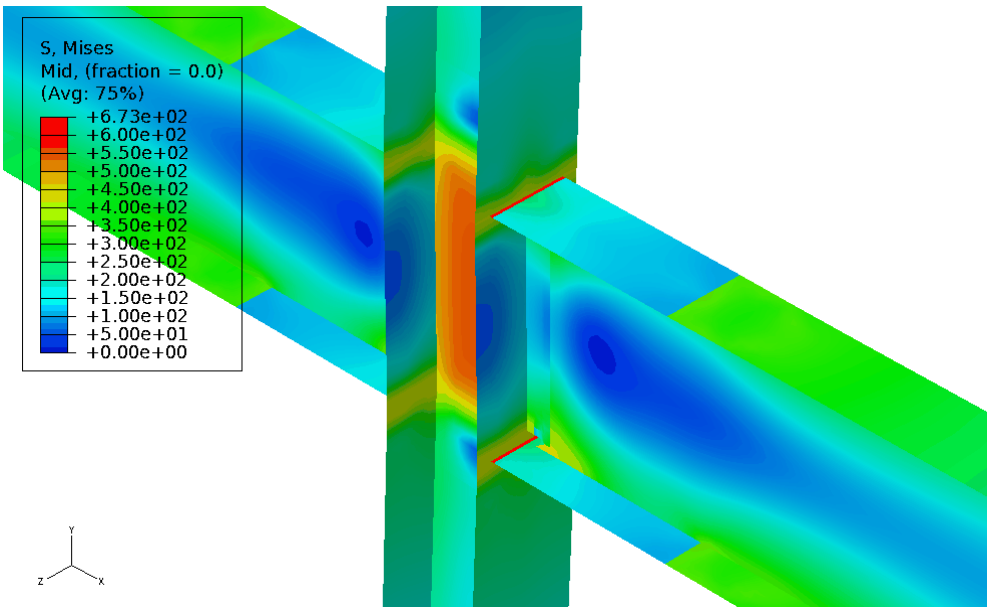

(b) Magnified view

Figure 5.32 Von Mises stress contour of Specimen 7 at 4% drift ratio

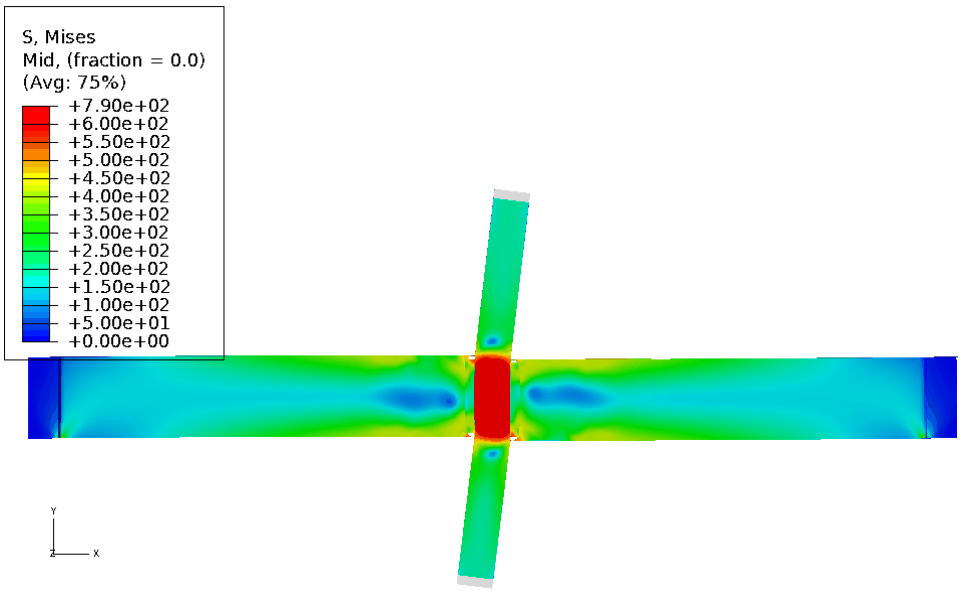

(a) Global view

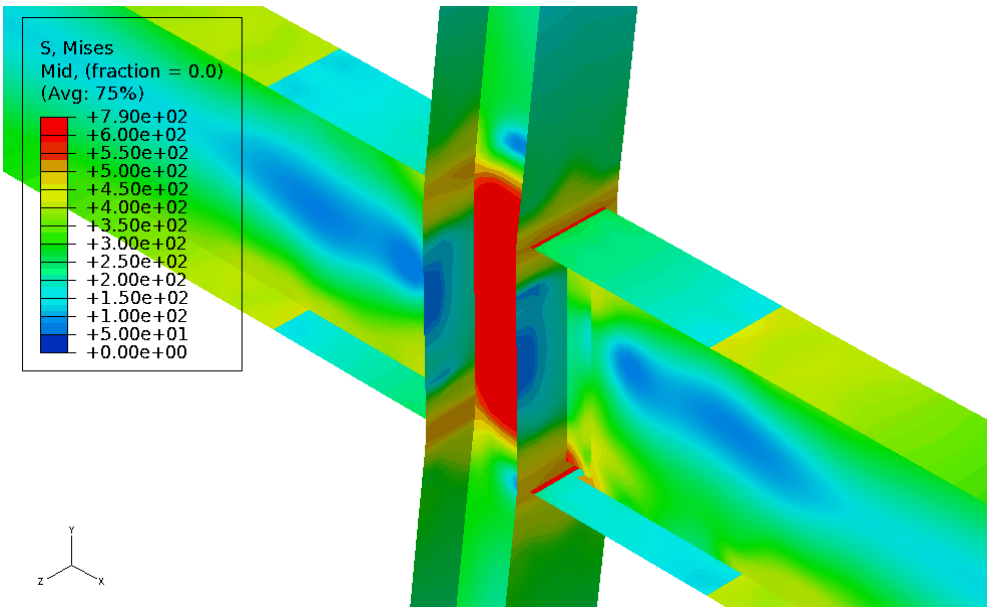

(b) Magnified view

Figure 5.33 Von Mises stress contour of Specimen 7 at 10% drift ratio

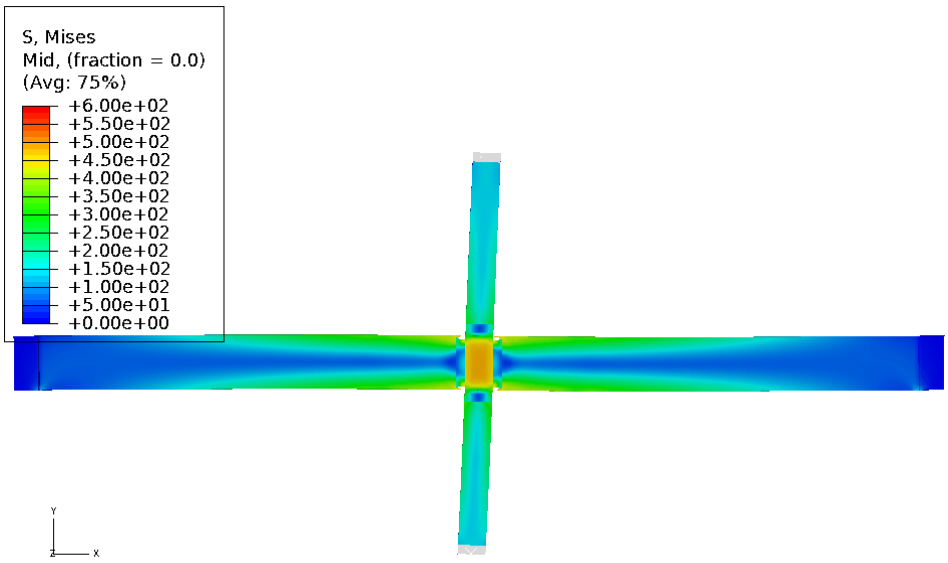

(a) Global view

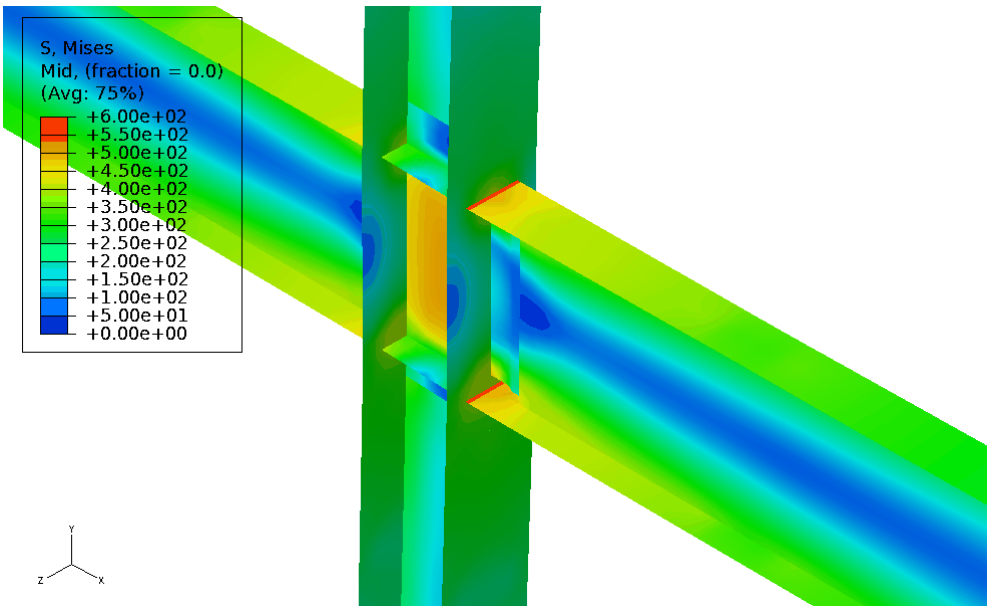

(b) Magnified view

Figure 5.34 Von Mises stress contour of Specimen 8 at 4% drift ratio

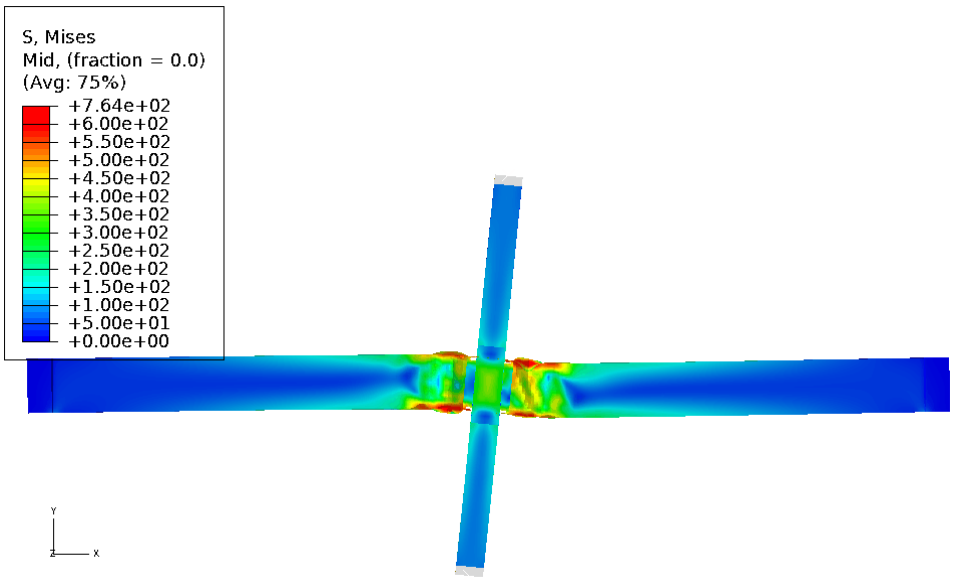

(a) Global view

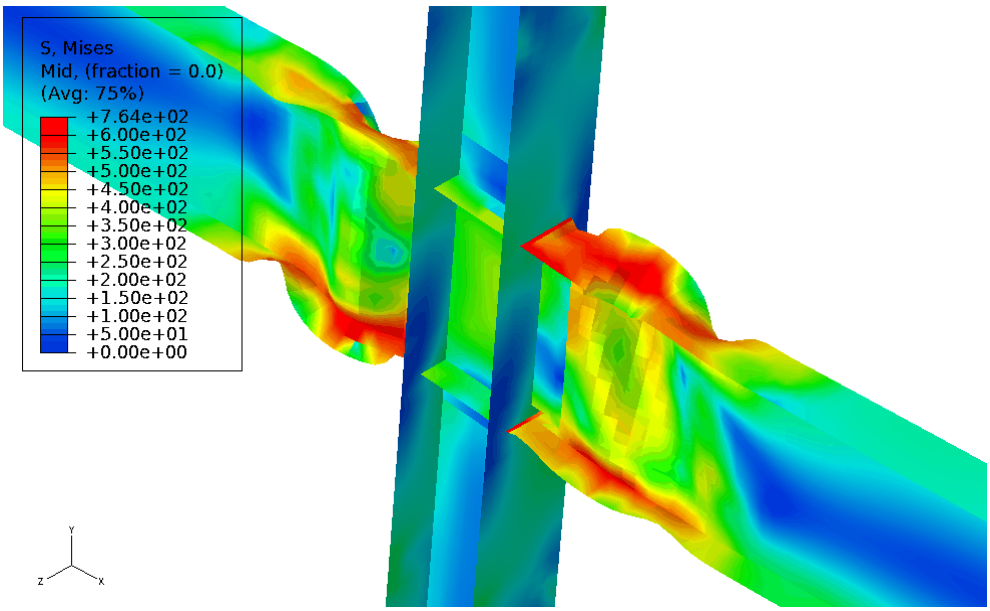

(b) Magnified view

Figure 5.35 Von Mises stress contour of Specimen 8 at 10% drift ratio

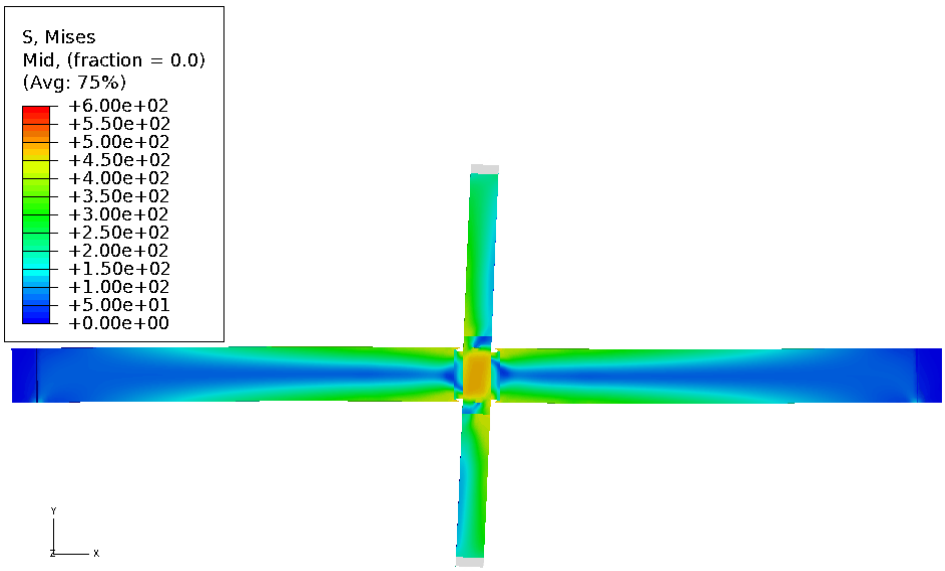

(a) Global view

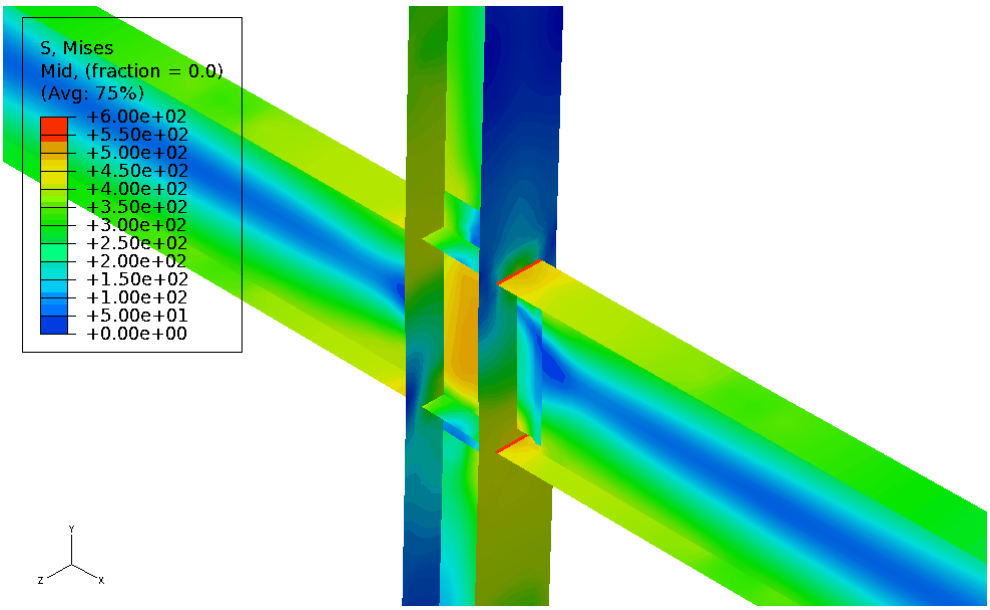

(b) Magnified view

Figure 5.36 Von Mises stress contour of Specimen 9 at 4% drift ratio

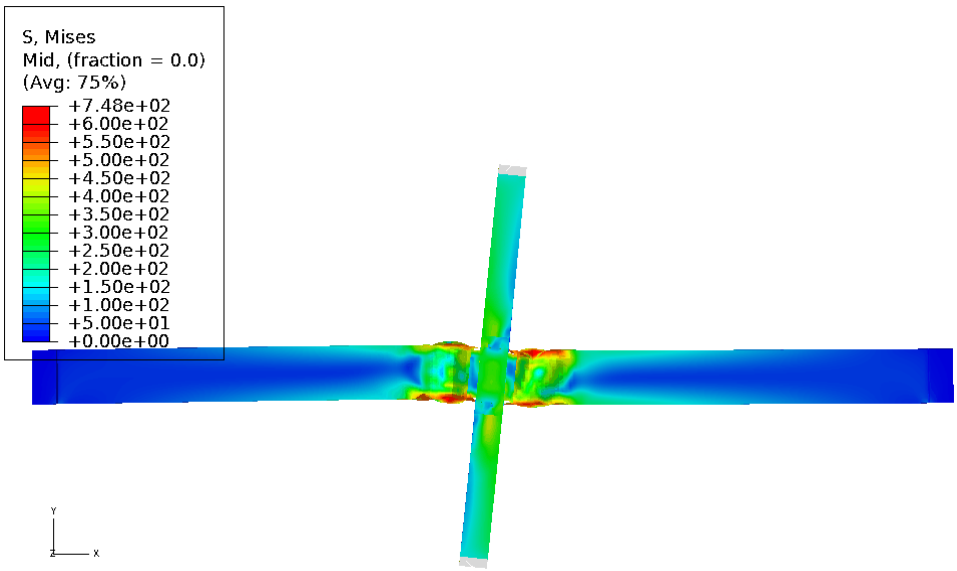

(a) Global view

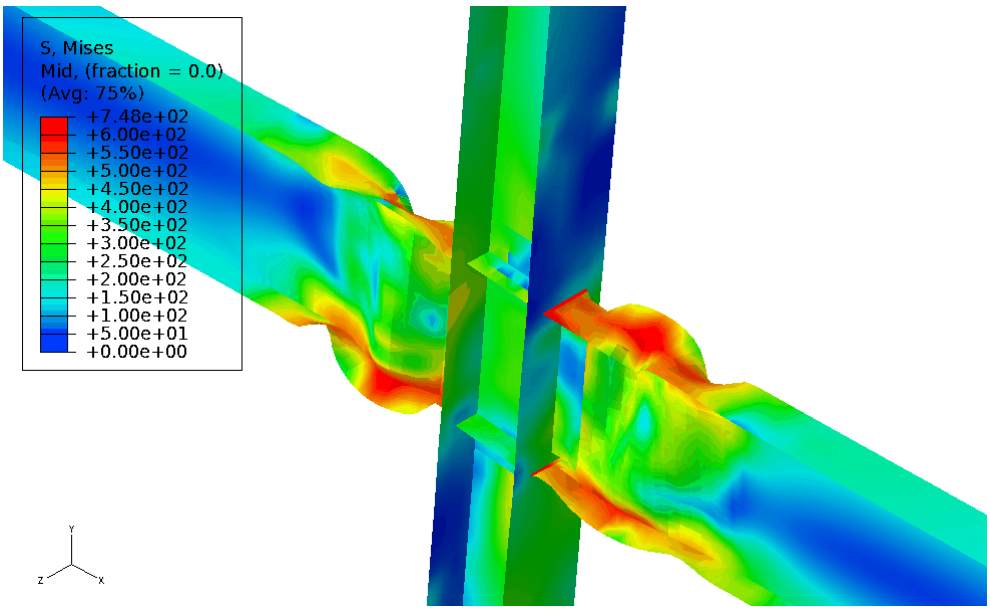

(b) Magnified view

Figure 5.37 Von Mises stress contour of Specimen 9 at 10% drift ratio

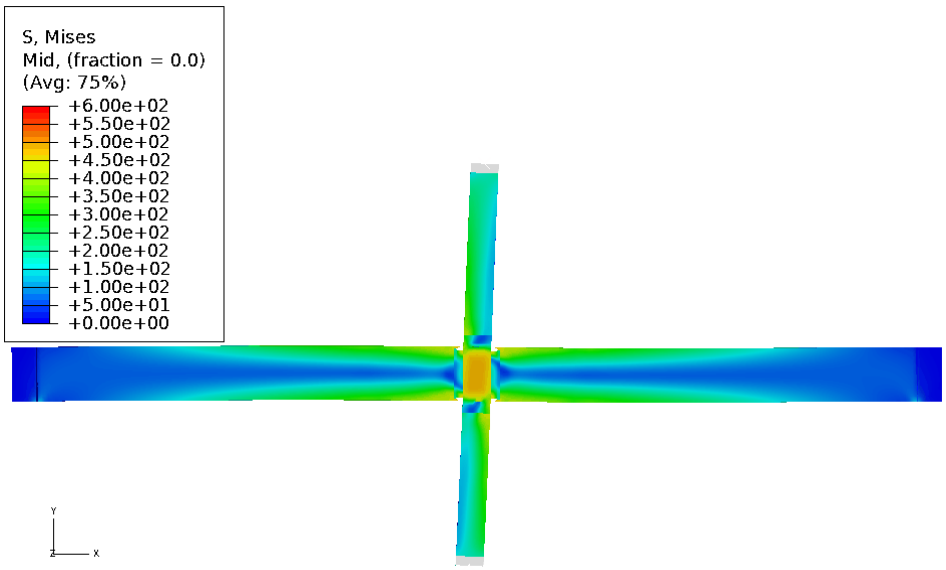

(a) Global view

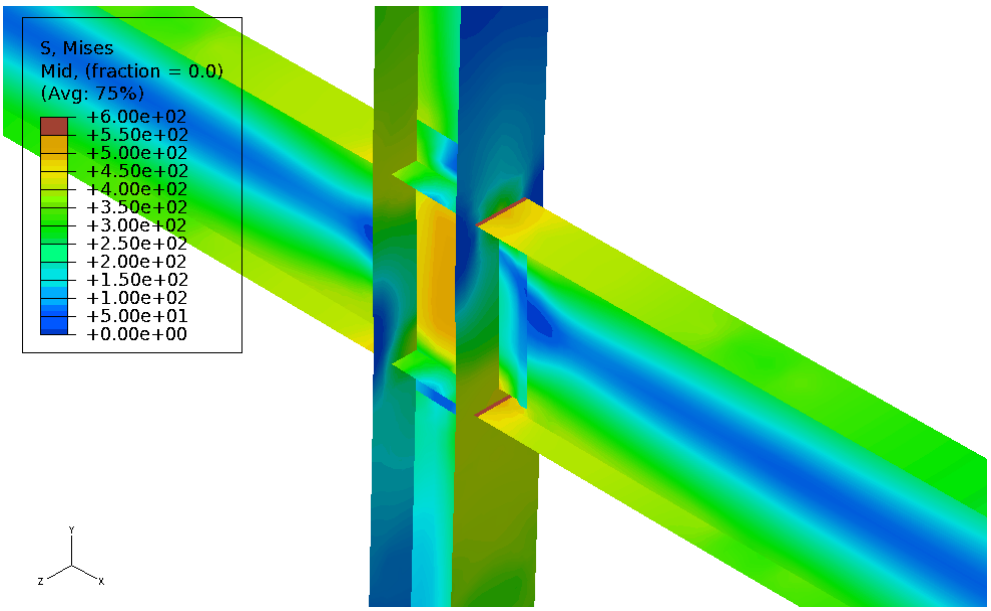

(b) Magnified view

Figure 5.38 Von Mises stress contour of Specimen 10 at 4% drift ratio

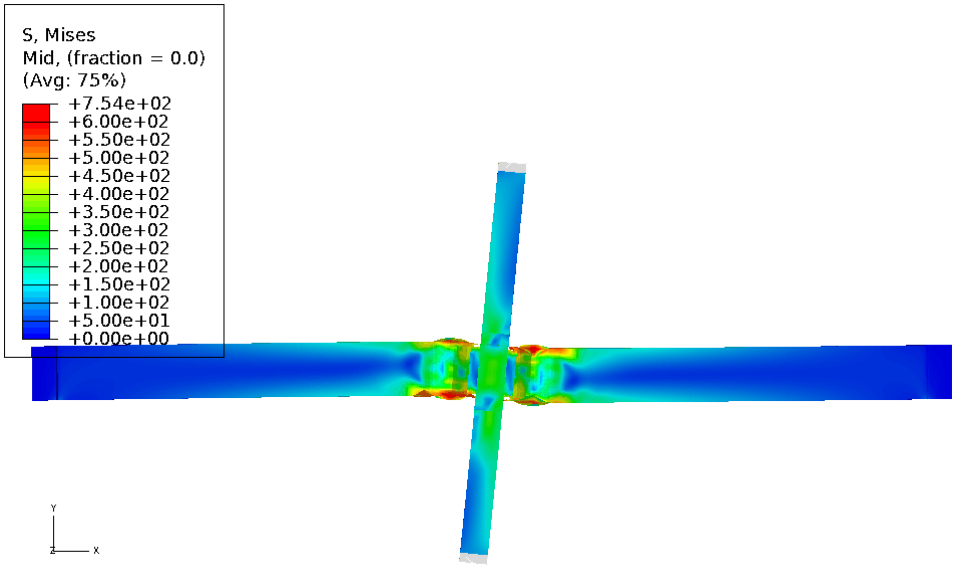

(a) Global view

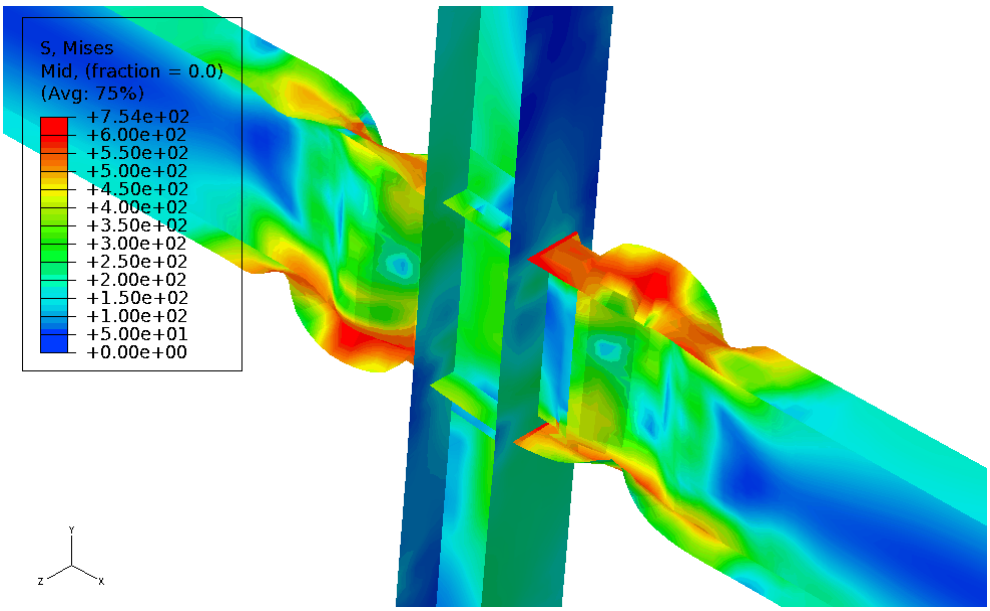

(b) Magnified view

Figure 5.39 Von Mises stress contour of Specimen 10 at 10% drift ratio

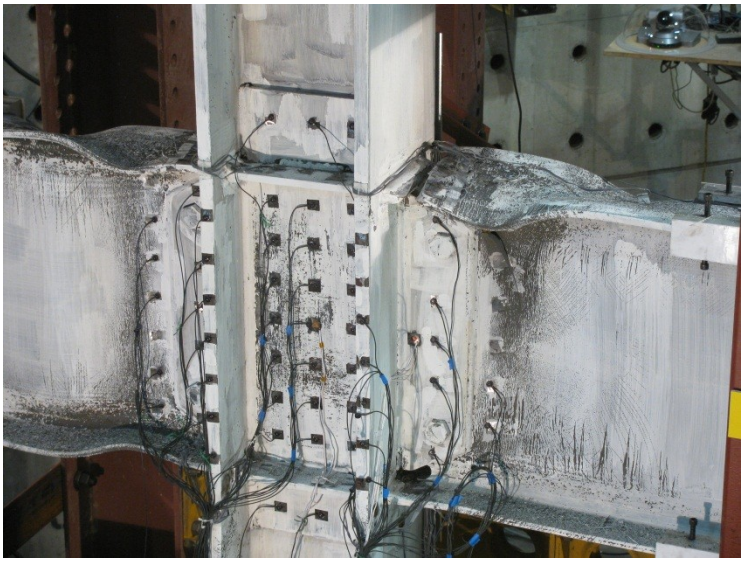

Figure 5.40 Photo of Specimen 8 when the experiment was finished

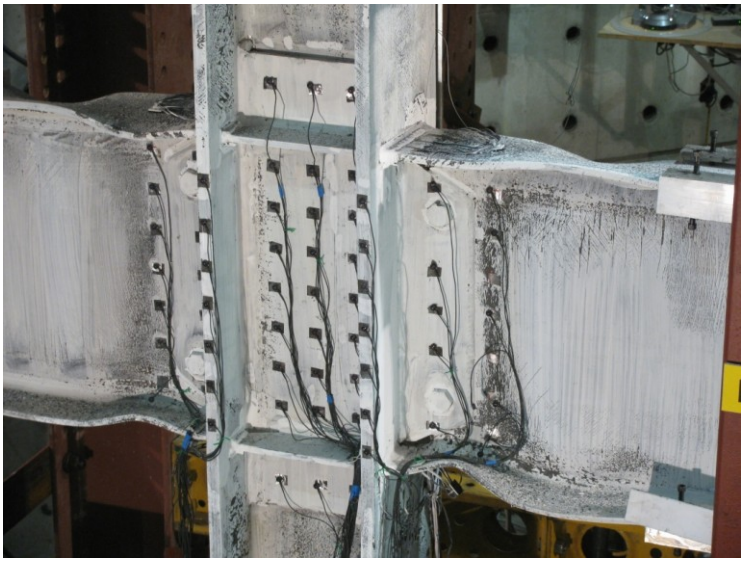

Figure 5.41 Photo of Specimen 9 when the experiment was finished

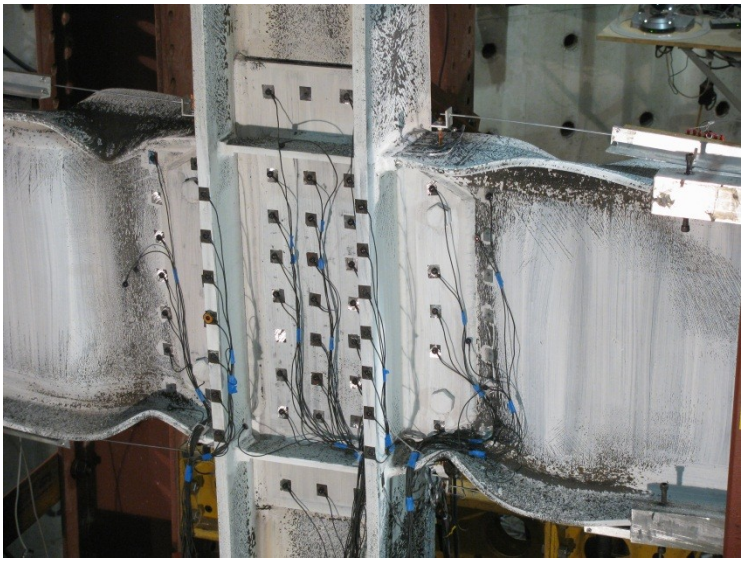

Figure 5.42 Photo of Specimen 10 when the experiment was finished

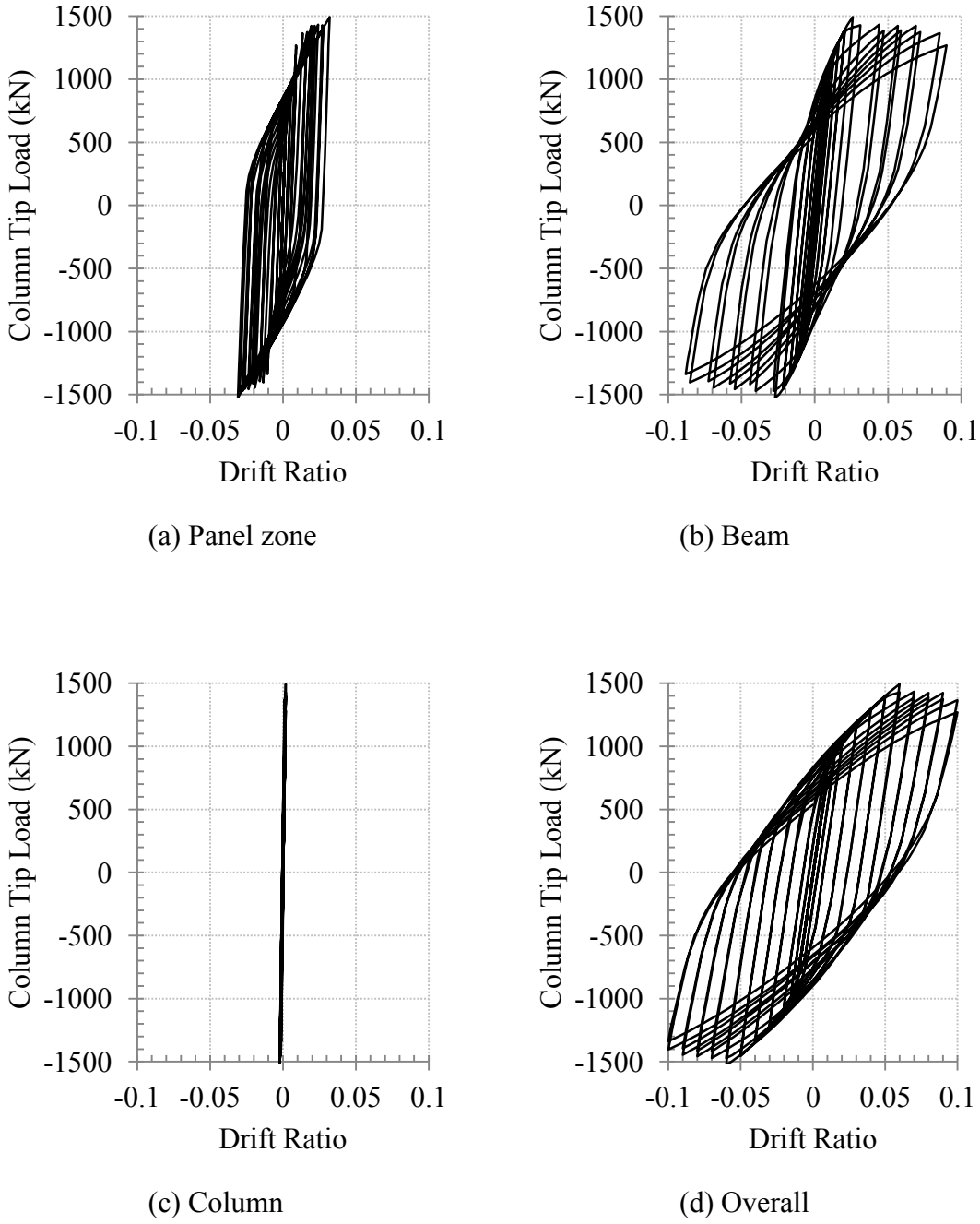

(a) Panel zone

(b) Beam

(c) Column

(d) Overall

Figure 5.43 Column tip displacement contributions from the components of Specimen 1

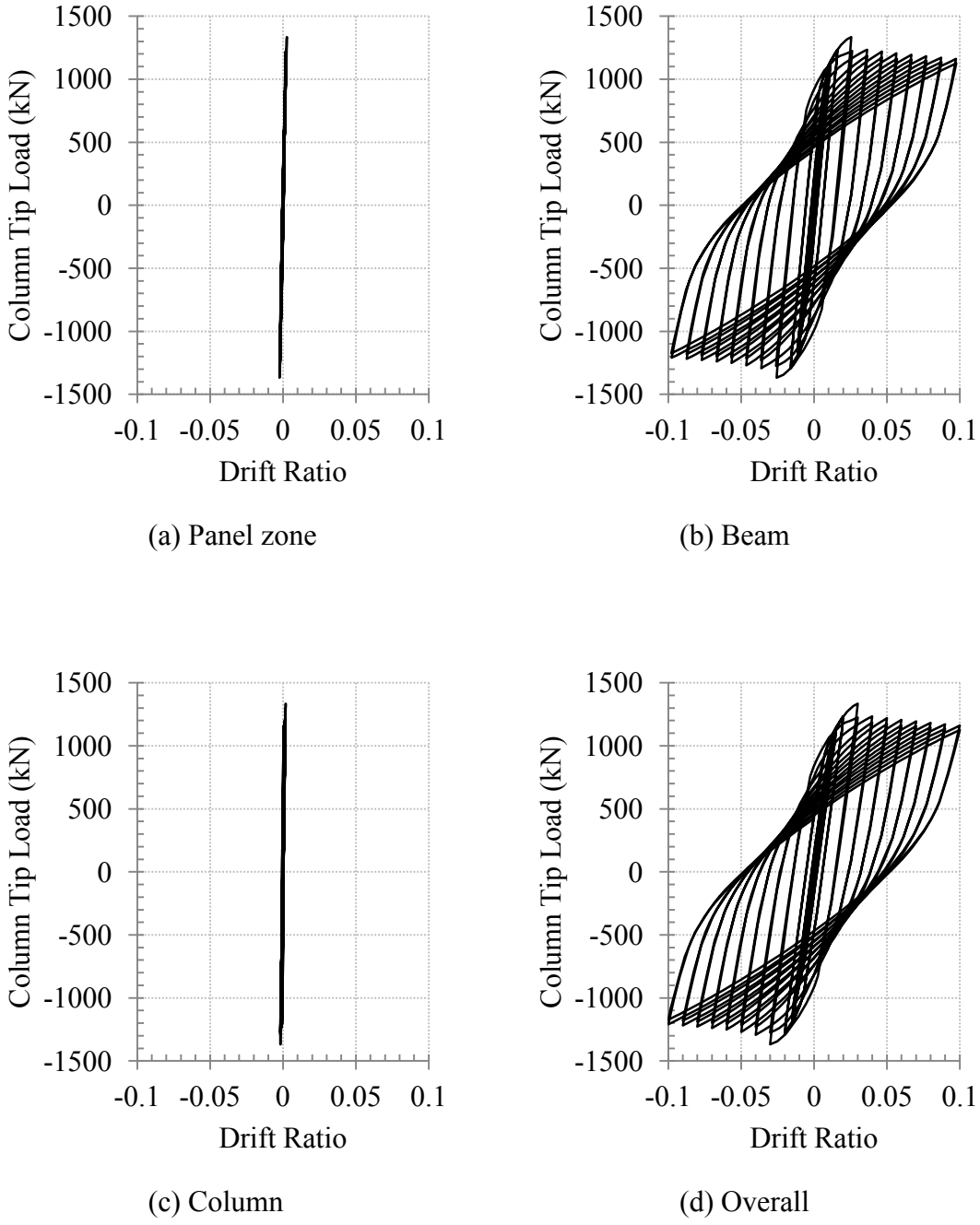

(a) Panel zone

(b) Beam

(c) Column

(d) Overall

Figure 5.44 Column tip displacement contributions from the components of Specimen 2

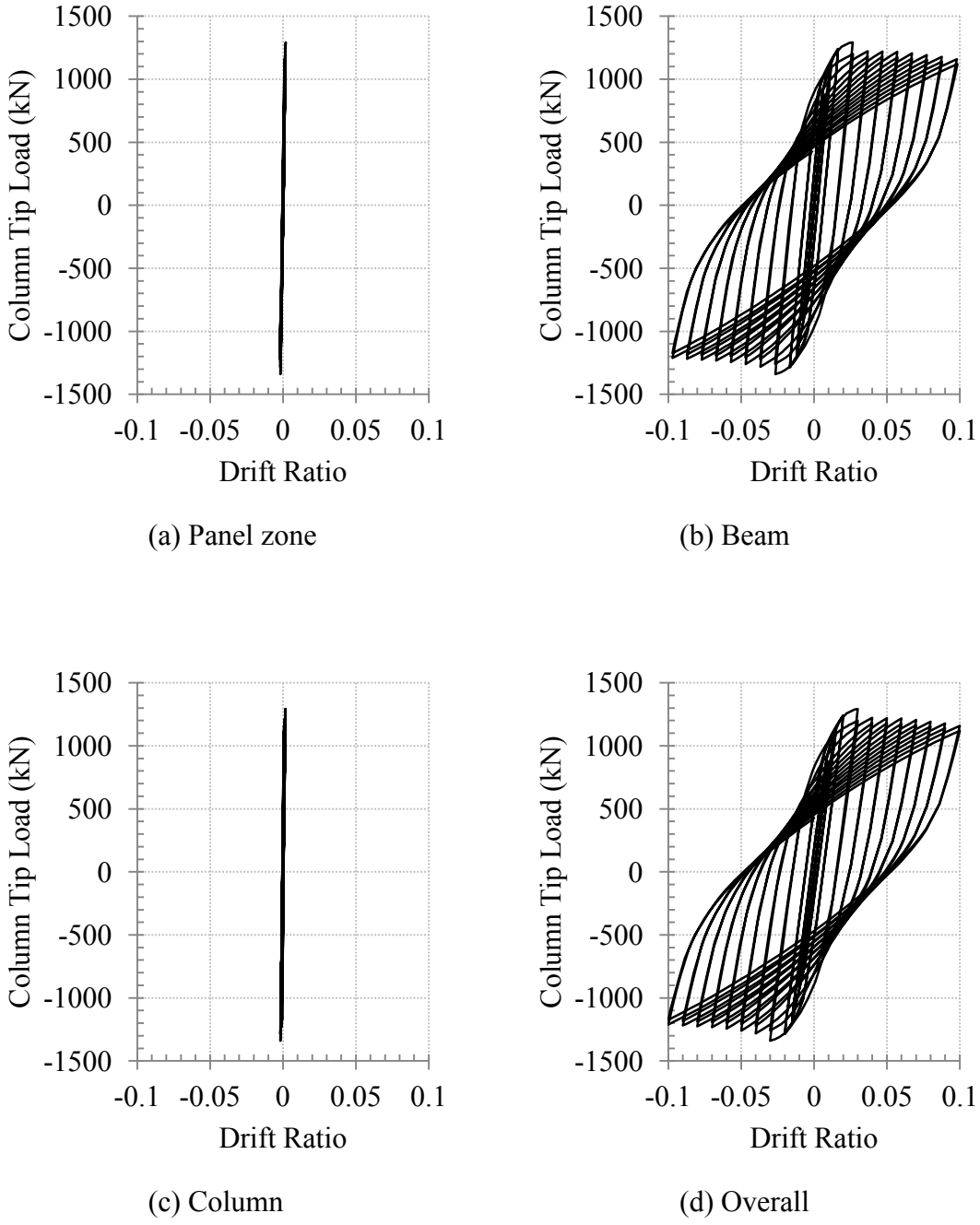

(a) Panel zone

(b) Beam

(c) Column

(d) Overall

Figure 5.45 Column tip displacement contributions from the components of Specimen 3

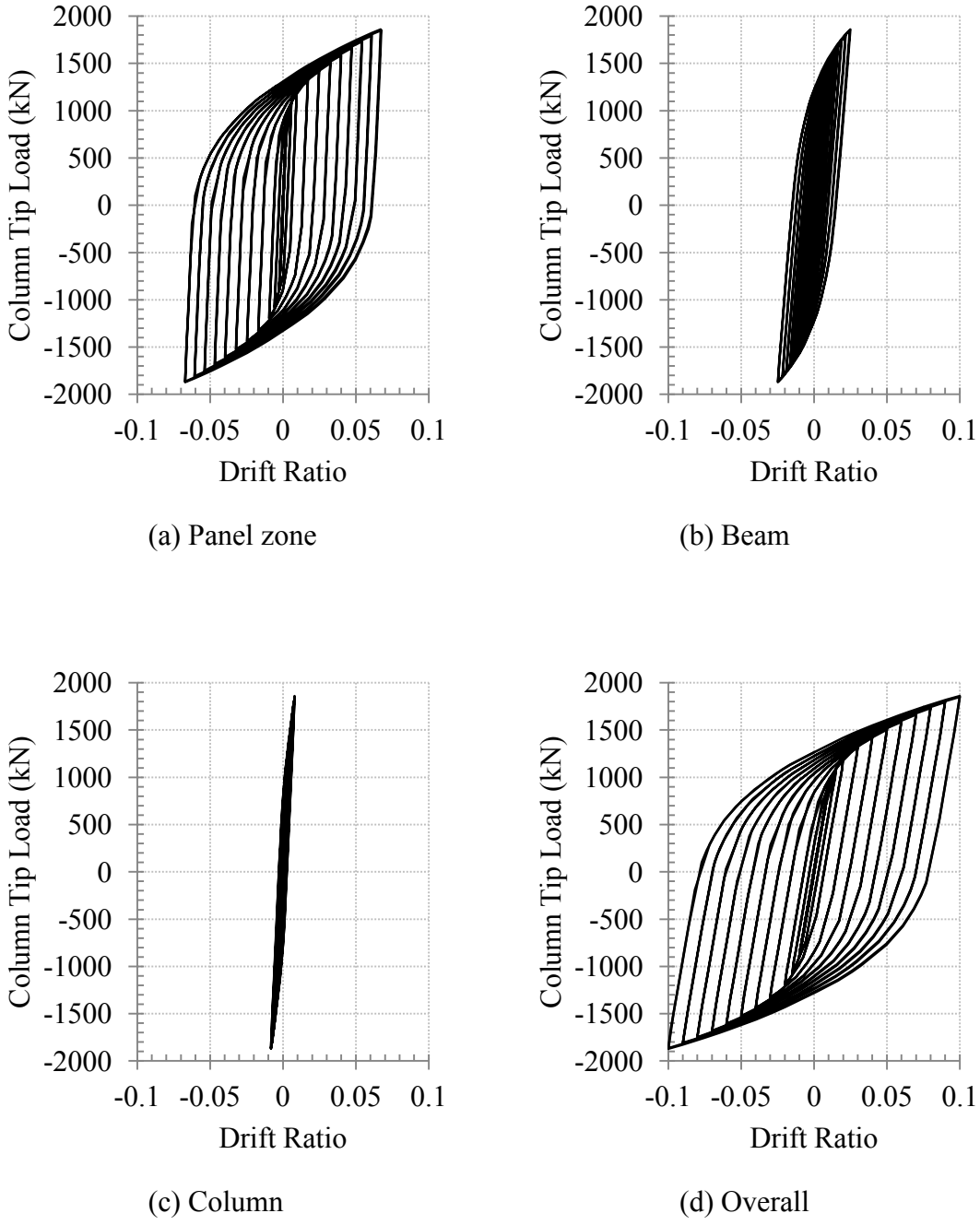

(a) Panel zone

(b) Beam

(c) Column

(d) Overall

Figure 5.46 Column tip displacement contributions from the components of Specimen 4

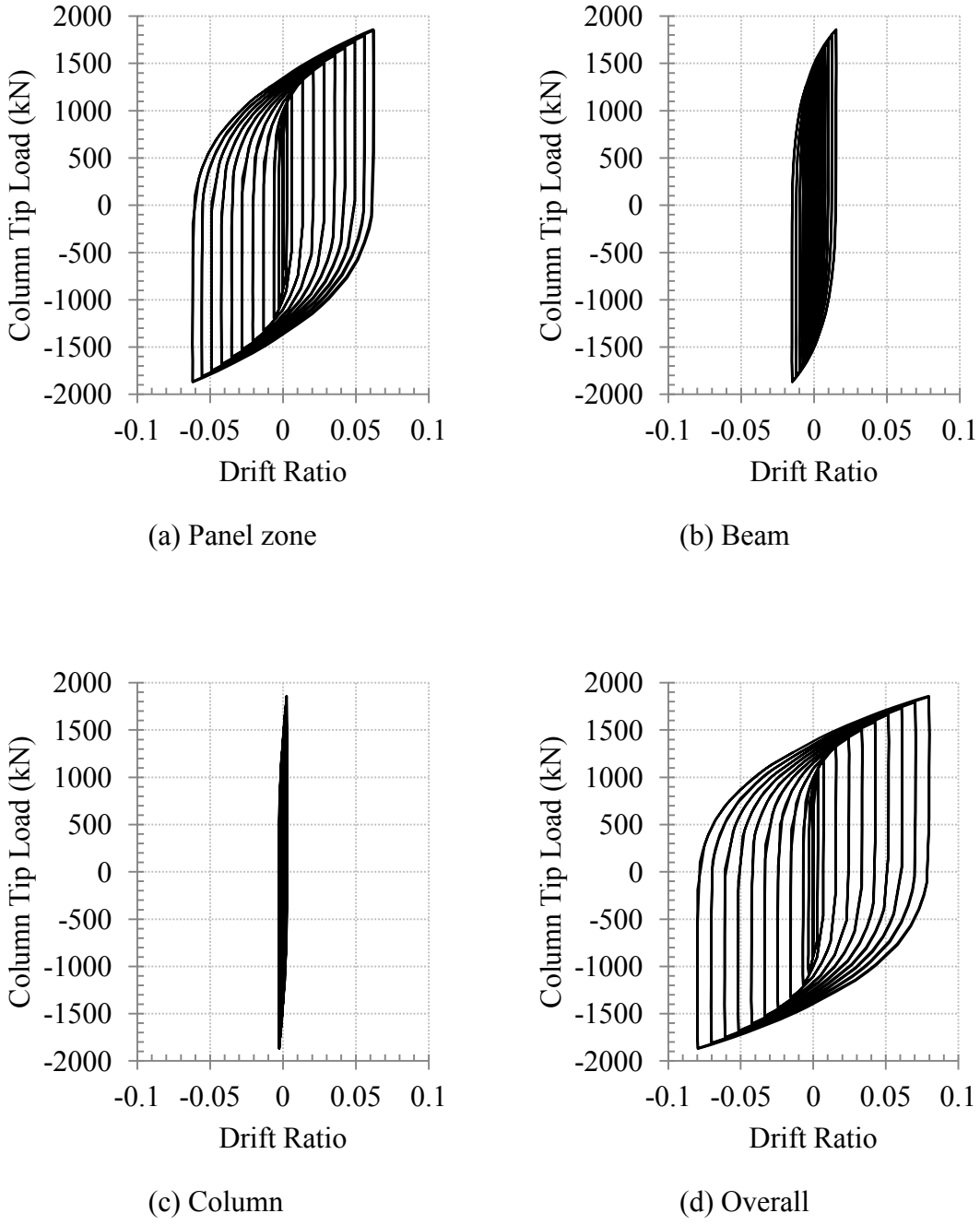

(a) Panel zone

(b) Beam

(c) Column

(d) Overall

Figure 5.47 Column tip displacement contributions from the components of Specimen 4 due to plastic deformation

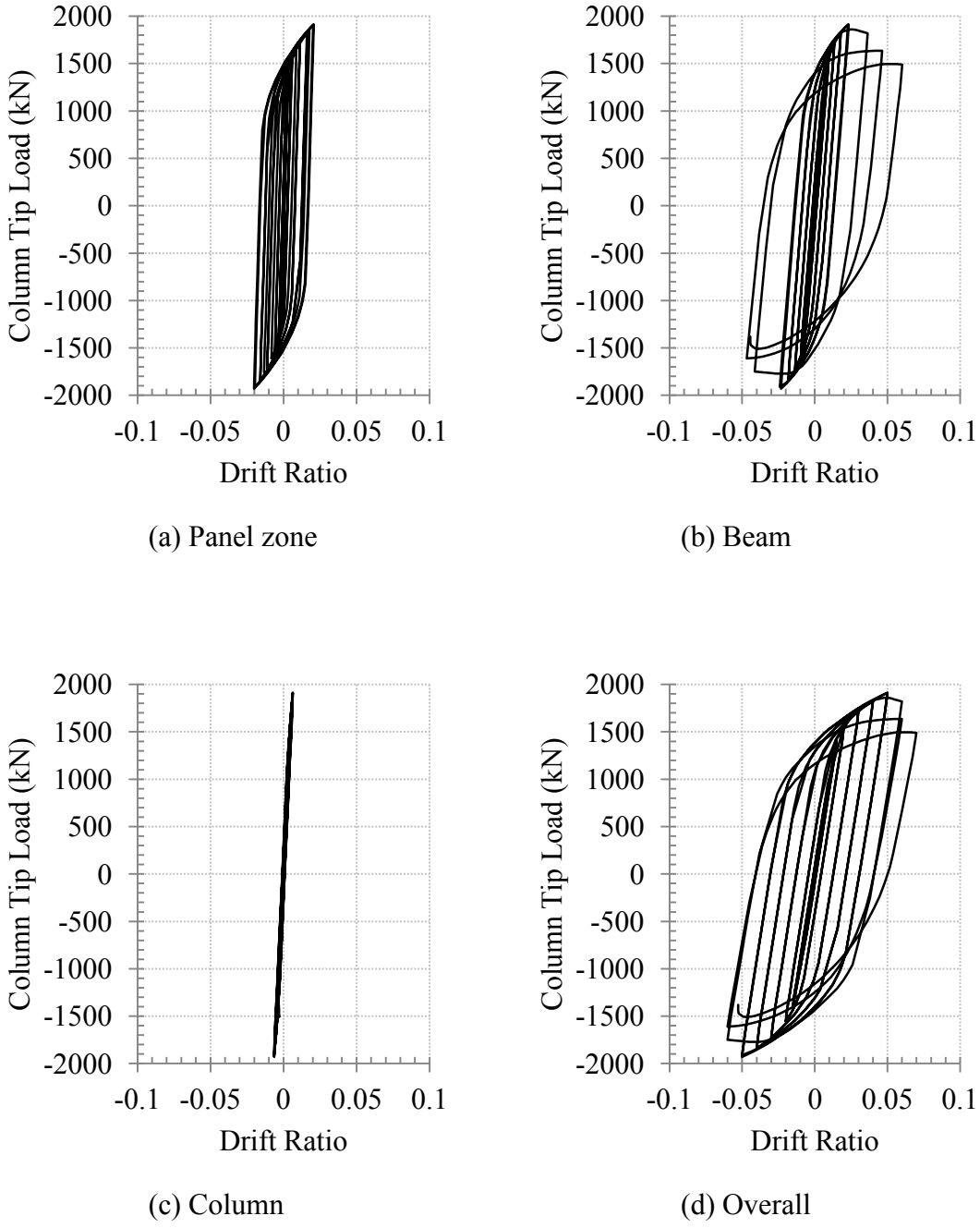

(a) Panel zone

(b) Beam

(c) Column

(d) Overall

Figure 5.48 Column tip displacement contributions from the components of Specimen 5

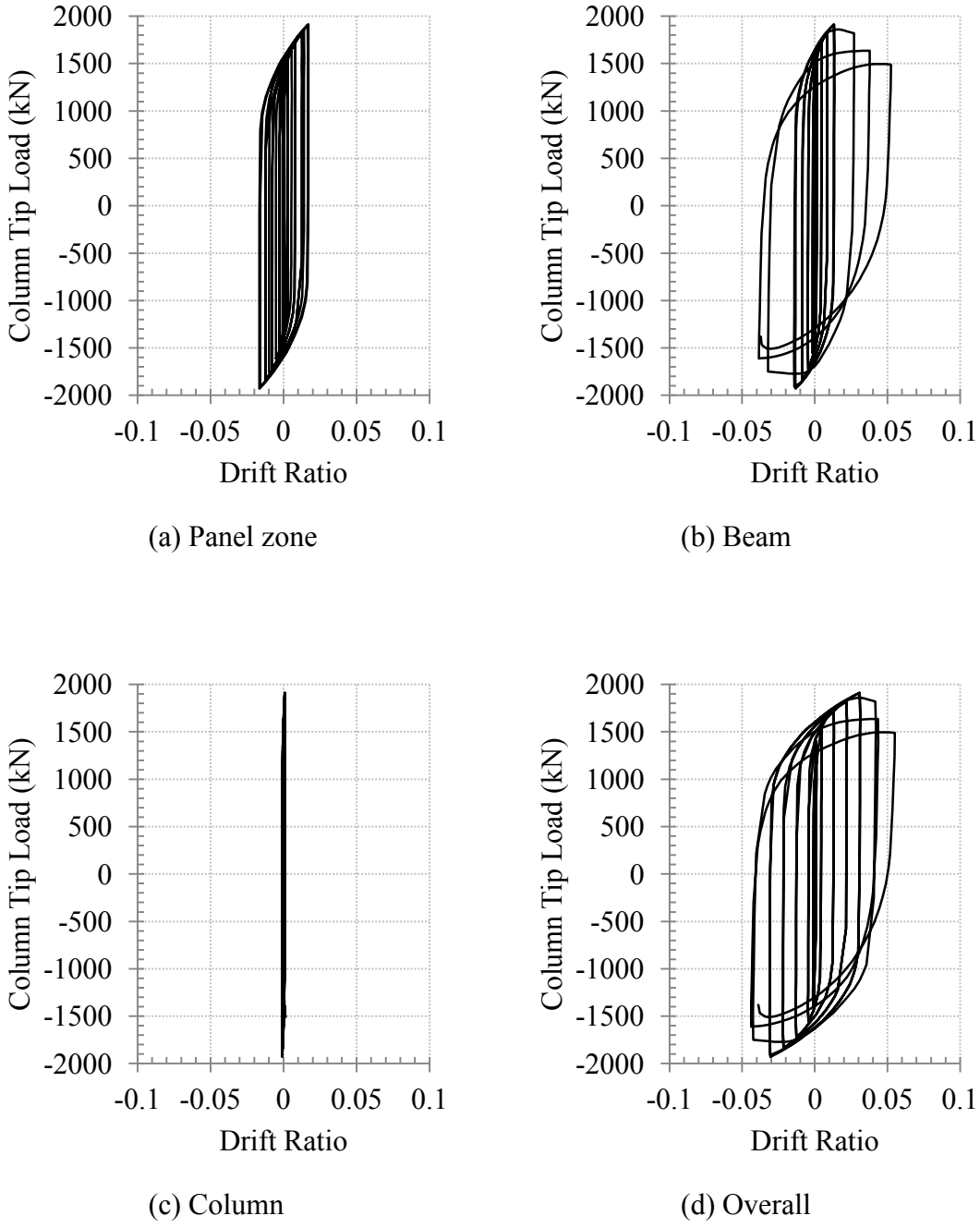

(a) Panel zone

(b) Beam

(c) Column

(d) Overall

Figure 5.49 Column tip displacement contributions from the components of Specimen 5 due to plastic deformation

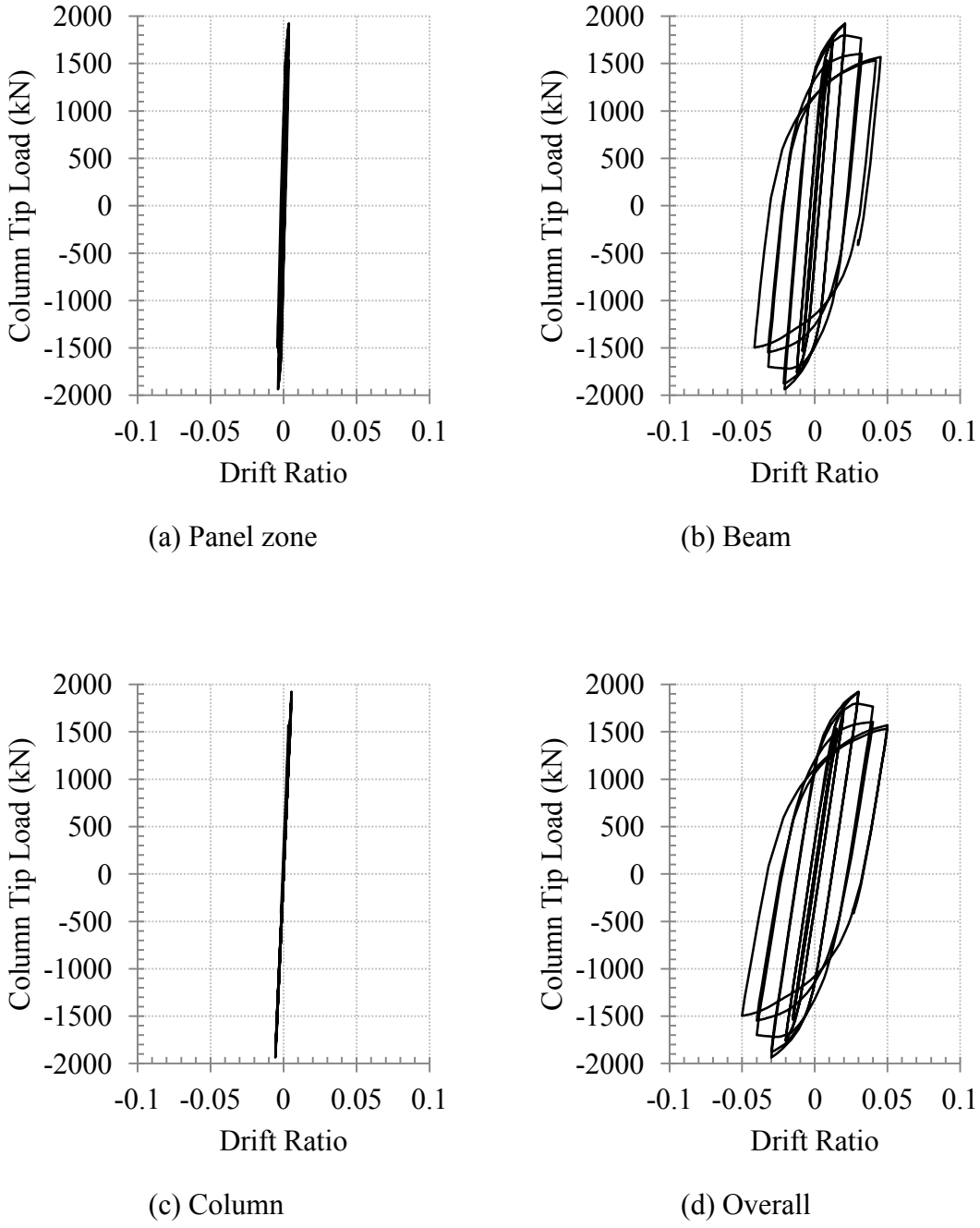

(a) Panel zone

(b) Beam

(c) Column

(d) Overall

Figure 5.50 Column tip displacement contributions from the components of Specimen 6

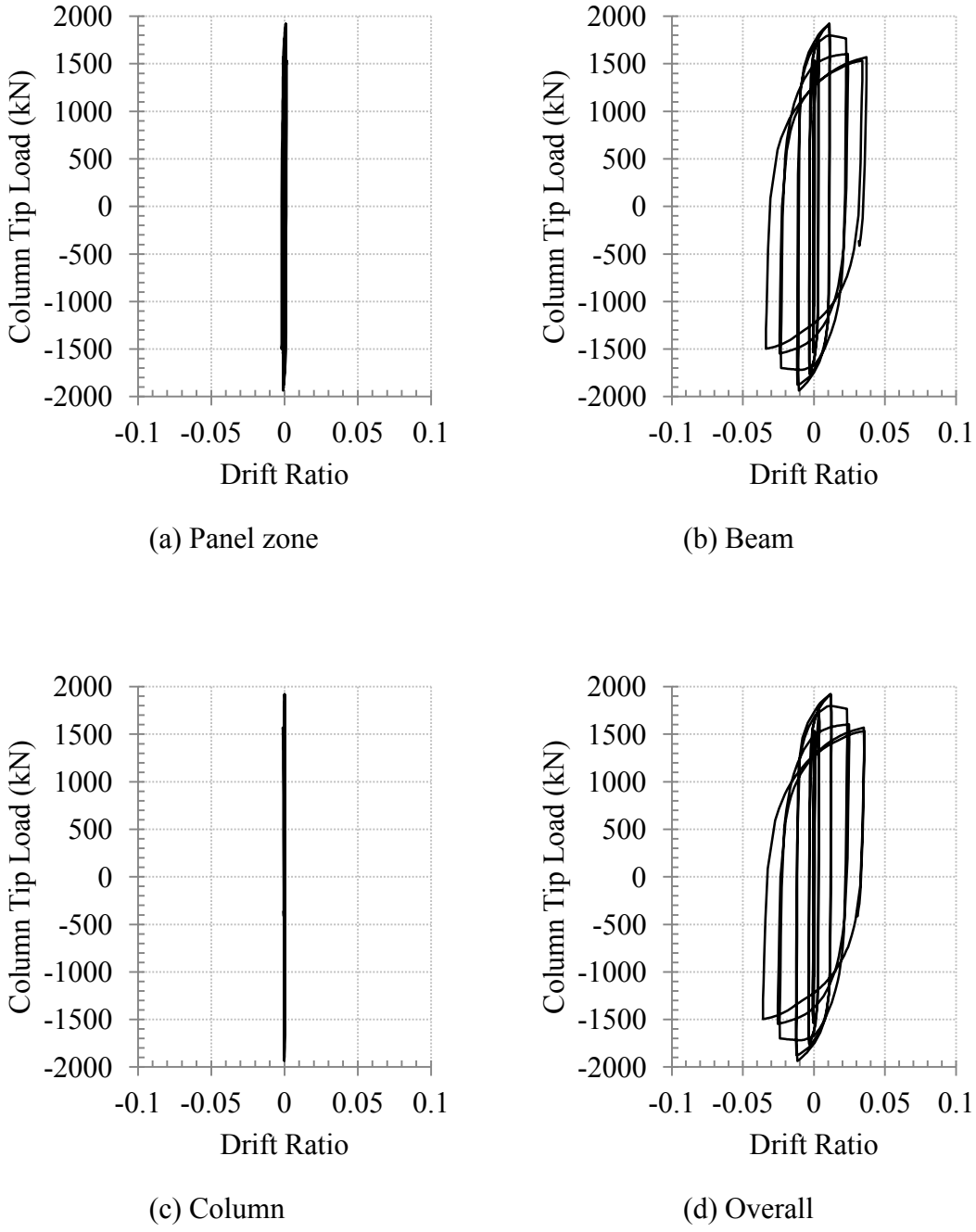

(a) Panel zone

(b) Beam

(c) Column

(d) Overall

Figure 5.51 Column tip displacement contributions from the components of Specimen 6 due to plastic deformation

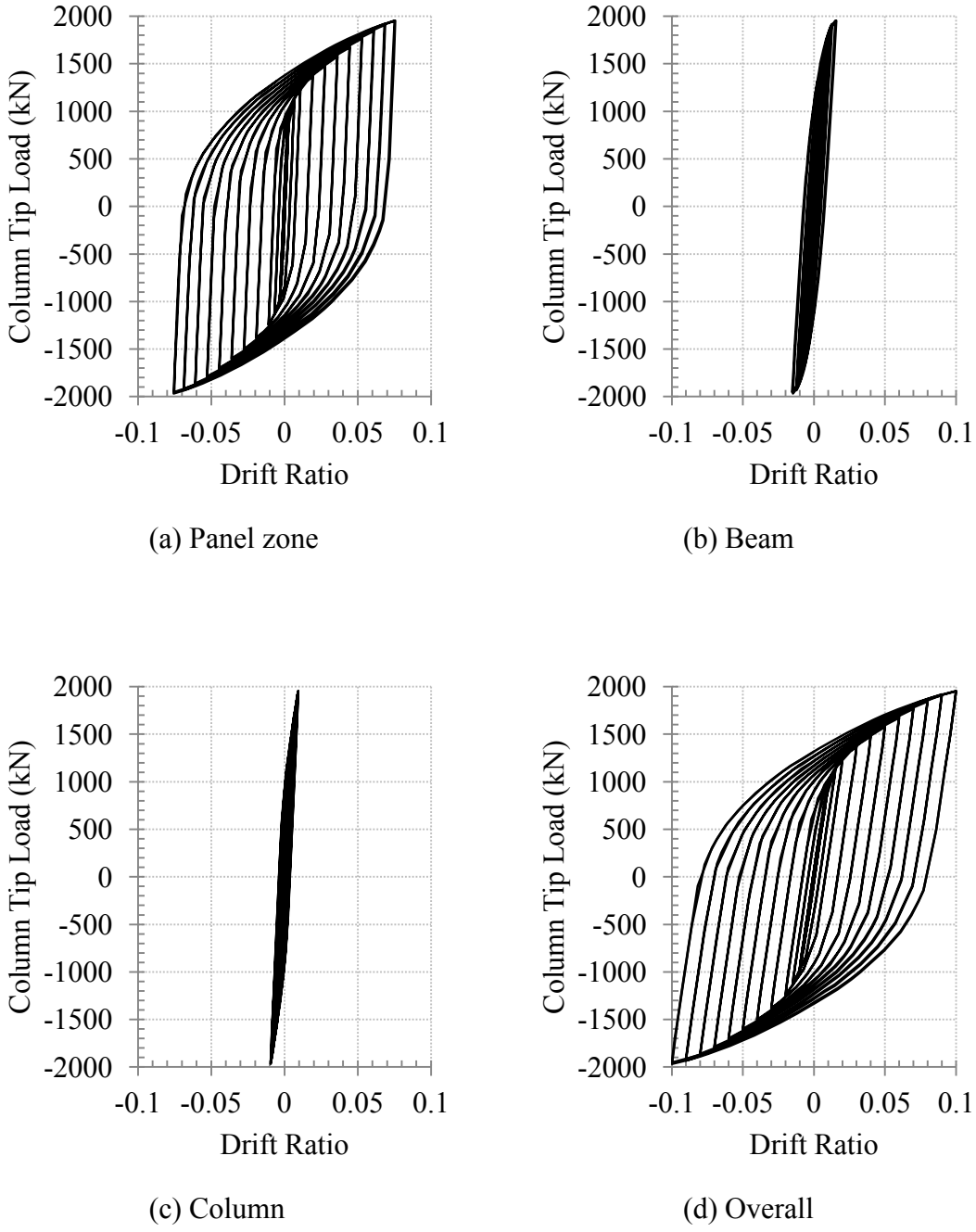

(a) Panel zone

(b) Beam

(c) Column

(d) Overall

Figure 5.52 Column tip displacement contributions from the components of Specimen 7

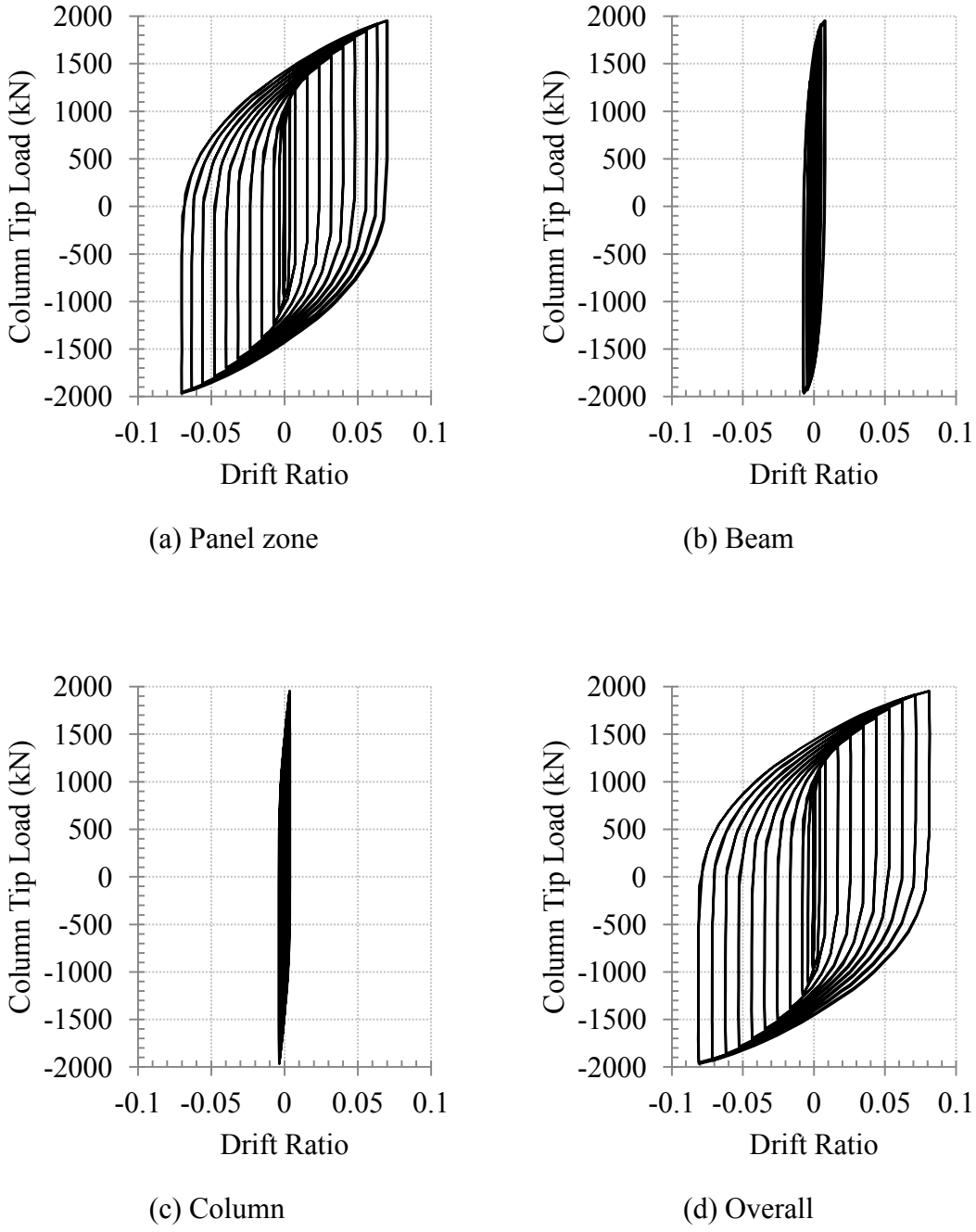

(a) Panel zone

(b) Beam

(c) Column

(d) Overall

Figure 5.53 Column tip displacement contributions from the components of Specimen 7 due to plastic deformation

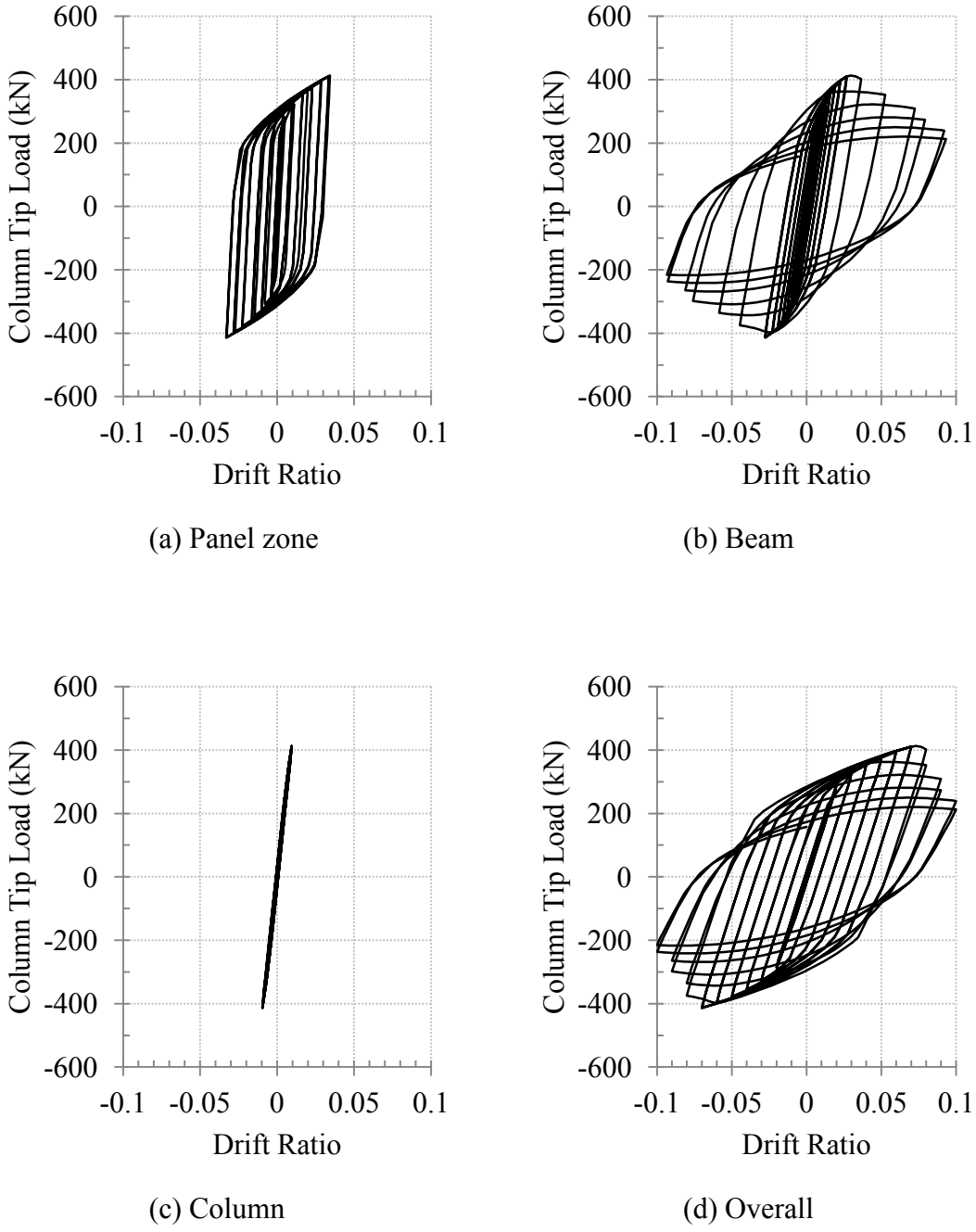

(a) Panel zone

(b) Beam

(c) Column

(d) Overall

Figure 5.54 Column tip displacement contributions from the components of Specimen 8

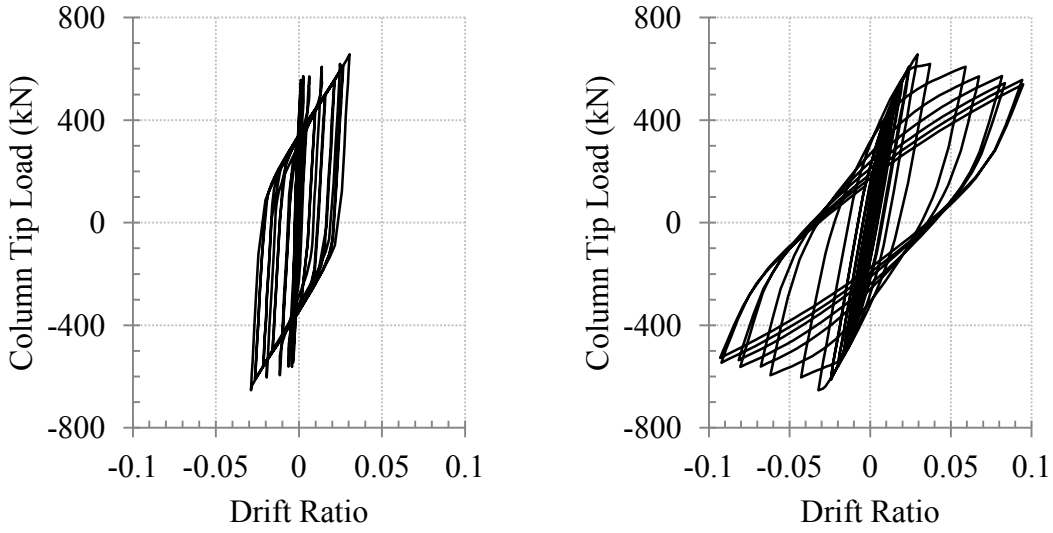

(a) Panel zone

(b) Beam

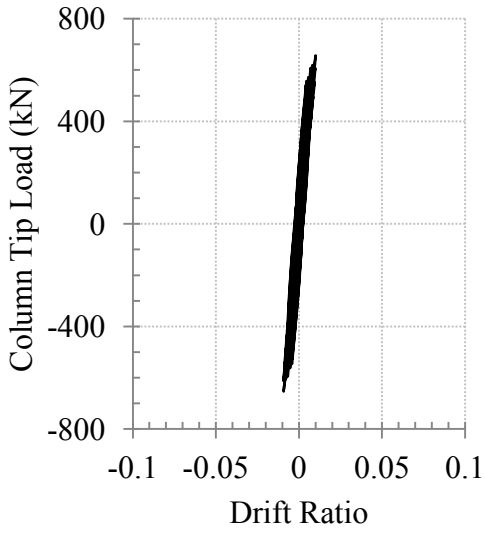

(c) Column

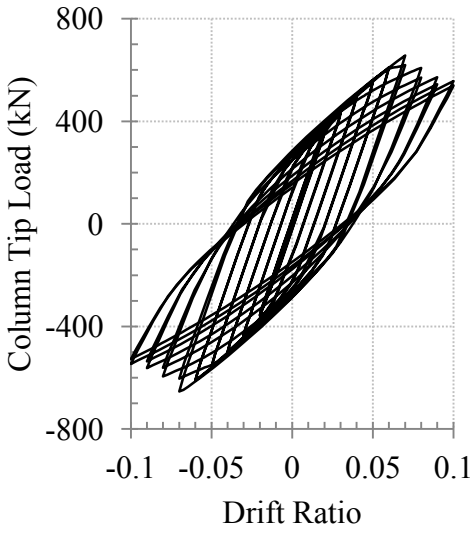

(d) Overall

Figure 5.55 Column tip displacement contributions from the components of Specimen 9

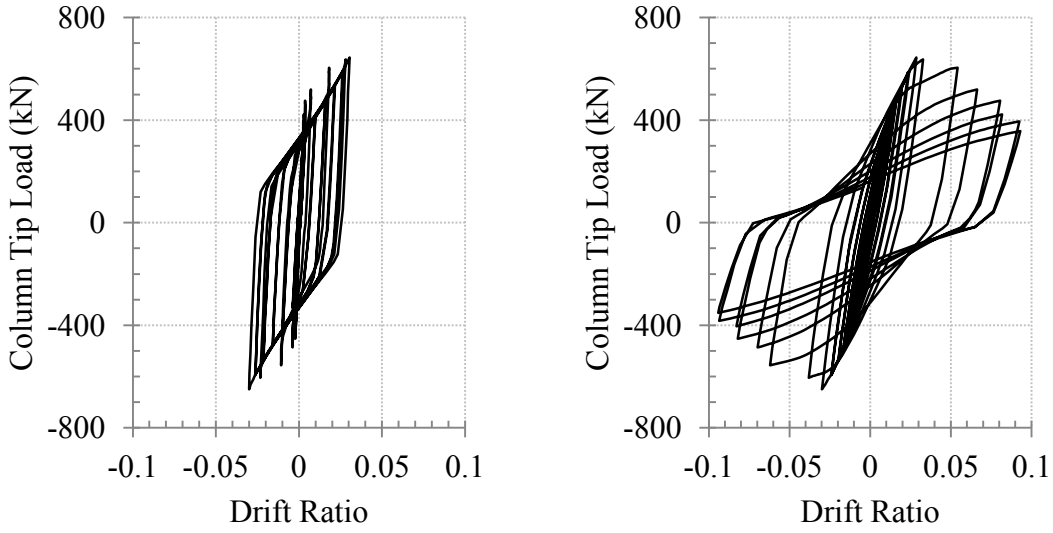

(a) Panel zone

(b) Beam

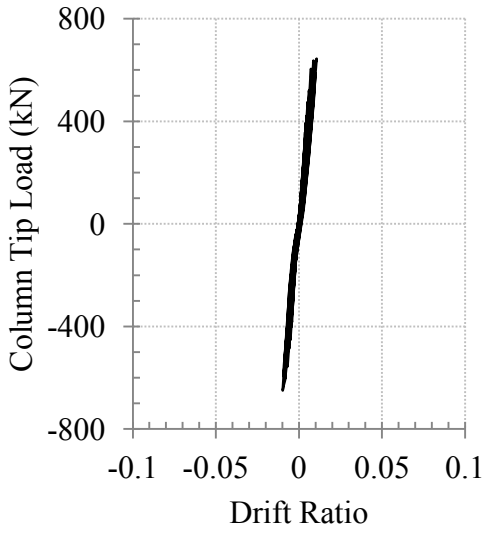

(c) Column

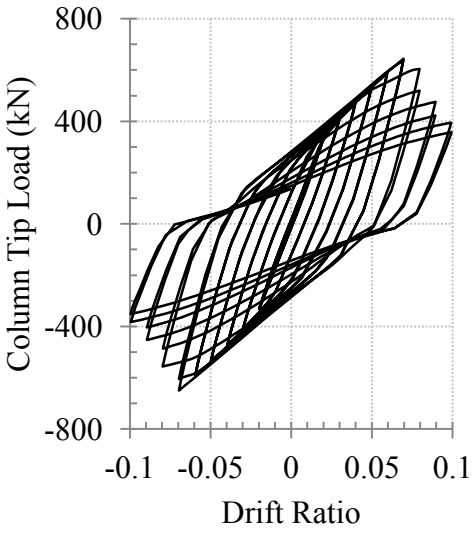

(d) Overall

Figure 5.56 Column tip displacement contributions from the components of Specimen 10

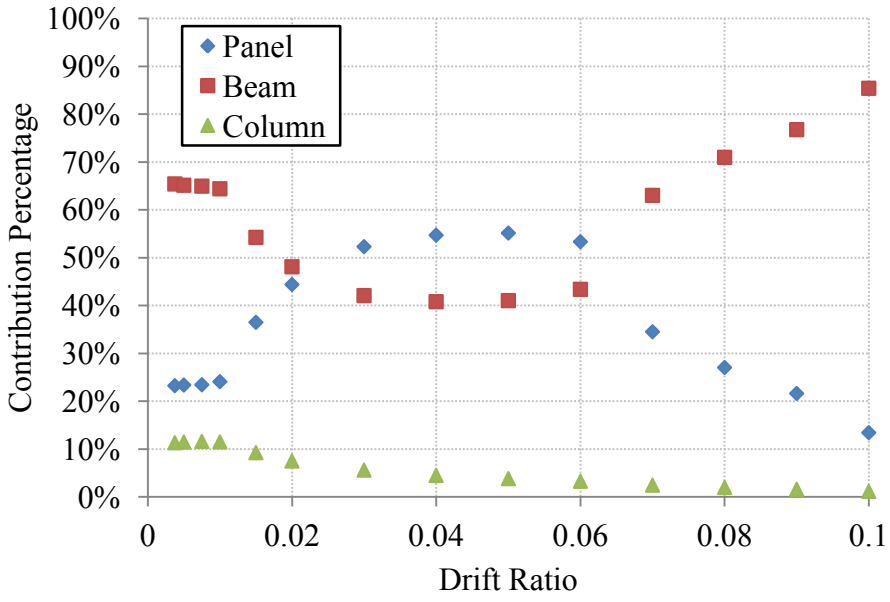

Figure 5.57 Evolution of the displacement contribution percentages of Specimen 1

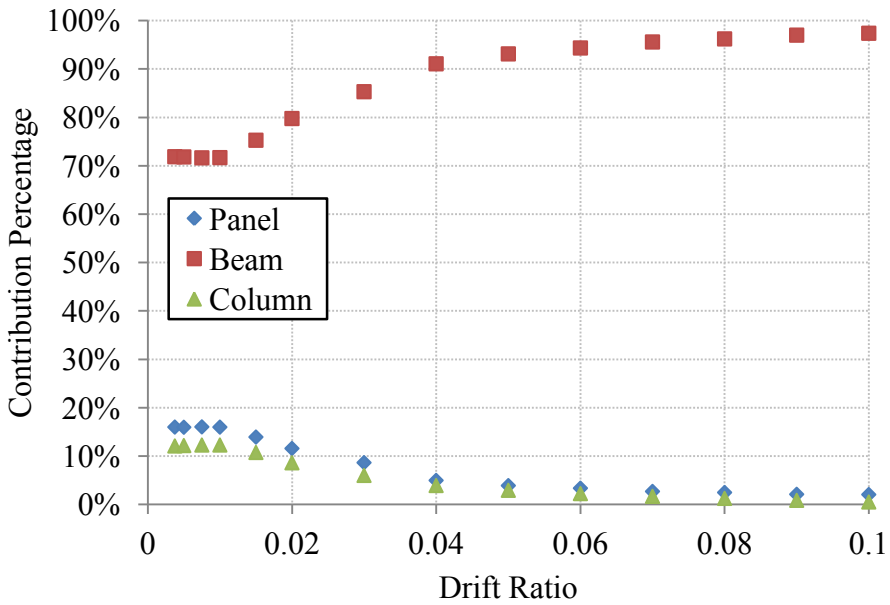

Figure 5.58 Evolution of the displacement contribution percentages of Specimen 2

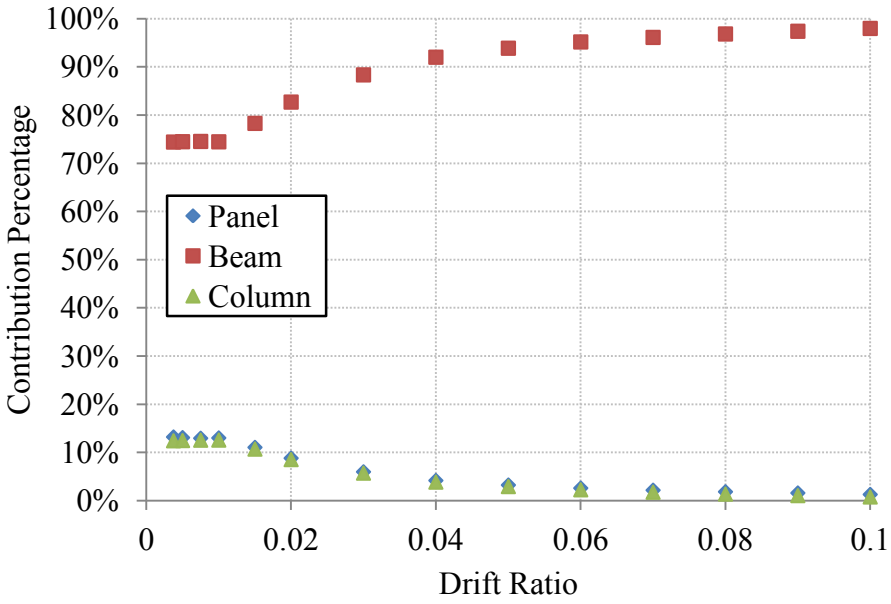

Figure 5.59 Evolution of the displacement contribution percentages of Specimen 3

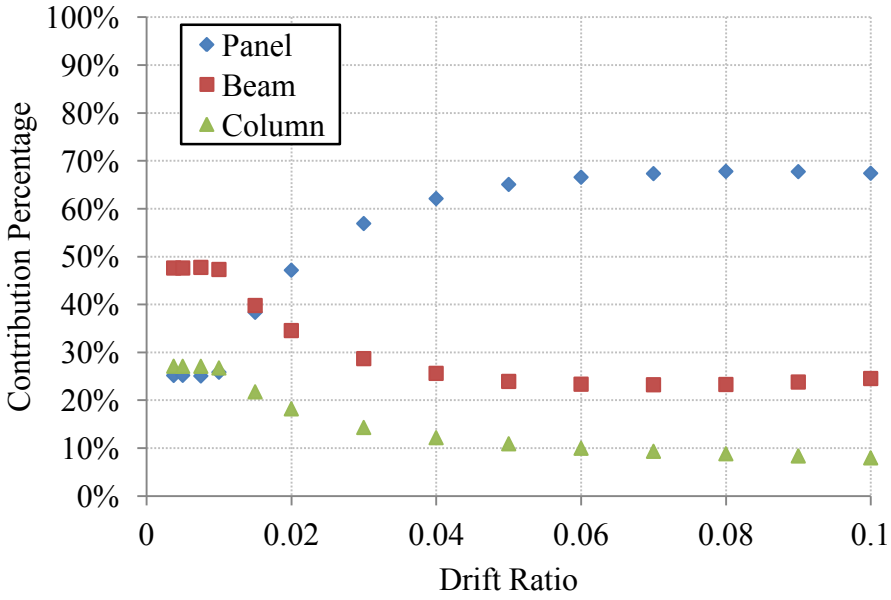

Figure 5.60 Evolution of the displacement contribution percentages of Specimen 4

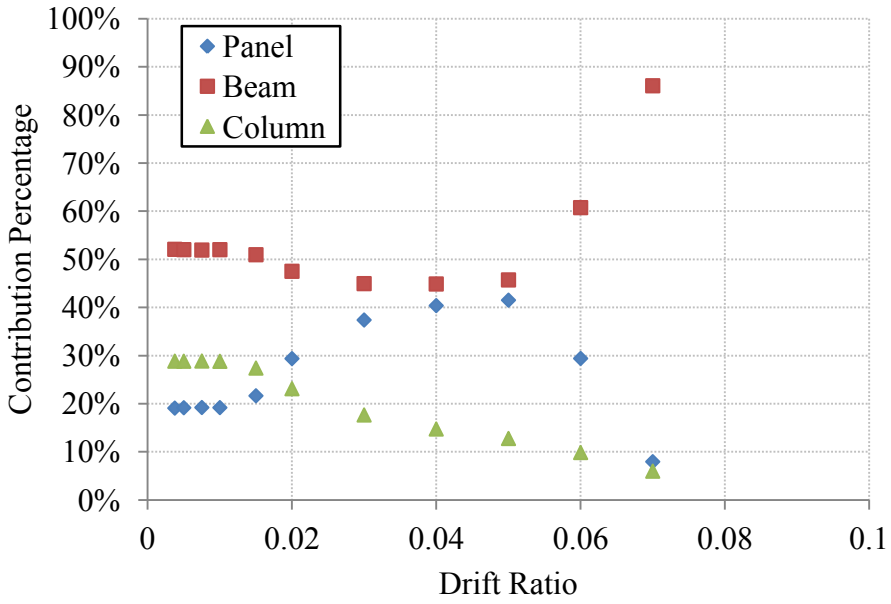

Figure 5.61 Evolution of the displacement contribution percentages of Specimen 5

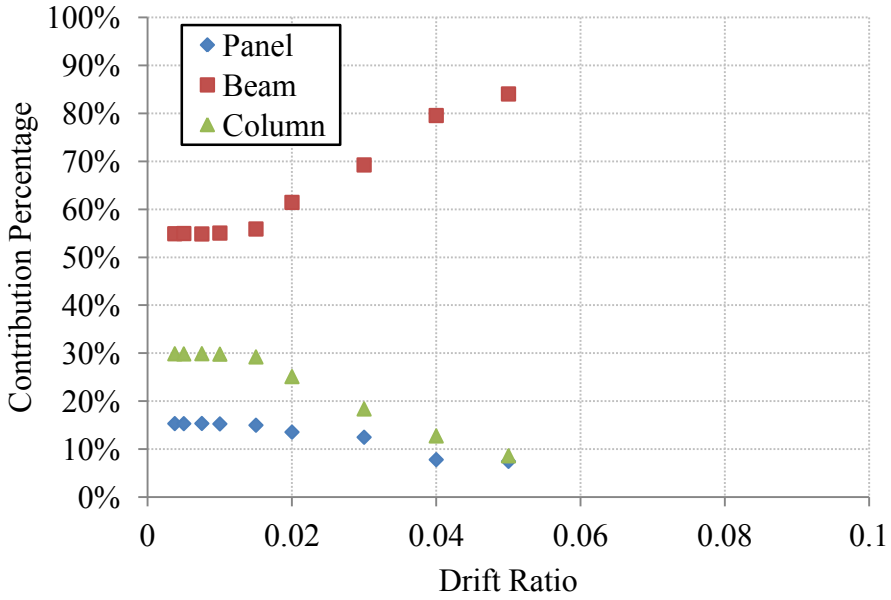

Figure 5.62 Evolution of the displacement contribution percentages of Specimen 6

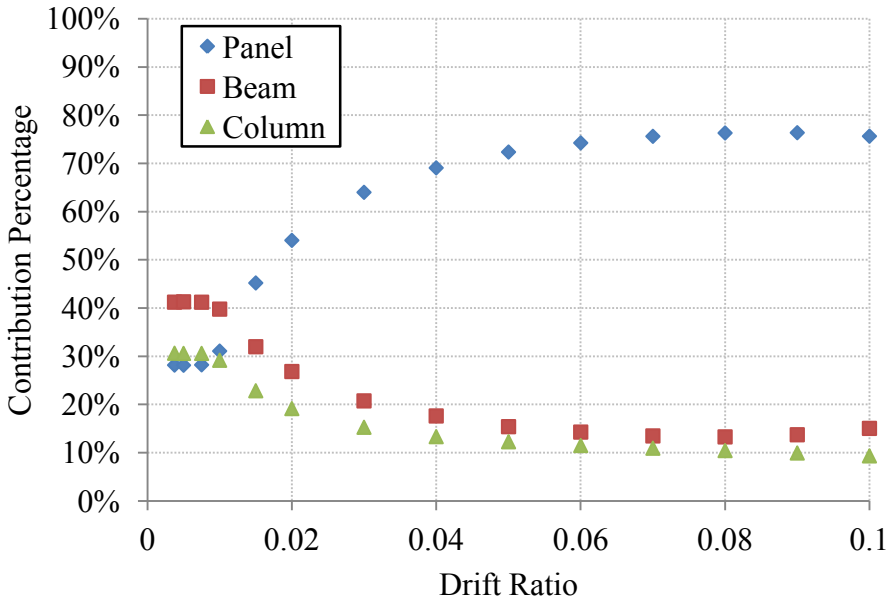

Figure 5.63 Evolution of the displacement contribution percentages of Specimen 7

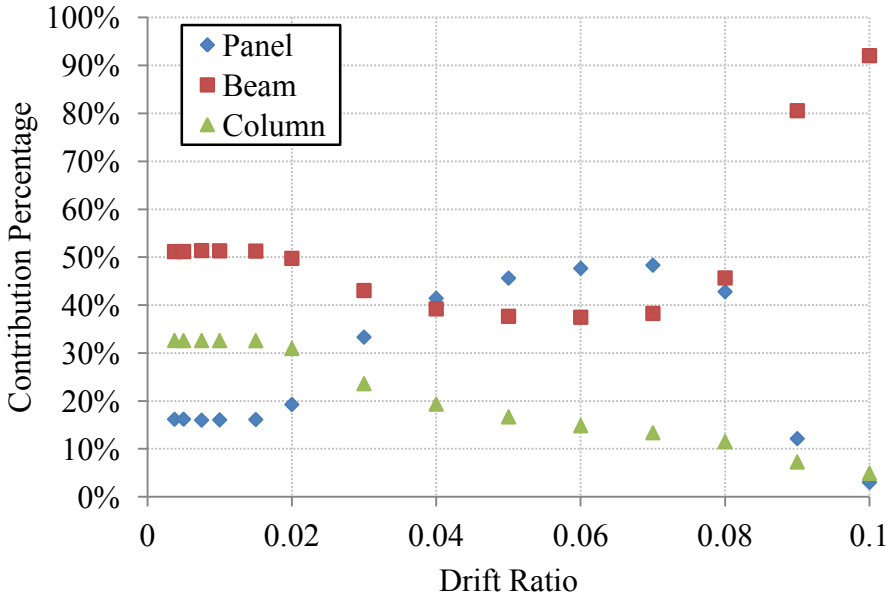

Figure 5.64 Evolution of the displacement contribution percentages of Specimen 8

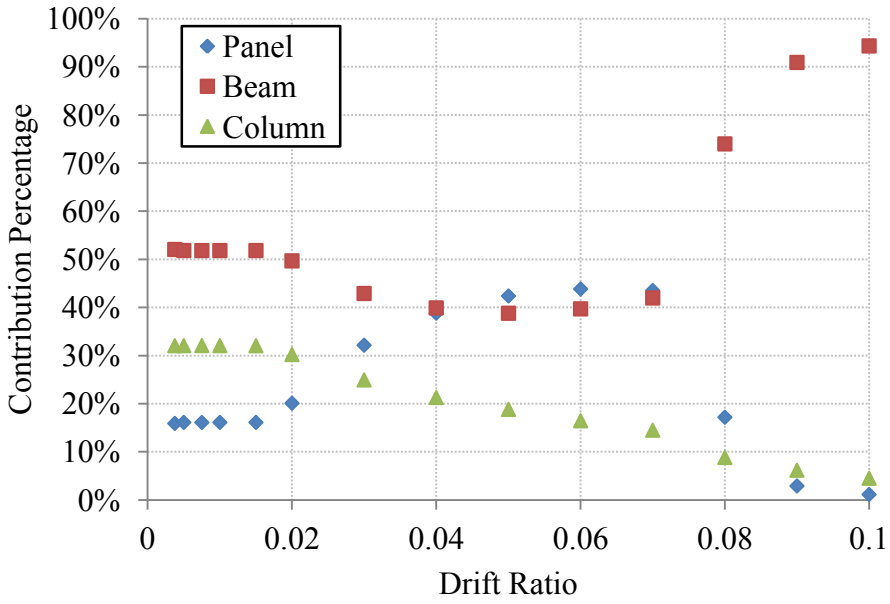

Figure 5.65 Evolution of the displacement contribution percentages of Specimen 9

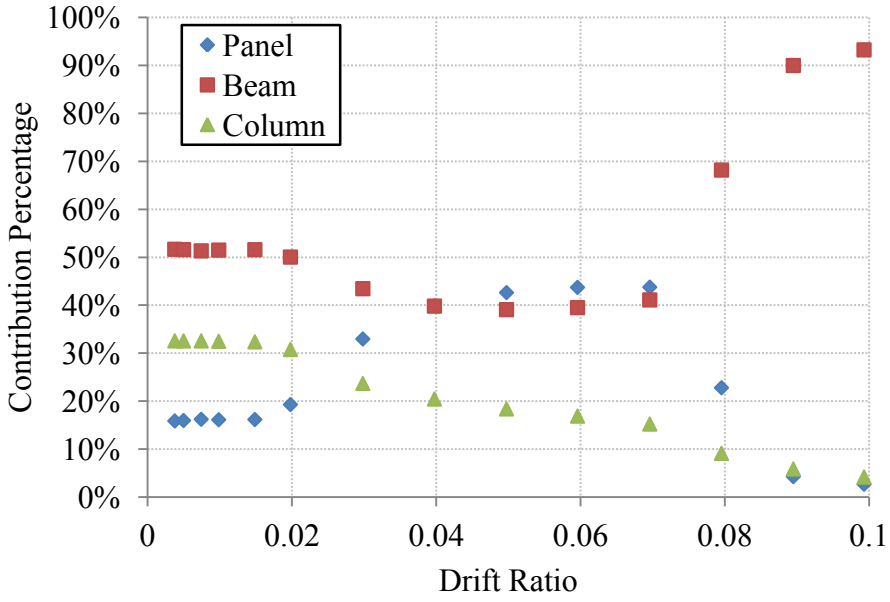

Figure 5.66 Evolution of the displacement contribution percentages of Specimen 10

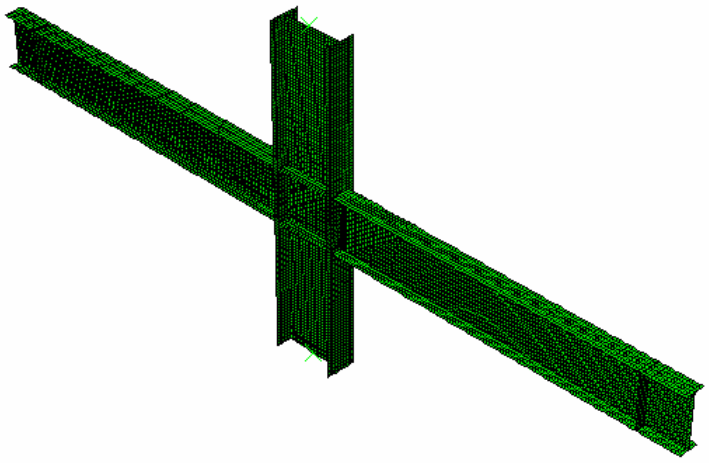

Figure 5.67 Global finite element model of Specimen 1

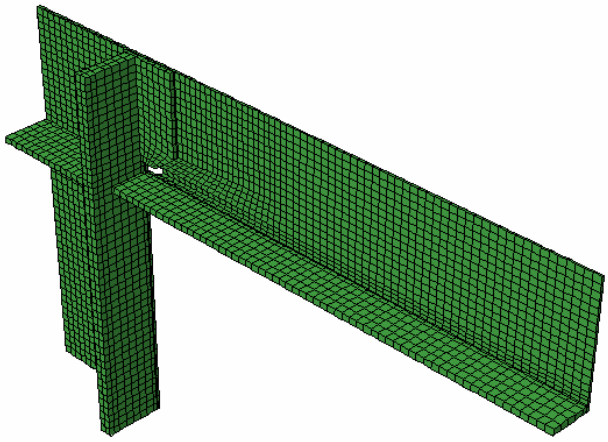

Figure 5.68 Local finite element model of Specimen 1

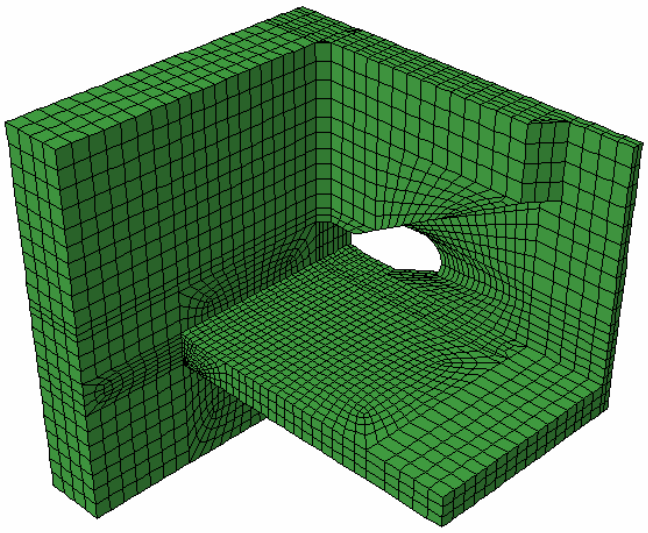

Figure 5.69 Sub-local finite element model of Specimen 1

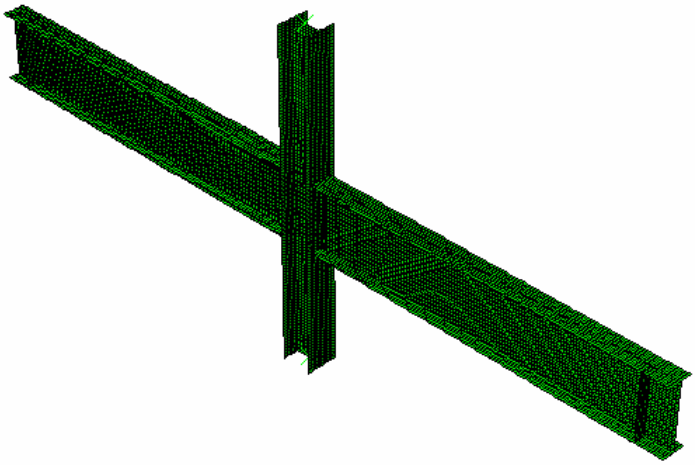

Figure 5.70 Global finite element model of Specimens 4 and 7

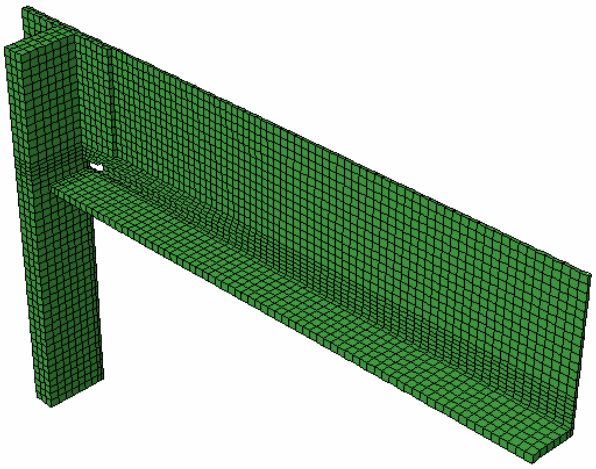

Figure 5.71 Local finite element model of Specimen 4

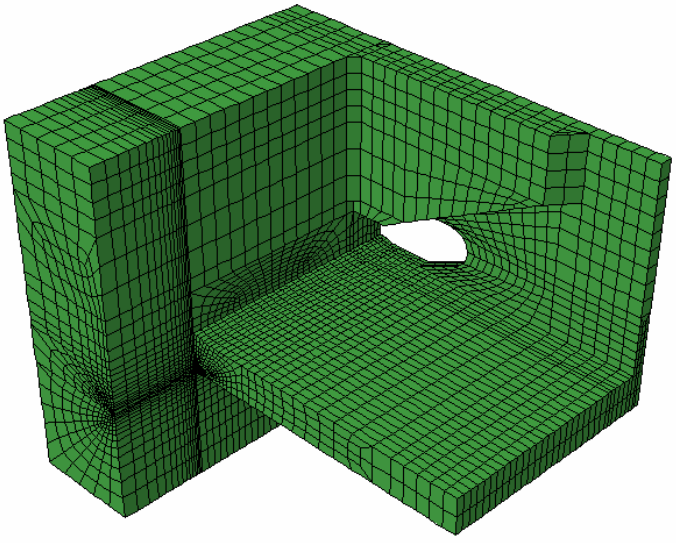

Figure 5.72 Sub-local finite element model of Specimen 4

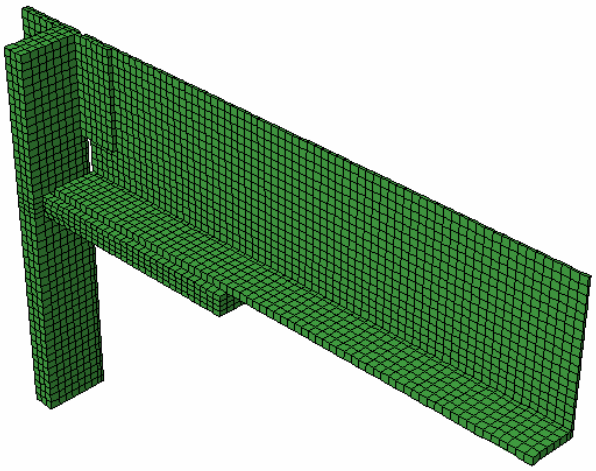

Figure 5.73 Local finite element model of Specimen 7

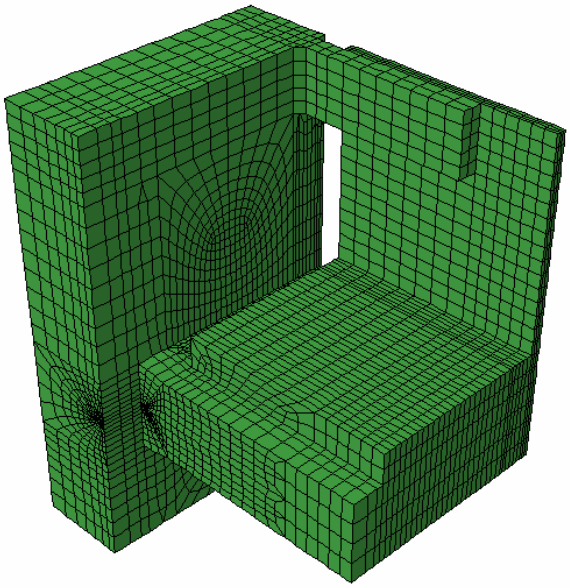

Figure 5.74 Sub-local finite element model of Specimen 7

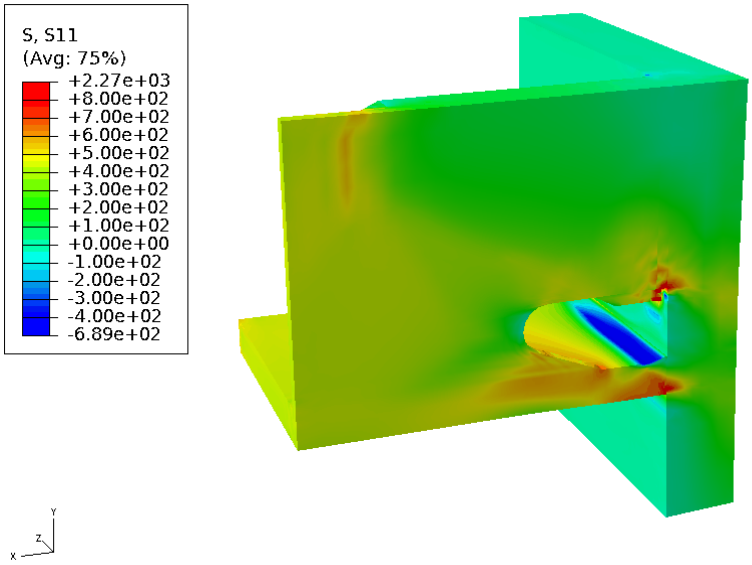

Figure 5.75 Contour of normal stress in the longitudinal direction – Specimen 1 sub-local model

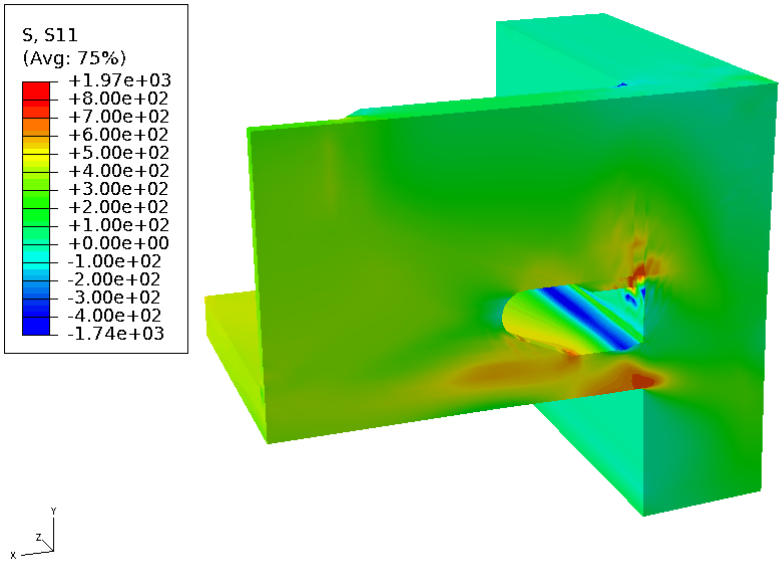

Figure 5.76 Contour of normal stress in the longitudinal direction – Specimen 4 sub-local model

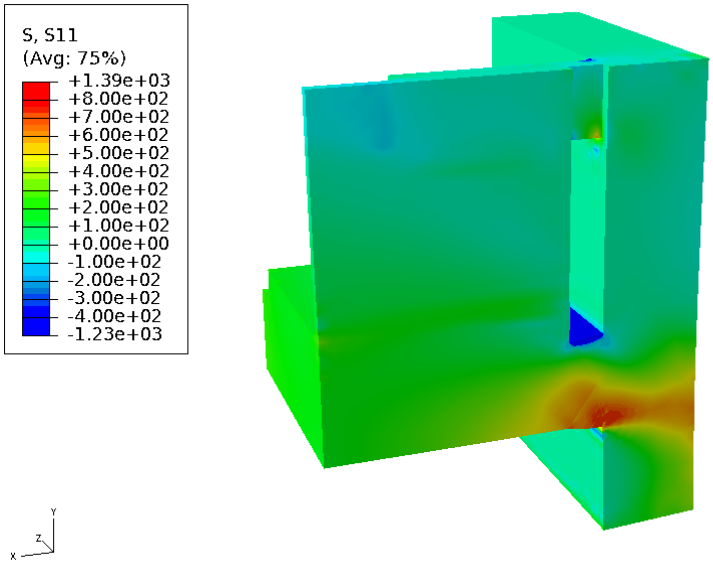

Figure 5.77 Contour of normal stress in the longitudinal direction – Specimen 7 sub-local model

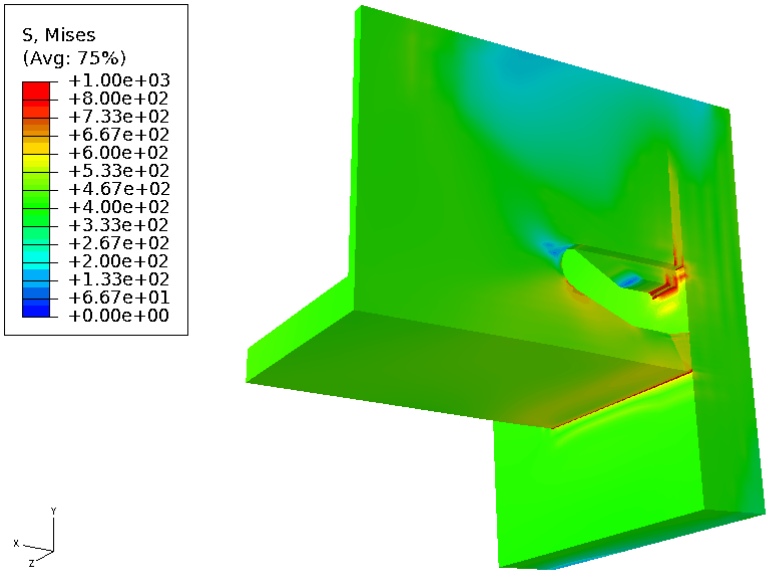

Figure 5.78 Von Mises stress contour of Specimen 1 sub-local model

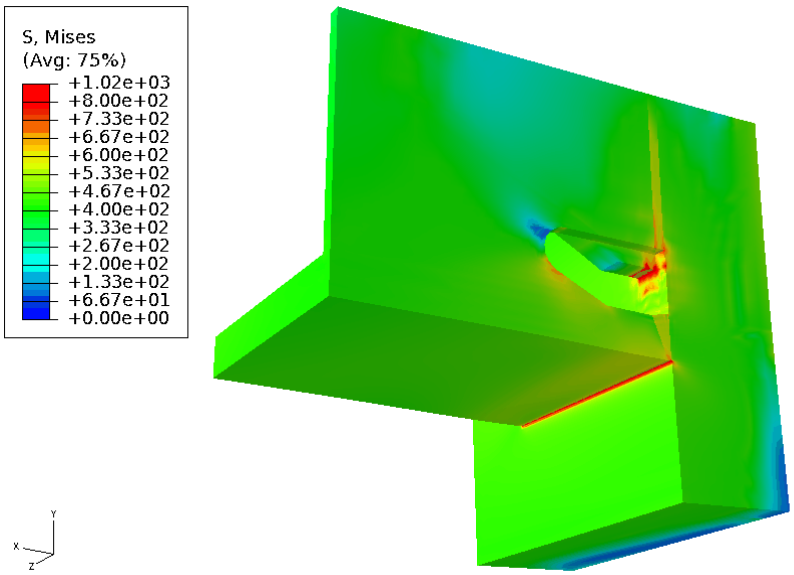

Figure 5.79 Von Mises stress contour of Specimen 4 sub-local model

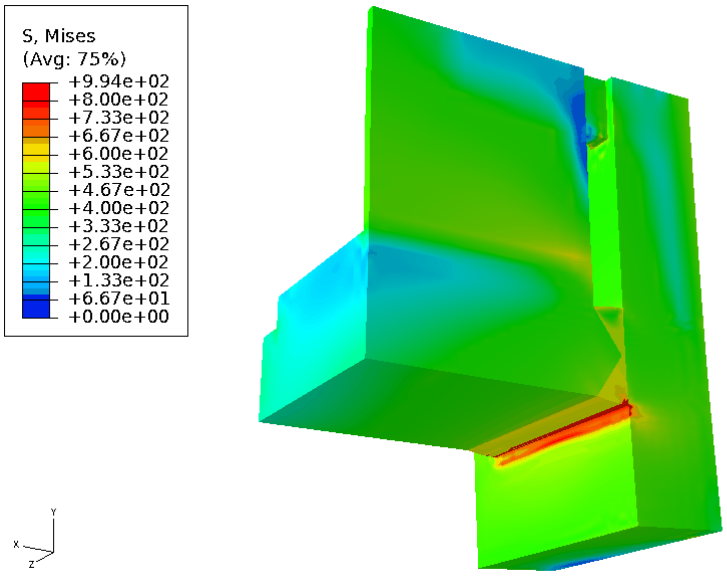

Figure 5.80 Von Mises stress contour of Specimen 7 sub-local model

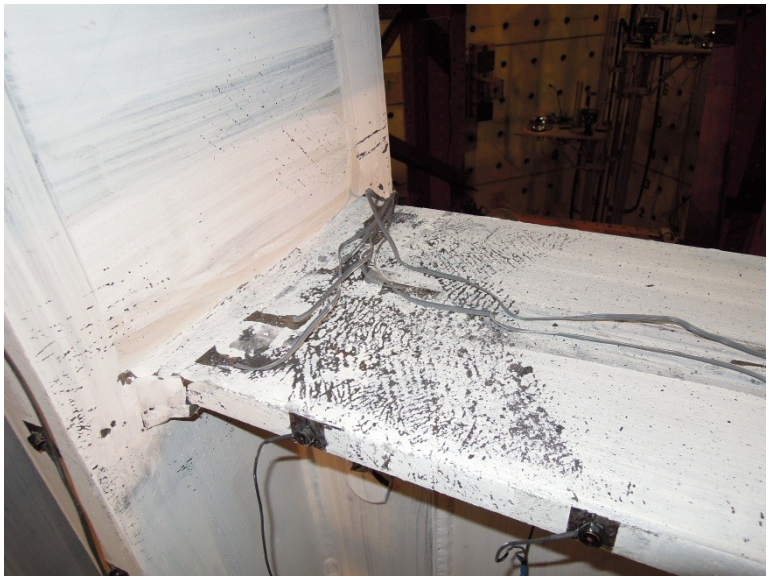

Figure 5.81 Photo of the east beam top flange of Specimen 4 after the first loading cycle of 4% drift ratio

Figure 5.82 Photo of the west beam bottom flange of Specimen 4 after the second loading cycle of 6% drift ratio

Figure 5.83 Photo of the east beam bottom flange of Specimen 4 after the first loading cycle of 7% drift ratio

Figure 5.84 Photo of the east beam bottom flange of Specimen 4 when the final fracture occurred

APPENDIX B

TABLES

Table 2.1 Analyses matrix of the 30 notched round bar models subject to constant strain amplitude cyclic loadings

Steel Grades	AP50		AP70		AP110	
Notch Radii (mm)	1	2	1	2	1	2
Strain Amp. (%)	0~0.6	0~0.6	0~0.6	0~0.6	0~0.6	0~0.6
	0~0.8	0~0.8	0~0.8	0~0.8	0~0.8	0~0.8
	0~1.0	0~1.0	0~1.0	0~1.0	0~1.0	0~1.0
	0~1.2	0~1.2	0~1.2	0~1.2	0~1.2	0~1.2
	0~1.4	0~1.4	0~1.4	0~1.4	0~1.4	0~1.4

Table 3.1 Material identification indices used in a loading cycle

t(s)	0	0.2	0.4	0.6	0.8	1.0	1.2	1.4	1.6	1.8	2.0	2.2	2.4	2.6	2.8	3.0	3.2	3.4	3.6	3.8	4.0
A	0	1	2	3	4	5	6	7	8	9	10	9	8	7	6	5	4	3	2	1	0
B	0	2	4	6	8	10	12	14	16	18	20	18	16	14	12	10	8	6	4	2	0
C	0	3	6	9	12	15	18	21	24	27	30	27	24	21	18	15	12	9	6	3	0

Table 3.2 Allocation percentage created for three synthetic materials, of the time elapsed in each stage of the crack initiation progression

Type	Stage I	Stage II	Stage III
A	30%	30%	40%
B	20%	60%	20%
C	50%	20%	30%

Table 3.3 Parameters of the 4 competitive FTDNNs used in the dynamic array

Network	Number of Time Delays	Number of Neurons in the Hidden Layers
1	6	15, 6
2	6	10, 4
3	12	8, 4
4	3	8, 4

Table 4.1 Number of cycles at each strain amplitude of the basic loading mode

Strain Amplitude (%)	Number of Cycles
±0.0075	6
±0.01	6
±0.015	6
±0.02	4
±0.03	2
±0.04	2
±0.06	2
±0.08	2
±0.1	2
±0.12	2
±0.14	2
±0.16	2
±0.18	2
±0.2	2

Table 4.2 Analyses matrix of the 60 notched round bar models subject to stepwise increasing strain amplitude cyclic loadings

Steel Grades	AP50		AP70		AP110	
Notch Radii (mm)	1	2	1	2	1	2
Magnification Factor of the Basic Loading Mode	1	1	1	1	1	1
	2	2	2	2	2	2
	3	3	3	3	3	3
	4	4	4	4	4	4
	5	5	5	5	5	5
	6	6	6	6	6	6
	7	7	7	7	7	7
	8	8	8	8	8	8
	9	9	9	9	9	9
	10	10	10	10	10	10

Table 4.3 Parameters of the 10 competitive FTDNNs used in the dynamic array

Network	Number of Time Delays	Number of Neurons in the Hidden Layers
1	6	15, 6
2	6	10, 4
3	12	8, 4
4	3	8, 4
5	8	12, 3
6	10	15, 5
7	12	8, 4
8	12	15, 4
9	4	6, 2
10	10	8, 4

Table 4.4 Parameters selected for linear transformations

θ_x	θ_y	θ_z	x_T(mm)	y_T(mm)	z_T(mm)
90˚	0˚	0˚	70	35	2.1
170˚	0˚	80˚	210	-21	0
115˚	29˚	57˚	140	-266	-3.5
0˚	90˚	0˚	350	0	-42
15˚	30˚	-30˚	3.5	-11.2	0
57˚	29˚	115˚	21	7	56
0˚	0˚	90˚	35	-3.5	70
29˚	57˚	115˚	490	-630	-252
57˚	115˚	29˚	700	0	0

Table 4.5 Selected tested specimens from published papers

Investigators	Denotation	Column Shape	Girder Shape	$t_{doubler\ plate}$ (in.)
Engelhardt et al. 2000	DBBWWPZ	W14×283	W36×150	N/A
Kim et al. 2010	SP2	H-300×300×10 ×15	H-400×200×8 ×13	N/A
Ricles et al. 2002	T2	W14×311	W36×150	N/A
	T3	W14×311	W36×150	N/A
Lee et al. 2005(a) and 2005(b)	CR1	W14×283	W24×94	N/A
	CR2	W14×193	W24×94	0.625
	CR3	W14×176	W24×94	2@0.5
	CR5	W14×145	W24×94	2@0.625

Table 4.6 Analytic model parameters of selected tested specimens

Denotation	Model Level	No. of Nodes	No. of Elements	Minimum Size (mm)
DBBW-WPZ	Global	14699	14438	30
	Local	29620	5134	20
	Sublocal	73704	16413	3
SP2	Global	11510	11352	15
	Local	15183	2433	15
	Sublocal	23870	4789	3
T2	Global	11119	10922	25
	Local	33113	5283	20
	Sublocal	79636	17760	3
T3	Global	11119	10922	25
	Local	33171	5289	20
	Sublocal	80907	18100	3
CR1	Global	12866	12565	20
	Local	14730	2296	20
	Sublocal	77800	17255	3
CR2	Global	12880	12608	20
	Local	14522	2166	20
	Sublocal	56566	12090	3
CR3	Global	13362	13126	20
	Local	14984	2241	20
	Sublocal	55387	11917	3
CR4	Global	12252	12254	20
	Local	13191	1950	20
	Sublocal	49960	10519	3

Table 5.1 Test matrix of newly designed beam-to-column joint specimens

Specimen Set	Specimen Denotation	Beam	Column	Doubler Plate Thickness (in.)	Beam to Column Connection	Ru/ ΦRn	Panel Zone Strength	Column Axial Stress (ksi)	Target Column Vertical Load (kips)
Deep Column Set	1	W30×108	W33×263	0	WUF-W	1.53	Very Weak	15.5	1200
	2	W30×108	W33×263	1/2	WUF-W	1.06	Balanced	15.5	1200
	3	W30×108	W33×263	2@1/2	WUF-W	0.85	Strong	15.5	1200
Jumbo Column Set	4	W36×150	W14×398	0	WUF-W	1.62	Very Weak	0	0
	5	W36×150	W14×398	2@1/2	WUF-W	1.13	Balanced	0	0
	6	W36×150	W14×398	2@9/8	WUF-W	0.9	Strong	0	0
	7	W36×150	W14×398	0	BFP	1.62	Very Weak	0	0
Small Column Set	8	W24×55	W12×106	5/8	WUF-W	1.63	Very Weak	0	0
	9	W24×55	W12×106	5/8	WUF-W	1.63	Very Weak	25	780
	10	W24×55	W12×106	5/8	WUF-W	1.63	Very Weak	varies*	varies*

* Tensile force in the column is 8 times the real-time magnitude of the horizontal load

Table 5.2 Analytic model parameters of newly designed specimens

Specimen	Model Level	No. of Nodes	No. of Elements	Minimum Size (mm)
1 ~ 3	Global	15918	15096	40
1	Local	28395	4557	25
	Sublocal	49062	10101	3
4 ~ 7	Global	18264	17458	40
4	Local	26245	4158	25
	Sublocal	104386	23567	3
7	Local	28124	4738	25
	Sublocal	118430	27327	3
8 ~ 10	Global	11160	10364	40

Table 5.3 Prediction of low cycle fatigue crack initiation life of several newly designed specimens made by artificial neural arrays

Specimen	Crack Initiation Life (s)	Loading Cycle
1	163.5	1@4%
4	198.2	1@5%
7	211.5	1@5%

APPENDIX C

COMBINED TRANSFORMATION COMPRISING RIGID TRANSLATION, ROTATION, AND NODAL DISPLACEMENT DUE TO EXTERNAL LOADING

Refer to Fig. C.1. It is assumed that a 2-D rectangular solid is subject to a tensile force in the *y* direction. The transformation of the top right corner can be derived as

$$\mathbf{\Delta_D} = \mathbf{X'} - \mathbf{X} = \begin{bmatrix} x_o' \\ y_o' \end{bmatrix} - \begin{bmatrix} x_o \\ y_o \end{bmatrix} = \begin{bmatrix} x_o + dx \\ y_o + dy \end{bmatrix} - \begin{bmatrix} x_o \\ y_o \end{bmatrix} = \begin{bmatrix} dx \\ dy \end{bmatrix} = \mathbf{D}, \tag{C-1}$$

where **D** is the nodal displacement output from finite element analysis.

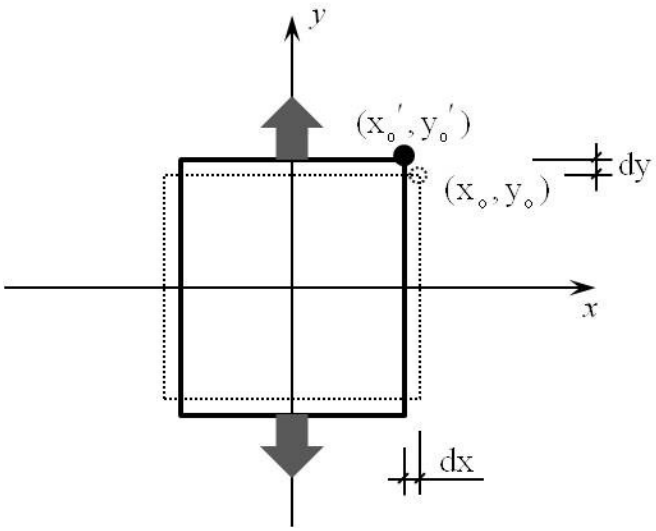

Figure C.1 Transformation due to external loading

Refer to Fig. C.2. If the same rectangular solid is subject to a rigid translation **T**, where the origin is translated to the point (x_T, y_T), the transformation of the top right corner is then

$$\mathbf{\Delta_T} = \mathbf{X'} - \mathbf{X} = \begin{bmatrix} x_o + x_T \\ y_o + y_T \end{bmatrix} - \begin{bmatrix} x_o \\ y_o \end{bmatrix} = \begin{bmatrix} x_T \\ y_T \end{bmatrix} = \mathbf{T}. \tag{C-2}$$

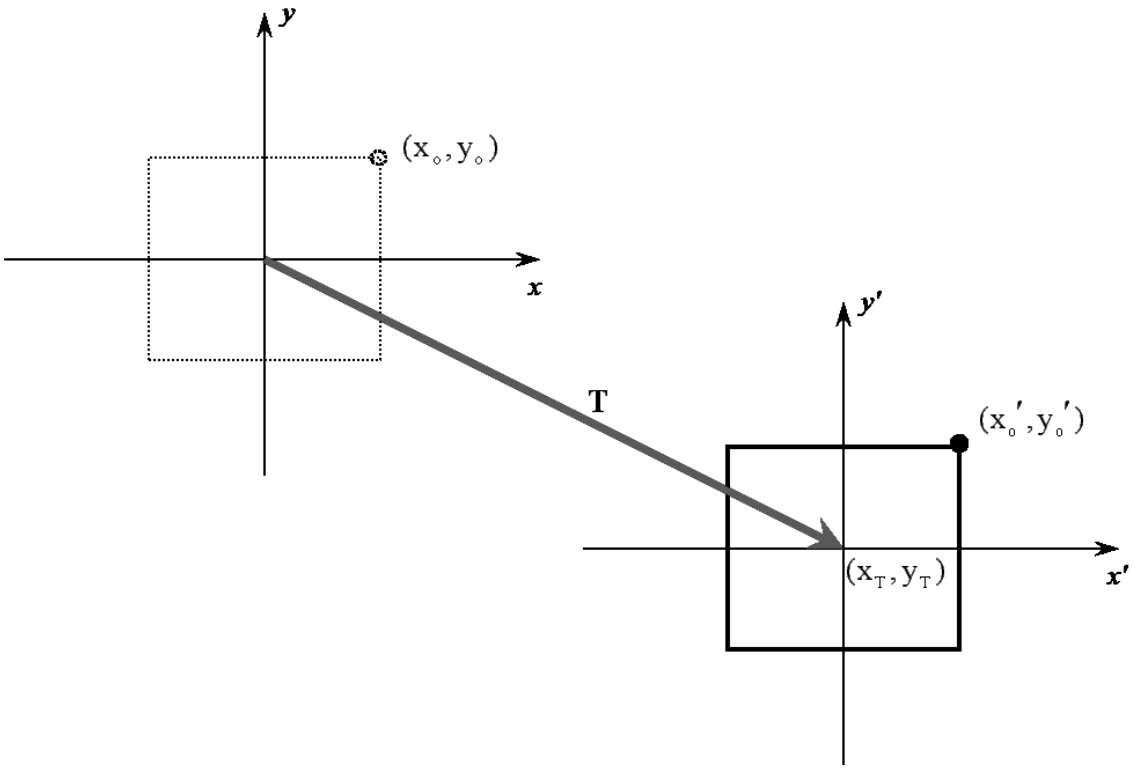

Figure C.2 Transformation due to rigid translation

Refer to Fig. C.3. The transformation of the same point due to a counter-clock rotation of angle θ about the origin can be derived as below,

$$\boldsymbol{\Delta}_{\mathbf{R}} = \mathbf{X}' - \mathbf{X} = \begin{bmatrix} x_o \cos\theta - y_o \sin\theta \\ x_o \sin\theta + y_o \cos\theta \end{bmatrix} - \begin{bmatrix} x_o \\ y_o \end{bmatrix} = \begin{bmatrix} \cos\theta & -\sin\theta \\ \sin\theta & \cos\theta \end{bmatrix} \begin{bmatrix} x_o \\ y_o \end{bmatrix} - \begin{bmatrix} x_o \\ y_o \end{bmatrix}$$

$$= \left(\begin{bmatrix} \cos\theta & -\sin\theta \\ \sin\theta & \cos\theta \end{bmatrix} - \begin{bmatrix} 1 & 0 \\ 0 & 1 \end{bmatrix} \right) \begin{bmatrix} x_o \\ y_o \end{bmatrix} = (R - I)\mathbf{X}, \qquad \text{(C-3)}$$

where R is the rotation matrix and I is the identity matrix.

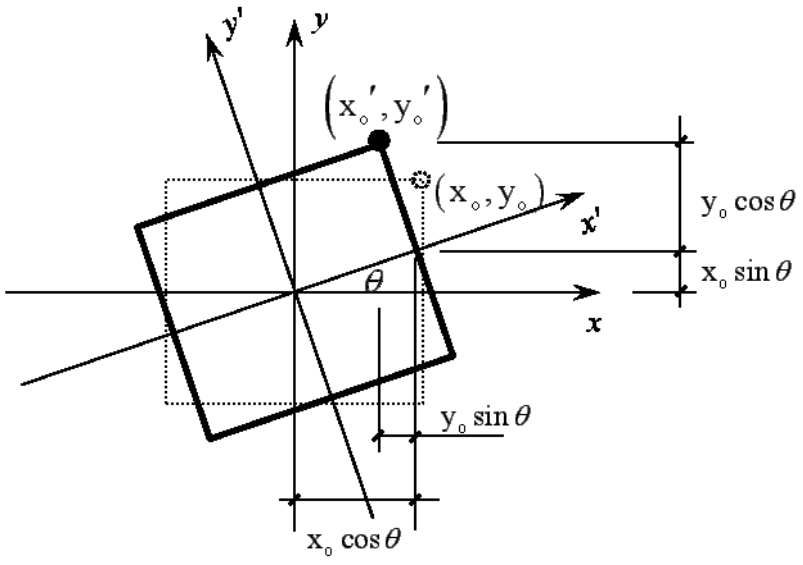

Figure C.3 Transformation due to counter-clock rotation

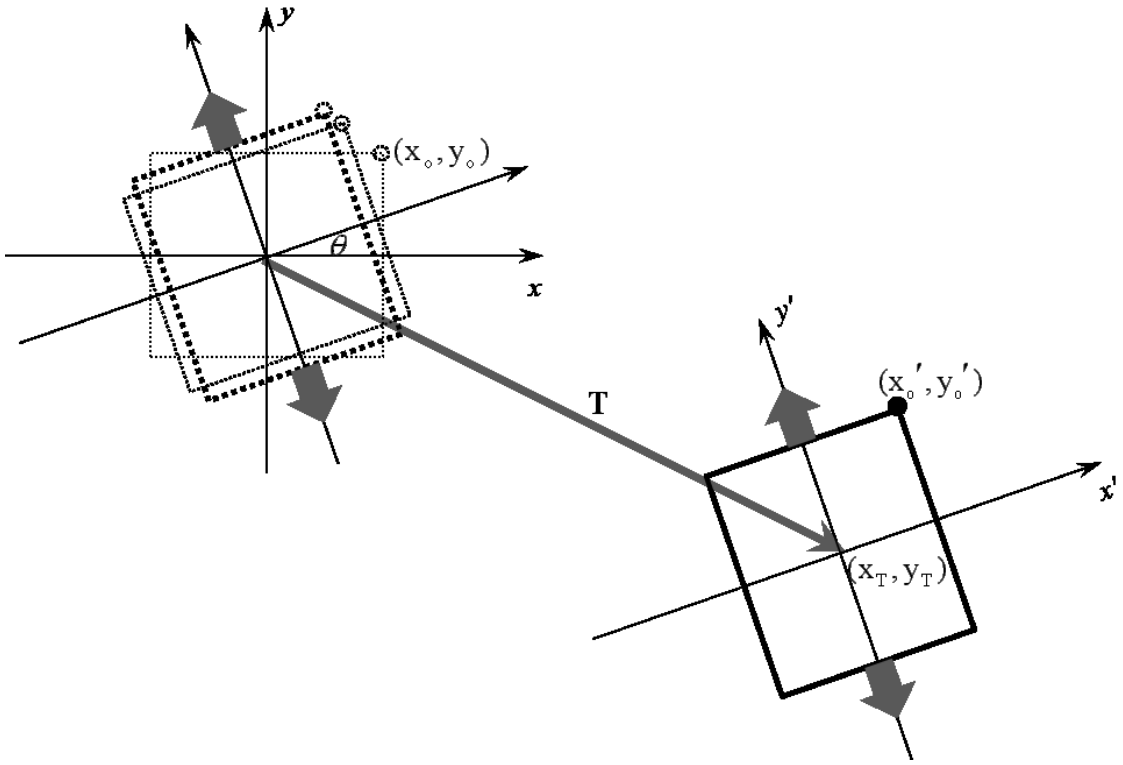

Figure C.4 Combined transformation

Figure C.4 shows a combined transformation associated with a rigid translation **T**, a rotation of angle θ about the origin, and a nodal displacement due to external loadings. This transformation has the following form:

$$\boldsymbol{\Delta}_{\mathbf{C}} = \mathbf{X}' - \mathbf{X} = \left(\begin{bmatrix} \mathrm{x}_{\mathrm{T}} \\ \mathrm{y}_{\mathrm{T}} \end{bmatrix} + \begin{bmatrix} (\mathrm{x}_{\mathrm{o}} + \mathrm{dx})\cos\theta - (\mathrm{y}_{\mathrm{o}} + \mathrm{dy})\sin\theta \\ (\mathrm{x}_{\mathrm{o}} + \mathrm{dx})\sin\theta + (\mathrm{y}_{\mathrm{o}} + \mathrm{dy})\cos\theta \end{bmatrix} \right) - \begin{bmatrix} \mathrm{x}_{\mathrm{o}} \\ \mathrm{y}_{\mathrm{o}} \end{bmatrix}$$

$$= \begin{bmatrix} \mathrm{x}_{\mathrm{T}} \\ \mathrm{y}_{\mathrm{T}} \end{bmatrix} + \begin{bmatrix} \cos\theta & -\sin\theta \\ \sin\theta & \cos\theta \end{bmatrix} \begin{bmatrix} \mathrm{x}_{\mathrm{o}} + \mathrm{dx} \\ \mathrm{y}_{\mathrm{o}} + \mathrm{dy} \end{bmatrix} - \begin{bmatrix} \mathrm{x}_{\mathrm{o}} \\ \mathrm{y}_{\mathrm{o}} \end{bmatrix}$$

$$= \begin{bmatrix} \mathrm{x}_{\mathrm{T}} \\ \mathrm{y}_{\mathrm{T}} \end{bmatrix} + \begin{bmatrix} \cos\theta & -\sin\theta \\ \sin\theta & \cos\theta \end{bmatrix} \begin{bmatrix} \mathrm{dx} \\ \mathrm{dy} \end{bmatrix} + \left(\begin{bmatrix} \cos\theta & -\sin\theta \\ \sin\theta & \cos\theta \end{bmatrix} - \begin{bmatrix} 1 & 0 \\ 0 & 1 \end{bmatrix} \right) \begin{bmatrix} \mathrm{x}_{\mathrm{o}} \\ \mathrm{y}_{\mathrm{o}} \end{bmatrix}$$

$$= \mathbf{T} + R\mathbf{D} + (R - I)\mathbf{X}. \tag{C-4}$$

For a 3-D solid in space, the aforementioned combined transformation of an arbitrary node belonging to the solid also has the expression of

$$\boldsymbol{\Delta}_{\mathbf{C}} = \mathbf{T} + R\mathbf{D} + (R - I)\mathbf{X}, \tag{C-5}$$

where $\mathbf{T} \equiv \begin{bmatrix} \mathrm{x}_{\mathrm{T}} & \mathrm{y}_{\mathrm{T}} & \mathrm{z}_{\mathrm{T}} \end{bmatrix}^T$, $\mathbf{D} \equiv \begin{bmatrix} \mathrm{dx} & \mathrm{dy} & \mathrm{dz} \end{bmatrix}^T$, $\mathbf{X} \equiv \begin{bmatrix} \mathrm{x}_{\mathrm{o}} & \mathrm{y}_{\mathrm{o}} & \mathrm{z}_{\mathrm{o}} \end{bmatrix}^T$, I is the three-dimension identity matrix and R is the rotation matrix. The spatial rotation matrix is the product of the three basic rotation matrices,

$$R = R_x R_y R_z \tag{C-6}$$

where R_x, R_y, and R_z correspond to the rotation about x, y, and z axis, respectively (as shown in Fig. C.5 ~ C.7), and are calculated as

$$R_x = \begin{bmatrix} 1 & 0 & 0 \\ 0 & \cos\theta_x & -\sin\theta_x \\ 0 & \sin\theta_x & \cos\theta_x \end{bmatrix}, \tag{C-7}$$

$$R_y = \begin{bmatrix} \cos\theta_y & 0 & \sin\theta_y \\ 0 & 1 & 0 \\ -\sin\theta_y & 0 & \cos\theta_y \end{bmatrix}, \tag{C-8}$$

$$R_z = \begin{bmatrix} \cos\theta_z & -\sin\theta_z & 0 \\ \sin\theta_z & \cos\theta_z & 0 \\ 0 & 0 & 1 \end{bmatrix}. \tag{C-9}$$

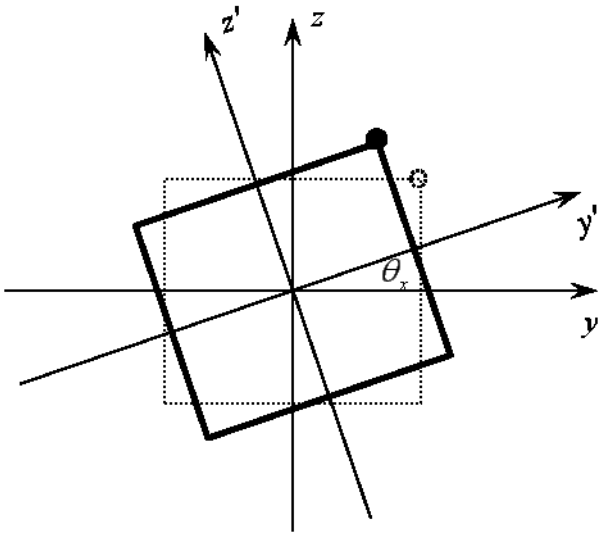

Figure C.5 Counter-clock rotation about *x* axis

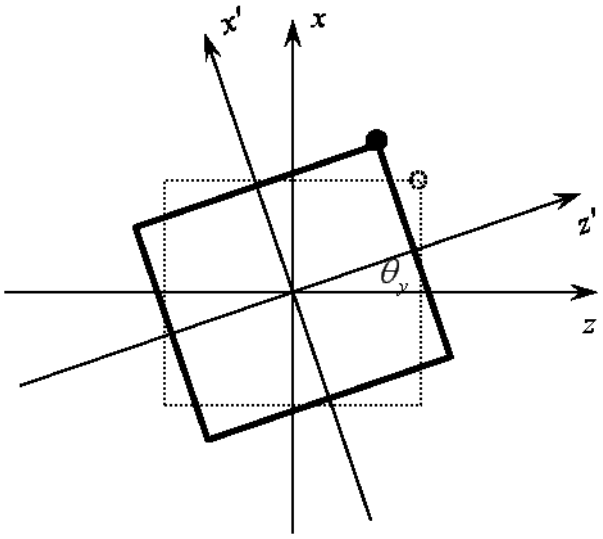

Figure C.6 Counter-clock rotation about *y* axis

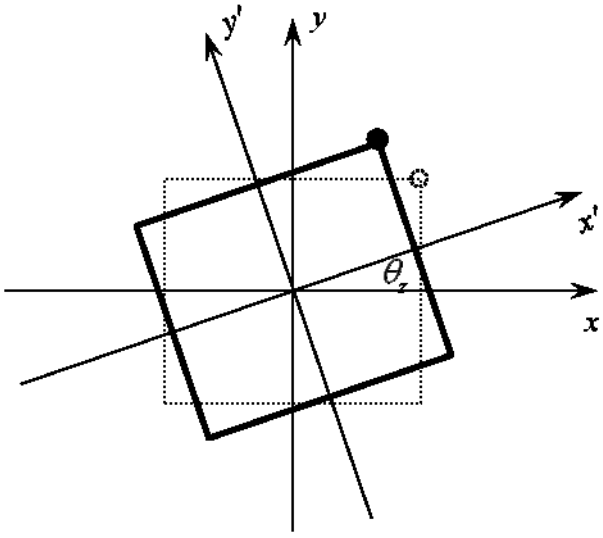

Figure C.7 Counter-clock rotation about *z* axis